Université du Québec
Institut National de la Recherche Scientifique
Centre Energie, Matériaux et Télécommunications

Design of 3-Dimensional Ni-based Electrocatalysts for the Oxygen Evolution Reaction

Par

Minghui Hao

Thèse présentée pour l'obtention du grade de

Philosophiae Doctor (Ph.D.)

en sciences de l'énergie et des matériaux

Jury d'évaluation

Président du jury et Examinateur interne	Ana Tavares Professeur à l'INRS-ÉMT
Examinateur externe	Elena Baranova Professeur à l'Université d'Ottawa
Examinateur externe	Bruno Pollet Professeur à l'Université du Québec à Trois-Rivières
Directeur de recherche	Daniel Guay Professeur à l'INRS-ÉMT

REMERCIEMENTS

RÉSUMÉ

L'electrolyse de l'eau est reconnue comme l'une des technologies les plus prometteuses pour la conversion d'énergie durable. Un processus typique d'électrolyse de l'eau implique deux réactions de dégagement de gaz (GER), à savoir la réaction de dégagement d'hydrogène (HER) et la réaction de dégagement d'oxygène (OER). Pour obtenir une OER hautement efficace, l'atténuation de l'apport d'énergie élevé causé par ses 4 processus de transfert d'électrons et le transport de masse des produits d'oxygène est la clé. Les catalyseurs à base de Ni sont des matériaux alternatifs aux catalyseurs de métaux nobles pour l'OER en milieu alcalin grâce à leur riche abondance et leur haute résistance à la corrosion électrolytique. En termes d'activité intrinsèque pour l'OER, en général, le Ni métallique ou ses entités catalytiques réelles, soit le $Ni(OH)_2$/NiOOH, sont beaucoup moins actifs que IrO_2 ou RuO_2. Notamment, après nano-structuration et fonctionnalisation de la surface, son activité apparente pourrait être compétitive ou supérieure à celle de IrO_2 ou RuO_2. Les nanostructures pourraient conférer aux électrodes non seulement une grande surface, mais également des propriétés aérophobes, facilitant la libération de bulles pour le GER. Les modifications hétéroatomiques de la surface du catalyseur aident à améliorer l'activité intrinsèque, y compris la fréquence de renouvellement et l'hydrophilie locale. Il serait impératif d'apprendre comment ces deux approches se sont construites ensemble pour les catalyseurs d'OER de nouvelle génération.

Dans cette thèse de doctorat, nous avons étudié des électrodes Ni avec des architectures 3D pour l'OER par électrodéposition. Dans le premier projet, nous avons synthétisé des réseaux de nanofils de Ni (Ni NW) en utilisant l'électrodéposition de systèmes modèles à travers une membrane poreuse en oxyde d'aluminium. Cette nanostructure autoportante de Ni présente des surfaces électrochimiquement actives considérablement améliorées. Ce mérite conduit à une réduction concomitante de la surtension d'OER obtenue dans l'électrolyte de KOH 1M. Dans le deuxième et troisième projet, nous avons synthétisé des mousses de Ni fractal avec une méthode de modèle des bulles d'hydrogène. Ces mousses de Ni présentent une structure primaire poreuse et une structure secondaire plus poreuse de type chou-fleur. Ils peuvent développer une grande surface activée électrochimiquement, jusqu'à 270 fois celle d'une plaque de Ni. Ils présentent également un caractère super-aérophobe qui maximise la surface de contact entre l'électrolyte et les sites actifs de l'électrode, même dans des conditions de fort dégagement d'O_2. De plus, lorsqu'elle est décorée avec une quantité minimale d'Ir déposé par une réaction de remplacement galvanique, l'électrode 3D de Ni atteint une activité exceptionnelle pour l'OER, et ses conditions de mouillage dans la structure poreuse sont davantage améliorées, entraînant une surtension de 195 mV à 10 mA cm^{-2} et une pente de

Tafel de 46 mV déc^{-1}. Une telle activité fait de l'anode de Ni poreuse l'un des catalyseurs d'OER à base de Ni les plus performants rapportés à ce jour.

Mots clés : Nickel ; réseaux de nanofils ; électrode poreuse 3D ; électrolyse de l'eau alcaline ; super-aérophobie ; super-hydrophilie ; spectroscopie d'impédance électrochimique ; émission acoustique

ABSTRACT

Water electrolysis is recognized as one of the most promising technologies for sustainable energy conversion. A typical water electrolysis process involves two gas evolution reactions (GER), namely hydrogen evolution reaction (HER) and oxygen evolution reaction (OER). For achieving highly efficient OER, mitigating the high energy input caused by its 4 electron transfer processes and mass transport of oxygen products is the key. The Ni-base catalysts will be alternative materials of noble metal catalysts for OER in an alkaline medium thanks to their rich abundance and high resistance to electrolyte corrosion. In terms of intrinsic activity for OER, in general, metallic Ni or its actual catalytic entities $Ni(OH)_2$/NiOOH is much less active than IrO_2 or RuO_2. Notably, after nano-structuring and surface functionalization, its apparent activity could be competitive or superior to that of IrO_2 or RuO_2. Nanostructures could impart electrodes not only large surface area but also aero-phobic properties, facilitating the bubble releasing for GER. Heteroatom modifications of catalyst surface help improve intrinsic activity, including the turnover frequency and local hydrophilicity. It would be imperative to learn how those two approaches built up together for the new generation OER catalysts.

In this doctoral dissertation, we constructed Ni electrodes with 3D architectures for OER through electroplating. In the first project, we synthesized Ni nanowires (Ni NW) arrays using template electrodeposition through a porous aluminum oxide membrane. This self-supporting Ni nanostructure display significantly enhanced electrochemically active surfaces. This merit leads to a concomitant reduction of the OER overpotential obtained in 1M KOH electrolyte. In the second and third projects, we synthesized fractal Ni foams with a hydrogen bubble templating method. The Ni foams display a porous primary structure and a more porous cauliflower-like secondary structure. They can develop a large and electrochemically activated surface area, up to 270 times that of a Ni plate. They also exhibit a super-aerophobic character responsible for maximizing the contact area between the active sites of electrode and electrolyte, even under conditions of high O_2 evolution. In addition, when decorated with a minimal amount of Ir by the galvanic replacement reaction, the 3D Ni electrode achieves an outstanding activity for OER, and its wetting condition in the porous structure is further improved, resulting in an overvoltage of 195 mV at 10mA cm^{-2} and a Tafel slope of 46 mV dec^{-1}. Such activity makes the porous Ni anode one of the best performing Ni-based OER catalysts reported to date.

Keywords: Nickel; nanowire arrays; 3D porous electrode; alkaline water electrolysis; super-aerophobicity; super-hydrophilicity; electrochemical impedance spectroscopy; acoustic emission

SOMMAIRE RÉCAPITULATIF

1.1   Contexte

Les énergies renouvelables variables (ERVs), telles que l'énergie solaire et l'énergie éolienne, sont des sources d'énergie prometteuses pour les activités humaines. Cependant, en raison de leur nature intermittente et des demandes énergétiques inconstantes des activités humaines, leur intégration directe dans le réseau électrique est limitée par les coupures d'énergie. Le monde a besoin d'un système de stockage d'énergie pour les ERVs afin d'élargir la pénétration des énergies renouvelables dans le portefeuille énergétique et ainsi réduire les émissions de CO_2 et atténuer la crise énergétique. Un système "Power-to-gas" est composé d'une série de technologies qui convertissent les énergies instantanées en combustible gazeux stable, tel que les énergies renouvelables ou l'énergie excédentaire dans les réseaux électriques. Il offre une perspective prometteuse pour résoudre la crise énergétique à laquelle notre société humaine est confrontée.

Dans un projet du type "power-to-gas" (Figure 2.1), « l'hydrogène vert » produit à partir d'énergie renouvelable par électrolyse de l'eau peut être distribué à divers utilisateurs finaux (tels que l'industrie, les transports, les bâtiments et les centrales électriques) et être reconverti en électricité grâce aux piles à combustible lorsque nécessaire. Plus encore, l'hydrogène vert pourrait être utilisé dans le procédé de méthanisation pour produire du méthane à partir du CO_2. L'hydrogène agit comme un vecteur énergétique idéal pour la conversion de l'énergie. C'est l'élément le plus abondant sur terre. Lorsqu'il entre dans le cycle énergétique "power-to-gas" et "gas-to-power", aucun polluant n'est émis. La génération d'électricité à partir de H_2 via une pile à combustible est plus efficace que la combustion de combustibles fossiles via les moteurs à combustion interne conventionnels, car ces derniers sont soumis à la limitation du cycle de Carnot. La densité énergétique de l'hydrogène (143 MJ kg^{-1}) est presque trois fois supérieure à celle des carburants à base d'hydrocarbures (environ 50 MJ kg^{-1}). L'établissement d'un réseau de gaz utilisant l'hydrogène comme vecteur énergétique peut réduire considérablement le coût de la distribution d'énergie. Par exemple, le coût de transport de l'hydrogène par gazoduc est environ 10 à 20 fois inférieur au coût de transport de l'électricité par câble, alors que ce dernier souffre des pertes d'énergie par transport d'électricité.

Par conséquent, la promotion de la production d'hydrogène vert à grande échelle (à l'échelle du gigawatt) est nécessaire pour atteindre prochainement des émissions nettes nulles. Cependant, le déploiement des projets "power-to-gas" est principalement freiné par le coût élevé de la production d'hydrogène. Actuellement, le coût de l'hydrogène vert est estimé à 4-6 \$/kg, tandis que l'hydrogène produit industriellement par reformage du méthane coûte environ 1 \$/kg. Cet obstacle lié au coût de production de l'hydrogène est atténué par les

innovations dans le développement d'électrolyseurs d'eau rentables et performants et par la forte baisse du prix de l'électricité des énergies renouvelables, qu'on observe depuis la dernière décennie. Selon l'Agence internationale pour les énergies renouvelables (IRENA), une réduction de 80% du coût de l'hydrogène peut être atteinte prochainement en combinant des percées dans les prix de l'électricité, les coûts d'investissement de l'électrolyseur, l'efficacité de l'électrolyseur, *etc.* (Figure 2.2).

Pour atteindre une efficacité élevée de dégagement d'hydrogène, la tension de la cellule pour entraîner l'ensemble du système d'électrolyse doit être réduite. La haute tension pour l'électrolyse électrochimique de l'eau est principalement causée par les surtensions des deux réactions de dégagement gazeux, à savoir la réaction de dégagement d'hydrogène (HER) à la cathode et la réaction de dégagement d'oxygène (OER) à l'anode. Les surtensions dépendent fortement de l'électrocatalytique des matériaux. Par conséquent, la recherche de matériaux électrocatalytiques appropriés (hautement actifs, abondants sur terre et électrochimiquement stables) pour l'OER et la HER est la tâche la plus urgente et la plus difficile pour développer l'électrolyse de l'eau et doit être accomplie grâce à des conceptions rationnelles de matériaux d'électrode. Au cours des dernières décennies, des efforts continus ont été consacrés à la réduction des surtensions pour l'OER et la HER. Ce travail se concentre principalement sur deux approches : soit augmenter le rapport surface/volume des catalyseurs grâce à la nanotechnologie et augmenter l'activité intrinsèque de chaque site actif grâce à des ajustements fins des énergies libres d'adsorption pour les intermédiaires de réaction comme H* ou HO*.

La recherche de matériaux alternatifs pour les catalyseurs avancés de métaux nobles afin de réduire les coûts d'investissement des électrolyseurs a conduit à de nombreuses innovations en matière d'électrocatalyseurs. Les matériaux à base de métaux de transition 3D sont des alternatives prometteuses en raison de leur faible prix, de leur bonne stabilité et de leur activité élevée. D'énormes efforts ont été consacrés au développement d'électrocatalyseurs d'OER à base de Ni pour les électrolyseurs d'eau alcaline. L'incorporation d'hétéroatomes dans des composés Ni est l'une des approches les plus prometteuses pour optimiser l'activité intrinsèque du matériau Ni. De plus, les effets de défauts induits par l'incorporation d'hétéroatomes pourraient contribuer à améliorer intrinsèquement les conditions de mouillage du matériau nanostructuré.

Lors de la construction de matériaux Ni structurés en 3D haute performance, il est impératif d'améliorer les propriétés de mouillage de la surface de l'électrode. Aux fortes densités de courant, les bulles d'hydrogène et d'oxygène générées à l'interface électrode/électrolyte couvrent une grande partie de la surface de l'électrode, bloquant ainsi partiellement les sites

actifs de l'électrode. La présence d'une bulle provoque une augmentation de la résistance de la solution et une diminution notable de la surface électrochimiquement active (EASA). Les deux effets entraînent une augmentation de la tension de la cellule.

Dernièrement, les électrodes super-aérophobes pour les applications dans les réactions de dégagement de gaz ont reçu de plus en plus d'attention. En effet, la mouillabilité de ces électrodes super-aérophobes peuvent faciliter le détachement des bulles des électrodes et par conséquent diminuer la couverture des bulles sur la surface des électrodes, réduisant ainsi la surtension pour l'OER et la HER aux fortes densités de courant. Cependant, peu de travaux ont été effectués pour corréler le comportement des bulles avec la propriété super-aérophobe des électrodes afin d'optimiser leur activité catalytique, peut-être en raison de l'absence d'une méthode appropriée pour évaluer le comportement des bulles lors des réactions gazeuses. De plus, l'hydrophilie apparente ne doit pas être le seul facteur à prendre en compte pour décrire la capacité d'une électrode poreuse tridimensionnelle à libérer des bulles lors du dégagement dynamique de gaz, la capillarité dans les milieux poreux doit également être pris en considération. Dans un tel contexte, un suivi *in-operando* du comportement des bulles, notamment de leur piégeage dans l'électrode poreuse et de leurs effets sur la surtension de réaction, est essentiel.

1.2   Hypothèses et Méthodologie

La construction de structures d'électrodes tridimensionnelles (3D) avec un rapport surface/volume élevé est bénéfique pour le développement de catalyseurs pour la OER. Les électrodes 3D pour l'OER sont classiquement synthétisées en utilisant des mousses de Ni comme support, et des structures spécifiques telles que des nanofils et des nanofeuilles sont généralement les sous-structures des architectures hiérarchiques. Cependant, la taille des pores des mousses de Ni commerciales est de l'ordre de centaines de microns, ce qui pourrait limiter le rapport surface/volume. Par conséquent, la construction d'électrodes Ni compactes, poreuses et autoportantes est la première option de notre stratégie de conception. Une promotion drastique de l'activité pour la OER est attendue grâce à cette tentative en raison de l'augmentation de l'EASA du matériau Ni. Cet effet sera étroitement étudié à travers les déterminations de l'EASA et les tests de la performance pour l'OER des matériaux synthétisés. De plus, la taille des pores ou l'espacement des parois volontairement réduits dans l'électrode poreuse pourrait contribuer à améliorer l'hydrophilie des structures, et donc à réduire le blocage de l'oxygène des sites actifs selon l'équation Equation 2.13, notamment parce que la pression capillaire pour les pores étroits peut contribuer à empêcher l'invasion de gaz pendant l'OER. Néanmoins, cet effet doit être évalué avec prudence, car le transport d'oxygène dans les milieux poreux pourrait laisser du gaz stationnaire piégé dans les structures. Les

vérifications de l'accessibilité des pores étroits à l'électrolyte et de leur activité pour l'OER exigent une foule d'analyses à partir de différentes technologies de caractérisation.

Une autre tentative de cette thèse consiste à appliquer une modification d'hétéroatome au squelette de Ni 3D conçue pour améliorer encore son activité pour l'OER. Les identifications des compositions de surface et leur effet sur l'activité pour l'OER doivent être évalués.

Dans l'ensemble, la conception rationnelle de catalyseurs Ni applicables à la réaction de dégagement d'oxygène nécessite une compréhension approfondie des paramètres affectant la structure, la morphologie et la composition des espèces de surface des matériaux. Dans cette thèse, plusieurs méthodes de caractérisation telles que la microscopie électronique à balayage (SEM), La microscopie électronique à transmission (MET), la spectroscopie photoélectronique à rayons X (XPS) et les caractérisations électrochimiques (EC) sont utilisées pour obtenir la meilleure compréhension des propriétés physiques et électrochimiques des matériaux synthétisés. De plus, la technologie de détection d'émission acoustique *in-operando* a été récemment développée pour surveiller le transport des bulles d'oxygène dans l'électrode 3D.

1.3   Objectives

À travers ce travail de thèse, nous nous concentrons sur le développement d'électro-catalyseurs de Ni nanostructurés en 3D pour l'électrolyse de l'eau en milieu alcalin. L'objectif de recherche comprend : i) la fabrication d'électrodes Ni tridimensionnelles conçues pour optimiser les performances de l'électrolyse de l'eau en milieu alcalin ; ii) des méthodes de fonctionnalisation des électrodes Ni 3D par dopage pour de meilleures activités catalytiques intrinsèques ; iii) des méthodes pour réduire l'occupation des bulles à la surface de l'électrode, à la fois en surface et dans la structure poreuse, pendant le dégagement gazeux. Ces objectifs sont atteints à travers trois projets connexes :

- Réseaux de nanofils de Ni (Ni NW) autoportés pour l'OER lors de l'électrolyse alcaline de l'eau ;
- Modèle de bulle d'hydrogène des catalyseurs de mousse Ni fractale (Ni DHBT) pour l'OER en milieu alcalin ;
- Décoration de catalyseurs en mousse fractale de Ni (Ir/Ni DHBT) par l'Ir pour l'OER avec des études sur le comportement des bulles grâce à la détection d'émission acoustique *in-operando*.

1.4 Réalisation du premier projet

1.4.1 Synthèse des dépôts de Ni NW

L'électrodéposition galvanostatique de Ni a été réalisée à partir de solutions aqueuses de 0,1 M NiCl$_2$·6H$_2$O et de NH$_4$Cl 2 M à travers une membrane poreuse d'oxyde d'aluminium anodique (AAO). Une couche de titane (400 nm) a été pulvérisée en courant continu à l'arrière de l'AAO pour assurer le contact électrique obligatoire pour l'électrodéposition de Ni. Une électrode au calomel saturé (SCE) et une gaze de Pt ont été utilisées respectivement comme électrode de référence et contre-électrode. L'électrodéposition de Ni a été réalisée à l'aide d'un potentiostat (Solartron 1480) pendant des durées allant jusqu'à 3 h. Après l'électrodéposition de Ni, la membrane AAO a été dissoute dans du KOH 1 M pendant 1 h à température ambiante et soigneusement rincée avec de l'eau désionisée, et immédiatement caractérisée par les méthodes électrochimiques. Tous les potentiels mesurés dans 1 M KOH sont rapportés *vs.* RHE en utilisant E$_{RHE}$ = E$_{SCE}$ + 1,04 V. La surface géométrique des électrodes de travail en Ni était de 0,15 cm^2 dans tous les cas.

1.4.2 Caractérisation physique de Ni NW

Les observations TEM ont été effectuées avec un microscope électronique à transmission à balayage (FEI Titan 80–300) équipé d'une source d'électrons à émission de champ à haute luminosité et d'un spectromètre à perte d'énergie électronique ultrarapide (EEL). Dans les cas où une analyse en coupe transversale de la structure NW devait être effectuée, une zone ultramince a été soigneusement soulevée à l'aide de la technique du faisceau ionique focalisé (FIB). Les analyses de topographie de surface haute résolution ont été réalisées à l'aide du microscope FEI-Magellan SEM. La cartographie élémentaire détaillée nécessaire pour résoudre la distribution spatiale de Ni et O a été réalisée à l'aide de la technique de spectroscopie de perte d'énergie électronique (EELS) dans le TEM. Le processus impliquait une acquisition en série des spectres EEL à chaque pixel de l'image de champ sombre annulaire (ADF) et un traitement ultérieur pour extraire les bords Ni-L$_{2,3}$, O-K et Ti-L$_{2,3}$. La cartographie de la distribution spatiale de ces arêtes individuelles a révélé la distribution relative des éléments Ni, O et Ti, respectivement.

1.4.3 Caractérisation électrochimique et performances pour l'OER

La caractérisation électrochimique dans du KOH 1 M saturé avec le bullage d'argon a été réalisée dans une cellule électrochimique artisanale, en utilisant une gaze de Pt et une électrode au calomel saturée comme contre-électrode et l'électrode de référence, respectivement. Des voltammogrammes cycliques (CV) ont d'abord été enregistrés jusqu'à l'obtention de caractéristiques à l'état d'équilibre. Ensuite, les électrodes ont été soumises à

un potentiel en circuit ouvert (OCP) de 10 min avant l'enregistrement des courbes de chronopotentiométrie (CP) à 10 mA cm^{-2} pendant 30 min. La séquence ci-dessus a été systématiquement appliquée à toutes les électrodes rapportées. Les résultats ont été comparés avec une plaque de Ni commerciale et avec des films de Ni électrodéposés obtenus sans aucune membrane AAO sur la feuille de Ti. La résistance de la solution a été mesurée par spectroscopie d'impédance électrochimique (EIS) et utilisée pour corriger les potentiels des chutes ohmiques. Les mesures EIS dans la gamme de potentiel OER ont été obtenues après une polarisation de 10 min (avec potentiel de 1,5 à 1,6 V) entre 0,1 Hz et 200 kHz à l'aide d'un analyseur de fréquence (Solartron 1255B). Les spectres d'impédance électrochimique ont été ajustés à des modèles de circuits équivalents à l'aide du programme d'ajustement complexe des moindres carrés non linéaires (CNLS) dans Zview (Scribner Associates).

1.4.4 Résultat et discussion

La Figure 4.2 illustre les vues de dessus et en section des Ni NWs synthétisés. L'image SEM à faible grossissement (Figure 4.2a) révèle un emballage relativement dense des faisceaux de nanofils ressemblant à celui d'une structure de réseau en forme de brosse. Comme le montre la Figure 4.2b, une image SEM détaillée à haute résolution indique que certains nanofils ont une section transversale oblongue (petit diamètre = 310 nm et grand diamètre = 410 nm), mais la plupart d'entre eux ont une section transversale circulaire. La Figure 4.2c illustre la structure en coupe transversale. Une mesure de la taille sur la longueur des nanofils indique que les Ni NWs synthétisés vierges mesuraient généralement environ 12 μm de longueur.

La surface électrochimiquement active (EASA) des réseaux de nanofils tels que synthétisés a été évaluée par CV dans 1 M KOH à 25 mV s^{-1} (Figure 4.9A). La charge pendant le balayage vers l'avant, Q_a, a été utilisée pour évaluer l'EASA de Ni. En effet, dans cette gamme de potentiel (-0,10 et 0,45 V), le Ni peut être oxydé de manière réversible en α-Ni(OH)$_2$ lors du balayage de potentiel direct, et réduit en Ni métallique lors du balayage arrière. Après 150 cycles potentiels, des réponses CV à l'état d'équilibre sont obtenues, avec un exemple représentatif affiché à la Figure 4.9. Les valeurs mesurées de Q_a se sont avérées proportionnelles à la longueur des nanofils (Figure 4.10), ce qui signifie que la conversion réversible Ni/α- Ni(OH)$_2$ se produit sur toute la longueur de Ni NW et que la surface globale des nanofils est accessible à l'électrolyte. La pente de la courbe est de 0,70 mC μm^{-1} est très proche de la pente attendue (0,55 mC μm^{-1}) calculée sur la base de considérations purement géométriques, en assumant des cylindres idéaux avec un diamètre, une longueur et une densité de surface similaires, et une hypothèse selon laquelle la charge de α-Ni(OH)$_2$ sur une surface idéale est de 0,514 mC cm^{-2}. La différence entre les valeurs prédites et mesurées peut

provenir de l'incertitude de la valeur d'étalonnage ou des diamètres mesurés, du fait que le diamètre NW varie légèrement de bas en haut et de la rugosité de surface à l'échelle nanométrique (Figure 4.6). Il convient de mentionner que l'ordonnée à l'origine de la ligne droite est différente de zéro. Une raison à cela pourrait être que le fond de chaque Ni NW à l'interface avec le film mince de Ti n'a pas une forme parfaitement cylindrique.

Des changements considérables se produisent dans le CV des nanofils de Ni lors de l'extension de la limite supérieure du potentiel de sommet à des valeurs plus élevées. Dans le premier CV suivant la plage de potentiel restreinte utilisée sur la Figure 4.9A, deux pics anodiques à 0,23 et 1,44 V ont été observés dans le balayage vers l'avant, et une seule contribution cathodique a été observée à 1,34 V dans le balayage vers l'arrière. La transition quasi réversible supérieure implique le processus bien connu de stockage de charge d'oxyde de nickel β-Ni(OH)$_2$/β-Ni(OOH). Le dixième profil voltamétrique n'affiche plus l'épaulement anodique à 0,23 V (voir Figure 4.9A et Figure 4.9B), et le pic anodique à 1,44 V et le pic cathodique à 1,34 V sont mieux définis que lors du premier CV. Ces observations démontrent que la plupart des espèces α-Ni(OH)$_2$ ne sont plus présentes, mais ont été converties en phases β-Ni(OH)$_2$, ce qui entraîne également une vitesse plus faible pour la réaction de dégagement d'hydrogène. Cela garantit que la charge Q_a mesurée était exclusivement associée à la formation d'espèces α-Ni(OH)$_2$. Des tentatives antérieures pour déterminer à la place l'EASA de Ni en utilisant la transition redox Ni(II)/Ni(III) à potentiel plus élevé ont été proposées, mais l'incertitude dans la porosité et la structure de ces phases multicouches rend la présente procédure plus fiable.

La formation de Ni NWs se traduit par une énorme augmentation de l'EASA. En utilisant Q_a comme mesure, l'EASA d'une plaque de Ni et d'un film mince de Ni électrodéposé de la même taille (0,15 cm^2) sont respectivement de 0,14 et 0,78 mC, contre 18,0 mC pour l'échantillon de réseau Ni NW avec le plus long (19 µm) nanofil. Il s'agit d'un facteur de 130 et 10 d'augmentation de l'EASA, respectivement. Dans ce qui suit, nous déterminerons si toute la surface des nanofils est accessible à l'électrolyte et capable de participer à la réaction de dégagement d'oxygène ou si la limitation du transport de masse de l'oxygène dissous, la migration ionique dans les pores, ou des effets d'occlusion de bulles se produisent, limitant ainsi les bénéfices attendus en augmentant l'EASA.

Les profils de chronopotentiométrie, avec une densité de courant appliquée de 10 mA cm$^2_{geo}$, ont été enregistrés dans 1 M KOH pendant 30 min (Figure 4.11A). Les potentiels OER sur les réseaux de Ni NW diminuent continuellement avec l'augmentation de la longueur moyenne de Ni NW, et les valeurs de potentiel initiales de 1,65 et 1,60 V sont obtenu pour des Ni NWs de 2,5 et 19 µm de long, respectivement. Il convient de mentionner que toutes les valeurs de

potentiel OER observées sur les Ni NW sont inférieures à celles du film Ni électrodéposé (1, 68 V), ce qui confirme l'activité pour l'OER initiale améliorée sur les électrodes Ni NW. Au fil du temps, le potentiel correspondant sur toute électrode de Ni augmente, en particulier pour le film Ni obtenu par électrodéposition sans membrane AAO, pour lequel le potentiel monte à 1,83 V. Pour obtenir des données quantitatives sur la stabilité de l'OER, les potentiels initiaux (1 min) et finaux (30 min) sont tracés sur la Figure 4.11B. Il est simple de conclure que les électrodes de Ni NW plus longues sont plus stables pour l'évolution de l'O_2 à 10 mA cm^{-2}. Les valeurs de potentiel finales après 30 min d'électrolyse sont tracées sur la Figure 4.11C en fonction de Q_a. Une diminution significative du potentiel pour l'OER a été trouvée pour les Ni NWs avec des valeurs Q_a élevées, qui étaient supérieures à 200 mV pour le Ni NW de 18 μm de long. La diminution évidente du potentiel pour l'OER sur les électrodes de Ni NW plus longues peut s'expliquer par la densité de courant intrinsèque qui est plus faible pour les électrodes avec l'EASAs plus grandes. Même si le potentiel pour l'OER peut être affecté par de nombreux autres effets, le facteur déterminant dans ce travail est la surface de Ni améliorée pour les nanostructures 1D ordonnées.

Une analyse de Tafel pour les films de Ni, des électrodes de Ni NW de 3 μm de long et 17 μm de long, aux potentiels d'électrode dans la région de l'OER est donnée à la Figure 4.12. Ces points sont les courants mesurés à différents potentiels, qui sont tracés avec les potentiels corrigés par la chute ohmique. Les pentes de Tafel sont *ca.* 58 ± 10 mV dec^{-1} pour les électrodes à couche mince et Ni NW, indiquant un coefficient de transfert de 1. Les valeurs dans la littérature sur les électrodes plates de Ni sont d'environ 46 mV dec^{-1} ce qui est cohérent avec le résultat actuel compte tenu de l'erreur indiquée et d'une certaine incertitude dans le facteur de rugosité. Sur les réseaux hiérarchiques des nanofils de $Ni(OH)_2$ avec des caractéristiques beaucoup plus petites qu'ici, la pente de Tafel rapportée était de 123 mV dec^{-1}. Ce résultat peut ne pas être directement comparable puisque les effets de porosité peuvent augmenter la pente de Tafel. L'accord entre les électrodes à couche mince et les films de Ni NW et l'indépendance des pentes de Tafel avec les longueurs des nanofils confirment que l'OER est contrôlé par la cinétique de l'OER dans cette plage de surtension et que le transport de masse d'oxygène dissous, la migration ionique dans les pores ou l'occlusion de bulles les effets ne sont pas significatifs.

La Figure 4.13 montre les spectres d'impédance électrochimique des électrodes aux potentiels d'électrode dans la région de l'OER, obtenus après que les mesures en régime permanent de la Figure 4.12 ont été effectuées. Les spectres de l'impédance de l'électrode à couche mince de Ni ne montrent qu'un seul demi-cercle déprimé. En comparaison, les données de l'impédance de Ni NWs affichent un demi-cercle supplémentaire aux hautes fréquences. Sur les Ni NWs, la forme du deuxième demi-cercle à haute fréquence ne change pas avec le

potentiel d'électrode, bien que sa forme diffère entre les Ni NW courts (3 µm) et longs (17 µm). Ceci indique que le demi-cercle à haute fréquence est lié à la porosité et non à la cinétique de l'OER. Le modèle de ligne de transmission pour les électrodes poreuses comprenant un réseau de pores identiques a été bien décrit dans les références. En général, la théorie prédit une plus petite caractéristique à haute fréquence indépendante du potentiel liée à la géométrie des pores et un demi-cercle déformé plus grand et dépendant du potentiel lié à la cinétique interfaciale. C. Hitz et A. Lasia ont découvert expérimentalement et théoriquement que pour la réaction de dégagement d'hydrogène sur Ni poreux, l'impédance de l'électrode poreuse peut être étroitement approchée par deux demi-cercles déformés modélisés par deux combinaisons parallèles résistance-CPE en série. Avec la résistance de la solution R_{el} en série, ce circuit équivalent dit 2CPE s'est également avéré correspondre aux présents résultats, ce qui reflète la nature similaire des deux systèmes : réactions d'évolution gazeuse au niveau des électrodes poreuses de Ni en solution alcaline pour lesquelles le transport de masse de réactif (H_2O ou OH^-) est rapide. Dans le cas de l'électrode à couche mince de Ni, le circuit avec une seule combinaison résistance-CPE parallèle "1CPE" a été utilisé (Figure 4.13A). Les ajustements au circuit équivalent 2-CPE pour l'OER aux électrodes de Ni NW sont illustrés sur les Figure 4.13B et Figure 4.13C.

La Figure 4.16A montre la variation des valeurs de capacitance effective (C_{eff}) en fonction du potentiel appliqué pour une série de Ni NW de différentes longueurs. On voit clairement que toutes les électrodes de Ni affichent un C_{eff} qui diminue légèrement lorsque le potentiel appliqué augmente de 1,49 à 1,59 V. La Figure 4.16B montre la variation de C_{eff} sur des Ni NW de 2,5 et 17 µm de long déterminé en faisant passer le potentiel de 1,49 à 1,59 V puis de 1,59 à 1,49 V. Comme attendu des résultats précédents, la capacité effective diminue légèrement à mesure que le potentiel est rendu plus positif (balayage anodique). Cependant, on constate que cette diminution de la capacité effective est totalement réversible, car les valeurs de C_{eff} sont indépendantes de la direction de balayage. Cela est vrai à la fois pour les Ni NWs les plus courts et les plus longs étudiés dans la présente étude et reflète la diminution de C_{eff} observée sur la surface plate (voir la Figure 4.17). Ceci suggère fortement que le changement de la capacité effective représente un changement de l'état de surface avec le potentiel.

1.5 Réalisation du deuxième projet

1.5.1 Synthèse de Ni DHBT

La méthode d'électrodéposition galvanostatique (-2 A cm^{-2}) à partir d'une solution aqueuse de 0,1 M NiCl$_2$·6H$_2$O et 2 M NH$_4$Cl a été utilisé pour obtenir des mousses fractales de Ni avec une structure primaire en nid d'abeille et une structure secondaire en forme de chou-fleur. Ces

électrodes seront désignées par Ni DHBT (modèle de bulle d'hydrogène dynamique) puisque le dépôt de Ni et l'évolution de H_2 se produisent simultanément. Dans tous les cas, des plaques de Ni commerciales ont été utilisées comme substrats. Les films ont été déposés sur une des faces des substrats de Ni de 1 cm x 1 cm. Les plaques de Ni ont ensuite été scellées dans des tubes de verre courbés (angle de 90°) de sorte que la surface de l'électrode soit maintenue en position verticale et que la face arrière du substrat Ni ne soit pas exposée à l'électrolyte. Dans tous les cas, la surface exposée était de 1 cm^2. Une électrode au calomel saturé (SCE) et une gaze Pt ont été utilisées respectivement comme électrode de référence et contre-électrode. Par souci de clarté, toutes les valeurs de potentiel d'électrode ont été converties à l'échelle de l'électrode à hydrogène réversible (RHE). La distance entre le compteur et l'électrode de travail a été fixée à 5 mm. L'électrodéposition de Ni a été réalisée à l'aide d'un multipotentiostat Solartron 1480 A pour des durées (T_d) allant jusqu'à 550 s. L'efficacité faradique pour le procédé de galvanoplastie de Ni était de 27 ± 8%, indépendamment de la durée de dépôt. Après déposition, les dépôts électrolytiques poreux de Ni ont été rincés à l'eau et séchés sous un courant d'Ar.

1.5.2 Caractérisation physique des dépôts Ni DHBT

Les morphologies de surface des films de Ni poreux ont été caractérisées par microscopie électronique à balayage (SEM) (JEOL, JSM-6300F) et les épaisseurs ont été mesurées par analyse de section avec SEM. Des mesures de rayons X à dispersion d'énergie (EDX, VEGA3 TESCAN) ont été effectuées pour déterminer la teneur en Fe. Les mesures d'angle de contact ont été effectuées comme suit. Des images de gouttelettes d'eau et de bulles d'air en contact avec la surface de l'électrode ont été capturées par une caméra Panasonic CCD (modèle GP-MF552). Les volumes de la goutte d'eau et de la bulle d'air étaient de 5 μL dans les deux cas. Les angles de contact ont été calculés à l'aide du logiciel ImageJ avec le plugin Dropsnake.

1.5.3 Caractérisation électrochimique et performances pour l'OER

La caractérisation électrochimique dans du KOH 1 M saturé en Ar a été réalisée dans un système conventionnel à trois électrodes, en utilisant une gaze de Pt et une électrode de calomel saturée comme contre-électrode et électrode de référence, respectivement. L'électrode de travail et la contre-électrode n'étaient pas séparées par une membrane. La solution (70 mL) a été agitée par bullage d'Ar. La distance entre l'électrode de travail et la contre-électrode était de 5 mm. Après une période de 10 min dans des conditions de potentiel de circuit ouvert (OCP), des voltammogrammes cycliques (CV) (50 mV s^{-1}) avec différentes fenêtres de potentiel (0,5 à 1,4 V, 0,5 à 1,6 V et 0,5 à 1,9 V) ont été réalisés jusqu'à l'obtention de caractéristiques potentiodynamiques à l'état d'équilibre. Le dernier CV a été enregistré à 5 mV s^{-1}. L'oxydation galvanostatique a été réalisée à 10 mA cm^{-2} pendant 15 min puis à 250

mA cm^{-2} pendant 15 min. Cette séquence a été systématiquement appliquée à chaque électrode de Ni étudiée dans ce travail afin d'assurer une conversion complète du Ni en β-Ni(OH)$_2$. La chute ohmique a été mesurée par spectroscopie d'impédance électrochimique (EIS) et une correction pour la chute ohmique a été appliquée manuellement à toutes les valeurs de potentiel mentionnées ci-dessous.

Dans certains cas, les CV et les courbes de polarisation ont été enregistrés dans un électrolyte KOH 1 M additionné de Fe. Dans ces cas, la concentration de Fe variait entre 0 et 10 ppm grâce à l'ajout de FeCl$_2$·6H$_2$O.

Les mesures EIS dans la gamme de potentiel de l'OER (de 1,44 à 1,49 V) ont été obtenues après une polarisation de 10 min entre 0,01 Hz et 200 kHz à l'aide d'un analyseur de fréquence (Solartron 1255B). L'ajustement à l'équation de de Levie a été effectué en utilisant Zview, avec l'élément de de Levie en série avec la résistance de la solution et une inductance pour modéliser l'artefact de câblage typique observé à haute fréquence. Les valeurs de R_{ct} et C_{dl} ont été dérivées des paramètres ajustés, et donc, le logiciel ne fournit pas d'erreur standard pour eux, mais un argument naïf de propagation d'erreur suggère que leurs erreurs standard sont de l'ordre de 5%.

1.5.4   Résultats et discussion

Les caractéristiques morphologiques des films Ni DHBT tel que déposés sont illustrées à la Figure 5.1. Tous les paramètres d'électrodéposition sont restés les mêmes (-2 A cm^{-2} dans 0,1 M NiCl$_2$·6H$_2$O + 2 MNH$_4$Cl) à l'exception des temps d'électrodéposition (T_d). Comme on le voit sur la Figure 5.1A-D, l'augmentation de Td a entraîné une augmentation progressive des épaisseurs de film de Ni, d'env. 35 μm pour T_d = 50 s jusqu'à 220 μm pour T_d = 450 s. La masse déposée de Ni a augmenté de manière linéaire jusqu'à 100 mg cm^{-2} pour T_d = 450s (voir Figure 5.2). La porosité des films, calculée à partir de la masse déposée et de l'épaisseur mesurée, varie entre 30 et 50 %. La stabilité mécanique des films déposés sur une durée plus longue (T_d = 550 s) est mauvaise, certaines parties se détachant du substrat au rinçage, ce qui a pour effet de stabiliser la masse déposée. Les micrographies SEM en coupe des Figure 5.1A à Figure 5.1D montrent également qu'il existe de nombreux vides le long de la structure dendritique observée dans les films. La plupart de ces vides s'étendent de la surface du film au substrat sous-jacent de la plaque de Ni.

À partir des micrographies SEM en vue de dessus (Figure 5.1E à Figure 5.1H), des pores de taille micrométrique sont observés à la surface des films, avec un diamètre de pore variant entre 10 et 30 μm. Une densité de pores plus faible et un diamètre de pores plus grand sont obtenus pour des temps de dépôt accrus. Ceci est typique de l'électrodéposition de métal sous dégagement d'hydrogène vigoureux (films de DHBT). Dans tous les cas, les parois des pores

présent une structure secondaire de type chou-fleur très poreuse, avec un diamètre de pores beaucoup plus petit (généralement inférieur à 500 nm). La structure vue sur la Figure 5.1 a été observée sur toute la surface géométrique de 1 cm^2 des dépôts. On s'attend à ce que des structures de Ni similaires puissent être formées sur des substrats avec des surfaces géométriques beaucoup plus grandes.

Des mesures d'angle de contact sur des bulles d'air captives à la surface de films Ni DHBT ont été effectuées, et des résultats représentatifs sont affichés sur la Figure 5.3. L'angle de contact d'une bulle d'air augmente d'env. 139° pour plaque Ni à env. 160° pour les films Ni DHBT, indépendamment des temps de déposition. Des angles de contact améliorés ont été récemment rapportés sur des plaques rugueuses de Ni ablatées au laser (164°) par rapport aux plaques de Ni (126°). Des mesures complémentaires d'angle de contact avec l'eau ont également été réalisées pour évaluer l'hydrophilie des films Ni DHBT, indispensable pour assurer le mouillage de la structure poreuse des films Ni DHBT et le bon contact de l'électrolyte avec les sites actifs à la surface. Pour ce faire, des expériences de gouttes sessiles ont été réalisées (5 μL d'H$_2$O désionisée) (voir Figure 5.3). Les films Ni DHBT présentaient des propriétés superhydrophiles, avec des angles de contact bien inférieurs à 25°, témoignant de la forte affinité des films Ni DHBT envers les molécules d'eau. A des fins de comparaison, Ahn *et al.* ont récemment rapporté des valeurs d'angle de contact de 30° et 42° pour des électrodes de Ni en forme d'aiguille et de chou-fleur hautement hydrophiles, respectivement. En revanche, des angles de contact beaucoup plus grands (69°) ont été enregistrés sur une plaque de Ni, ce qui est cohérent avec des études indépendantes d'angle de contact avec l'eau sur des plaques de Ni (70 ± 3°).

Les propriétés électrochimiques des revêtements Ni DHBT ont d'abord été déterminées par des mesures CV. Après des cycles de potentiel répétitifs jusqu'à ce que la formation d'un dépôt d'oxyde de Ni hydraté soit atteinte, des profils CV à l'état d'équilibre ont été obtenus et sont présentés à la Figure 5.5. Tous les CV de Ni DHBT présentent une oxydation importante (à environ 1,41 V) et le pic de réduction (à environ 1,28 V), dont les intensités augmentent avec les épaisseurs de film. Pour chaque électrode Ni DHBT, le rapport entre la charge anodique (Q_a) et cathodique (Q_c) de cette transition redox est resté similaire, avec une valeur moyenne d'env. 1,00 ± 0,13. On a constaté que les valeurs de Q_a augmentaient continuellement de 62 ± 4 mC cm^{-2} pour T_d = 50 s à 539 ± 57 mC cm^{-2} pour T_d = 450 s (Figure 5.6). Ces valeurs correspondent à des facteurs d'amélioration d'EASA d'environ 30 et 270, respectivement, en considérant la valeur Q_a d'une plaque Ni commerciale comme référence (2,1 ± 0,1 mC cm^{-2}).

Des expériences de polarisation (250 mA cm^{-2}) ont été réalisées sur des électrodes Ni DHBT dans 1 M KOH. Les résultats correspondants sont présentés sur la Figure 5.9A. Des potentiels

stables ont été obtenus pour les électrodes Ni DHBT dès le début des expériences. En revanche, une augmentation progressive du potentiel a été observée pour les plaques de Ni nues au cours des 10 premières minutes d'électrolyse. Pour des périodes d'électrolyse plus longues, le potentiel OER des plaques de Ni s'est stabilisé à 2,05 V. Il convient de noter que les comportements électrochimiques présentés à la Figure 5.9A ont été obtenus de manière reproductible pour toutes les trois électrodes de Ni différentes (voir la Figure 5.10). Sur la Figure 5.9B, les surtensions corrigées par la chute ohmique atteinte après 15 min d'électrolyse à +250 mA cm^{-2}, η_{250}, sont tracés par rapport au temps de dépôt. Il y a une différence d'environ 300 mV entre le η_{250} de la plaque Ni et les films Ni DHBT les plus performants. Comme indiqué précédemment, Q_a est directement proportionnel au temps de dépôt (Figure 5.6) et peut être utilisé comme mesure indirecte de l'EASA. La Figure 5.11 montre que les valeurs E_{250} des films Ni DHBT évoluent linéairement avec Q_a tracé sur une échelle semi-logarithmique, ce qui est le comportement attendu si tout le matériau constituant les films Ni DHBT est impliqué dans l'OER. Ceci suggère que, même à haute densité de courant (250 mA cm^{-2}) et pour les films plus épais, l'électrolyte a accès à toute la structure poreuse et que les bulles d'O$_2$ ne conduisent pas à une diminution des sites catalytiques de Ni disponibles.

Afin de corréler clairement la propriété OER améliorée à la structure 3D des films Ni DHBT, une série de mesures EIS a été effectuée. Les spectres d'impédance de la Figure 5.15 montrent les caractéristiques classiques associées aux électrodes poreuses : une région indépendante du potentiel aux hautes fréquences dont la forme dépend de la géométrie des pores, mais qui est une ligne à 45° pour les pores de section uniforme et un demi-cercle à basse fréquence réfléchissant la réaction sur les parois des pores, avec un diamètre dépendant du potentiel qui est la résistance de transfert de charge. Le modèle de la ligne de transmission défini par l'équation de de Levie en série avec la résistance de la solution et une inductance (non illustrée) pour décrire les artefacts de câblage à haute fréquence a donné d'excellents ajustements aux données (Figure 5.15).

Ces dernières années, les activités des catalyseurs pour l'OER ont été jugées par le potentiel requis pour oxydation de l'eau à une densité de courant de 10 mA cm^{-2}, une métrique pertinente pour la synthèse de combustible solaire. Comme le montre la Figure 5.12C, la surtension à 10 mA cm^{-2}, η_{10}, du meilleur film Ni DHBT est de 250 mV. Pour les applications dans les électrolyseurs, une comparaison à une densité de courant beaucoup plus grande doit être faite.

Plusieurs raisons peuvent expliquer les performances des films Ni DHBT. Il ne fait aucun doute que l'augmentation de l'EASA des films Ni DHBT, par rapport aux plaques Ni, est en partie responsable de l'amélioration des performances pour l'OER. Comme indiqué dans la Figure

5.11, l'EASA des films Ni DHBT est entièrement accessible à l'électrolyte et participe à la réaction d'évolution de l'O$_2$. Cependant, cette mesure de l'EASA a été effectuée dans une région de potentiel où aucun dégagement de gaz ne se produit. En raison de la structure poreuse des films Ni DHBT, on aurait pu s'attendre à ce que, à un potentiel plus positif dans la région de l'OER, les bulles d'O$_2$ puissent augmenter la résistance de l'électrolyte et/ou être responsables de l'occlusion de certains des pores. Cependant, ce n'est pas ce qui est observé, et les données EIS du Table 5.1 montrent que la capacité à double couche est constante dans la région de potentiel où la pente de Tafel de 29 mV dec^{-1} est observée. Cela indique que l'occlusion des sites actifs de Ni par des bulles d'O$_2$ n'est pas un facteur limitant.

Il est indéniable que la faible pente de Tafel (29 mV dec^{-1}) est un facteur majeur contribuant aux performances des films Ni DHBT. Sur les films Ni DHBT, la pente Tafel de 29 mV dec^{-1} est observée sur une plage de densités de courant qui dépasse de loin celle de la plaque Ni. En effet, la « région à faible pente de Tafel » s'étend jusqu'à 100 mA cm^{-2} sur les films Ni DHBT alors qu'elle est limitée à 5 mA cm^{-2} sur la plaque Ni. Cette différence frappante est en partie responsable de l'augmentation des performances des films Ni DHBT et doit être liée à leurs différentes morphologies.

Comme décrit dans la partie de contexte, des rapports récents ont montré que la morphologie des électrodes a un impact sur la force d'adhérence des bulles de gaz à la surface et le diamètre de détachement des mêmes bulles de gaz lors de la libération. En effet, la force d'adhésion et le diamètre de détachement des bulles de gaz sont diminués par la nanostructuration de la surface de l'électrode. Selon ce que l'on appelle dans la littérature la corrélation de Fritz, il existe une relation linéaire entre le diamètre de détachement de la bulle de gaz d'une surface et son angle de contact avec l'eau. Comme mentionné précédemment, l'angle de contact avec l'eau diminue de 60° à moins de 25° en raison de la géométrie fractale de l'électrode Ni DHBT. L'angle de contact amélioré des bulles d'air, qui est une conséquence directe de l'augmentation de l'hydrophilie, se traduit par des forces d'adhésion des bulles plus petites sur la surface de l'électrode (et un temps de résidence plus court), ainsi qu'un rayon plus petit du plan de contact entre la bulle d'air et la surface de l'électrode (et donc plus grande surface de contact entre l'électrolyte et les sites actifs de l'électrode). La diminution significative de la force d'adhésion et du diamètre de détachement des bulles de gaz résultant de la nanostructuration de l'électrode devra être confirmée par des mesures indépendantes comme ce qu'on présentera dans le troisième projet.

1.6 Réalisation du troisième projet

1.6.1 Préparation de l'électrode Ni DHBT et sa modification par Ir

Une tige de Ni a été insérée dans une cellule électrochimique artisanale et a été utilisée comme

substrat pour l'électrodéposition d'un film de Ni poreux. Seule la base circulaire (0,32 cm^2) a été exposée à l'électrolyte. Les films de Ni poreux ont été préparés par la méthode de modélisation dynamique des bulles d'hydrogène (DHBT) rapportée dans [30]. Le dépôt a été effectué pendant 450 s à -2 A cm^{-2} dans un électrolyte 0,1 M NiCl$_2$·6H$_2$O + 2 M NH$_4$Cl. Ensuite, les échantillons ont été soigneusement rincés avec de l'eau désionisée. Ils seront appelés films Ni DHBT dans les sections suivantes. Certains des échantillons ont ensuite été immergés dans une solution de HCl 0,01 M ou de K$_2$IrCl$_6$ 0,001 M plus HCl 0,01 M pendant 20 heures maximum. Ces derniers échantillons ont été notés Ir/Ni DHBT.

1.6.2 Caractérisation physique des films Ni/DHBT et Ir/Ni DHBT

La morphologie de surface des films Ni DHBT et Ir/Ni DHBT a été sondée par microscopie électronique à balayage (SEM) à l'aide d'un SEM VEGA3 TESCAN et d'un SEM ultra-haute résolution FEI Magellan fonctionnant entre 1 keV et 2 keV d'énergie incidente pour l'imagerie. Une cartographie par rayons X à dispersion d'énergie (EDX) a été réalisée pour évaluer les compositions du film. Les diagrammes de diffraction des rayons X (XRD) ont été obtenus à l'aide d'un diffractomètre à rayons X Bruker D8 Advance avec un rayonnement Cu K$_{\alpha1}$ et Cu K$_{\alpha2}$ moyen pondéré à 1,5418 Å. Les données ont été recueillies dans la plage 2θ de 30° à 95°, la taille du pas était de 0,02 degré et le temps de comptage était de 2 secondes par pas.

1.6.3 Caractérisation électrochimique

Les mesures électrochimiques ont été effectuées dans une cellule électrochimique artisanale avec une maille de Pt comme contre-électrode et une électrode au calomel saturé (SCE) comme électrode de référence. Les potentiels ont été convertis par rapport à l'électrode à hydrogène réversible (RHE) selon l'équation $E_{RHE} = E_{SCE} + 0,242$ V $+ 0,059$ V $\times$ pH. La plupart des mesures électrochimiques ont été effectuées dans un électrolyte KOH 1 M (pH = 13, 5) préparé avec de l'eau désionisée et KOH.

Un potentiostat Solartron 1480 a été utilisé pour les mesures électrochimiques et un analyseur de fréquence Solartron 1255B a été utilisé pour les mesures de spectroscopie d'impédance électrochimique (EIS). Pour chaque mesure, la résistance non compensée, Ru, a été déterminée au potentiel de circuit ouvert (OCP) en prenant l'intersection à haute fréquence du tracé de Nyquist mesuré entre 0,01 Hz et 200 kHz.

Avant les mesures de voltammogrammes cyclique (CV), tous les échantillons ont été immergés dans de l'électrolyte KOH 1 M à l'OCP pendant 15 min. Ensuite, des balayages CV à une vitesse de balayage de 50 mV s^{-1} ont été enregistrés entre -0,1 et 1,5 V *vs.* RHE jusqu'à l'obtention de CV stables. Des CV stables ont été obtenus après 50 cycles. Tous les CV présentés dans cette étude ont été enregistrés à 5 mV s^{-1} après l'application de la procédure

décrite ci-dessus.

Des mesures de spectroscopie d'impédance électrochimique (EIS) entre 0,01 Hz et 200 kHz avec une amplitude de 10 mV ont été effectuées après qu'un potentiel constant a été appliqué à l'électrode pendant 5 min. Ces conditions étaient suffisantes pour que l'électrode atteigne un courant d'état stable. Le potentiel d'électrode a été varié de 1,44 à 1,49 V dans la région de l'OER.

1.6.4 Détection des bulles d'oxygène par émission acoustique

Les mesures d'émission acoustique ont été effectuées dans une cellule électrochimique artisanale à trois électrodes, équipé d'un capteur piézoélectrique (R6A, Mistras) et d'un système de détection d'émission acoustique (1283 USB AE Node, Mistras). Une tige cylindrique de Ni a été utilisée comme substrat. Des revêtements Ni DHBT et Ir/Ni DHBT ont été déposés sur une des deux bases du cylindre de Ni. De l'autre côté, le capteur était relié au système de détection. Le capteur piézoélectrique n'était pas en contact avec l'électrolyte. Le centre du capteur et la tige du Ni étaient alignés sur un axe commun. De la graisse de silicone et du ruban Kapton sont appliqués entre la tige Ni et le capteur pour minimiser l'entrefer et les isoler électriquement l'un de l'autre. Des courants positifs variant de 0,3 mA cm^{-2} à 6,6 mA cm^{-2} ont été appliqués sur l'électrode de travail pour générer des bulles d'O$_2$. Au cours de l'OER, des signaux acoustiques pulsés d'une amplitude supérieure à 28 dB ont été enregistrés et comptés comme des événements discrets d'émission acoustique. Le traitement des données des événements AE a été effectué à l'aide du logiciel AEwin (Mistras). Pour chaque événement AE, la fréquence maximale a été déterminée par transformée de Fourier dans AEwin.

1.6.5 Caractérisation de surface par XPS

Les mesures de spectroscopie photoélectronique à rayons X (XPS) ont été effectuées à l'aide d'un instrument VG Escalab 220i-XL équipé d'une source Al Kα. Des films Ni DHBT et Ir/Ni DHBT fraîchement préparés ont été introduits dans la chambre à vide pour être séchés pendant la nuit juste après leur préparation. Aussi, certains échantillons ont été analysés après leur caractérisation électrochimique. La même procédure a été suivie. Ces échantillons sont notés post-EC Ni DHBT et post-EC Ir/Ni DHBT. L'ajustement des données a été effectué avec le logiciel CasaXPS en utilisant les soustractions de fond de Shirley. Pour la correction de charge de surface, le pic C 1s à 284,8 eV a été utilisé comme référence.

1.6.6 Résultats et discussion

Des films Ni DHBT poreux tridimensionnels ont été déposés sur des substrats de plaque de Ni par a méthode d'électrodéposition galvanostatique. La Figure 6.2 montre que les films Ni DHBT ont une structure interconnectée en forme de chou-fleur avec des diamètres de pores

variant entre 10 et 30 µm. Cette structure a été décrite en détail dans le projet précédent.

Un balayage SEM à haute résolution a été réalisée pour sonder la structure interne des films. On voit sur la Figure 6.3a que les films Ni DHBT sont composés des granules de Ni recouvert de nanofeuilles en forme de flocons. La décoration par l'Ir des films Ni DHBT (Ir/Ni DHBT) a été réalisée en immergeant des électrodes Ni DHBT fraîchement préparées dans une solution de précurseur 0,001 M K_2IrCl_6 + 0,01 M HCl. La morphologie d'un film Ir/Ni DHBT après 17 h d'immersion est représentée sur les Figure 6.3b. Aucun changement dans la morphologie des films n'a été observé par rapport aux films Ni DHBT vierges. A titre de comparaison, un film de Ni DHBT fraîchement préparé a été immergé pendant 17h dans une solution de HCl 0,01 M (sans K_2IrCl_6), ci-après dénommé Ni DHBT corrodé. Encore une fois, aucun changement de morphologie n'a été observé (Figure 6.3c). Le rapport atomique Ir/Ir+Ni après 17 h d'immersion, tel que déterminé par analyse EDX, était de 0,3 %.

Les mesures XPS ont été effectuées juste après la préparation des revêtements Ni DHBT et Ir/Ni DHBT. La Figure 6.4a montre les niveaux de cœur Ni 2p des deux électrodes. Pour le Ni DHBT tel que préparé, des pics sont observés à 852,8 eV et 870,1 eV qui sont respectivement attribués aux niveaux de cœur 2p 3/2 et 2p 1/2 du Ni métallique. Des pics au niveau du cœur de Ni 2p 3/2 et Ni 2p 1/2 sont également observés à 856,4 et 874,1 eV, qui sont attribués à l'hydroxyde de Ni ou à l'oxyhydroxyde de Ni. Les pics au niveau du cœur 3p du Ni métallique et de l'hydroxyde de Ni ou de l'oxyhydroxyde de Ni sont observés à 66,3 et 68,0 eV, respectivement. Dans le cas de l'Ir/Ni DHBT, des pics de niveau de cœur Ir 4f 7/2 et Ir 4f 5/2 sont observés à 60,4 et 63,5 eV, respectivement. Ils sont attribués à l'iridium métallique, ce qui est cohérent avec l'équation Equation 6.3 décrivant les mécanismes sous-jacents à la réaction galvanique. Après immersion dans la solution contenant de l'Ir, il ne reste presque plus de Ni métallique à la surface. D'après les données XPS, le rapport atomique de surface Ir / (Ir+Ni) est de 5,3 %, bien supérieur à celui déterminé à partir des mesures EDX qui sont plus sensibles au volume. Cela reflète le fait que les atomes d'Ir sont situés à la surface de l'électrode.

L'ajustement des pics de Ni 2p 3/2 a été réalisé en utilisant deux composants à 855,4 eV et 856,9 eV (Figure 6.11), qui, selon Ratcliff et $al.$, sont attribués respectivement à Ni^{2+} et Ni^{3+}. Il n'y avait aucune preuve d'un pic à 854,0 eV qui pourrait être attribué à NiO. Suite à l'OER, le rapport Ni^{3+}/Ni^{2+} est de 0,23:1 et 0,58:1 pour les films Ni DHBT et Ir/Ni DHBT, respectivement. L'état Ni^{3+} est généralement attribué à la création de lacunes dans $Ni(OH)_2$ ou à la présence de NiOOH [47–51]. Il a été montré ailleurs que la mouillabilité de l'électrode Ni est augmentée par la présence d'une plus grande quantité de défauts (lacunes), et que NiOOH est plus hydrophile que $Ni(OH)_2$. Sur la base de ces preuves, on pourrait affirmer que le caractère hydrophile accru d'Ir/Ni DHBT par rapport au Ni DHBT a une influence sur les propriétés

électrocatalytiques de cette électrode, en particulier sur la manière dont les bulles d'oxygène se forment et se détachent de l'électrode. Cela va être étudié à travers les données d'émission acoustique enregistrées au cours de l'OER.

L'activité pour l'OER des films Ni DHBT et Ir/Ni DHBT a été étudiée par des mesures de chronopotentiométrie à 10 mA cm^{-2} (Figure 6.9a). Le potentiel se stabilise rapidement jusqu'à sa valeur d'équilibre. Dans le cas de Ni DHBT et Ir/Ni DHBT après 20h d'immersion, les surtensions corrigées par la chute ohmique étaient respectivement de 323 mV et 195 mV. L'effet du temps d'immersion, et donc de la quantité d'atomes d'Ir, sur la surtension à 10 mA cm^{-2}, η_{10}, est représenté sur la Figure 6.9b. La surtension a diminué de façon exponentielle avec l'augmentation du temps d'immersion, avec une constante de décroissance exponentielle de 1,9 h. En comparaison, η_{10} du Ni DHBT corrodé (17 h) était de 327 mV, presque identiques à la valeur du Ni DHBT vierge. L'activité accrue d'Ir/Ni DHBT par rapport à la fois au Ni DHBT et au Ni DHBT corrodé pourrait être due à l'augmentation observée de l'EASA, telle qu'évaluée par Q_c, et à la présence d'atomes d'Ir à la surface de l'électrode.

La Figure 6.9c montre les courbes de potentiel corrigé par la chute ohmique en fonction de log (j) (courbes de Tafel) des films Ni DHBT, Ni DHBT corrodé et Ir/Ni DHBT immergés 17h. Le tracé de Tafel du Ni DHBT corrodé est presque superposable à celui du Ni DHBT. Les courbes de Tafel de Ni DHBT et Ir/Ni DHBT ont montré un comportement linéaire dans la gamme de courant entre 1 et 100 mA cm^{-2}. Le Ni DHBT présentait une pente de Tafel de 52 mV dec^{-1} et une densité de courant d'échange de $7,9 \times 10^{-6}$ mA cm^{-2}. L'Ir/Ni DHBT avait une pente de Tafel similaire (49 mV dec^{-1}), mais une densité de courant d'échange beaucoup plus grande de $7,9 \times 10^{-4}$ mA cm^{-2}. C'est un facteur 100 fois supérieur à celui du Ni DHBT. La similitude entre les pentes de Tafel suggère que l'étape déterminant la vitesse pour l'OER sur Ni DHBT et Ir/Ni DHBT est la même, et l'OER procède avec le même mécanisme sur les deux électrodes.

La Figure 6.12a montre le schéma du système de détection acoustique en combinaison avec une configuration de cellule électrochimique à trois électrodes. Avec cette configuration, les événements AE pendant l'OER ont été détectés. Avec les électrodes Ni DHBT et Ir/Ni DHBT, les événements AE ne se sont produits que lors de l'application d'un courant anodique (Figure 6.13). Les signaux acoustiques ont été mesurés à 6,6 mA cm^{-2} pendant 300 s. Les fréquences maximales de tous les événements AE ont été traduites en taille de bulle à l'aide de l'équation de Minnaert (équation Equation 6.5). La distribution des tailles de bulles est représentée sur la Figure 6.12c, et la moyenne de la taille des bulles par rapport au temps d'électrolyse est représentée sur la Figure 6.12d. Pour Ni DHBT, il existe deux principales populations de bulles, centrées à 137 et 157 μm de diamètre. Pour Ir/Ni DHBT, des bulles de 137 et 157 μm de diamètre sont présentes, mais il y avait un plus grand nombre de bulles de diamètre compris

entre 80 et 130 μm. Tout cela fait que le diamètre moyen des bulles sur Ni DHBT est de 140 μm contre 125 μm pour Ir/Ni DHBT (Figure 6.12d). Comme le montrent la Figure 6.14 et la Figure 6.15, le diamètre moyen des bulles de Ni DHBT et Ir/Ni DHBT est indépendant de la densité de courant entre 1 et 6,6 mA cm^{-2}. Les mesures à une densité de courant plus élevée n'ont pas pu être effectuées, car le détecteur était saturé. Sur Ir/Ni DHBT, il y a une réduction importante de la taille des bulles par rapport à Ni DHBT, qui est attribuée à l'augmentation de l'hydrophilie de la première électrode par rapport à la seconde.

Les mesures EIS ont été effectuées à différents potentiels pour les films Ni DHBT et Ir/Ni DHBT (Figure 6.16). Les spectres EIS des deux électrodes affichent une ligne droite dans la région des hautes fréquences et un demi-cercle déprimé dans la région des basses fréquences. La forme de la ligne haute fréquence ne change pas avec le potentiel de l'électrode. Ceci indique que les caractéristiques de la réponse à haute fréquence n'étaient pas liées à la cinétique de l'OER. Il est connu que les caractéristiques dans la région des hautes fréquences des spectres EIS sont liées à la porosité de l'électrode. L'inclinaison de cette ligne par rapport à l'axe horizontal était de 45° et 22,5° pour les électrodes Ni DHBT et Ir/Ni DHBT, respectivement, ce qui indique que les structures poreuses de ces électrodes diffèrent grandement. Les électrodes Ni DHBT corrodées partagent la même ligne à 45° que celle observée pour le Ni DHBT (Figure 6.17), ce qui indique que l'exposition au HCl uniquement n'était pas suffisante pour modifier la structure poreuse de l'électrode.

L'équation de Levie utilisée pour ajuster les données EIS est basée sur un modèle de ligne de transmission qui suppose que les pores sont parallèles avec une forme en coupe indépendante de la profondeur. Les données EIS du Ni DHBT et du Ni DHBT corrodé suivent l'équation de Levie, ce qui suggère que de simples pores parallèles soient présents. Ceci est représenté schématiquement sur la Figure 6.18a, où seule la structure primaire des pores existe. Cependant, la géométrie réelle des pores pourrait être en forme de branche, comme illustré sur la Figure 6.18b, avec une structure de pores secondaire qui existe, mais reste inerte sur les revêtements Ni DHBT et Ni DHBT corrodés. Dans ce cas, le modèle de pore simple serait toujours suffisant pour expliquer les résultats de l'EIS.

Alternativement, la géométrie réelle des pores pourrait être en forme de branche, comme illustré sur la Figure 6.18c, avec une structure de pores secondaire qui existe, mais qui est active et contribue à la réponse EIS. La prise en compte de la structure des pores primaires et secondaires illustrée à la Figure 6.18c a été obtenue à l'aide d'un modèle pour les pores ramifiés décrit dans l'article de Itagaki.

La Figure 6.19 montre une simulation des données EIS de Ni DHBT où seuls les pores primaires ont été considérés. Tous les paramètres ont été optimisés à l'aide d'ajustements

CNLS, et les paramètres d'ajustement sont présentés dans le Table 6.1. Le diamètre et la longueur des pores primaires ont été fixés à 22 µm et 95 µm pour être cohérents avec les micrographies SEM. Comme le montre la Figure 6.19, l'accord entre les données ajustées et expérimentales de Ni DHBT est excellent, et la raie à 45° à haute fréquence est bien prise en compte. Cela n'est pas surprenant étant donné que l'expression mathématique de l'impédance des pores primaires dans le modèle de Itagaki est identique à l'équation de Levie, et que l'équation de Levie donnait un bon ajustement de la région haute fréquence pour Ni DHBT.

Selon le modèle de pores ramifiés d'Itagaki, les structures fractales avec des pores primaires et secondaires ayant une forme cylindrique donnent une ligne droite dans la région des hautes fréquences, avec une inclinaison de 22,5°. Donc, les données EIS d'Ir/Ni DHBT ont été ajustées en utilisant les mêmes paramètres pour les pores primaires et aussi en tenant compte de la présence de pores secondaires. Encore une fois, l'accord entre les données ajustées et expérimentales d'Ir/Ni DHBT est excellent (Figure 6.19). Les paramètres utilisés pour l'ajustement sont donnés dans le Table 6.1. Ces témoignages concordent avec le fait que la structure d'Ir/Ni DHBT (ou Ni DHBT) est fractale. Par conséquent, on a émis l'hypothèse que les pores secondaires occupaient 30% de la surface de la paroi des pores primaires, que le diamètre des pores secondaires était de 30% du diamètre des pores primaires et que la longueur des pores secondaires était de 30% de la longueur des pores primaires selon les paramètres (voir Table 6.1). Pour Ir / Ni DHBT, les données EIS dans la région des hautes fréquences suggèrent que la structure des pores primaire et secondaire est accessible.

La Figure 6.21c montre la variation de C_{dl} en fonction du potentiel de Ni DHBT, de films Ir/Ni DHBT immergés pendant 17 h et de films Ni DHBT corrodés. Encore une fois, en comparant Ni DHBT et Ni DHBT corrodé, il n'y avait presque aucune variation de la capacité de la double couche après immersion dans HCl uniquement. En revanche, au potentiel d'électrode le plus bas, il y avait presque un facteur 6 d'augmentation de C_{dl} après immersion dans 0,01 M HCl et 0,001 M K_2IrCl_6. Ces résultats sont cohérents avec ceux trouvés précédemment par intégration de la charge sous le pic cathodique associé à la réduction de $Ni(OH)_2$ (Q_c).

Sur la Figure 6.9c, à tout potentiel donné, il existe un facteur de différence de 175 entre la densité de courant de Ni DHBT et Ir/Ni DHBT. Cette différence d'activité est due à la présence d'iridium, car l'immersion de l'électrode Ni DHBT dans une solution acide ne contenant pas de cations Ir^{4+} n'entraîne qu'une augmentation marginale de l'activité de l'électrode. Nous avons montré que l'iridium agit à différentes échelles pour améliorer l'activité électrocatalytique de l'électrode pour l'OER. Premièrement, l'iridium augmente la surface électrochimique active de l'électrode en favorisant la création d'un réseau de pores secondaires, ou en activant un réseau de pores secondaires déjà présent dans l'électrode Ni DHBT, mais inactif avant l'immersion

de l'électrode dans la solution contenant cations Ir^{4+}. L'autre effet de l'iridium est d'augmenter l'hydrophilie de l'électrode, ce qui entraîne une diminution de la taille des bulles d'oxygène et, comme discuté ci-dessus, une diminution moins drastique de l'EASA à mesure que le courant pour l'OER augmente. Par conséquent, pour tenir compte de ces deux effets de l'iridium, les tracés de Tafel de Ni DHBT et Ir/Ni DHBT illustrés à la Figure 6.9c, qui sont exprimés par rapport à la surface géométrique, ont été normalisés par les valeurs de capacité mesurées à chaque potentiel d'électrode, en supposant une valeur de 470 µF cm^{-2} pour la capacité spécifique à double couche. La normalisation par la capacité mesurée dans la plage de potentiel où se déroule l'OER tient compte (i) de l'augmentation de l'EASA qui se produit en raison de l'immersion de l'électrode dans une solution contenant des cations Ir^{4+} qui a été discutée à la Figure 6.6c, et (ii) de la diminution de l'EASA due à la présence de bulles d'oxygène sur la surface de l'électrode qui a été discutée sur la Figure 6.21c et la Figure 6.21d. Les tracés de Tafel normalisés par l'EASA des électrodes de Ni DHBT et d'Ir/Ni DHBT sont illustrés à la Figure 6.9d. Une fois ces deux effets sur les pentes de Tafel pris en compte, les différences observées entre l'électrode Ni DHBT et l'électrode Ir/Ni DHBT doivent être attribuées à l'activité catalytique de l'iridium. Comme on le voit sur la Figure 6.9d, il existe toujours une différence d'un facteur 33 entre l'activité intrinsèque de Ni/DHBT et Ir/Ni DHBT. Ceci n'est pas vraiment surprenant, car l'activité intrinsèque des oxydes/hydroxydes d'iridium est supérieure à celle des oxydes/hydroxydes de nickel. Par conséquent, on s'attend à ce que la présence d'un grand nombre de petites particules d'iridium (environ 4,3 nm de diamètre) à la surface de Ni DHBT contribue à augmenter l'activité électrocatalytique intrinsèque de l'électrode pour l'OER.

1.7 Conclusion

À partir de ces trois projets, on peut conclure que la construction de supports minces ordonnés de Ni 3D aiderait à exposer plus de sites actifs, faciliterait le transport des bulles et favoriserait ainsi les performances pour l'OER. En comparaison, la construction en 3D de supports stochastique et hautement poreux peut augmenter considérablement l'exposition des sites actifs tout en réduisant la couverture des bulles de surface pendant l'OER. Les développements futurs pour optimiser les supports en mousse Ni stochastique devraient se concentrer sur l'amélioration de ses conditions de mouillage interne, ce qui pourrait être réalisé grâce à une gestion des défauts qui altère l'hydrophilie intrinsèque.

1.8 Composition de la thèse

Cette thèse est principalement composée de 7 chapitres. L'idée principale de la thèse sera présentée dans le premier chapitre. Le deuxième chapitre commencera par un examen général de la stratégie de stockage d'énergie "power-to-hydrogen" et de la nécessité de

développer des électro-catalyseurs hautement efficaces et peu coûteux pour l'OER. Ensuite, le mécanisme fondamental d'OER sera discuté en ce qui concerne la thermodynamique, la cinétique d'OER et leurs implications pour la conception des catalyseurs. Une revue générale des électro-catalyseurs à base de Ni pour les OER sera donnée. Dans la dernière moitié du chapitre, les différents facteurs affectant l'activité catalytique et leur stratégie de conception de catalyseur correspondante seront passés en revue. Le troisième chapitre comprendra les méthodes de construction de matériaux en 3D à base de Ni, leur rationalité et leurs procédures. Aussi, les méthodes de caractérisation de base utilisées dans cette thèse et leur principe seront introduits. Le quatrième chapitre présente l'article dans lequel nous avons étudié les nanofils de Ni pour l'OER. Le cinquième chapitre décrit nos travaux sur les électrodes en mousse fractale de Ni pour l'application des OER via la méthode de modèle des bulles d'hydrogène. Le sixième chapitre décrira soumis portant sur les électrodes en mousse de Ni fractale modifiée à l'Ir conçue pour l'OER. Dans le dernier chapitre, quelques conclusions seront tirées. Aussi, quelques perspectives sur les travaux futurs seront données.

TABLE DES MATIÈRES

LISTE DES FIGURES

LISTE DES TABLEAUX

1   GENERAL INTRODUCTION

Electrochemical water electrolysis for hydrogen fuel production has been regarded as one of the most appealing technologies in energy storage. To achieve high-efficiency of hydrogen evolution, the cell voltage that drives the whole electrolysis system must be reduced. The high voltage for electrochemical water electrolysis is mainly caused by the overpotentials of the two gas evolving reactions, namely the hydrogen evolution reaction (HER) at the cathode and the oxygen evolution reaction (OER) at the anode. The overpotentials are highly dependent on the electrocatalytic of materials. Consequently, seeking highly active, earth-abundant, and electrochemically stable electrocatalytic materials for the OER and the HER is the most urgent and challenging task for developing water electrolysis. This task needs to be accomplished via rational designs of electrode materials. In the past few decades, continuous efforts have been dedicated to reducing the overpotentials for the OER and the HER. Those works focus mainly on two approaches: either to increase the surface-area-to-volume ratio of catalysts through nano-engineering or to increase the intrinsic activity of each active site through fine tunings of adsorption free energies for H* or HO* reaction intermediates [1].

Innovations in the field of electrocatalysis tend to search for alternative materials for the state-of-art noble metal catalysts to reduce the capital costs of water electrolyzers. 3d-transition metal-based materials are promising alternatives due to their low price, good stability, and high activity. Enormous efforts have been devoted to developing Ni-based OER electrocatalysts for alkaline water electrolyzers. Heteroatom incorporation into Ni compounds is one of the critical approaches to optimizing Ni material's intrinsic activity. Also, the synergetic defect effects induced by heteroatom incorporation could help to intrinsically enhance the wetting conditions of nanostructured material [2].

To construct high-performance 3D structured Ni materials, improving the wetting properties of the electrode surface is imperative. At large current densities, the bubbles of hydrogen and oxygen generated at the electrode/electrolyte interfaces cover a significant part of the electrodes' surface, thereby partially blocking the active sites of the electrode. The presence of a bubble causes an increase in the solution resistance and a notable reduction of the electrochemically active surface area (EASA). Both effects result in a rise in the cell voltage [3].

Lately, super-aerophobic electrodes for applications in gas evolving reactions have been receiving more and more research attention. That is because their wetting properties can facilitate bubbles' detachment from electrodes and consequently

decrease the bubble coverage at the surface of electrodes, thereby reducing the overpotentials for the OER and the HER at high current densities. Thus, the operating current density at which the electrocatalytic materials can achieve their maximum utilization can be extended to a broader range. However, only a few studies have been devoted to correlating the bubbles' behavior to the super-aerophobic property of electrodes to optimize their catalytic activities, perhaps for the lack of a suitable method to evaluate the bubbles' behavior during gas involving reactions. Besides, the apparent hydrophilicity shouldn't be the only factor to be examined when describing the ability of a 3-dimensional porous electrode to release bubbles during dynamic gas evolutions. In such context, *in-operando* monitoring of the bubbles' behavior, including their entrapment in porous electrode and their effects on the overpotential of reaction, is highly needed.

This thesis works is focused on developing 3D nanostructured Ni electrocatalysts for alkaline water electrolysis. The research objective includes i) fabrication of 3-dimensional Ni electrodes designed to optimize the catalytic performance for alkaline water electrolysis; ii) methods to functionalize 3D Ni electrodes through doping for better intrinsic catalytic activities in alkaline water electrolysis; iii) methods to reduce the bubble occupancy on the electrode surface (both on the surface and in the porous structure) during gas evolution. Those objectives are achieved through three related projects:

- Self-supported Ni nanowires arrays for the OER in alkaline water electrolysis
- Hydrogen bubble templating of fractal Ni foam catalysts for the OER in alkaline media
- Ir decoration of fractal Ni foam catalysts for the OER, with investigations of bubble behavior through *in-operando* acoustic emission detection

In the first project, we aimed at fabricating ordered nanostructures using the electro-deposition method and establishing a suitable protocol for the characterization of Ni material. In the second project, we intended to construct stochastic structures to enhance surface wetting and extend the exposure of active sites using Ni electrodeposition. In the third project, we made surface modifications of fractal Ni foam supports to optimize its intrinsic activity and used the acoustic emission method to probe the internal wetting conditions in the 3D structures.

This thesis is composed of seven chapters, including this introduction. The second chapter will present a general review of the Power-to-Hydrogen energy storage strategy and the need to develop highly efficient and low-cost electrocatalysts for the

OER. Then, the fundamental mechanism of the OER will be introduced in the scope of thermodynamics, kinetics, and their implications for the designing of OER catalysts. A general review of the Ni-based electrocatalysts for the OER will be given. In the last half of the chapter, the different factors affecting the catalytical activity and their corresponding catalyst designing strategy will be reviewed. The third chapter will include the methods to construct 3D Ni-based materials, their rationality, and procedures. Also, the basic characterization methods used in this thesis and their principle will be introduced. The fourth chapter presents the article in which we investigated Ni nanowires for OER applications. The fifth chapter described our work on fractal Ni foam electrodes for OER applications through the hydrogen bubble templating method. The sixth chapter will describe the article submitted that deals with Ir modified fractal Ni foam electrodes designed for the OER. In the last chapter, some conclusions will be made. Also, some perspectives about future works will be given.

2   LITERATURE REVIEW

2.1   Power-to-hydrogen energy storage and electrocatalysts

Variable renewable energies (VRE), such as solar energy and wind power, are promising energy sources for human activities. However, due to their intermittent nature and the inconstant energy demands of human activities, their direct integration into the power grid is limited by the energy curtailments. The world needs an energy storage system for VRE to enlarge the penetrations of renewable energy in the energy portfolio and thus to reduce CO_2 emissions and mitigate the energy crisis. A Power-to-gas system is composed of a series of technologies that convert instantaneous energies, such as renewable energy or the surplus energy of power grids, into stable gas fuels [4]. It offers a promising prospect to solving the energy crisis that our human society is facing.

In a power-to-gas system (Figure 2.1), "green hydrogen" produced with renewable energy through water electrolysis can be distributed to various end-users, such as industry, transport, buildings, and power plans, and be converted back into electricity through fuel cells whenever needed. Also, green hydrogen could be used in the methanation process to produce methane from CO_2. Hydrogen acts as an ideal energy carrier for energy conversion. It's the most abundant element on earth. When it enters into the power-to-gas and gas-to-power energy cycle, no pollutant is emitted. The electricity generation from H_2 through a fuel cell is more efficient than burning fossil fuels through the conventional internal combustion engines because the latter is subjected to the Carnot cycle limitation [5]. Also, the hydrogen's energy density (143MJ kg^{-1}) is almost three times that of hydrocarbon-based fuels (around 50MJ kg^{-1}) [6]. Establishing a gas grid using hydrogen as an energy carrier can vastly reduce the cost of energy distribution. For example, hydrogen transport cost by gas pipeline is about 10-20 times lower than electricity transport cost by a cable while the latter suffers from energy losses by electricity transmission [7], [8].
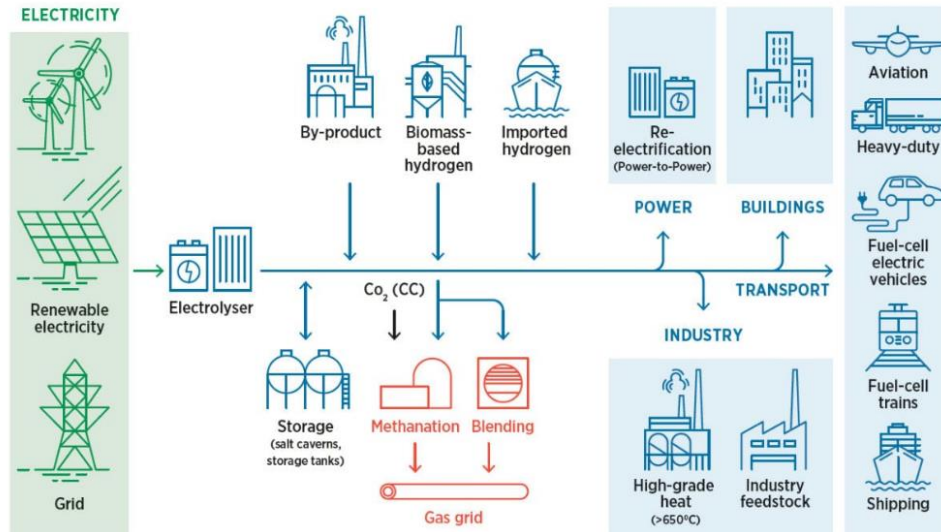
Figure 2.1 Prospect for the Power-to-Gas energy storage system [4]

Therefore, promoting green hydrogen production on a large scale (gigawatts scale) is necessary for reaching net-zero emission shortly [4]. However, the deployment of power-to-gas projects is primarily impeded by the high cost of hydrogen production. Currently, the green hydrogen cost is estimated to be 4-6$/kg, while industrially produced hydrogen through steam methane reforming costs approximately 1$/kg [9]. This barrier from hydrogen production cost is being mitigated by innovations in developing cost-effective and high-performance water electrolyzers and by the sharply falling electricity price of renewable energy, which has been observed since the last decade [10]. According to the International Renewable Energy Agency (IRENA), a 80% reduction in hydrogen cost can be achieved soon by combining breakthroughs in electricity prices, the capital costs of electrolyzer, the electrolyzer efficiency, *etc.* [11] (Figure 2.2).
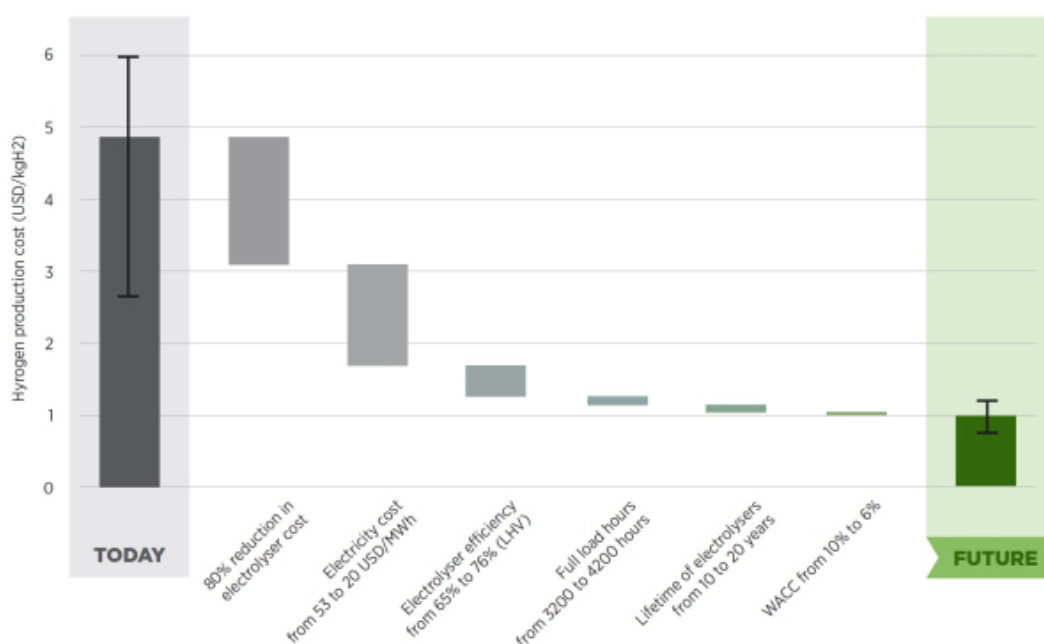
Figure 2.2 Cost reduction of hydrogen production cost [11]

Searching for cost-effective and high-performance electrocatalysts for water electrolyzers is vital to reduce the hydrogen production price. Water electrolysis includes two heterogeneous gas evolution reactions: the hydrogen evolution reaction (HER) and the oxygen evolution reaction (OER). The state-of-the-art electrocatalysts for water electrolyzers in acidic solution are Pt for the HER and IrO_2 or RuO_2 for the OER. However, they are all precious noble metal compounds, so their low abundance and high costs limit their use in large-scale commercial applications. Tremendous efforts have been devoted to searching for alternatives to noble-metal electrocatalysts over the past few decades. Progresses in developing 3d transition-metal-based materials (such as Fe, Co, Ni) as alternative electrocatalysts for electrolyzers have shown a great potential of transition metal oxides (or hydroxide), sulfides, selenides, and phosphide for applications in water electrolysis, due to their low cost and high resistivity to corrosion in strong acidic or alkaline conditions [12], [13]. Furthermore, being modulated through diverse strategies developed up to now, including nanoarchitecture, facet engineering, defect engineering, element doping, interface engineering, and alloying [14], non-noble electrocatalysts could be competitive with or superior to that of the state-of-the-art noble electrocatalysts. Ni-based electrocatalysts emerge as a large family of alternative candidates for cost reduction of water electrolysis. In another aspect, a great variety of noble-metal-based electrocatalysts have been investigated for reducing noble metal loading while maintaining their high catalytical activities [15]. Those achievements are realized through approaches such as nanoarchitecture, heteroatom incorporation, defect and strain engineering,

6

interface/hybrid engineering, and single atomic construction [15], [16]. In such context, it has become a mainstream trend in designing electrocatalysts to use 3d transition-metal materials as catalyst support to enlarge the catalytic surface area and to modify the materials by adding heteroatoms such as Pt, Ir, Ru or other 3d transition metals to tune the intrinsic activities for OER and HER applications [17], [18].

In the following chapter, some fundamental insights about water electrolysis will be reviewed. The reaction path and descriptors of catalytic activity for the oxygen evolution reaction will be emphasized. Then, some physical and electrochemical properties of Ni compounds and some of the recently developed Ni-based electrocatalysts will be described. The influence of catalyst structure and heteroatom incorporation on the catalytic activity will be discussed. Finally, some physical and electrochemical characterization methods used to access those effects will be introduced.

2.2 Water electrolysis and the OER

2.2.1 Generality

The discovery of water electrolysis dates back to 1789 by Paets van Troostwijk and Johan Rudolph Deiman [19]. Driven by DC electrical power source, water can be split into oxygen and hydrogen. This process involves two gas evolution reactions: the hydrogen evolution reaction (HER) and the oxygen evolution reaction (OER), which happen respectively on the cathode and anode of an electrochemical cell. The overall reaction of water electrolysis is:

Equation 2.1

$$H_2O(l) \rightarrow H_2(g) + \frac{1}{2}O_2(g) \qquad \Delta E^0 = -1.23V$$
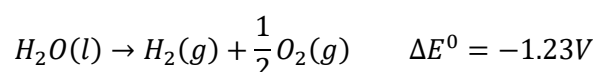
The ΔE^0 represents the theoretical cell potential at standard conditions. It is determined by the reaction's Gibbs free energy (or thermodynamically maximum reversible work) of water electrolysis which is:

Equation 2.2

$$\Delta G^0 = -nF\Delta E^0$$

The Gibbs free energy, 237.13kJ mol^{-1}, is deduced from the enthalpy ΔH and entropy ΔS changes during water electrolysis that:

Equation 2.3

$$\Delta G = \Delta H - T\Delta S$$

It implies that the cell voltage of the water electrolyzer could be reduced by operating at high temperatures [20].

Despite that the thermodynamic of water electrolysis is pH-independent, the reactants of the HER and the OER in acid and alkaline conditions are different [21]. The reaction equations for the HER and the OER in acid and alkaline conditions are summarized in Table 2.1:

Table 2.1 Reactions for HER and OER in acid condition and alkaline condition

	Acid condition	Alkaline condition
HER	$2H^+ + 2e^- \rightarrow H_2$	$2H_2O + 2e^- \rightarrow H_2 + 2OH^-$
OER	$2H_2O \rightarrow 4H^+ + O_2 + 4e^-$	$4OH^- \rightarrow O_2 + 2H_2O + 4e^-$

Compared to the one in acidic conditions, the primary reactant of the HER in alkaline condition is water rather than the proton. The additional water dissociation step in alkaline condition results in the activity of Pt catalyst being 2-3 times lower than in acidic conditions [15], [22]–[24]. However, from overall considerations, alkaline water electrolysis is easier for the design of catalysts because very few cost-effective transition metals can withstand corrosion and exhibit high activities for the OER in acid conditions [25]–[27]. In other words, most of the nonprecious OER electrocatalysts perform better in alkaline conditions than in acid conditions. And, as it will be presented in the following, the sluggishness of the OER kinetics limits more the overall efficiency of water electrolysis than the HER kinetics. Therefore, the development of transition metal catalysts for the OER in alkaline environment should be an imperative task. Additionally, the water dissociation problem of the HER and its consequent catalyst mismatch in alkaline water electrolysis could be addressed by decorating nonprecious metals on noble metal substrates [23], [28].

2.2.2 Classification of water electrolysis

Generally, there are three main types of water electrolysis, alkaline electrolysis (AEL), proton-exchange membrane electrolysis (PEMEL), solid oxide electrolysis (SOEL or high-temperature electrolysis). They are classified mainly by their actual electrolyte: AEL uses alkaline KOH solutions as electrolyte; PEMEL uses polymer electrolyte, which allowing proton transports within the membrane, and its working environment is

acid; SOEL uses solid oxygen-ion conducting electrolyte [29], [30]. As a result, their cell configurations and operating conditions are vastly different [31] (Figure 2.3).
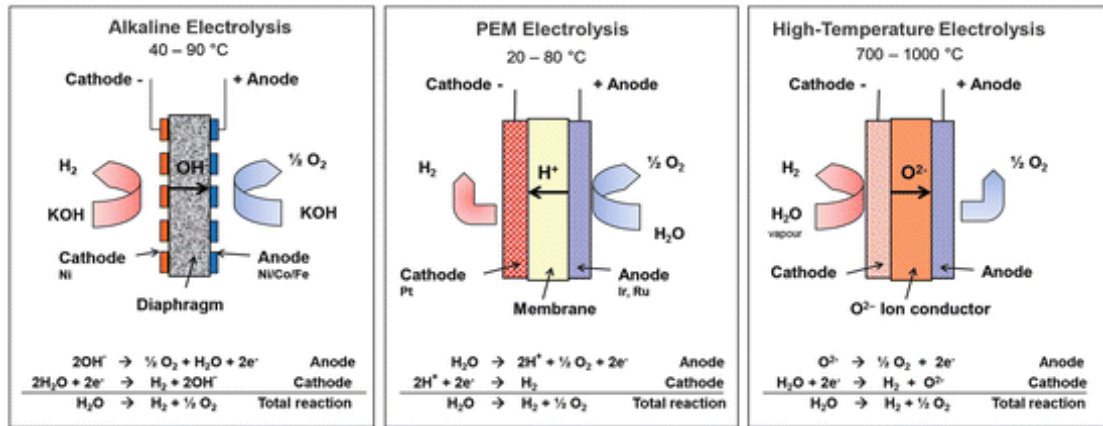
Figure 2.3 Schematic presentation of Alkaline electrolysis, PEM electrolysis and Solid oxide electrolysis [31]

Among them, SOEL has high electrical efficiency (74–81%) compare to 63–70% for AEL and 56–60% for PEMEL. SOEL is regarded as the most promising electrolysis process for future large-scale hydrogen production [32]. As is suggested from the thermodynamic point of view, the operation under high temperature could reduce the cell voltage (Equation 2.3). However, limited by the stability problems due to the degradations of catalysts under high temperature, its development is still at the laboratory scale.

PEMEL is already a commercialized technology. Its high energy conversion efficiency comparing to AEL and its high purity hydrogen production are all significant advantages. In a PEM electrolyzer, the presence of a proton-exchange membrane can essentially reduce the ohmic losses due to ion transport and efficiently prevent the gas crossover. The electrocatalysts are usually thin layers that are coated on the proton-exchange membrane. Outside of the catalyst layer, there are gas diffusion layers on both sides of the electrode (anode and cathode). The gas diffusion layer plays a vital role in PEMEL, as it can act both as a current collector and diffusion media for the generated gas phase [33]. This rationally designed cell assembly, together with the high-performing electrocatalyst (usually noble metals and their oxides), contributes to the high efficiency of PEMEL. However, the acid operation condition limited the utilization of non-precious material and is responsible for the large capital cost of PEMEL.

Alkaline water electrolysis is the most mature type compared to PEMEL and SOEL, thanks to its long developing history. It has long been used in the industry for hydrogen

production. The foundation of industrial alkaline water electrolyzers dates back to the beginning of the 20th century [34]. Conventional alkaline water electrolyzer comprises three main components, the anode, the cathode, and the separator or diaphragm, which prevent the mixing of produced hydrogen and oxygen content. Industrial AEL usually uses stainless steel or nickel-based electrodes as anode and cathode and KOH solution as electrolyte [35]. The significant advantage of AEL is the low capital cost due to the utilization of low-cost catalyst materials. Under alkaline conditions, many 3d transition metals such as Ni, Co, Fe, and Mn under alkaline conditions show excellent corrosion resistance. However, AEL suffers from limitations such as the low energy conversion efficiency caused by the ohmic losses in the diaphragm and active site blocking of catalysts by bubble coverage [36]. To overcome these limitations, some recent innovations for AEL adopt the cell designing ideas from PEMEL. The construction of a zero-gap electrolyzer configuration could help to vastly reduce the ohmic losses from the diaphragm [37], [38]. Moreover, through advanced catalyst design, a highly porous and hydrophilic gas diffusion electrode could be synthesized to replace the conventional mesh shape electrodes. This approach helps enlarge the active surface area of catalysts and counteract the bubble blocking effects under gas evolution conditions [39], [40].

2.2.3 Thermodynamics and kinetics of OER

It should be noted that the OER involves four-electron transfer processes (Table 2.1), so its mechanism is more complicated than the HER. Moreover, the HER has a much faster reaction rate in terms of exchange current density (current in an equilibrium state) than the OER [41], which is attributed to a weaker interaction of hydrogen with the catalyst sites than oxygen [42]. Due to the sluggishness of the OER kinetics limiting the overall efficiency of water electrolysis, searching for high-performance OER electrocatalysts has attracted many research concerns. The sluggishness of the OER reaction manifests itself as a considerable potential input in addition to its thermodynamic potential (1.23 V for OER), which is termed overpotential, to drive the reaction at a given current density. This excess potential is attributed to many factors such as the density of active sites, the electronic conductivity, the mass transport and the geometric or electronic effects of heterogeneous catalysts [12], [13], [43]–[45]. Among those factors, the last one has attracted the most research attention because it is related to the intrinsic activity of catalysts and offers an ideal space for realizing rational designing of electrocatalysts.
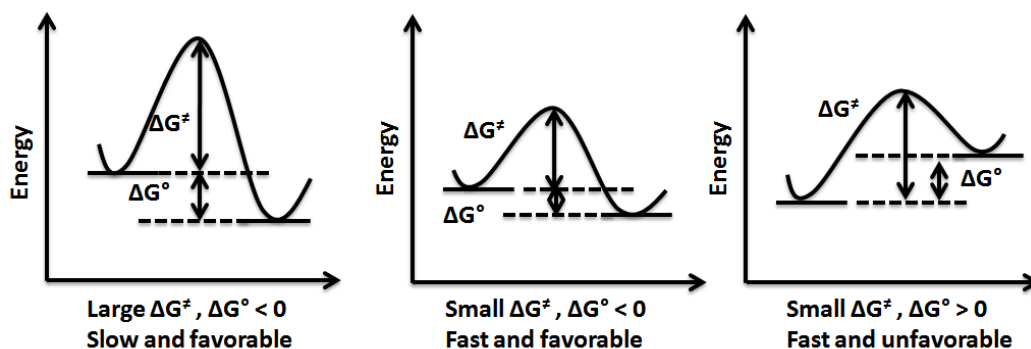
Figure 2.4 Activation energy and reaction energy for reaction rate [46]

For a simple one-step reaction, the energy difference between the reactant and product is defined as the reaction free energy ΔrG (Gibbs free energy), a thermodynamic term. The standard reaction free energy is represented as ΔrG^0 for the reaction under standard conditions. Its sign tells whether the reaction under its corresponding condition can occur spontaneously (for ΔrG<0). For the reaction in an electrochemical cell, the ΔrG is dependent on the potential E through the relationship:

Equation 2.4

$$\Delta rG = -nFE$$

It means that a thermodynamically unfavorable reaction can be altered to favorable by changing the applied potential on an electrode. To make the reaction proceed, merely keeping the ΔrG<0 is not sufficient, as an energy barrier should be surmounted to make the reactant reach a transition state. This energy barrier is called the activation energy $\Delta G^{\neq}$ (Figure 2.4). The activation energy governs the kinetic rate of a reaction through the Arrhenius equation:

Equation 2.5

$$k = \frac{k_B T}{h} e^{\frac{-\Delta G^{\neq}}{RT}}$$

For the consideration of reducing the energy loss and enhancing the reaction rate, the activation energy has to be reduced as minimum as possible. To achieve this, suitable catalyst should be identified. The role of an electrocatalyst is to help forming the reaction intermediates and reduce the activation energy. Several mechanisms for the OER have been proposed. However, the four coupled electron-proton paths proposed by Rossmeisl *et al.* [47]–[49], for which only one electron is transferred to the catalyst in each step, have been the most widely adapted [50]–[52]. With this mechanism, one

can use density functional theory (DFT) to predict the activity trends among different catalytic materials. The four coupled electron-proton steps of OER are as following:

$$H_2O(l) + \, ^* \, \rightleftharpoons \, HO^* + H^+ + e^-$$

$$\Delta G_1 = \Delta G_{HO^*} - \Delta G_{H_2O(l)} - eU + k_bT \ln a_{H^+}$$

$$HO^* \rightleftharpoons O^* + H^+ + e^-$$

$$\Delta G_2 = \Delta G_{O^*} - \Delta G_{HO^*} - eU + k_bT \ln a_{H^+}$$

$$H_2O(l) + O^* \rightleftharpoons HOO^* + H^+ + e^-$$

$$\Delta G_3 = \Delta G_{HOO^*} - \Delta G_{O^*} - eU + k_bT \ln a_{H^+}$$

$$HOO^* \rightleftharpoons \, ^* + O_2(g) + H^+ + e^-$$
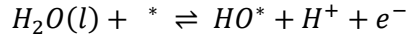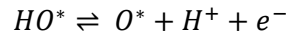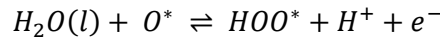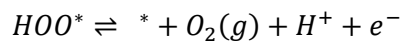
$$\Delta G_4 = \Delta G_{O_2(g)} - \Delta G_{HOO^*} - eU + k_bT \ln a_{H^+}$$

For every elementary step, the reaction free energy ΔG_{1-4} can be deduced from the binding energies of their corresponding intermediates as a function of the electrode potential U [47], [48]. For different electrocatalysts, the binding energies of intermediates are different depending on the geometric or electronic configurations of active sites [43]. The difference yields different reaction free energy for a given U. The sum of the elementary reaction steps is equal to the overall OER reaction free energy ΔG_{OER} (ΔG_{OER}=4x1.23eV when U=0V):

Equation 2.6

$$\sum_{i=1}^{4} \Delta G_i(U) = \Delta G_{OER}(U)$$

It should be noted that the thermodynamically determined reaction free energies are not rigorously direct descriptors of the electrocatalysts' activity because, as mentioned above, the overpotential and reaction rates are dominated by the activation energy [53]. However, there is a linear relationship within a class of materials between the reaction free energy and the activation energy according to the Brønsted–Evans–Polanyi (BEP) relationship [43], [54], that $\Delta G^{\neq} = \beta \Delta rG$ where β denotes the BEP coefficient (0 < β < 1). According to the Marcus theory, these two energy values follow a quadratic relationship [55], [56]. So, it means that the ΔG of every elementary step can be used as a rough approximation of the corresponding activation energies. Thus, practical descriptors of electrocatalysts' activity can be identified. Given it is quite challenging to determine the activation energy of reaction intermediates, this approximation is a very important approach to guide innovations of electrocatalysts.
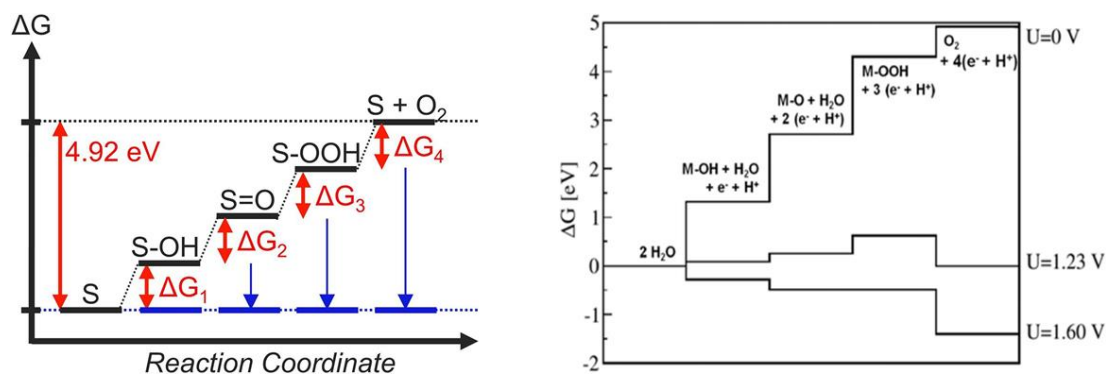
Figure 2.5 Left: The thermodynamic landscape of an ideal OER catalyst at U = 0 V (black lines) and U = 1.23 V (blue lines); Right: The free energies of the intermediates on O-*-covered RuO₂ at three different potentials [49], [55]

For multiple-step reactions like the OER, the slowest reaction step determines the overall reaction rate (rate-determining step, RDS), and the step with the highest activation energy determines the operating overpotential (potential-determining step, PDS) [57]. Often the RDS and PDS correspond to the same step due to its high reaction free energy [58], and so identifying the PDS through ΔG of elementary steps will be feasible and efficient. Using DFT calculations, the ΔG of elementary steps could be traced while increasing the electrode potential (Figure 2.5 left). For zero potential (U^0=0V), all the steps are uphill. The addition of energy by an overpotential η (η=U-U^0) to the first reaction step will reduce ΔG_1 by $e\eta$ and to the second step will reduce ΔG_2 by $2e\eta$ etcetera. Then, when all the steps become downhill following the increase of U, the overall reaction becomes thermodynamically favorable. In other words, the overpotential at which all the steps are downhill is a necessary but not sufficient criterion for the overall reaction to take place at an appreciable rate, and this overpotential is often termed as the thermodynamic overpotential [41], [48], [55].

Another important application of such a DFT approach is to determine the PDS of the OER. When the electrode potential U reaches the standard equilibrium potential E^0 (1.23V) of OER (zero overpotential), the step which requires the most reaction free energy would be the potential-determining step [50], [58], for example, the third step in Figure 2.5 (right) is identified as the PDS. For an ideal catalyst, the ΔG of every elementary step at this potential should be equal to zero, as the sum of ΔG equals zero. However, for real catalysts, this idealized case is plagued with a limitation because the energies of reaction intermediates are correlated. It was revealed by Man *et al.* and M. Koper *et al.* that the binding energy of HOO* and that of HO* have a constant difference (3.2eV), resulting in a relationship between ΔG_2 and ΔG_3 that [47], [58]:

Equation 2.7

$$\Delta G_2 + \Delta G_3 = 3.2\ eV$$

This so-called scaling relationship implies that either the second or third electron-proton transfer step is the potential-determining step and gives the OER a minimum thermodynamic overpotential of 0.37 V. Thus, the theoretical value of $\Delta G_O^* - \Delta G_{HO}^*$ (ΔG_2) could be used as a single descriptor for the OER activity and the plot of volcano curves (Figure 2.6) could be used to compare and predict the activity trends among catalysts [47], [51], [52], [58].
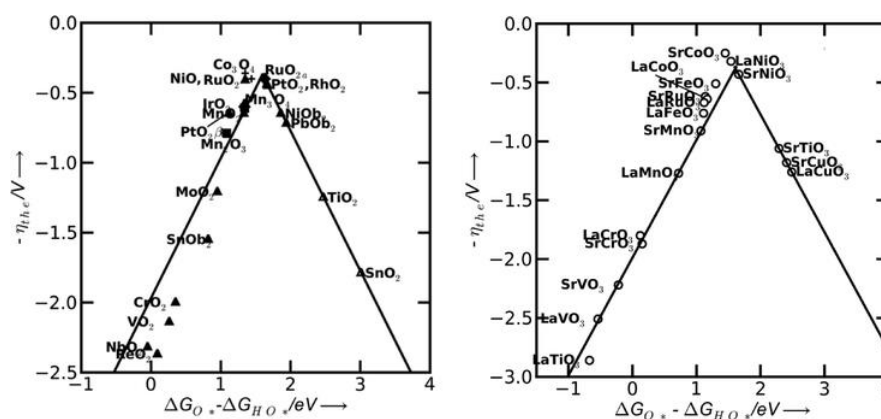
Figure 2.6 Activity trends towards oxygen evolution for different materials [47]

According to the Sabatier principle, the binging energies of reaction intermediates should neither be too weak nor too strong to get an optimum reaction rate. Thus, a volcano relationship between the catalyst activities and their intermediates binding energies applies. The calculations of theoretical overpotentials and $\Delta G_O^* - \Delta G_{HO}^*$ from DFT and scaling relationship agree well with the Sabatier principle and the trends from experimental observations [47]. Therefore, this approach reveals a fundamental understanding of the multistep mechanism of OER.

2.3   Ni-based electrocatalysts for OER

As was mentioned above, alkaline water electrolyzers allow for the utilization of cost-effective 3d transition metals such as Ni, Fe, Co as electrode materials. This advantage is vital to reduce the capital cost of water electrolyzers. Ni metal is often used as electrode materials to construct 3D structures due to its stability in harsh alkaline conditions and its flexibility to be synthesized into different shapes. Nano-structured Ni nanoparticles, nanosheets, nanowires, nanotubes, foams and hierarchical structures can serve as direct catalysts or catalyst supports to increase the electrochemically active surface area and facilitate gas transport during gas evolution [16]–[18], [59].

In another aspect, from DFT calculations and using $\Delta G_O* - \Delta G_{HO}*$ as a descriptor, Ni oxide and Co oxide are located at the top of the activity volcano plot (Figure 2.7). This fact accounts for the critical role of Ni materials in OER catalysts. Ni-based and Co-based electrocatalysts hold a significant part of the newly designed OER electrocatalysts in the recent decades. Ni-based materials, including Ni metal, alloys, oxides, hydroxide (or oxyhydroxides), sulfides, selenides, phosphide, and NiFe layered double hydroxide (LDH) have shown great potentials for the OER in AEL [13], [60]–[64].
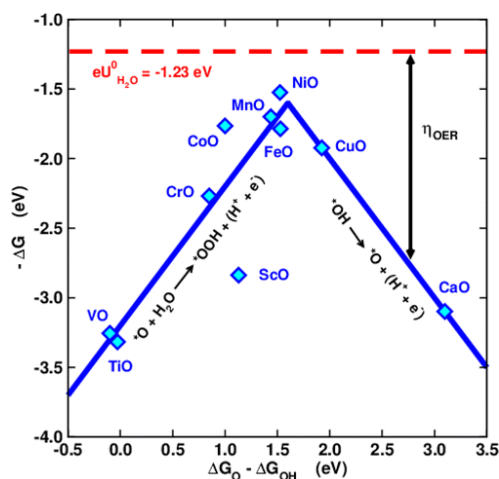
Figure 2.7 Sabatier-type volcano plot for the pristine (001) surfaces of the monoxides [65]

The theoretical OER activity of Ni oxide occupies the top of the volcano curve due to its moderate adsorption energy difference between O* and HO* reaction intermediates, as is shown in Figure 2.7 [65]. $\Delta G_O* - \Delta G_{HO}*$ is approximately 1.5 eV for NiO, very close to the top of the Volcano plot. However, in alkaline conditions, NiO is not the active species because there is a change in the structure and the oxidation state of the nickel surface compounds in the potential region where the OER takes place [66].

When the surface of Ni or Ni oxide is exposed to alkaline aqueous solutions, its surface undergoes a passivation process, which results in the formation of a thin Ni hydroxide layer ($Ni(OH)_2$) [67], [68]. Further, under positive bias potential, the $Ni(OH)_2$ would be oxidized into NiOOH, the transformation happens at a potential around 1.5V *vs.* RHE [69]. There exist, two different phases of $Ni(OH)_2$, namely α-$Ni(OH)_2$ and β-$Ni(OH)_2$, according to the Bode scheme (Figure 2.8) [70]. Upon aging, α-$Ni(OH)_2$ can be irreversibly transformed to β-$Ni(OH)_2$. When they go through charging, β-$Ni(OH)_2$ will be oxidized to γ-NiOOH or β-NiOOH. The redox reaction of $Ni(OH)_2$ to NiOOH occurs before the OER reaction, so the actual catalytically active species is NiOOH [65]. Similar transitions of oxidation state from $M(OH)_2$ to MOOH before the OER are equally

15

observed for other transition metals like Ni, Co, Fe, Mn, and the observed activities follow the order Mn < Fe < Co < Ni, due to their difference in OH-M adsorption bond strength [71].
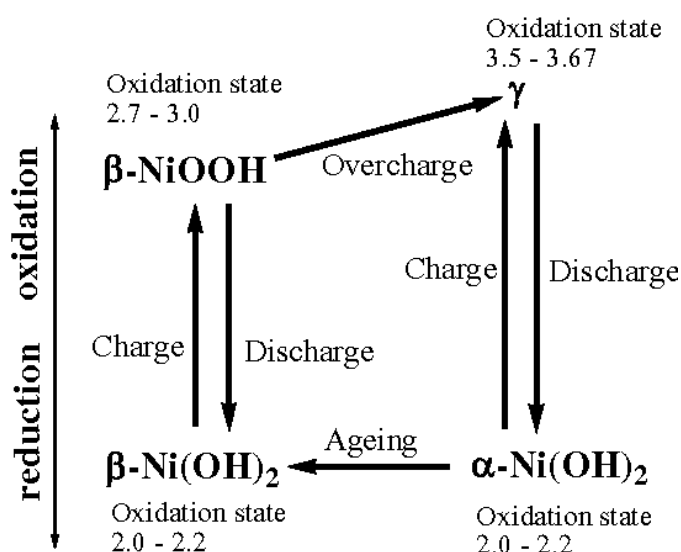
Figure 2.8 The Bode scheme for the Ni(OH)2/NiOOH redox transformation [68]

The OER descriptor ΔG_O*- $\Delta G_{HO}*$ of NiOOH is around 1.84eV, which is 0.24eV positive than the optimal 1.6eV. Therefore, the adsorption energies of the reaction intermediates on NiOOH need to be tuned to achieve an optimal intrinsic activity. Heteroatom incorporations or structure modifications such as the introduction of defects or strain engineering are the most efficient approaches to this end, and their effects will be discussed in the following sections.

2.4   Effect of heteroatom incorporation

Both geometrical (facet) and electronic (composition) factors contribute to modulate the adsorption energies of reaction intermediates on the active sites [43]. However, Ni (oxy)hydroxides are usually in an amorphous phase in alkaline solution, and they will undergo reconstructions under anodic oxidation process [72], [73]. Thus, facet engineering of NiOOH is difficult to achieve. In contrast, tuning the composition of surface Ni compounds through introducing foreign metal elements is highly feasible.

The most successful examples of this approach are the Fe modified Ni oxides/hydroxides, which could shift the OER overpotentials to as low as about 200mV at 10 mA cm^{-2} water electrolysis [74]–[76]. The effect of iron on the activity of Ni oxides/hydroxides has been studied for a long time since the seminal work of Corrigan [77], who found that even 1 ppm iron contamination in the electrolyte would dramatically enhance the activity of Ni oxide electrode and significantly reduce its OER

16

overpotentials. However, the mechanism of how iron contributes to promoting nickel's catalytical activity is still not fully understood. Theoretical DFT calculations made by the Koper's group [65] showed that doping of NiOOH with 3d transition metals including Cr, Mn, Fe, Co, Cu, and Zn would cause only limited changes in the OER overpotential when considering NiOOH as the active site. However, if the dopant metals are the actual active sites, the overpotential of doped NiOOH would change significantly. In this case, NiFeOOH and NiMnOOH are sitting at the top of the volcano curve, which corresponds to the optimal OER value of of 1.6eV. This evidence implies that the active site in Fe modified Ni oxides/hydroxides are iron rather than nickel, which agrees with the works reported by Friebel *et al.* [78]. Another explanation for the Fe effect is led by the work of Trotochaud *et al.* that the Fe impurity enhances the activity of NiOOH through a Ni–Fe partial-charge-transfer activation process and enhances the conductivity of the formed film [79].

Despite the lack of a full understanding, the synergetic effect of Fe on Ni compounds is ubiquitously observed in NiFe oxides, hydroxide, sulfides, selenides, phosphide, and NiFe layered double hydroxide [80]–[82]. It is also worth noting that the introduction of electronegative components such as S, P, Se could aid Ni-based catalysts to optimize the conductivities, finely tune the electronic structures, and expose more active sites [64], [83]. However, their stabilities under harsh OER conditions are problematic because, under anodic polarization, the surface compounds would be eventually transformed into oxyhydroxide [74], [81], [84].

Another trend in designing heteroatom electrocatalysts is to either dope or decorate noble metal elements such as Ir and Ru, which are recognized as the most active material for the OER, onto low-cost 3d transition metal supports. Through heteroatom engineering, the surface chemical composition and electronic structures can be tuned to favor the OER [85]. By this means, the intrinsic activities of Ni-based catalysts could be greatly promoted, and the loadings of noble metal could be reduced in comparison with pure noble metal catalysts. For instance, Feng *et al.* reported IrCoNi porous hollow nanocrystals for water electrolysis [86]; Li *et al.* synthesized minimal Ir-incorporated (as low as 0.57 wt%) $Co_xNi_{1-x}O$ nanowire arrays that reveal a low overpotential of 260 mV for OER at 10mA cm^{-2} [87]; and the Ir doped NiV LDH reported by Li *et al.* exhibit excellent catalytic properties with OER overpotential of 203mV at 10mA cm^{-2} [88].

More interestingly, at the cutting edge of the catalysis field during the recent few years, single-atom catalysts (SACs) are drawing more and more attention [89], [90]. The SACs are defined as atomically dispersed metal ions (usually noble metal ions)

anchored on supports such as Ni metals, metal oxides, or layered double hydroxides. This achievement permits the maximum utilization of active species and a synergetic coupling between the anchored atoms and the underneath support, which would play an essential role in improving the electrocatalyst activity. For example, with only 0.45 wt.% ruthenium loading on CoFe layered double hydroxides, the resulting material can achieve an overpotential of 198 mV at 10 mA cm^{-2}, with a small Tafel slope of 39 mV dec^{-1} for the OER [91]. Elsewhere, an overpotential as low as 200 mV at 10 mA cm^{-2} for the OER was achieved by atomically dispersed Ir (1.3 wt%) on NiFe/Ni core-shell nanowires [92]. Finally, Zhang *et al.* demonstrated that Au decoration (0.4 wt%) can cause charge redistribution of active sites in NiFe LDH and results in a 6-fold OER activity enhancement [93].

Generally, the heteroatom modifications would simultaneously cause inhomogeneity of electrode surface and thus beneficially enlarge the exposure of active sites. From this point of view, the heteroatom effect and the nanoarchitecture effect that will be discussed in the next section are interconnected.

2.5 Effect of nanoarchitecture

Quantitatively, the activity of an electrode is governed by the intrinsic activity of the catalytic material and the number of active sites S. The current of an electrode is given by the following equation that defines also the turnover frequency (TOF), which is a measure of the intrinsic activity of the material per active site [94]:

Equation 2.8

$$j(\eta) = \frac{i(\eta)}{A} = S * TOF(\eta) * \frac{nF}{AN_A}$$

where j, i, η denote the catalytic current density, catalytic current, the overpotential respectively; A, S, n, TOF denote the superficial electrode area, number of surface sites, number of electrons transferred per molecule and the average turnover frequency of all sites, respectively.

As can be deduced from the equation, the current density under a given overpotential, or in other terms the "apparent electrode activity," is directly proportional to the number of active sites. The intrinsic activity of the catalyst and the number of active sites have to be evaluated separately to understand the origins of the activity of a given catalyst. However, in practice, there is no direct way to measure TOF. Neither is there a universal way to count the number of active sites due to differences in catalysts' nanostructure, porosity, and lattice structure [95]. Therefore, it is crucial for every

specific electrocatalyst study to develop a feasible way to identify the electrochemically active sites and estimate the electrochemically active surface area.

Nevertheless, enlarging the exposure of active sites per geometric area is considered a simple and effective manner to optimize the OER efficiency. This strategy has now been widely applied in developing advanced electrocatalysts. With the rapid development of synthesis techniques in the past decade, many artificial nanostructures have been synthesized with different characteristic dimensions. They either have functional shapes such as nanowires and nanosheets, or have porous structures that are self-supported to serve directly as electrodes or catalyst supports such as carbon cloth, metal felts, metal foams. Also, they can have hierarchical structures with both functionalities and self-supported porous skeletons [96]. Moreover, via the rising 3D printing technologies, much more ordered and elaborate architectures can be fabricated for OER applications, for example Ir catalyst with 3D woodpile-structures [97].

Another way of increasing the exposure of active sites is heteroatom modifications, as was mentioned above. The Ni-based electrocatalyst is usually covered by an outer hydroxide layer formed by the synthesis procedure or reconstruction under the OER conditions. The heteroatom-modified heterogeneous surface can facilitate the generation of defects during the formation of the Ni hydroxide layer. Thus, defect-rich hydroxides are frequently encountered in heteroatom-modified Ni-based materials. Such defects are often recognized as Ni^{3+} defect sites or richness of NiOOH content in the hydroxide layer [73], [98]–[100].

All those nanoarchitecture technologies are conceived to maximize the utilization of catalytically active materials. However, at large current densities, slow mass transport of reactants or products may hinder the activity in compact porous electrodes. For the OER in AEL, the generally high concentration of reactant OH^- will not cause mass transport issues. Still, the diffusion of produced O_2 bubbles could be hampered by adhesion or entrapment and reduce the accessibility of electrolytes to the catalyst surface. From such considerations, the construction of hydrophilic electrode materials are drawing more and more research attention.

2.6 Effect of wetting

During the OER, oxygen would preliminarily be generated in the form of dissolved oxygen in the electrolyte. Oversaturation of oxygen in the vicinity of the anode will cause bubble nucleation [101]. Defects like pits and crevices are preferential sites for heterogeneous bubble nucleation [102]. Then bubble nucleus undergoes growths and

detachments on the topmost surface of an electrode. During those processes, bubble occupations on the electrode surface will isolate the catalyst's active sites and cause an increase of OER activation overpotential. Moreover, the presence of bubbles in electrolytes would add to the cell ohmic overpotential. Therefore, constructing bubble-repellent surface to facilitate bubble detachment and transport is energetically profitable.

The critical departure diameter for a bubble on an upward-facing electrode in the absence of electrolyte flow is descript by the Fritz correlation [103]:

Equation 2.9

$$D_d^* = 0.02\theta \left(\frac{\sigma}{g(\rho_l - \rho_g)} \right)^{1/2}$$

where θ denotes the contact angle of a solid surface in a liquid-solid-gas triple-phase contact line (TPCL), σ denote the interfacial tension. For 0°<θ<90°, the solid surface is defined as hydrophilic; for 90°<θ<180°, the solid surface is defined as hydrophobic. Accordingly, it is generally accepted, despite the opposite trend in the analog pool boiling process [103], that the more hydrophilic the surface is, the easier tiny bubbles can detach from the surface, causing less bubble blocking of the surface. Following this consideration, super-hydrophilic or super-aerophobic electrocatalysts have been developed for gas evolution reactions [104]–[107]. For example, the nanostructured nanoplatelets of MoS_2 film is thought to have discontinuous TPCL, which largely enhances the surface hydrophilicity and facilitates the bubble removal during the HER [108].
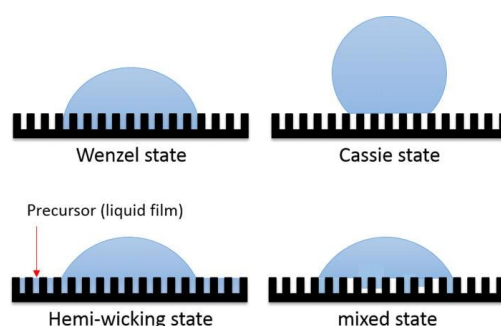
Figure 2.9 Wetting state on hydrophilic and hydrophobic micro-textured surfaces [109]

In general, when two substances are in contact, there will be a difference in surface energy. When the contact is between a drop of liquid and a solid surface, this difference will force the droplet to deform into a partial or complete spherical shape. The angle between the planar of the substrate and the tangent line of the droplet at the TPCL is defined as the contact angle. Using Young's equation, the contact angle of a smooth

and flat solid surface depends on the interfacial tensions of the solid-liquid, solid-gas, and liquid-gas interfaces, denote hereafter as γ_{sl}, γ_{sg}, and γ_{lg} respectively. They are related through the following equation:

Equation 2.10

$$\gamma_{sg} = \gamma_{sl} + \gamma_{lg} \cos \theta$$

Here the contact angle θ is a measure of the intrinsic property of the solid and depends on the surface energy of the material (mJ m^2).

However, if the surface is rough, the measured (or apparent) contact angle θ* will be altered according to the wetting state equations. The Wenzel wetting state (Figure 2.9) applies for a homogeneous wetting regime where a droplet of liquid thoroughly wets the underneath solid, and θ* depends on the intrinsic contact angle and the roughness ratio r_s:

Equation 2.11

$$\cos \theta^* = r_s \cos \theta$$

This equation means that roughing will enhance a surface's wetting property (hydrophilic or hydrophobic). The Wenzel wetting state is still an idealized model to describe the wetting phenomenon. However, heterogeneous wetting, where the air bubble is trapped underneath the droplet often appears in the real world. The Cassie-Baxter wetting equation is usually used to describe the heterogeneous wetting:

Equation 2.12

$$\cos \theta^* = r_s f_s \cos \theta + f_s - 1$$

The factor fs denotes the fraction of the solid surface wet by the liquid droplet in this equation. Both the Wenzel and Cassie-Baxter models emphasize the contribution of roughness to the surface wetting properties, and they serve to explain the apparent contact angle measured under static wetting conditions. The more complex is the surface structure, the smaller is the apparent contact angle for an intrinsically hydrophilic material. The strategy to construct a super-hydrophilic surface is mainly based on reducing the apparent contact angle of an electrode surface. It was found in this thesis based on measurements under static conditions that increasing the layer thickness of the complex structure will help improve the roughness and reduce the apparent contact angle [110].

It should be noted that the above discussed increasing roughness approach focuses on constructing a 2D super-hydrophilic at the outmost layer of the electrode to prevent

bubble blockage. However, this concept is still too simple to accounts for the accessibility of electrolyte to the whole electrode structure under OER conditions. As the gas evolution is a dynamic process, in which invasion and drainage of the wetting phase take place alternatively in the internal structure of 3D structured electrodes, metastable Cassie wetting state, hemi-wicking state or mixed wetting state (Figure 2.9) [109], [111], in which gas is trapped in the internal pores of an electrode, are often observed for gas evolution reactions [112]–[115]. Therefore, investigations of the wetting conditions of a 3D structured electrode should be focused on both measuring contact angle of the outer surface under static conditions and investigating the gas behavior or water uptake in the internal structures during the OER, analogically to the ones in assessing porous transport layers in PEM electrolyzer [116]. The latter is challenging and may need *in-operando* technologies such as electrochemical impedance spectroscopy, acoustic emission detecting, high-speed optic camera, or even X-Ray Computed Tomography.

The effect of defects on hydrophilicity has been well studied for carbon-based materials (like graphene and graphite) [2]. The defects could increase the surface energy of the material and thus enhance its intrinsic hydrophilicity (decrease the inherent contact angle θ). Surprisingly, there are only a few reports about such an effect on metallic material, probably because this effect won't cause a significant change of θ for metal, and its detection is beyond the sensibility range of contact angle measurement. However, in microporous media, the evolution of intrinsic hydrophilicity could induce a more pronounced effect than it exerts on the apparent contact angle measured on a 2D plane. In a porous media, whether the liquid phase can wet a pore depends on the pore size, r_c, the intrinsic hydrophilicity of the material ($\cos\theta$) and the interfacial tension σ. According to the Young-Laplace equation, the critical pressure threshold to prevent the water from being invaded by air is [117]:

Equation 2.13

$$P_c = \frac{2\sigma\cos\theta}{r_c}$$

For a given pore size, the higher the intrinsic hydrophilicity ($\cos\theta$) is, the higher the pressure barrier will be, the more difficult the pore will be invaded by air. If the pore size is on the microscale or nanoscale, then a tiny alteration of $\cos\theta$ would cause a considerable variation of P_c. It should be noted here that the intrinsic hydrophilicity is a local surface property of pore walls and is independent of the topology of macropores. So, to promote the wetting conditions of porous media, the critical factor

would be the intrinsic hydrophilicity of material, and its optimization should rely on defect management.

3   SYNTHESIS AND METHODOLOGY

According to the above understanding about the OER, constructing 3-dimensional (3D) electrode structures with a high surface-area-to-volume ratio is beneficial for the development of OER catalysts. 3D electrodes for the OER are conventionally synthesized using Ni foams as support, and specific structures such as nanowires and nanosheets are usually the substructures of the hierarchical architectures. However, the pore size of commercial Ni foams is in the range of hundreds of microns [118], which could limit the surface-area-to-volume ratio. Therefore, constructing compact, porous and self-supporting Ni electrodes is the first option of our designing strategy. A drastic promotion of the OER activity is expected through this attempt because of the increased EASA of Ni material. This effect will be closely investigated through the EASA determinations and testing of the OER performance of the synthesized materials. Moreover, the intentionally reduced pore size or wall spacing in the porous electrode could contribute to enhancing hydrophilicity of the structures and to reducing oxygen blocking of active sites according to Equation 2.13. This is because the capillary pressure of narrow pores can contribute to prevent gas invasion during OER. Nevertheless, this effect should be evaluated with caution, since the oxygen transport in porous media could leave stationary trapped gas in the structures [119]. The verification of narrow pore accessibility to electrolyte and their activity for OER demand a synthesis of analysis from different characterization technologies.

Another attempt of this thesis is to apply heteroatom modification on the designed 3D Ni skeleton for further improving its OER activity. The identifications of surface compositions and their effect on the OER activity should be evaluated.

Overall, rationally designing Ni catalysts applicable for oxygen evolution reaction requires a thorough understanding of the parameters affecting the materials' structure, morphology, and composition of surface species, *etc.* In this thesis, multiple characterization methods such as scanning electron microscopy (SEM), transmission electron microscopy (TEM), X-ray photoelectron spectroscopy (XPS), and electrochemical (EC) characterizations are used to achieve a better understanding of the physical and electrochemical properties of the synthesized materials. Additionally, the *in-operando* acoustic emission detection technology is newly developed to monitor the oxygen bubble transport in the 3D electrode. Their principles and the synthesis methods of materials are to be introduced in the following sections.

3.1 Nano-structuring of Ni electrode by template

Electrodeposition is a conventional bottom-up method for nanofabrication. Using a template (hard or soft template), one can readily tailor the nanoarchitecture of materials and produce highly ordered shapes [120]. Also, the controllable current and potential conditions offer other possibilities to produce desirable material morphologies. In this thesis, two unique nanostructures are investigated, arrays of Ni nanowire and fractal Ni foam. They are all synthesized by electrodeposition, however, using different templates.

The electrodepositions of Ni were conducted within an aqueous electrolyte of 0.1 M $NiCl_2$, and the 2 M NH_4Cl component was added to the electrolyte as a supporting electrolyte. The use of supporting electrolytes enhances the electrolyte conductivity and reduces the ohmic drop within the solution. During the deposition process, Ni deposits were formed on the cathode by reducing the Ni^{2+} ion into zero-valent Ni through the following reaction:

Equation 3.1

$$Ni^{2+} + 2e^- \rightarrow Ni(s) \qquad E_0 = -0.25V$$
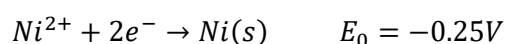
The standard potential of the Ni^{2+}/Ni redox reaction is -0.25 V, which is lower than the HER (E^0=0V), so the HER will be a competitive reaction for Ni deposition.

3.1.1 Ni nanowire templated by AAO membrane

To form Ni nanowires (NW) with the electrodeposition, we used the anodic aluminum oxide (AAO) membrane as a sacrificial template. An AAO membrane is a thin honeycomb film with open-pore channels as small as 5 nanometers in diameter. The pore diameter of AAO membrane used in this thesis is 200 nm. The AAO is an insulator, so it can't be used directly as a substrate. To address this problem, we deposited a thin Ti layer (400 nm) by sputtering at the AAO backside to ensure electrical contact mandatory for Ni electroplating (Figure 3.1).

The current density for NW deposition was maintained at a moderate -10 mA cm^{-2} to keep the side reaction rate as low as possible. It also ensures the uniform growth rate of NW in each pore channel, and as a result, the mean length of NW is uniquely dependent on the deposition time. After the electrodeposition procedure, the cell is thoroughly rinsed with deionized water and filled with 1M KOH solution to dissolve the AAO membrane. Thus, vertically aligned Ni NW arrays are left after AAO dissolution for successive characterizations.
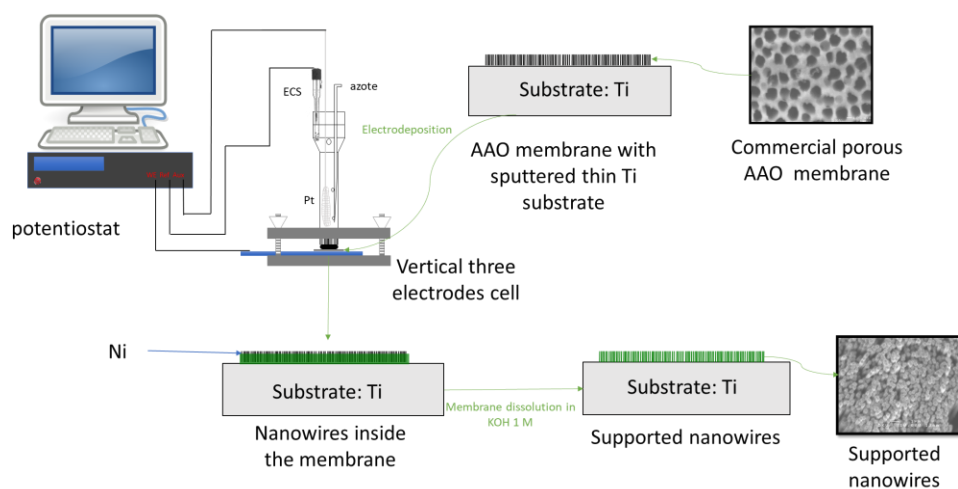
Figure 3.1 Ni nanowire electrodeposition using AAO membrane

3.1.2   Ni foam templated by hydrogen bubble

As was mentioned above, the hydrogen bubbles are side-products of Ni electro-deposition. However, from the point of view of constructing nanostructures, it can be used as a dynamic template to synthesis hierarchical Ni foams. In principle (Figure 3.2), the Ni deposit and hydrogen bubbles form simultaneously under intensive current density. The Ni deposit is restricted to grow around the space between hydrogen bubbles. Thus, a highly porous Ni network with dendritic walls will be left at the end of the electrodeposition.
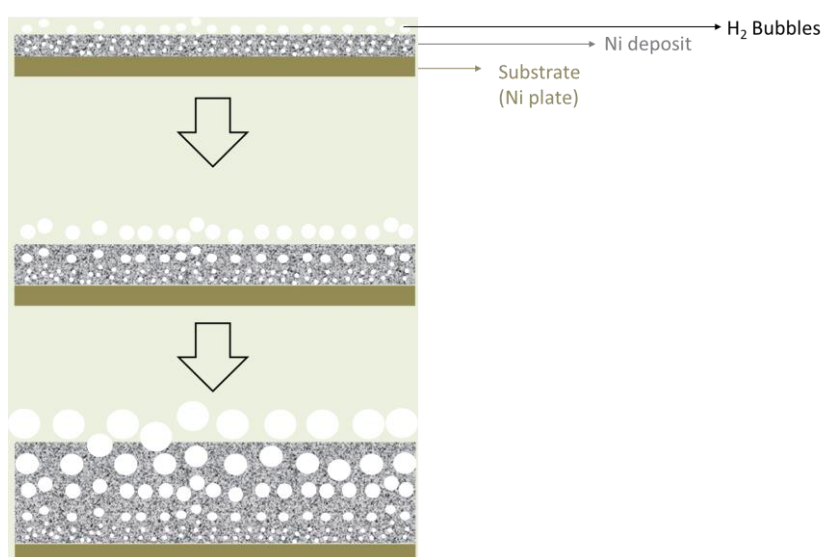
Figure 3.2 Hydrogen bubble templating method to synthesis Ni DHBT foam

This method is called the dynamic bubble templating approach and was first proposed by Shin *et al.* [118] to synthesize copper foams. Since then, a variety of similar structures synthesized using different materials has been reported. The as-synthesized metal foams process extensive pores, and the pores have hierarchical structures, which is beneficial for optimizing the surface hydrophilicity to reduce bubble coverage during the OER.

In this thesis, the flat Ni plates of $1cm^2$ are used as substrates. The current density for Ni DHBT foam deposition was maintained at $-2A\ cm^{-2}$ to keep enough generation of hydrogen bubbles. The distance between the counter and the working electrode was fixed at *ca.* 5 mm to reduce the solution resistance. After the electrodeposition procedure, the as-prepared electrodes were thoroughly rinsed by deionized water and were used for successive characterizations or modification.

3.2   Surface modification of Ni electrode by Ir

Metal ions have different reduction potentials, and the difference in reduction potentials will cause one metal ion with relatively high reduction potential (more noble) to oxidize the zero-valent metal whose reduction potential is relatively low (less noble) when they encounter [121]. This reaction is called galvanic replacement (GR) reaction, and it results in the former metal ion being reduced and deposited on the spot. GR reaction is often used to synthesis bimetallic electrocatalysts [122], core-shell, or hollow nanoparticles [121]. Using a noble metal to replace the surface atoms of 3d transition metal supports is an excellent strategy to reduce the loading of noble metals in electrocatalysts.

The GR reaction between Ir and Ni could be [123]:

Equation 3.2

$$[IrCl_6]^{2-} + 2Ni \rightleftarrows Ir + 2Ni^{2+} + 6Cl^-$$
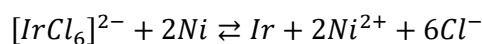
Given that the standard potential for $IrCl_6^{2-}/Ir$ is +0.88V *vs.* SHE and that Ni^{2+}/Ni is -0.25V *vs.* SHE, this reaction could happen spontaneously. However, because of Ni's passivation layer (Ni oxide or hydroxide), this reaction can be prohibited if a nickel oxide layer is present. So, the GR reaction between Ir and Ni should be conducted in a moderate acid solution (Figure 3.3).

$$2\,H^+ + Ni \rightleftharpoons H_2 + Ni^{2+}$$

2-Galvanic replacement of Ni by Ir

$$[IrCl_6]^{2-} + 2\,Ni \rightleftharpoons Ir + 2\,Ni^{2+} + 6\,Cl^-$$
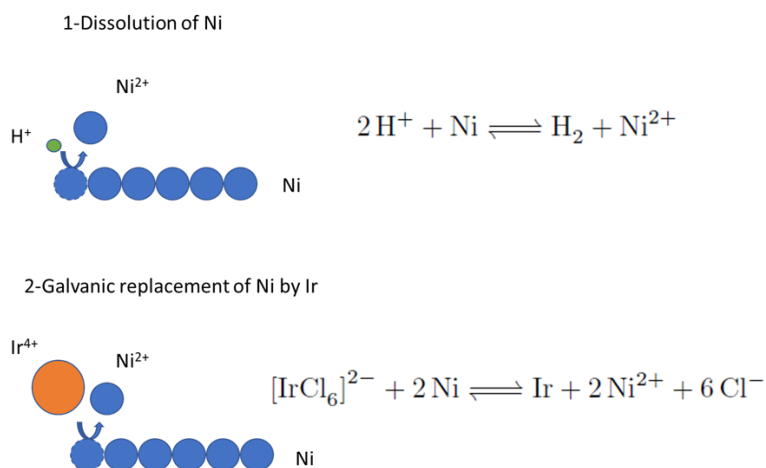
Figure 3.3 Simultaneous dissolution and galvanic replacement reactions for Ni surface modification

Inspired by this mechanism, we intended to modify the Ni DHBT foam support with GR reaction and synthesize the Ir-decorated Ni DHBT electrode. The modification was accomplished by immersing freshly prepared Ni DHBT film into 0.001 M K_2IrCl_6 + 0.01 M HCl precursor solution for up to 20 hours.

3.3 Morphology and structure characterization

In principle, the signals that we observe in materials through modern physical characterization methods such as electron microscopy (SEM and TEM) and XPS are always generated by the processes of interaction (with or without excitation) between incident radiation and material. Only the source of radiation, the sensor, and the mechanism of interactions vary from technique to technique.

3.3.1 Scanning electron microscopy (SEM)

The scanning electron microscope (SEM) is an analytical technique serving to observe the morphology of materials. It uses a thin beam of electrons emitted by an electron gun as a probing source. Electromagnetic lenses focus the electron beam onto the sample. The interaction between the electrons and the sample causes the formation of lower energy secondary electrons. They are amplified, then detected, and converted into an electrical signal. This process is performed at each point of the sample by scanning. The set of signals helps to reconstruct the topography of the sample and to provide a landform image.

In principle, a scanning electron microscope has three detectors corresponding to the three products of the interaction: secondary electrons, backscattered electrons, and X-ray photons.

- Secondary electron: A primary electron from the incident beam collides with the sample. When it interacts with the electrons of an atom, it emerges with a loss of energy. A secondary electron is emitted as a consequence of the ionization of the atom. This process is called inelastic scattering. The detection of these electrons provides information on the sample's topography to a depth of 10 nm. Analysis of these electrons provides a characteristic image of the surface. These electrons represent an excellent tool for observing the contours the morphology of the sample.

- Backscattered electron: A primary electron from the incident beam can collide with the atom without losing kinetic energy. It does not exchange energy with atoms in the sample but undergoes a Coulomb interaction with the "diffusing" atoms. This process is called elastic scattering, and the incident electron is called elastically backscattered. The higher the atom's atomic number, the stronger the signal is, and the brighter the image area. The image obtained is, therefore, a function of the chemical composition of the sample. The backscattered electrons provide useful supplementary information of the sample under test.

- Emission of an X photon: In some cases, an electron from an inner shell of the atom is ejected by the collision of the primary electron. It will be replaced by an electron from the upper shell. A photon with energy equal to the difference between the two levels of electronic energy is then emitted. Another electron will fill the void in the upper layer from an even higher layer with the emission of a photon, and a cascade is thus created. The study of X photons allows both qualitative and quantitative analysis of the sample's chemical composition, and this method is called Energy-dispersive X-ray spectroscopy (EDX).

This thesis conducted SEM and EDX characterizations with JEOL, JSM-6300F and VEGA3 TESCAN microscopes in INRS-EMT. Our collaborators at Macmaster university provided the high-resolution SEM analysis.

3.3.2 Transmission electron microscopy (TEM)

The transmission electron microscope (TEM) is a powerful tool to analyze materials' composition, morphology, and electronic structure. The TEM uses a high voltage electron beam emitted by an electron gun. Electromagnetic lenses are used to focus the electron beam onto the sample. As it passes through the sample or its atoms, the electron beam produces different kinds of radiation. The detector can analyze the transmitted electrons, then translates the signal into a contrasted image. Moreover,

the analysis of the X radiation emitted provides additional measurements on the composition and crystallography of the sample.

There are two main types of interactions between electrons and the matter they pass through: elastic or inelastic. During an elastic interaction, the primary electron interacts with a nucleus of the material's atoms through coulomb force, and it will be elastically scattered. It contributes to forming the images of the sample. During an inelastic interaction, the primary electron loses a large part of its energy due to the interaction with the nuclei. The loss of energy contains information on the sample's composition. Each of these two types of interactions has a certain probability of occurring. It is possible to separate electrons based on the energy they lost in the sample using a filter or an energy analyzer. Elastically scattered electrons make it possible to obtain information on the object's geometry (either by diffraction or by imaging). Inelastically scattered electrons can provide local chemical information (nature of the element, bonds, electronic structure local). This technique is called electron energy loss spectroscopy (EELS).

The TEM and EELS characterizations were conducted on Ni nanowire samples to study its outer layer compositions, and our collaborators in Macmaster university also provided those works.

3.3.3   X-ray photoelectron spectroscopy (XPS)

X-ray photoelectron spectroscopy (XPS) is an analytical technique to investigate the surface elemental composition and electronic state of atoms in materials. It is a surface-sensitive analytic method that probes the material within a depth of 1-10nm. Its source of radiation is a beam of X-rays emitted from Al Kα (with E_{photon}=1486.6eV) or Mg Kα (with E_{photon}=1253.6eV) [124]. When the monochromatized X-rays interact with the atoms of a sample, the photoelectrons will be emitted through the photoelectric effect. The measured kinetic energy of photoelectrons enables determination of core level binding energy with:

Equation 3.3

$$E_B = h\nu - E_k - \Phi$$

The E_B, hν, E_k, and Φ denote the binding energy, the incident photon energy, the kinetic energy, the spectrometer work function, respectively. Electrons emitted from different orbitals of different elements have different binding energies. The characteristic binding energies help one to identify the element under test and their chemical states.

Moreover, with the sensitivity factors, one can also quantify the concentrations of elements.

Due to the merit of surface sensibility, XPS is a suitable technique to examine the surface property changes induced by the galvanic replacement reaction of Iridium on Ni DHBT film and their subsequent effects on catalyzing OER. X-ray photoelectron spectroscopy measurements were performed on Ni DHBT and Ir/Ni DHBT before and after the OER electrochemical characterization.

3.4 Electrochemical characterization

The conventional electrochemical characterizations are usually performed in a three-electrode system. The working electrode can act as either the anode or cathode of the cell following the study interest. In such a configuration, the potential at the working electrode (WE) can be readily monitored and controlled while ignoring the contributions from the counter electrode. It allows one to study a half-cell reaction exclusively. A general setup schematic of the three-electrode system is shown in Figure 3.4. The Pt mesh is used as a counter electrode (CE). The saturated calomel electrode (SCE) is used as a reference electrode (Ref). All the potentials were converted relative to the reversible hydrogen electrode (*vs.* RHE) following the equation $E_{RHE} = E_{SCE} + 0.242$ V $+ 0.059$V *pH. All characterization was performed in 1M KOH electrolyte. The three-electrode cell is connected with a potentiostat,which can apply various electrochemical techniques.
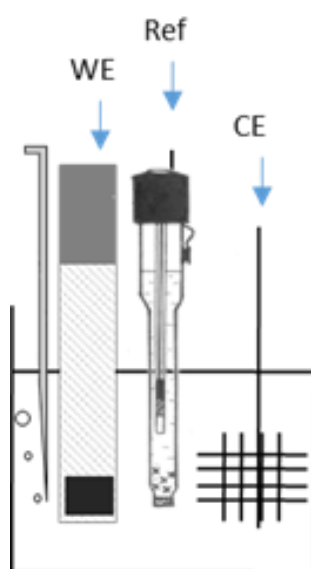
Figure 3.4 Three electrode system configuration

Through electrochemical characterization, we intend to gather three kinds of information. The first is the critical parameters concerning the OER performance; the

31

second is information about the electroactive species; the third is the quantity of the surface area of the electrode.

3.4.1 OER performance

In this study, one primary purpose of electrochemical characterization is to test the OER performance. There are usually three distinct regions in a typical OER polarization curve where the overpotential is plotted as a function of the logarithm of current density (Figure 3.5) [125]:
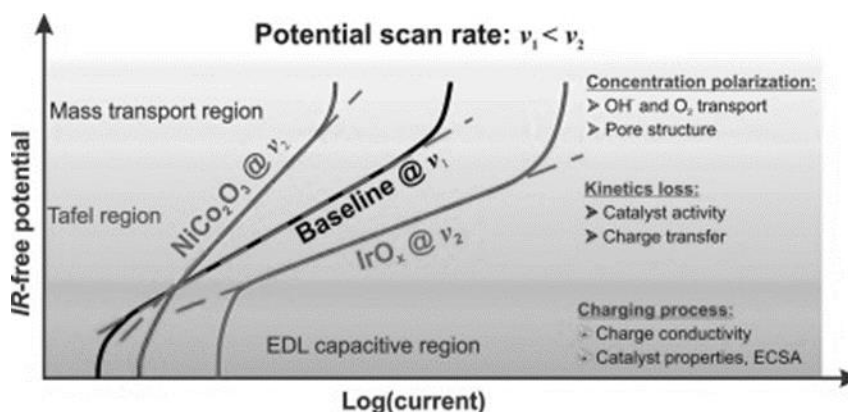
Figure 3.5 Schematic representation of Tafel plots depending both on applied catalyst and scan rate
[125]

- When the overpotential η is low, the E-i relation resides in the activation region (EDL capacitive region in Figure 3.5). The kinetics of the OER is governed by the well-known Butler–Volmer equation. Under quasi-reversible condition the total current I and overpotential η on the anode side follow:

Equation 3.4

$$I = I_0 \left[exp\left(\frac{\alpha nF\eta}{RT}\right) - exp\left(\frac{-(1-\alpha)nF\eta}{RT}\right) \right]$$

In this equation, the I_0, α, n denote the exchange current density, charge transfer coefficient, number of electrons. This parameter is highly related to the number of active sites, S, and the activation energy, E_a, of catalyst. An increase of S and a decrease of E_a will translate into a rise in I_0.

- When the overpotential is significant, the E-i relation resides in the Tafel region. In this case, the reverse reaction on an anode is negligible, and the Butler–Volmer equation simplifies to Tafel equation:

Equation 3.5

$$I = I_0 exp\left(\frac{\alpha_a nF\eta}{RT}\right)$$

$$\text{or } \log I = \log I_0 + \frac{\alpha_a nF}{2.303RT}\eta$$

In the plot of overpotential in the function of log (current), this region gives a linear slope which is called the Tafel slope. The Tafel slope is a critical parameter to evaluate the catalyst activity. A low Tafel slope signifies a high catalytical activity. The exchange current density I_0, another critical factor for activity, can also be obtained by extrapolating the linear part to the log (current) axis.

- When the overpotential is higher, the mass transport of reactant or oxygen transport will take control, and the E-i relation will be in the mass transport region.

The Tafel region is ideal for OER characterizations because the charge transfer governs the current and potential, and the reaction rate presents the catalytical activity.

The OER performance should be tested under a fixed current density using the chrono-potentiometry method. During such tests, the potential of the working electrode is monitored through time and then is converted to overpotential by subtracting the equilibrium potential of OER (E^0=1.23V) and the ohmic potential drop within the solution:

Equation 3.6

$$\eta = E - E^0 - iR_s$$

Conventionally, the overpotential for an electrocatalyst to reach a 10 mA cm^{-2} current density, which represents the current for solar water splitting under 10% solar-to-fuel efficiency, is regarded as a critical value to compare the OER activity among electrocatalysts. The Tafel plot (Figure 3.5) could be obtained by conducting chronopotentiometry tests point by point for different current densities and extracting the Tafel slope and I_0 from these data.

3.4.2 Electroactive species characterization

The identification and quantification of catalyst active sites are essential to understand the origin of the OER catalytic activity. The voltammetry is very useful for identifying and quantifying electroactive species on the surface of catalysts. It is a study on the electrode behavior when the applied potential steps with time. Voltammetry measurements are performed by monitoring the current as a function of the potential. As the applied potential changes, the current changes instantaneously depending on the electrochemical laws. Cyclic voltammetry can perform forward and backward scans of potential in a given potential range.

For example, $Ni(OH)_2$ is the surface compound of most Ni-based catalysts, and its redox couple NiOOH is recognized as the actual active species to catalyze the OER. The transition from $Ni(OH)_2$ to NiOOH always takes place before the OER and may sometimes overlap with it. The redox reaction of $Ni(OH)_2$/NiOOH has an oxidation peak and a reduction peak in the voltammogram, both of which can be used for quantification purposes. Noble metals such as Ir would be oxidized in alkaline water electrolysis, and that can be observed in the CV voltammogram. Moreover, at the negative potential, they usually have underpotential adsorption and desorption reactions with H+ in solution near the onset potential of HER. Their peaks are critical features to determine the electrochemically active surface areas.

3.4.3 EASA determination

The electrochemically active surface area (EASA) is an essential factor to be determined when examining the activity of electrocatalysts, especially for the 3D structured materials. It is more accurate to use EASA to represent the density of active sites of material than the other metrics, such as the mass loading or the surface area determined by BET (Brunauer–Emmett–Teller) method. This is because the OER mainly happens on the surface of the catalyst and the actual electrolyte/electrode interface depends on the wetting conditions of the material. There may exist a variety of methods to determine the EASA. Each one is applicable to a particular type of electrocatalysts.

The underpotential deposition method is widely used to determine EASA for noble metals. Take the hydrogen underpotential deposition (H_{upd}) as an example. The adsorption and desorption of H^+ only happen in one monolayer with the active sites, so the charge quantity for adsorption or desorption is proportional to the surface area and the transferred electron number.

The quantity of catalyst precursor, as was mentioned above, can also be used to determine EASA of Ni sites. Indeed, by integrating the CV peaks of $Ni(OH)_2$/NiOOH, one can calculate the quantity of charge Q consumed for oxidation or reduction. If one assumes that the redox reaction corresponds to one monolayer of Ni sites, then EASA can be calculated. Additionally, the oxidation reaction of metallic is also used for EASA determination. In a specific potential range, the redox $Ni/\alpha\text{-}Ni(OH)_2$ is reversible. However, it needs caution when operating because the $\alpha\text{-}Ni(OH)_2$ can be easily and reversibly transformed into $\beta\text{-}Ni(OH)_2$.

Another most used way is to determine the double layer capacitance, which originates from the Helmholtz layer. This way is achieved either by CV scans in the potential range with no redox reactions or by impedance measurements and fittings.

3.5 Electrochemical impedance spectroscopy

Electrochemical impedance spectroscopy (EIS) is a powerful tool to study electrode/electrolyte properties and reaction kinetics. Unlike the above-described DC electrochemical methods, EIS uses sinusoidal current or potential perturbations to probe the impedance of an EC system in the function of signal frequency. The impedance of an EC system is defined as [126]:

Equation 3.7

$$Z(f) = \frac{F[E(t)]}{F[I(t)]} = \frac{\tilde{E}(f)}{\tilde{I}(f)}$$

The symbol F denotes the Fourier transform through which the time domain variable is transformed into a function of frequency. For simplifying calculations, the impedance is usually expressed in complex numbers with a real part Re(Z) and an imaginary part Im(Z):

Equation 3.8

$$Z(\omega) = Re(Z) + j \cdot Im(Z) = Z'(\omega) + j \cdot Z''(\omega)$$

In which the ω is the angular frequency and ω=2πf. The electrical circuit of EC system determines how the impedance varies in function of frequency. And the electric circuits can be simplified into equivalent circuits composed of electrical elements like resistors R, capacitors C and inductors L. For each of the electrical elements, their impedance is:

Equation 3.9

$$Z_R = R$$

Equation 3.10

$$Z_C = \frac{1}{j\omega C}$$

Equation 3.11

$$Z_L = j\omega L$$

The idea to simulate the EC system by equivalent circuit helps one readily understand the EC system's behavior and extract quantitative information of the system. For example, the ohmic resistance in the electrolyte is often simulated by a simple resistor

Rs, which is called solution resistance. The EDL behaves like a capacitor and is often simulated by an idealized capacitor C_{dl}. The charge transfer of electrochemical reactions can be simulated by a resistor R_{ct}. The equivalent circuit of a simple EC system with charge transfer reaction is shown in Figure 3.6. All those values could be quantitatively extracted through proper fittings of the experimental EIS results with the right choices of equivalent circuits.
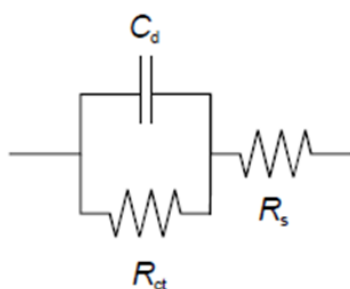
Figure 3.6 A simple equivalent circuit for an electrochemical system

The measurements of EIS are usually conducted with a frequency response analyzer (FRA). An FRA can generate a small amplitude sinusoidal perturbation in addition to the given DC steady-state potential (or current) and sweep its responses in a given frequency range. The probing and response signals are transformed with a fast Fourier transform to calculate impedance for each tested frequency.

The real and imaginary parts of impedances are usually plotted to present the EIS data (Figure 3.7). This form of plotting is called Nyquist plot (or complex plot). From the Nyquist plot, one can readily identify some features such as the solution resistance R_s, the coupling of charge transfer resistance R_{ct} and the electrical double layer capacitance C_{dl}, or the transmission lines:
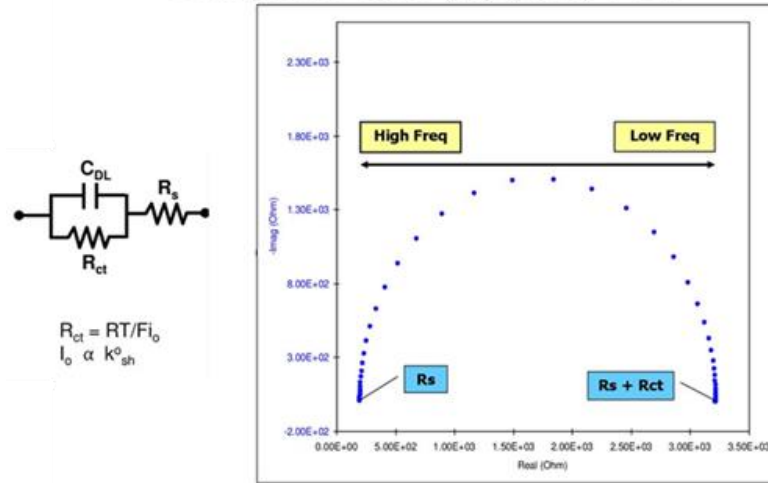
Figure 3.7 Nyquist plot example for simple equivalent circuit

- The solution resistance R_s between the working electrode and reference electrode in a three-electrode system usually behaves like a pure resistor, and its value can be determined by the intersection of the curve on the x-axis in the Nyquist plot. Strictly speaking, the resistance of wiring should also be included in this value. However, in most of case, it is negligible compared to the solution resistance.

- The coupling of R_{ct} and C_{dl} in parallel connection (Figure 3.7) produces a semicircle in the Nyquist plot. This semicircle is the key feature to determine an electrochemical system, as it contains both the kinetic descriptor and the EASA. However, in practice perfect semicircles are rarely observed and they usually appear with some degree of distortion. This phenomenon will be explained in the next section.

Those above-described impedance elements with their corresponding features never appear individually for the complex electrochemical system under test. They should be used as building blocks to construct the overall equivalent circuit for EIS fittings or simulations.

3.5.1 EIS fittings for experimental results

The purpose of EIS fitting is to determine the electrochemical parameters such as Rs, R_{ct} and C_{dl} from the experimentally measured impedance data. To establish the relationship between the impedance value and electrochemical system, the first fitting step is usually to construct the proper equivalent circuit to present the EC system regarding the features of EIS results. In modern EIS softwares such as Zview, there

are build-in equivalent circuits that are used to represent different EC systems. The choice of the proper equivalent circuit is the key for EIS fitting.

After the candidate equivalent circuits are chosen, then the mathematic formula of the equivalent circuits could be deduced. This process could be done automatically by the internal procedures of EIS software like Zview or by coding in the programing languages. Then, the fitting of experimental data could be executed through the complex nonlinear least-squares (CNLS) method. The validation of the equivalent circuit is a delicate process. Since different equivalent circuits can yield the same impedance results, they should be evaluated by statistical tests and observations from other measurements.

Despite the simplification by equivalent circuits, experimental EIS data can still be affected by several other factors, which make them deviate from the idealized equivalent circuit, such as the one shown in Figure 3.6. One of those factors is the inhomogeneity of the electrode surface. The inhomogeneity of the electrode/electrolyte interface will cause the EDL not to behave like an ideal capacitor [127]. This problem could be addressed by using a constant phase element (CPE) to replace the ideal capacitor in the equivalent circuit. The mathematical expression of CPE impedance is:

Equation 3.12

$$Z_{CPE} = \left[\frac{\cos(\phi\pi/2)}{T\omega^\phi}\right] - j\left[\frac{\sin(\phi\pi/2)}{T\omega^\phi}\right]$$

The CPE has two determining parameters, T in the unite of F $s^{\phi-1}$ cm^{-2} is related to the capacitance value, and φ is the exponent parameter with a value between 0 and 1. The CPE behavior is usually observed as a depressed semicircle in the Nyquist plot other than a perfect semicircle that a resistor and an ideal capacitor would produce. According to Brug's formula [128]:

Equation 3.13

$$C_{dl} = \left[T\left(\frac{1}{R_s} + \frac{1}{R_{ct}}\right)^{\phi-1}\right]^{\frac{1}{\phi}}$$

The effective double-layer capacitance can be determined using these two parameters. From Brug's formula, it can be seen that the CPE will approximate an ideal capacitor when φ approaches 1.

3.5.2 EIS simulations for porous electrode structures

Despite that the parameters such as R_s, R_{ct}, and C_{dl} could be easily extracted from fittings, those parameters are characteristic of the whole system are less able to explicitly describe the characteristic features of porous electrodes. In the case of very porous electrodes, the high-frequency impedance often shows linear features (Figure 3.8) rather than the slightly depressed semicircles.
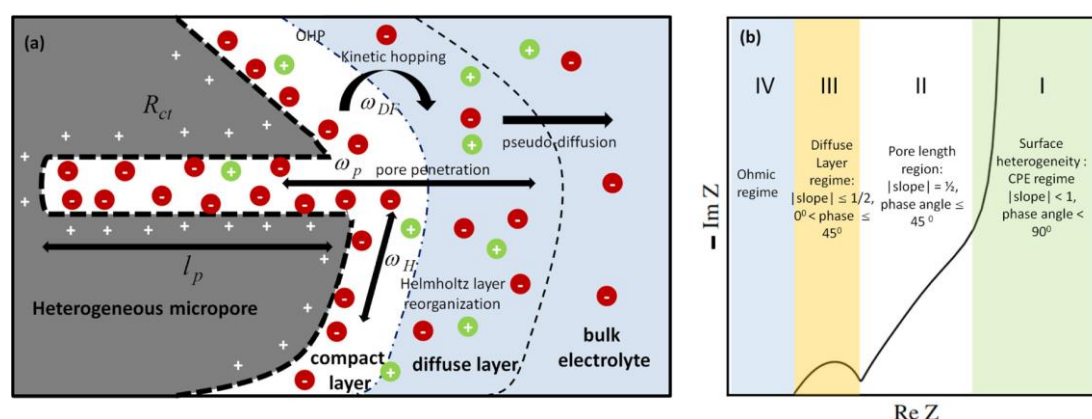
Figure 3.8 Heterogeneous pore with linear impedance behavior [129]

It was observed in this thesis that the linear parts of the Nyquist curve in the high-frequency region may contain important information especially for the porous electrodes because the structure effects on EIS often appear in high frequency and have linear features [126], [130]. The linear behavior of impedance in the Nyquist plot generally arises in two cases. Firstly, when the diffusion of redox species is involved in the EIS test, the Warburg impedance will be added into the faradic impedance in addition to the charge transfer resistance. It produces a linear relationship between the real and imaginary parts of impedance with a constant slope of 1 (tan 45°). However, since the EIS studies in this thesis are all performed in the Tafel region, and the mass transport effect is considered negligible with respect to the slow OER charge transfer kinetic, this Warburg element is not considered in our works. Secondly, the ladder-shaped transmission lines can yield similar behavior to the Warburg element. This transmission line behavior is often observed for the porous electrode. Its origin can be mathematically explained by the ohmic drop along the pore walls.

The transmission line model was established by De Levie [131] to model the ohmic drop in a cylindrical pore. Since then, it was often adopted to describe the linear high-frequency feature of impedance produced on a porous electrode. The mathematical expression of the transmission line model according to the De Levie equation is:

Equation 3.14

$$Z = \frac{R_\Omega}{\Lambda^{1/2}} coth(\Lambda^{1/2})$$

With $\Lambda = \frac{2\rho_s l^2 j\omega c_{dl}}{r}$ and $R_{\Omega,p} = \frac{\rho_s l}{\pi r^2}$, where the ρ_s, l, r, and c_{dl} represent the solution resistance of electrolyte (in Ω per unit length), the pore length, the cross-section radius of the pore, and the intrinsic double-layer capacitance per unit area respectively. It contains the geometrical dimensions of the pore. The linear behavior of impedance is understood according to the TLM that when the frequency is sufficiently high, the term coth($\Lambda^{1/2}$) in Equation 3.14 approximates to 1, then the equation simplifies to:

Equation 3.15

$$Z = \frac{R_\Omega}{\Lambda^{1/2}} = \frac{\frac{\rho_s l}{\pi r^2}}{\sqrt{\frac{2\rho_s l^2 j\omega c_{dl}}{r}}} = \frac{\frac{\rho_s}{\pi r^2}}{\sqrt{\frac{2\rho_s \omega c_{dl}}{r}}}(1-j)$$

in which the slope between the real part and the imaginary part of Z equals 1. The value of impedance in this approximation is independent of the length of the pore. This means that the pore has a semi-infinite length since the AC signal can't penetrate to the bottom of the pore in this high-frequency region. The length or the frequency range of the linear zone depends on the length of the pore. If the pores of an electrode can be simplified into cylindrical pores, then with proper estimations of the pore length, pore diameter, number of pores, and equivalent circuit basing on the porous electrode model, one can simulate the complex EC system on a porous electrode and make predictions on it.

The above model for simulation is only based on cylindrical pore geometry and is not accurate to simulate nanostructured materials, which have more complex geometries. For 3D electrodes, the hierarchical or fractal structure of the pores would further alter the high-frequency features, not only in length but also in the slope. According to the works of Lasia [126] and Itagaki *et al.* [130], the high-frequency responses on macropore structure show 45°-line (slope=1), and those on secondary pore structure show 22.5°-line (slope=0.41). In the second and third projects of the thesis, the expected 22.5°-line behavior was surprisingly not seen on the fractal Ni DHBT foam but instead seen on the Ir modified Ni DHBT foam with the same fractal structure. Through simulations with both the TLM for the macropores of our Ni foam and the secondary pore model for the micropores of Ni foam, we found that most of the secondary pores in pristine Ni DHBT are not electrochemically active, but in contrast, they became active after Ir modification. This observation is attributed to the bubble

coverage and wetting condition problems in the DHBT structure during the OER and motivated us to use *In-operando* acoustic emission measurements to validate the hypothesis.

3.6 *In-operando* acoustic emission detection of oxygen bubbles

As reviewed in the second chapter, the bubble coverage and inclusion in 3D electrodes will cause negative effects on OER performance. Conventional optical monitoring of the bubbles' coverage or entrapment in 3D structure is, in practice, challenging to realize because it demands sophisticated arrangement for the illumination conditions, especially when the bubbles are inside of a porous media. In contrast, passive acoustic emission (AE) detecting would be a simple and powerful method to realize *in-operando* monitoring of bubbles' behavior.

Passive acoustic emission (EA) detection is a non-destructive characterization technique that uses acoustic sensors to detect acoustic waves emitted by the abrupt release of energy. The source of AE waves can be cracks in solid, defect growth, frictions, leaks, gas evolutions, *etc.* [132]. In the case of bubble evolution, bubble formation, bubble detachment, bubble coalescence, and front displacement of a bubble in porous media could produce AE waves and propagate in liquid and solid phases. Those waves are dissipative and can be detected by a piezo-electric sensor closely attached to the container or by a hydrophone immersed in the liquid. It should be noted that the acoustic impedance of air (0.0004×10^6 kg/(m^{2}s)) is a lot smaller than liquid (1.48×10^6 kg/(m^{2}s)) or solid and allowing for minimal transmission of acoustic energy so that AE wave propagation would be prohibited by air and the contact of AE sensor should be mounted with couplant.

With a piezo-electric sensor, the pressure fluctuation is transformed into voltage signals. Usually, the weak AE signal is enhanced by an amplifier, and then the amplitude signal expressed in the AE decibel scale is:

Equation 3.16

$$dB = 20 \log \frac{V}{1\mu V} - (amplifier\ gain\ in\ dB)$$

An AE detecting system permits recognize the signal burst with a preset amplitude threshold and record the AE wave. A detected AE wave or a discrete AE event has the shape like in Figure 3.9 (left). It has many definable parameters such as the peak amplitude, duration, counts, *etc.* After Fourier transforms, there is another important parameter: the peak frequency.
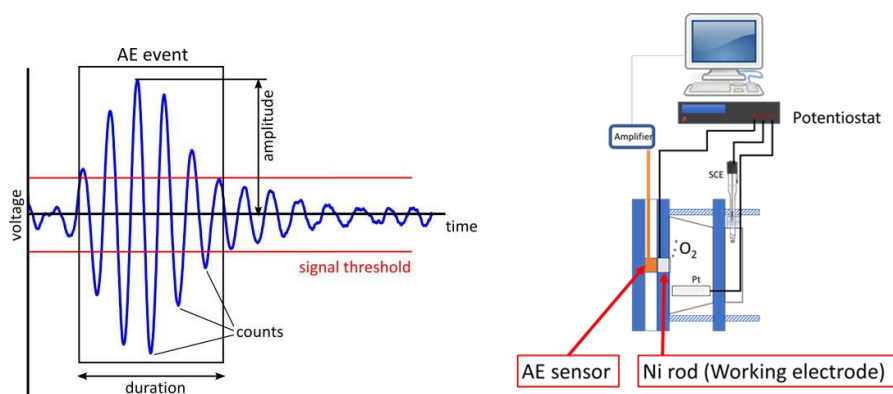
Figure 3.9 Left: A typical AE wave form; Right: In-operando AE detection integrated with EC system

Indeed, the natural frequency of a bubble's oscillation depends on the equivalent diameter of the bubble. According to the Minnaert equation [133]:

Equation 3.17

$$f_0 = \frac{1}{\pi D}\sqrt{\frac{3\gamma P^0}{\rho}}$$

where f_0 represents the natural frequency of a bubble, and D represents the bubble's diameter, γ, ρ, P^0 denote the polytropic coefficient, the liquid density, the ambient pressure respectively.

Therefore, with the AE sensor being closely attached to the working electrode outside of an electrochemical cell (Figure 3.9 right), the acoustic signal of each bubble generated by oscillation could be recorded, and the recorded AE waves of bubbles could be used for bubble counting and their sizes' determination [134].

3.7   Summary

This chapter has given detailed information about the principles and the functioning of the characterization techniques used. The principle of electrodepositions assisted by a template to construct 3D Ni electrodes has been explained, as well as the surface modification procedures to decorate the Ni skeleton with Ir. Then, the different electron microscopy technologies such as SEM and TEM are used to provide information on the morphology of Ni structures and compositions. Detailed information concerning the surface composition as well as the energy levels of electronic orbitals can be obtained with the XPS. The electrochemical measurements will provide information on the OER performance and information on the catalytic entities. The EIS measurements and simulations are proven to be a powerful tool to assess the accessibility of porous electrode surface to the electrolyte. Throughout all the three works in this thesis, it provides reliable measurements of the electrode capacitance and structure information

of the porous electrode (see in chapter 6). Finally, the newly developed *in-operando* acoustic emission detection used to monitor bubble behaviors during the OER was explained. Combining all these measurements makes it possible to better define the synthesized materials' physical and electrochemical properties.

In the following the main results obtained during this thesis are presented in the form of three separate articles:

- Article 1 in chapter 4-Vertically Aligned Ni Nanowires as a Platform for Kinetically Limited Water-Splitting Electrocatalysis, published in The Journal of Physical Chemistry C;
- Article 2 in chapter 5- Hydrogen Bubble Templating of Fractal Ni Catalysts for Water Oxidation in Alkaline Media, published in ACS Applied Energy Materials;
- Article 3 in chapter 6- The role of Ir decoration in activating multi-scale fractal surface in porous Ni DBHT for the OER, in submission.

Each article would be a showcase of how the above-mentioned methods being applied to optimize the OER performance of Ni based electrocatalysts.

4 VERTICALLY ALIGNED NI NANOWIRES AS A PLATFORM FOR KINETICALLY LIMITED WATER-SPLITTING ELECTROCATALYSIS

4.1 Abstract

Electrochemical templating through porous membranes is applied to form arrays of micrometer long Ni nanowires (NWs). Detailed structural and electrochemical characterization, including electrochemical impedance spectroscopy (EIS), was conducted to assess the electrocatalytic properties of these Ni NW arrays for the O_2 evolution reaction (OER) in 1 M KOH. Detailed structural analysis showed that Ni NWs have a diameter of *ca.* 350 nm and a mean 80 nm average distance between the NW center. For the longest NWs (20 µm long), the ratio between the pore opening and pore length is 0.4%. From detailed HR-TEM and EELS analysis providing information on the chemical state of atoms from quantitative analysis of the signals, Ni NWs are composed of a Ni metallic core surrounded by a $Ni(OH)_2$ layer that thickens from 10 to 20 nm after extensive electrochemical tests. Three different methods, namely, SEM geometry measurements, the α-$Ni(OH)_2$ charge method, and the capacitance method, were used to assess how the current varies with the NW length. The three different methods are all in agreement, and the current increases with length (or mass) precisely and only because of the surface area effect. The most surprising result is that the OER process occurs with exactly the same intrinsic catalytic activity at the bottom of these deep pores, and gas is evolved without any significant effects of electrolyte resistance, mass transport of dissolved oxygen, or bubble occlusion of the pores. Accordingly, vertically aligned 1D NWs can be used as an effective platform that mitigates the negative effects of gas evolution. Increasing the intrinsic activity by incorporating more active materials will further improve this type of electrode.

4.2 Introduction

The promise of hydrogen as a sustainable, secure, and clean alternative energy carrier to satisfy the growing global energy demand requires efficient, low-cost, and environmentally friendly production. Water electrolysis to generate hydrogen fuel, preferably driven by renewable energy, is a highly attractive means to produce hydrogen, but advanced electrolyzer systems are required for electrolytic H_2 production to become a commercially viable technology. Lately, new classes of anion exchange membranes (AEMs) have emerged with improved performance over their predecessors [135]–[139] improving the future prospect of commercialized anionic

polymer electrolyte membrane water electrolysers (APEMWEs). The prospect of new AEMs for alkaline APEMWEs that could match the performances of cationic exchange membranes in terms of ionic conductivity and longevity has spurred a renewed interest in research to improve catalyst performance for the oxygen evolution reaction (OER) in alkaline electrolyte. Recent papers in the literature have emphasized the critical importance of electrode composition in achieving high OER performance. Indeed, it turns out that pure Ni (with a $Ni(OH)_2$ film) is a rather poor catalyst for the OER. This has been known for a long time since the seminal work of Corrigan [140], but it was re-emphasized only recently [141]. Indeed, in rigorously Fe-free KOH electrolyte, Ni electrodes exhibit large overpotentials for the OER that is considerably reduced by a trace amount of Fe. The amount of Fe needed to "dope" Ni depends on the electrochemically active surface area of the electrode [140] and this has prompted a plethora of work aiming at finding the composition of Ni-based electrodes that would give optimal OER performances in terms of overpotential, current density, and stability. This work has recently been reviewed [142]–[144].

Another thrust of research is focusing on imparting the electrode surface with nanoengineering characteristics to improve OER performance by decreasing the bubbles' size, residence time, and detachment force through electrode surface nanoengineering. The adhesion force between a bubble and a solid originates from the triple phase (solid–liquid–gas) contact line. On a flat surface, this triple-phase contact line is continuous, while it becomes discontinuous and thus less important on a nanostructured surface. This translates into smaller bubble size and lower bubble adhesion force, thereby leading to improved electrochemical performances. These surfaces are known as "super-aerophobic", and several materials and electrodes have been investigated showing improved performance for electrolytic gas evolution reactions like the OER and the hydrogen evolution reaction (HER) upon nanostructuring of the electrode surface, namely, Ni [145], MoS_2 [108], NiMo- and NiFe-layered double hydroxide [146], Ni/Co oxide [147], NiCoP [148], CoS [149], and Pt [150].

Nanostructuring of the electrode surface through the creation of pores and cavities that extend to the bulk of the electrode (3D nanostructured electrode) increases the number of active sites accessible to the electrolyte, thereby increasing the current density at fixed overpotential. However, apart from good electronic conductivity, the electrode 3D structure must also not impose any mass-transport limitation of dissolved oxygen or ionic migration within the pores. Ideally, the OER of the optimal 3D nanostructured

electrode must be kinetically controlled in the same overpotential range as that observed on Ni thin films.

In this study, we synthesized arrays of micrometer long Ni nanowires with high surface area to ensure that OER current densities could be reached at low overpotentials. To do so, we used a template-assisted Ni electrodeposition procedure to prepare electrodes made of 1D Ni nanowires densely packed in a brush-like array structure. Careful structural characterization of pristine electrode indicates that Ni nanowires are covered with a thin $Ni(OH)_2$ layer (*ca.* 10 nm) that thickens by a factor of 2 (*ca.* 20 nm) after extensive use for the OER. Cyclic voltammetry, chronopotentiometry, and electrochemical impedance spectroscopy (EIS) measurements under O_2-evolving conditions indicate that both the electrochemically active surface area (measured by cyclic voltammetry in quiescent conditions) and the effective capacitance (measured in a potential region where the OER is occurring) scale with the nanowire length and calculated surface area, indicating full accessibility. This translates into the OER being kinetically limited, instead of diffusion-limited, even if the pore aspect ratio, which is defined as the ratio between the pore opening and pore length, is 0.4%. The overpotential at 10 mA cm^{-2} for the longest Ni NWs (20 μm) is ≈200 mV lower than on a bare Ni plate.

4.3   Experimental Section

4.3.1   Synthesis of Porous Ni Electrodeposits

Galvanostatic Ni electrodeposition (10 mA cm^{-2}) was performed from aqueous solutions of 0.1 M $NiCl_2 \cdot 6H_2O$ (Alfa Aesar, 99.95% Metals Basis) and 2 M NH_4Cl (Sigma-Aldrich, 99.99% Trace Metals Basis) through a porous aluminum anodic oxide (AAO) membrane (Anodisc25, Whatman International Ltd.). A titanium layer (400 nm) was DC sputtered at the AAO backside to ensure electrical contact mandatory for Ni electroplating. A saturated calomel electrode (SCE) and Pt gauze (Alfa Aesar, 99.9%) were used as reference and counter electrodes, respectively. Ni electrodeposition was carried out using a Solartron 1480 for durations up to 3 h. Following Ni electroplating, the AAO membrane was dissolved in 1 M KOH for 1 h at room temperature, thoroughly rinsed with deionized water (Millipore Milli-Q, resistivity 18.2 MΩ cm), and immediately characterized electrochemically. All the potentials measured in 1 M KOH are reported *vs.* RHE using $E_{RHE} = E_{SCE} + 1.04$ V. The geometric surface of the Ni working electrodes was 0.15 cm^2 in all cases.

4.3.2 Physical Characterization of Porous Ni Electrodeposits

TEM observations were carried out with an FEI Titan 80–300 cubed scanning transmission electron microscope equipped with a high-brightness field-emission electron source and ultrafast electron energy loss (EEL) spectrometer. In cases where a cross-sectional analysis of the NW structure needed to be carried out, an ultrathin area was carefully lift out using the focused ion beam (FIB) technique (see Figure 4.1). High-resolution SEM analyses were carried out using the FEI-Magellan SEM microscope. Detailed elemental mapping necessary to resolve the spatial distribution of Ni and O was carried out using electron energy loss spectroscopy (EELS)–spectrum imaging (SI) technique in the TEM. The process involved a serial acquisition of the EEL spectra at every pixel on the annular dark field (ADF) image and subsequent processing to extract the $Ni\text{-}L_{2,3}$, O-K, and $Ti\text{-}L_{2,3}$ edges. Mapping the spatial distribution of these individual edges revealed the relative distribution of Ni, O, and Ti elements, respectively. To further determine the chemical state of Ni in certain NW samples the comparison of their $Ni\text{-}L_3/L_2$ white-line intensity ratios was carried out, involving the subtraction of the continuum background under the power-law background stripped EELS spectrum by fitting a double ArcTan function. This procedure is considered accurate at estimating L_3/L_2 ratios of white lines [151].
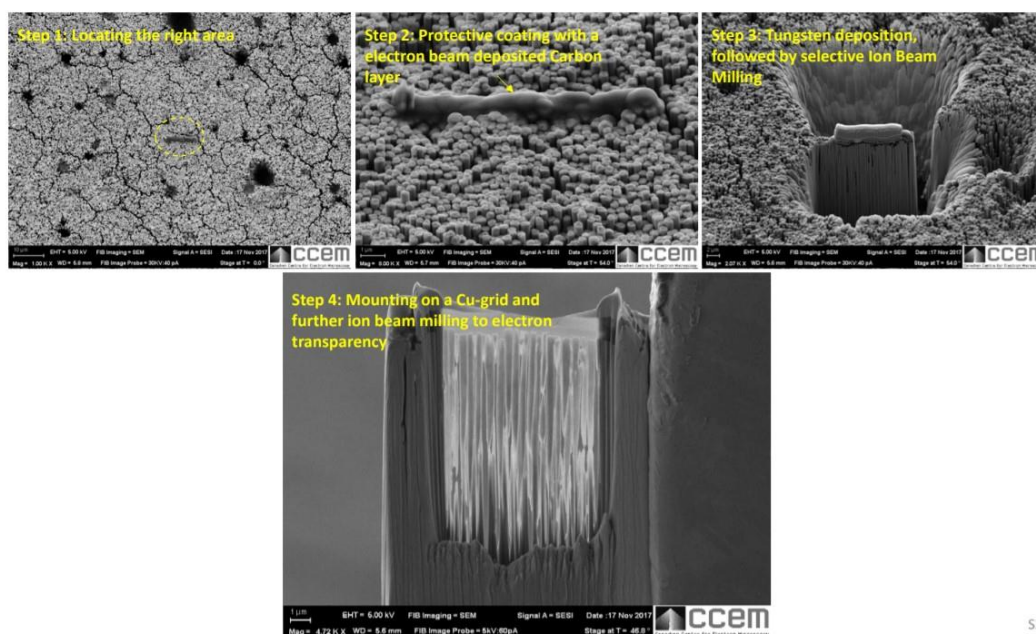
Figure 4.1 SEM images illustrating the stage-by stage lifting out of the TEM specimen using focused ion beam milling

4.3.3 Electrochemical Characterization and OER Performances

Electrochemical characterization in Ar-saturated (N50, Air Liquide) 1 M KOH (Sigma-Aldrich, 99.99% Trace Metals Basis) was conducted in a custom-built electrochemical cell [152], using a Pt gauze and a saturated calomel electrode as auxiliary and reference electrode, respectively. Cyclic voltammograms (−0.10 to 0.45 V *vs.* RHE, 25 mV s^{-1}) were first recorded until steady-state CV features were obtained. Then the electrodes were subjected to 10 min open-circuit potential (OCP) before chronopotentiometry curves were recorded (10 mA cm^{-2} for 30 min). The above sequence was systematically applied to all of the reported Ni NW electrodes. The results were compared with a commercial Ni plate (Sigma-Aldrich, thickness 0.125 mm, ≥99.9% metals basis) and with electrodeposited Ni films obtained without any AAO membrane on Ti foil (Alfa Aesar, 99% metals basis). The solution resistance was measured by electrochemical impedance spectroscopy (EIS) and used to correct potentials for ohmic drops. EIS measurements in the OER potential range were obtained following 10 min polarization (from 1.5 to 1.6 V) between 0.1 Hz and 200 kHz using an FRA Analyzer (Solartron 1255B). Electrochemical impedance spectra were fitted to equivalent circuit models using the complex nonlinear least-squares (CNLS) fitting program ZVIEW (Scribner Associates).

4.4 Results

4.4.1 Growth of Ni Nanowires and Morphology

Figure 4.2 illustrates the top-view and cross-sectional views of the typical pristine Ni nanowires (Ni NWs) synthesized. The low-magnification SEM image (Figure 4.2a) reveals a relatively dense packing of the NW bundles resembling that of a brush-like array structure. Detailed high-resolution SEM image (as shown in Figure 4.2b) indicates that some NWs have an oblong cross-section (small diameter = 310 nm and large diameter = 410 nm), but most of them have a circular cross-section. Figure 4.2c illustrates the NW structure in cross-section. A size measurement along the length of the NW indicates that the pristine NWs synthesized were typically about 12 μm long.
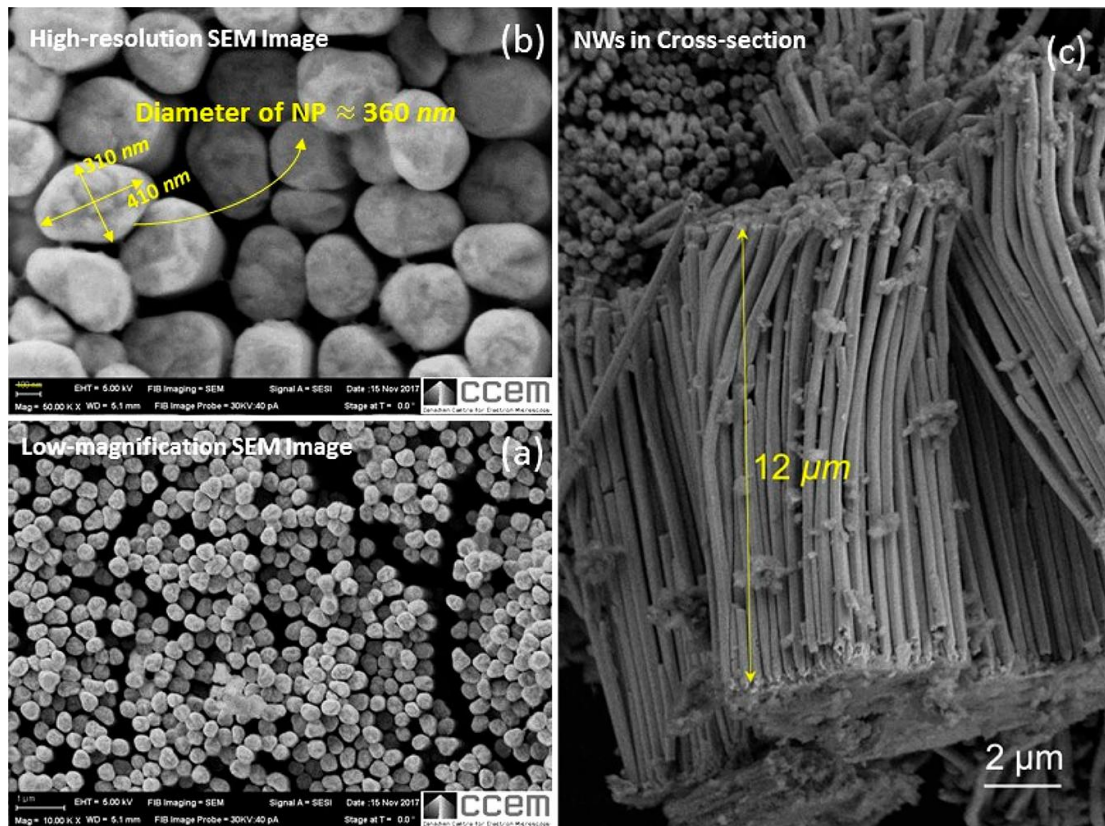
Figure 4.2 High-resolution SEM images of the Ni NWs synthesized revealing their cross-sectional and top views. (a) Low-magnification SEM image. (b) High-resolution SEM image. (c) Cross-sectional view of the NW structure.

The above Ni NWs were prepared by deposition using a porous AAO template membrane. Figure 4.3a displays an SEM micrograph of the as-received AAO membrane, which shows the expected close to hexagonal assembly of pore arrangement. The size of the openings was assessed by measuring the diameter of a collection of more than 100 pores (see Figure 4.3a, inset). The mean pore size is 184 ± 30 nm. Then, Ni was deposited using the setup described in the Experimental Section, and Figure 4.3b shows the SEM micrograph of the resulting Ni-filled membrane (before the AAO membrane was dissolved). The deposition time was adjusted to limit the deposition charge and to prevent Ni deposition on top of the AAO membrane. The hexagonal pore arrangement is preserved. The mean pore size is 197 ± 21 nm (see Figure 4.3b, inset). Under our deposition conditions, slow dissolution of the AAO template in acidic medium, which could have resulted in an increase of the pore size and/or modification of the hexagonal arrangement of pores, is negligible.

Then, the AAO membrane was dissolved in 1 M KOH, and Figure 4.3c depicts the Ni structures that have grown inside the AAO pores. As seen in Figure 4.3c, the Ni NWs are arranged as nanostructured filaments that mimic the pore structure of the as-

received AAO membrane. Finally, the pristine Ni NWs synthesized were subjected to an extensive electrochemical characterization in alkaline media. As seen in the corresponding SEM image shown in Figure 4.3d, the hexagonal structure of Ni NWs is again preserved and is not affected even if there is extensive polarization in the potential region where O_2 evolution has occurred. The mean diameter of Ni NWs in this case is estimated to be about 354 ± 38 nm (Figure 4.3d, inset), which is fairly close to that of the pristine samples (*i.e.*, NWs in Figure 4.2, 305 ± 38 nm).
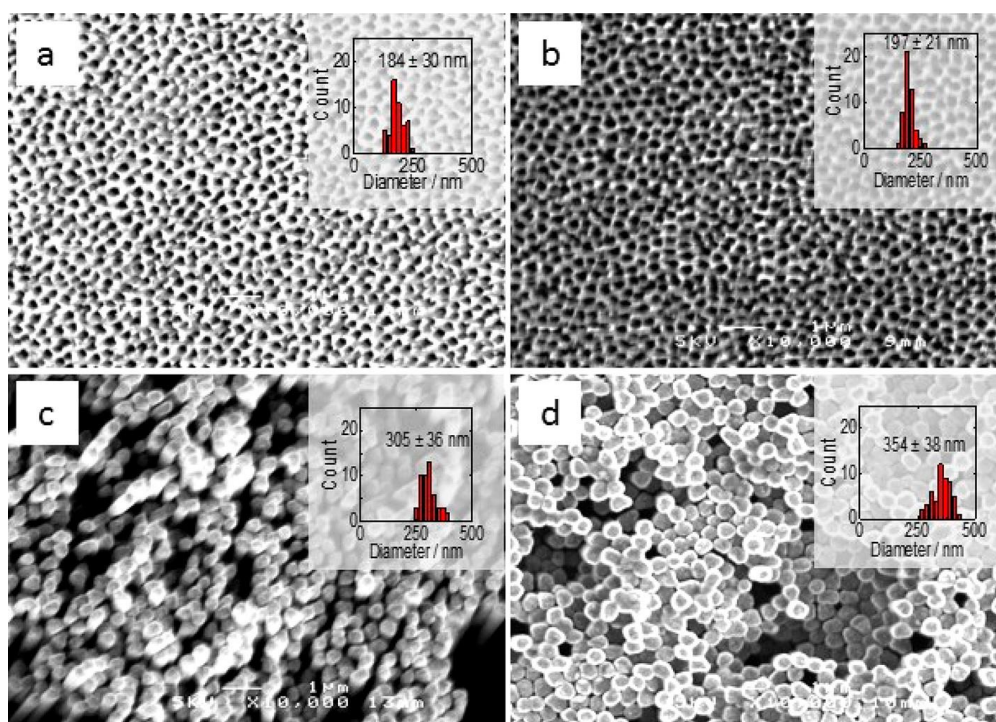
Figure 4.3 SEM top-view micrographs of (a) as-received AAO membrane; (b) Ni deposited in AAO membrane before the latter was removed; (c) Ni NW arrays just after the AAO membrane was dissolved; and (d) Ni NWs after extensive electrochemical characterization.

Figure 4.4 compares the high-resolution SEM images of these last two samples. As seen, the morphological features remained remarkably stable and did not significantly evolve following extensive electrochemical characterization. An estimation of packing fraction in Ni-NW array electrodes with segmentation analyses of the SEM images was performed (Figure 4.5). Both square and hexagonal packing of NWs was identified in pristine and electrochemically treated Ni NWs. The estimated packing fractions of pristine (82%) and electrochemically treated (84%) Ni NWs are almost identical and fall in between the values expected for ideally arranged square (79%) and hexagonal (91%) packing arrangement. The average spacing between two nanowires is *ca.* 80 nm in both cases. For the longest Ni NWs investigated in the present study (*ca.* 20 µm), the ratio between the average NW–NW spacing and NW length, which defined

the aspect ratio of the openings in the Ni NW array electrode, varies from 2.7% for the smallest to 0.4% for the longest NWs.

Cross-section and top-view SEM micrographs of Ni NW arrays prepared at different deposition times are shown in Figure 4.5. In each case, the samples are made of densely packed NWs arranged in a brush-like array. Ni NWs have a uniform diameter from bottom to top, which is expected since the diameter of the AAO pores does not vary between Figure 4.3a and Figure 4.3b. As far as we can tell from these micrographs, there are very few missing NWs. The NW length increases steadily as the deposition time is increased from 10 to 180 min. Indeed, Figure 4.5E shows that the NW length increases linearly with deposition time. Current efficiency values were computed for each sample. This was done by taking the ratio between the charge involved in Ni deposition and the total charge. The former was calculated by assuming that the mass of Ni contained in an assembly of Ni NWs can be obtained from the known pore diameter, length, and NW surface density, using Ni bulk density and a $2e^-$ process. The deposition current efficiency is *ca.* 13% and independent of NW length (electrodeposition time).
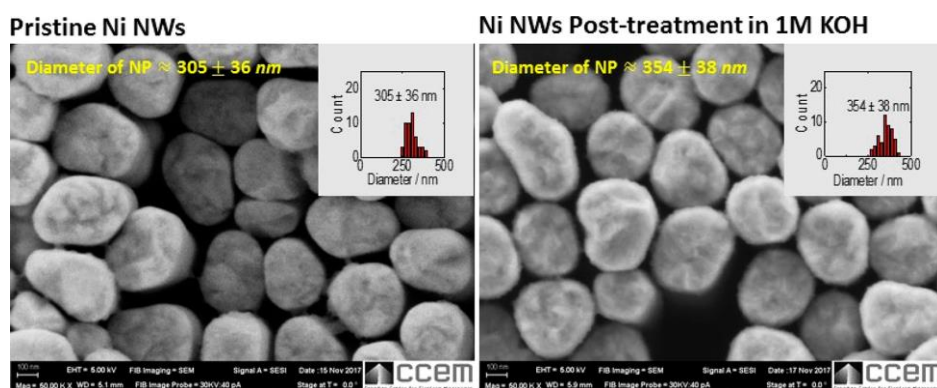
Figure 4.4 High-resolution SEM images comparing the morphology of pristine Ni NWs and those post electrochemical treatment under alkaline media.
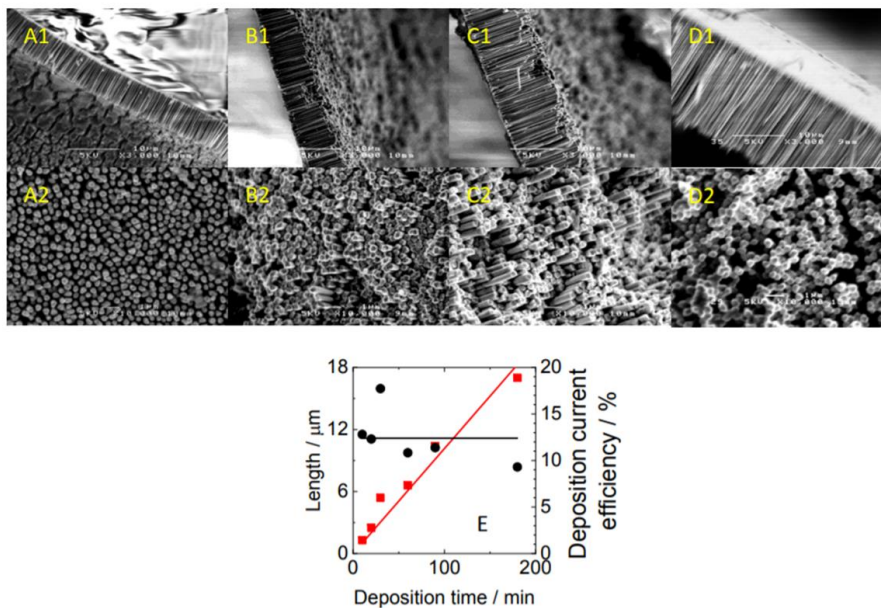
Figure 4.5 SEM micrographs for Ni NW (A, B, C, D) with different NW lengths after electrochemical characterization in 1M KOH. A1, B1, C1, D1 - side views of NWs; A2, B2, C2, D2 - top views of NWs. The mean lengths of A, B, C, D samples are 5.4 µm, 6.6 µm, 10.4 µm, 17 µm respectively. E, Variation of NW length and deposition current efficiency as a function of deposition time.

Figure 4.6a illustrates the cross-sectional view of the pristine Ni NWs discussed earlier in Figure 4.2. As evidenced by the EELS elemental mapping of the Ni-$L_{2,3}$, O-K, and Ti-$L_{2,3}$ edges in Figure 4.6b, the NWs seem to nucleate at the contact of the TiO$_x$ substrate and grow upward along the initial AAO template. An exception to this rule is regions such as that highlighted in yellow in Figure 4.6b where the metallic-Ni (depleted of both O and Ti) can be seen extending all along the TiO$_x$ substrate down to the bottom. This suggests that the nucleation of Ni and the further growth of the NW can possibly also take place in the absence of a TiO$_x$ phase. Unravelling this hypothesis would, however, require further modeling of the energetic considerations of the growth process that is beyond the scope of the present article.
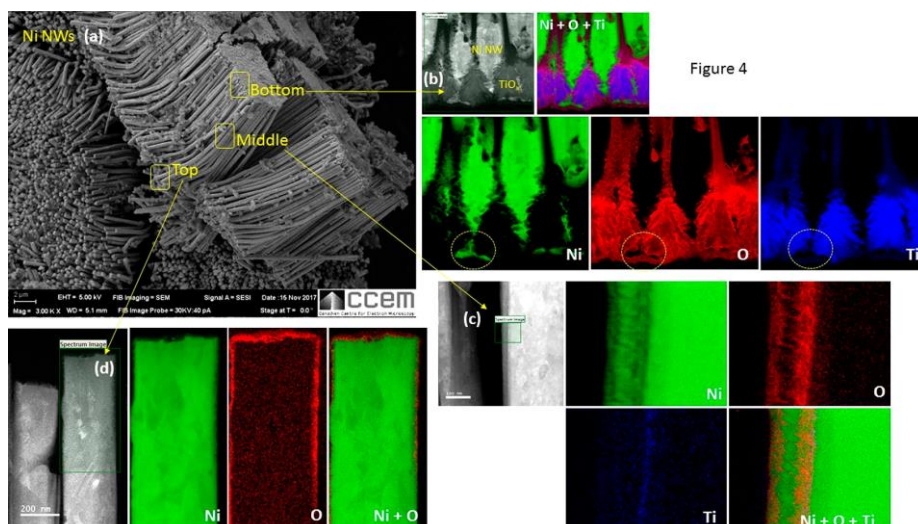
Figure 4.6 Compositional analyses of pristine Ni NWs with EELS. (a) Cross-sectional SEM view. (b), (c), and (d) Elemental mapping of Ni, O, and Ti over the bottom, middle, and top regions of a typical Ni NW.

Similar to the above analyses, we also carried out a detailed compositional analysis of the top and the middle regions of the NWs. As seen in Figure 4.6(c, d), both the top and the middle regions show significant enrichment in the O species at the surface (see Table 4.1). This suggests that the NW surfaces formed an oxide layer over the metallic core, and knowing the exact phase would be important from an electrochemical stability viewpoint (see further below for a detailed discussion on this). It is noteworthy to mention here that the oxide layer was still preserved even after exposing the NWs to extensive electrochemical characterization (29.4 at. % *vs.* 26.7 at. % in oxygen concentration was detected at the NW surfaces before and after, respectively). Also, to be noted here is that a close observation of the Ti maps in Figure 4.6b (NW bottom) and Figure 4.6c (NW middle region) reveals trace Ti-$L_{2,3}$ signals in the near-surface regions, suggesting some possible inclusions of the Ti structure mostly on the surface of the NW structure (see Ti signal map in Figure 4.6c). A thorough quantification of the Ti/O/Ni in these regions confirmed that such inclusions of Ti into the lattice are negligibly small (<1 at. %) particularly in the middle region of the NWs, but with an expected small level (<10 at. %) of inclusions in the regions closer to the TiO$_x$ substrate (see Table 4.1 for the quantified elemental concentrations).

Table 4.1 Quantification of Elemental Edges in EELS for the Pristine Ni NW Sample

EELS elemental quantification	Ti	O	Ni
middle region	<1.0 at. %	18.3 at. %	81.7 at. %
bottom region	8.1 at. %	29.4 at. %	62.5 at. %

In order to deduce the thermodynamic phase of the oxide layer formed (*i.e.*, NiO *vs.* Ni(OH)$_2$) in the two samples (NWs pre/post-treatment in 1 M KOH), we estimated their Ni-L$_3$/L$_2$ white-line intensity ratios over the core and surface regions. These were then compared against the corresponding white-line ratios of NiO and Ni(OH)$_2$ phases extracted from a detailed EELS analysis conducted separately.
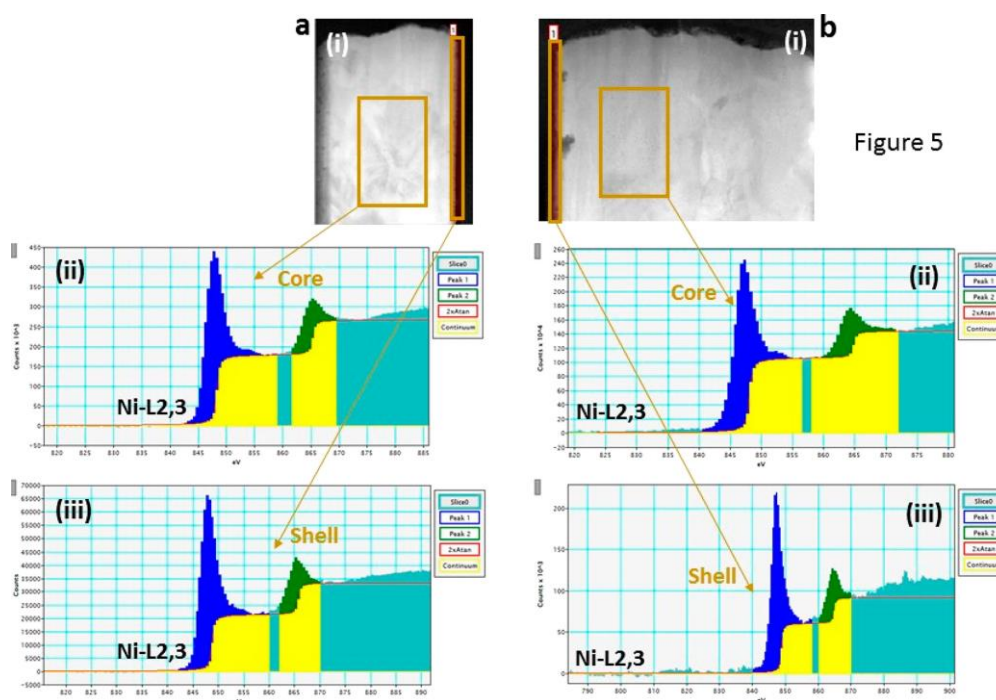
Figure 4.7 Detailed analyses of the Ni L$_3$/L$_2$ white-line intensity ratios to deduce the chemical state of Ni in the pristine (a) and electrochemically treated (b) Ni NWs. (ii) Spectrum extracted over the core region. (iii) Spectrum extracted over the shell region.

Figure 4.7(a(i), b(i)) illustrates the core/surface regions within the two NW samples. Figure 4.7(ii), (iii) shows the corresponding Ni edges from these regions. Note that the Ni edges shown have been stripped off of their original background using a power-law. The yellow continuum highlighted corresponds to the background not accounted for in the L$_3$/L$_2$ ratio estimation. The estimated L$_3$/L$_2$ white-line intensity ratios for the two NW samples along with the reference values for NiO, Ni(OH)$_2$, and metallic-Ni phases are tabulated in Table 4.2. As highlighted, the L$_3$/L$_2$ ratios in the core region for both NW samples are almost identical—comparable to the metallic Ni state. Similarly, the L$_3$/L$_2$ ratios in the shell region for both NW samples are similar—comparable to the Ni(OH)$_2$ state. Accordingly, there is no obvious change in the chemical state of Ni following the extensive electrochemical characterization apart from a factor of 2 thickening of the Ni(OH)$_2$ layer enclosing the metallic Ni core of each NW (see Figure 4.8). This is consistent with the fact that no obvious structural changes were detected from the

detailed comparison of their high-resolution SEM images apart from a slight increase of the mean diameter from 305 ± 36 nm to 354 ± 38 nm (see Figure 4.4).
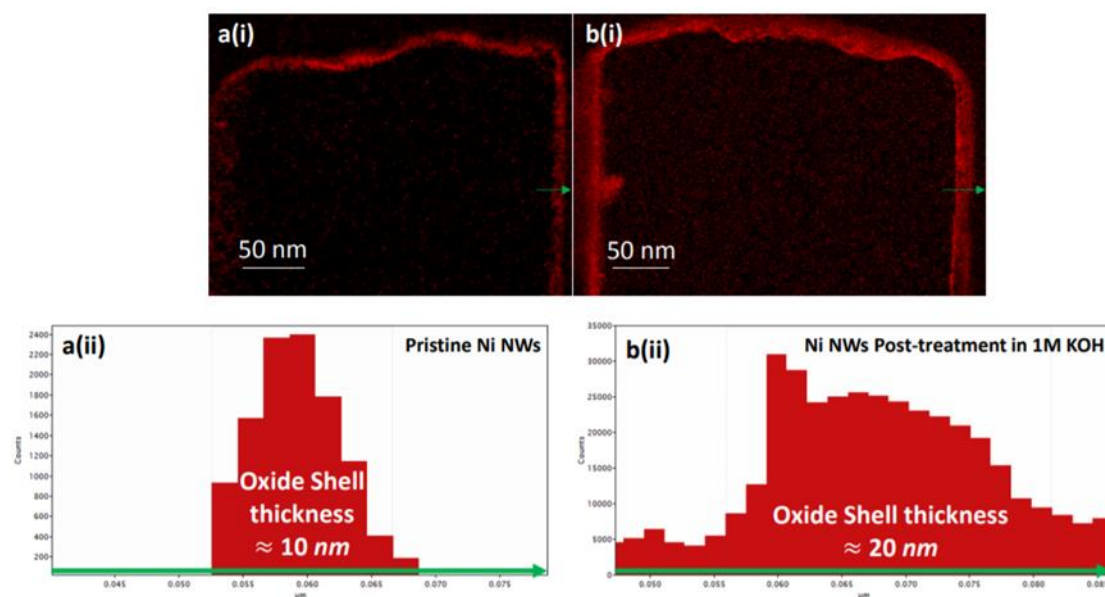
Figure 4.8 Spatially resolved Maps (i) and Line Profiles (ii) of the O-K edge in the case of (a) Pristine Ni NWs and (b) Ni NWs Post-treatment in 1M KOH.

Table 4.2 Comparison of L_3/L_2 White-Line Intensity Ratios of Pristine and Post-Treated Ni NWs with the NiO, Ni(OH)$_2$, and Ni References.

Estimated L_3/L_2 ratios	core region	shell region
pristine Ni NWs	3.38	3.63
Ni NWs post-treatment	3.41	3.56
Ni reference	3.3	
NiO reference	3.8; 4.0	
Ni(OH)$_2$ reference	3.6	

4.4.2 Electrochemical Characterization

Electrochemically active surface area (EASA), for the as-synthesized arrays of Ni NWs, was assessed by CVs in 1 M KOH at 25 mV s^{-1} (Figure 4.9A). The charge during the forward scan, Q_a, was used to evaluate the Ni EASA. Indeed, in this potential range (−0.10 and 0.45 V), Ni can be reversibly oxidized to α-Ni(OH)$_2$ during the forward potential scan and reduced back to metallic Ni in the backward scan [153]. Following 150 potential cycles, steady-state CV responses are obtained, with a representative

example displayed in Figure 4.9. Measured Q_a values were found to be proportional to the Ni NW length (Figure 4.10), which means that the reversible conversion Ni/α-Ni(OH)$_2$ is occurring over the entire Ni NW length and that the overall Ni NW surface is accessible to the electrolyte. The slope of the curve is 0.70 mC µm^{-1}, very close to the expected slope (0.55 mC µm^{-1}) based on pure geometrical considerations (ideal NW cylinders with similar diameter, length, and surface density) and an assumption that the α-Ni(OH)$_2$ charge on an ideal surface is 0.514 mC cm^{-2} [153]. The difference between the predicted and measured values may arise from uncertainty in the calibration value or the measured diameters, the fact that the NW diameter varies slightly from bottom to top, and surface roughness at the nanoscale level (Figure 4.6). It is worth mentioning that the Y-axis intercept of the straight line is different from zero. One reason for this could be that the bottom of each Ni NW at the interface with the Ti thin film does not have a perfectly cylindrical shape.
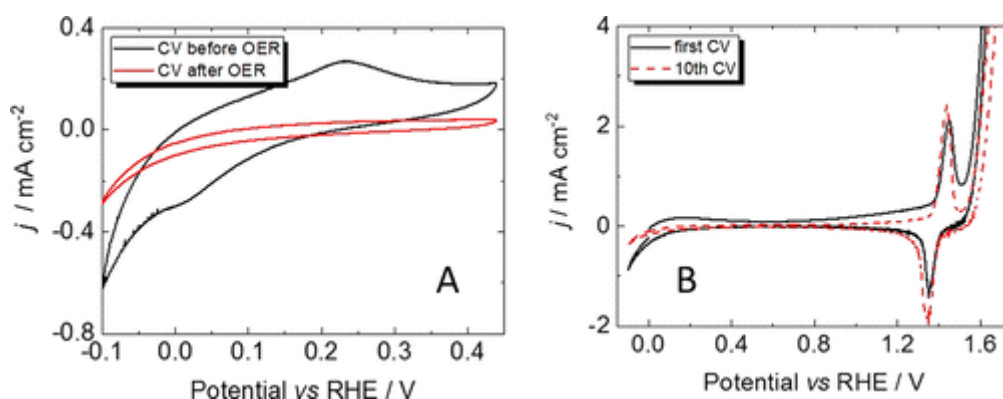
Figure 4.9 Stable CV (25 mV s^{-1}) for electrodeposited Ni thin film in 1 M KOH. In (A), the upper potential limit is restricted to 0.45 V to prevent the formation of β-Ni(OH)$_2$. In (B), the positive potential limit of CVs was extended.

Considerable changes occur in the CV of Ni NWs upon extension of the upper vertex potential limit to higher values. In the first CV following the restricted potential range used in Figure 4.9A, two anodic peaks at 0.23 and 1.44 V were observed in the forward sweep, and only one cathodic contribution was observed at 1.34 V in the backward sweep. The upper quasi-reversible transition involves the well-known β-Ni(OH)$_2$/β-NiOOH nickel oxide charge storage process. The 10th voltammetric profile no longer displays the anodic shoulder at 0.23 V (see Figure 4.9A and Figure 4.9B), and both the anodic peak at 1.44 V and cathodic peak at 1.34 V are better defined than during the first CV. These observations demonstrate that most of the α-Ni(OH)$_2$ species are no longer present but have been converted to β-Ni(OH)$_2$ phases, which also results in a lower rate for the hydrogen evolution reaction. This ensures the measured Qa Coulombic charge was exclusively associated with the formation of α-Ni(OH)$_2$ species.

Previous attempts to instead determine Ni EASA using the higher-potential Ni(II)/Ni(III) redox transition have been proposed, but uncertainty in the porosity and structure of these multilayer phases makes the present procedure more reliable.
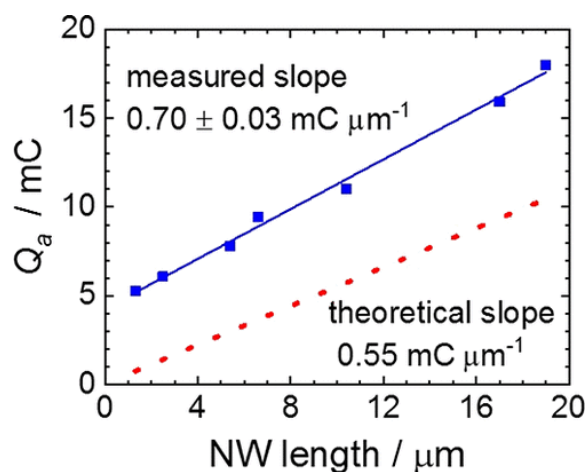
Figure 4.10 Variation of Q_a with respect to the measured Ni NW lengths. Q_a values were determined from CVs recorded between −0.10 and 0.45 V in 1 M KOH at 25 mV s^{-1}. The dotted red line corresponds to the charge expected based on a theoretical calculation assuming each NW is a perfect cylinder of known diameter and length and assuming the specific charge density for the conversion of Ni to α-Ni(OH)$_2$ is 0.514 mC cm^{-2}.

The formation of Ni NWs translates into a huge increase of the EASA. Using Q_a as measure, the EASAs of a Ni plate and an electrodeposited Ni thin film of the same size (0.15 cm^2) are 0.14 and 0.78 mC, respectively, compared to 18.0 mC for the Ni NW array sample with the longer (19 μm) nanowires. This is a factor of 130 and 10 increase of the EASA, respectively. In the following, we will focus our attention on assessing if the entire surface area of the nanowires is accessible to the electrolyte and able to participate in the oxygen evolution reaction or if mass-transport limitation of dissolved oxygen, ionic migration within the pores, or bubble occlusion effects are occurring, thereby limiting the benefits expected by increasing the EASA.

4.4.3 Oxygen Evolution Reaction

Chronopotentiometry profiles, with an applied current density of 10 mA cm$^2_{geo}$, were recorded in 1 M KOH for 30 min (Figure 4.11A). OER potentials at the Ni NW arrays continuously decrease with increasing Ni NW mean length, and initial potential values of 1.65 and 1.60 V are obtained for 2.5 and 19 μm long Ni NWs, respectively. It is worth mentioning that any of the OER potential values observed at Ni NWs are lower than at electrodeposited Ni film (1.68 V), which confirms the enhanced initial OER activity at Ni NW electrodes. As time progresses the corresponding potential on any Ni electrode increases, especially for the Ni film obtained through electrodeposition without an AAO

membrane, for which the potential rises to 1.83 V. To obtain quantitative data on the OER stability, initial (1 min) and final potentials (30 min) are plotted in Figure 4.11B. It is straightforward to conclude that the longer Ni NW electrodes are more stable for O_2 evolution at 10 mA cm^{-2}. The final potential values after 30 min electrolysis are plotted in Figure 4.11C as a function of Q_a. A significant decrease of the OER potential was found for Ni NW with high Q_a values, which was more than 200 mV for the 18 μm long Ni NW. The obvious diminution of OER potential on longer Ni NW electrodes can be explained by the intrinsic current density which is lower for the larger EASA electrodes. Even though the OER potential may be affected by many other effects, the governing factor in this work is the enhanced Ni surface area for the ordered 1D nanostructures.
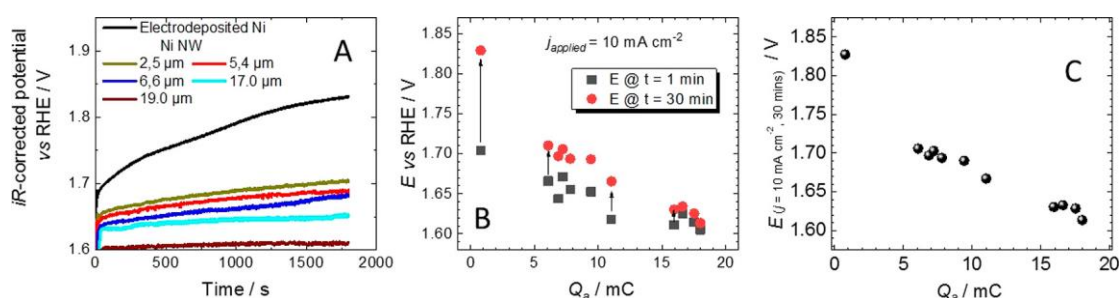
Figure 4.11 (A) Chronopotentiometric curves recorded at 10 mA cm^{-2} on different Ni samples. The electrolyte was 1 M KOH. The potential was corrected for the ohmic drop. (B) Influence of Q_a on the OER stability in 1 M KOH at j = 10 mA cm^{-2}. The iR-corrected potentials after 1 and 30 min of electrolysis are plotted. (C) iR-corrected potential after 30 min of electrolysis as a function of Q_a.

A Tafel analysis of Ni film, 3 μm long and 17 μm long Ni NW array electrodes, at electrode potentials in the OER region is given in Figure 4.12. These points are the steady-state currents for potential steps, which are plotted with the IRs-corrected potentials. The Tafel slopes are *ca.* 58 ± 10 mV dec^{-1} for the thin-film and NW electrodes, indicating a transfer coefficient of 1. Literature values on flat Ni electrodes are *ca.* 46 mV dec^{-1} [154]–[156] which is consistent with the present result considering the stated error and some uncertainty in the roughness factor. On hierarchical Ni(OH)$_2$ NW arrays with much smaller features than here, the reported Tafel slope was 123 mV dec^{-1} [157]. This result may not be directly comparable since porosity effects may be increasing the Tafel slope [131]. The agreement between the thin-film and NW electrodes and the independence of the Tafel slopes with the Ni NW lengths confirm that the OER is kinetically controlled in this overpotential range and that mass transport of dissolved oxygen, ionic migration within the pores, or bubble occlusion effects are not significant.
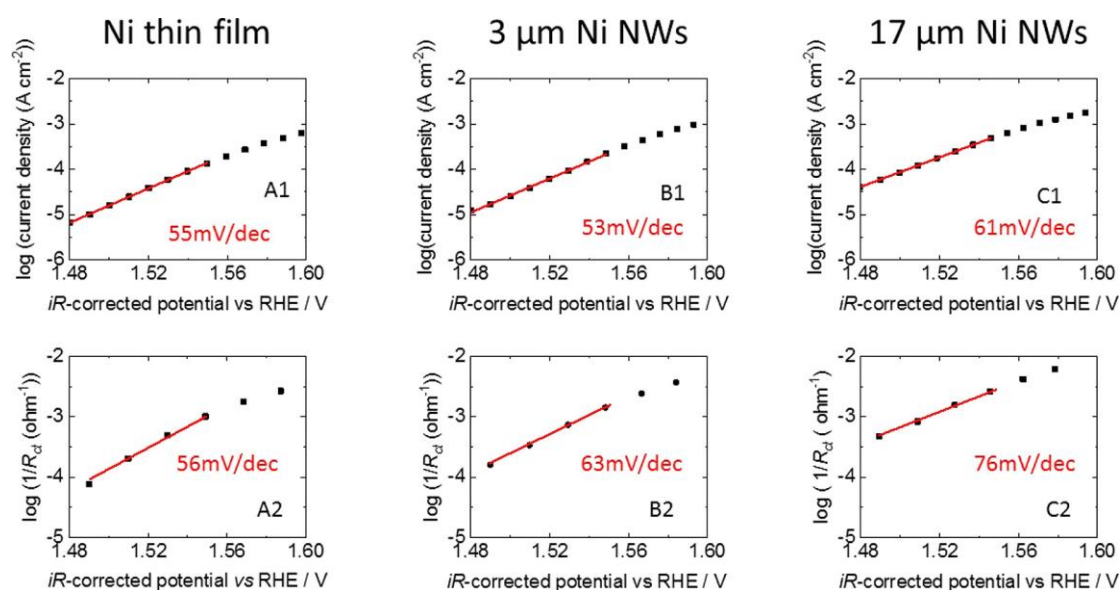
Figure 4.12 Variation of steady-state current density, j, (A1, B1, and C1) and log (1/R_{ct}) (A2, B2, and C2) with respect to iR-corrected potential. The data are shown for electrodeposited Ni thin film (A1 and A2), 3 μm NW electrode (B1 and B2), and 17 μm NW electrode (C1 and C2).

4.4.4 Electrochemical Impedance Spectroscopy on Ni NWs

Figure 4.13 shows the electrochemical impedance spectra of the electrodes at electrode potentials in the OER region, obtained after the steady-state measurements of Figure 4.12 were made. The EIS spectra of the Ni thin-film electrode show only one depressed semicircle. In comparison, the EIS data of Ni NWs display an additional semicircle at high frequencies. On Ni NWs, the shape of the high-frequency second semicircle does not change with the electrode potential, although its shape differs between short (3 μm) and long (17 μm) Ni NWs. This is an indication that the high-frequency semicircle is related to porosity and not to the electrode OER kinetics. The transmission-line model for porous electrodes comprising an array of identical pores has been well described [131], [158]. In general, the theory predicts a smaller high-frequency, potential-independent feature related to the pore geometry and a larger, potential-dependent distorted semicircle related to the interfacial kinetics. C. Hitz and A. Lasia [159] found experimentally and theoretically that for the hydrogen evolution reaction on porous Ni the porous electrode impedance may be closely approximated by two distorted semicircles modeled by two parallel resistor–CPE combinations in series. With the solution resistance Rel in series, this so-called 2CPE equivalent circuit was also found to fit the present results, which reflects the similar nature of the two systems: gas-evolving reactions at Ni porous electrodes in alkaline solution for which reactant (H_2O or OH^-) mass transport is fast. The dependence of the parameters of this model on the experimental conditions will be discussed, followed by their

relationship to the underlying porous electrode model. In the case of the Ni thin-film electrode, the circuit with only one parallel resistor–CPE combination "1CPE" was used (Figure 4.13A). The fits to the 2-CPE equivalent circuit for the OER at Ni NW electrodes are shown in Figure 4.13B and Figure 4.13C. Before accepting this as the final equivalent circuit, we used the F-test [160] to decide whether replacement of capacitors with CPEs was statistically justified. Acceptance required satisfying the F-test at the 99% confidence level and also that the error in the new fitted parameters was less than 30%. Both CPEs were justified using these criteria. Similarly, addition of a Warburg element representing diffusion in the finite-length pores ("short Warburg") in series with R_{ct} was found not to be justified.
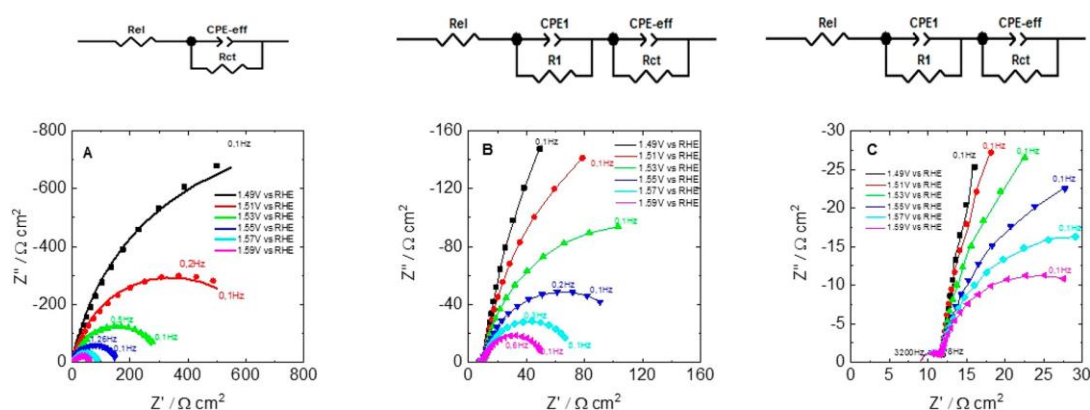
Figure 4.13 Measured (solid lines) and fitted (symbols) EIS plots measured on (a) electrodeposited Ni thin film; (b) 2.5 µm Ni NW electrode; and (c) 17 µm Ni NW electrode at different potentials. The equivalent electrical circuits used to fit the experimental data are also shown.

There is also the possibility that there are additional features, perhaps associated with slow mass transport of dissolved oxygen, which appear at frequencies lower than measured here. Lower-frequency features associated with diffusion of solution species have been seen before for NW arrays, *e.g.*, refs [161], [162]. This is a particular concern for Nyquist plots in which only part of the low-frequency semicircle is observed, though inspection of complex capacitance plots that visually enhance low-frequency features showed no low-frequency fine structure. The absence of lower-frequency features can be verified by extrapolating the fitted impedance function to zero frequency, $Z(\omega \rightarrow 0) = R_p$, and showing that it is equal to the slope of the steady-state polarization curve, dE/dj_{ss} [163]. In the case that the Tafel plot is linear, this relationship may be transformed into

Equation 4.1

$$\frac{RT}{\alpha F} = \frac{dE}{d(\ln j_{ss})} = \frac{j_{ss}dE}{dj_{ss}} = j_{ss}R_p$$

That is, the product of the steady state current and the low-frequency impedance should be constant and when multiplied by ln(10) = 2.303 should equal the Tafel slope. For the 2CPE circuit, $(R_1 + R_{ct})j_{ss}$ ln(10) was nearly constant (60–90 mV) and very close to the (iR-corrected) Tafel slope (see Figure 4.14), even though the current densities and R_{ct} each changed by more than an order of magnitude. In summary, the low-frequency relaxation is not significantly different from a parallel CPE resistor combination that represents the reaction kinetics, and there is no evidence for any significant mass-transport effects.
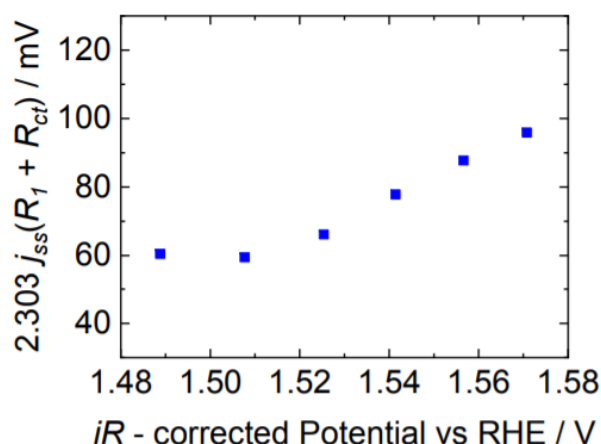
Figure 4.14 Product of Steady State Current Density and $R_p = R_1 + R_{ct}$ as a function of potentials on 17 μm Ni NWs.

The fitted parameters are given in Table 4.3, and the fits show excellent accordance with the experimental results (Figure 4.13). Also given there are the effective capacitances (C_{eff}) associated with a CPE, which were found using the Brug formula [128]:

Equation 4.2

$$C_{eff} = \left[T_2 \left(\frac{1}{R_{el}} + \frac{1}{R_{ct}} \right)^{\phi-1} \right]^{1/\phi}$$

An alternative form with R_{el} replaced by $R_{el} + R_1$ was also evaluated, but this made very little difference to the C_{eff} values obtained.

As the applied OER potential is increased, R_{ct} continuously decreased for both Ni electrodeposited film and Ni NW electrodes, with an exponential (Tafel) potential dependence as expected since $R_{ct} \approx R_p$. In all cases, the slope of log(1/R_{ct}) *vs.* potential curves is very similar to Tafel plots determined from the steady-state current density (see Figure 4.12). The C_{eff} values of both Ni thin films and NW arrays varied the same

way with potential (see below), indicating it reflects an intrinsic surface property. At any fixed potential, lower R_{ct} and larger C_{eff} values were obtained for long Ni NWs, as compared to short NW and electrodeposited Ni film (Table 4.3). Figure 4.15A and Figure 4.15B shows C_{eff} values determined at 1.49 V as a function of the Ni NW length and surface area, respectively. The proportional relationship between C_{eff} and either NW length or NW surface area confirms that the accessibility of the electrolyte along its axis is not restricted. These results are in close agreement with those discussed previously relating to the electrochemically active Ni surface area probed by CV (see Figure 4.10). In Figure 4.15B, the slope of the curve, representing the intrinsic capacitance per unit area, is 470 $\mu F\ cm^{-2}$. This is close to the C_{eff} for the flat electrodes (700 $\mu F\ cm^{-2}$), considering that the nanoscale roughness may be different.
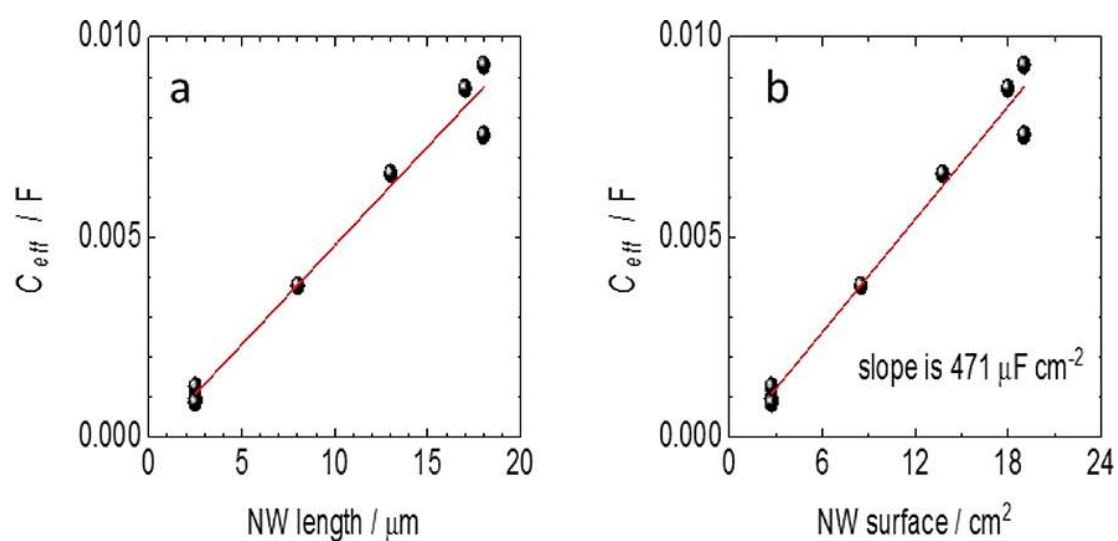
Figure 4.15 Effective capacitance in function of (a) NW length and (b) NW calculated surface area.

Table 4.3 Fitted Results from EIS Analyses

sample	E_{appl}/V *vs*. RHE	R_{ct}/Ω cm$^2_{geo}$	C_{eff}/mF cm$^{-2}_{geo}$
electrodeposited Ni film	1.49	1979 ± 94	0.72 ± 0.02
	1.51	736 ± 17	0.65 ± 0.02
	1.53	307 ± 4	0.60 ± 0.02
	1.55	148 ± 1	0.56 ± 0.02
	1.57	84.2 ± 0.5	0.52 ± 0.01
	1.59	56.1 ± 0.3	0.47 ± 0.02
3 μm Ni nanowires	1.49	931 ± 36	8.50 ± 0.08
	1.51	443 ± 7	7.74 ± 0.05
	1.53	204 ± 2	7.33 ± 0.05
	1.55	105.4 ± 0.6	7.02 ± 0.07
	1.57	61.7 ± 0.4	6.85 ± 0.10
	1.59	40.2 ± 0.2	6.62 ± 0.10
17 μm Ni nanowires	1.49	316 ± 30	58.16 ± 0.21
	1.51	180 ± 8	52.30 ± 0.22
	1.53	96 ± 2	47.93 ± 0.23
	1.55	58 ± 1	41.71 ± 0.24
	1.57	35.8 ± 0.3	41.86 ± 0.21
	1.59	24.6 ± 0.2	43.14 ± 0.30

Figure 4.16A shows the variation of C_{eff} values as a function of the applied potential for a series of NWs of different lengths. In some cases, duplicate samples were made (2.5 and 17 μm long NW), and the results are very reproducible. It can be clearly seen that all the Ni electrodes display a C_{eff} that is decreased slightly as the applied potential increases from 1.49 to 1.59 V. Figure 4.16B shows the variation of effective

capacitance on 2.5 and 17 μm long Ni NWs determined by stepping the potential from 1.49 to 1.59 V and then from 1.59 to 1.49 V. As expected from the previous results, the effective capacitance decreases slightly as the potential is made more positive (anodic sweep). However, it is found that this decrease of the effective capacitance is totally reversible as the C_{eff} values are independent of the sweep direction. This is true for both the shortest and the longest Ni NWs investigated in the present study and mirrors the decrease in C_{eff} seen on the flat surface (see Figure 4.17). This strongly suggests that the change in the effective capacitance represents a change in the surface condition with potential. This change could be related to a pseudocapacitance of some sort, perhaps associated with the tail end of the oxyhydroxide peak. However, the β-Ni(OH)$_2$/β-NiOOH transition is not reversible, and unlike what is observed, the C_{eff} values should be dependent on the sweep direction. As a pseudocapacitance with values roughly as expected for adsorption, this reversible change of C_{eff} could reflect the potential dependence of an adsorbed species on both Ni thin films and Ni NWs.
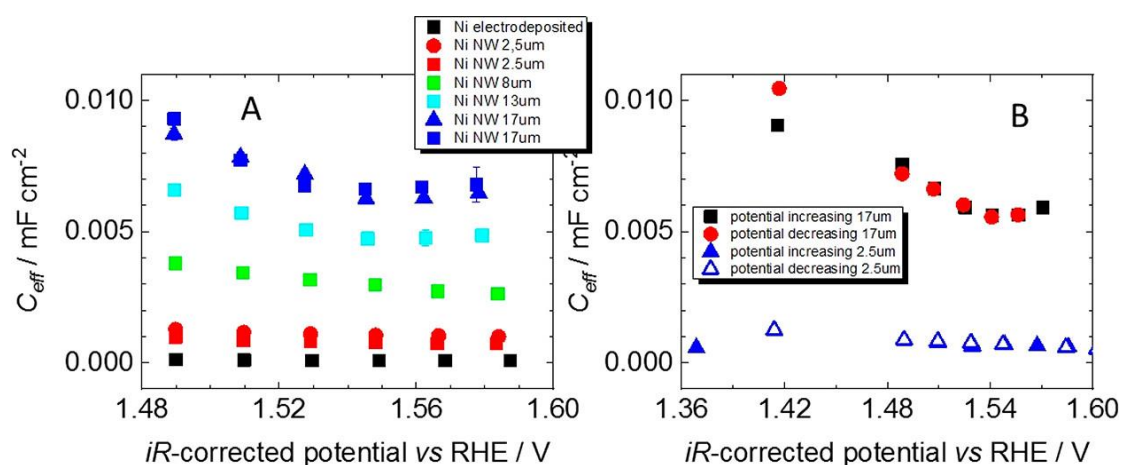
Figure 4.16 (A) Effective capacitance in function of potential on different Ni electrodes including duplicate experiments. (B) Effective capacitance in function of potential on 2.5 and 17 μm long Ni NW electrodes tested for increasing and then decreasing potentials.
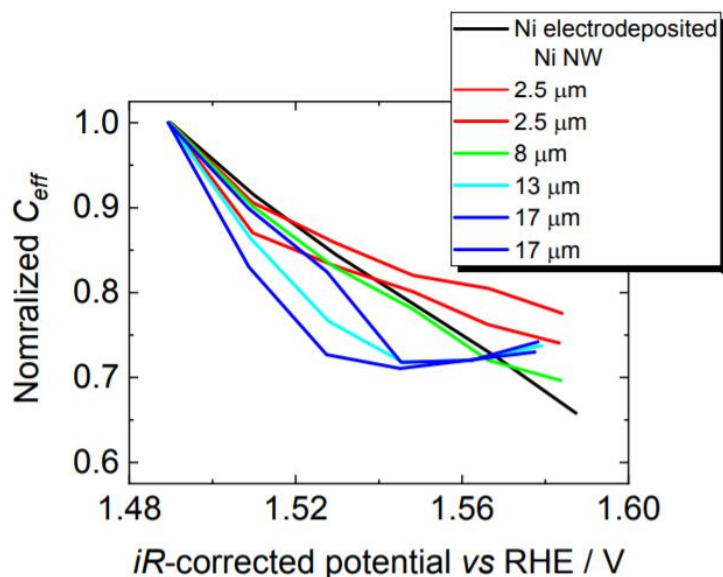
Figure 4.17 Normalized effective capacitance in function of potential. The C_{eff} value at 1.49V of each electrode is used as reference.

The near semicircular low-frequency relaxation exhibiting conventional charge-transfer kinetics and the full accessibility indicated by the proportionality between C_{eff} and calculated surface area or length raise the question as to whether porous electrode theory is required at all. In its simplest form the theory applies to single isolated electrolyte-filled pores, and then the electrode impedance is determined by taking the parallel impedance of individual pores. In the present case, there is a single interconnected electrolyte volume that seems quite unlike a pore. However, the NW array approximates a periodic 2-D structure in which the impedance of individual 2-D unit cells must be combined in parallel to give the "porous" electrode impedance. We follow a methodology similar to that of Mutha *et al.* [164]. In the present case, the array is hexagonal with one nanowire per unit cell. The theory for cylindrical pores therefore needs little modification for cylindrical nanowires: the curved surface (wall) area (a_{wall}) is the same, but the cross-sectional area of the electrolyte-filled pore (a_{pore}) is now the area of the unit cell minus the circular area of the nanowire.

In the present case the unit cell area is the reciprocal of the number density of NWs determined from the SEM images, and the NW area is known from the diameters, also measured from the SEM images. Furthermore, the flat Ni electrode has a 1-CPE interfacial impedance, so that the porous electrode theory gives the same equation as given by Hitz and Lasia [159] with the exception that their parameter a is slightly different. In the general case, $a^{-1} = a_{wall}nR_{pore}$ and $R_{pore} = \rho l/na_{pore}$ where l is the pore length and ρ is the resistivity of the electrolyte, and only a_{pore} is different from the

cylindrical pore case. With the known geometric factors and appropriate kinetic parameters, the low-frequency semicircle shape and size are well predicted, but the high-frequency feature should have size of the order of R_{pore}, which is much smaller than observed.

The key parameter determining the shape is the penetration depth of the a.c. signal, $\lambda = (a_{pore}|Zeq|/\rho\pi d)^{1/2}$, where d is the diameter of the nanowires and Z_{eq} the specific (Ohm cm^2) interfacial impedance of the pore walls on a real area basis. Z_{eq} was calculated as a parallel combination of a charge transfer resistance and CPE, with values taken from the fitted values for the low-frequency semicircle and scaled by the roughness factor to convert to a real area basis. This depth is independent of pore/wire length and decreases from 540 μm at 0 Hz to 24 μm at 100 Hz for the kinetic parameters at 1.59 V. It will be larger for more negative potentials, and we conclude that for the frequencies relevant for the low-frequency feature it is always much larger than the wire length. Therefore, the pore is fully accessible, and the kinetics solely determine the shape. This justifies the simplified analysis above that neglected the details of the porous electrode theory.

The same analysis predicts a high-frequency part that is a 45° line and not a semicircle. Such 45° lines have been observed for ideal pore geometries such as macroscopic microwire brush electrodes [165] or wire-in-capillary electrodes [166]. However, the shape of the high-frequency feature is known to depend on the pore shape, with semicircles predicted theoretically for pear-shaped pores [167] and observed experimentally for pressed powder porous Ni electrodes [159]. The present geometry seems far from these. However, as shown in Figure 4.18, the shape of the high-frequency part of the electrochemical impedance spectra evolves with the NW length and thus the pore aspect ratio since the NW–NW distance is fixed at *ca.* 80 nm in the present study. This is reminiscent of the findings of Hitz and Lasia, who showed that the high-frequency feature of spherical pores becomes flatter and more linear as the pore openings becomes larger [159]. This issue will need to be more closely investigated in the future.
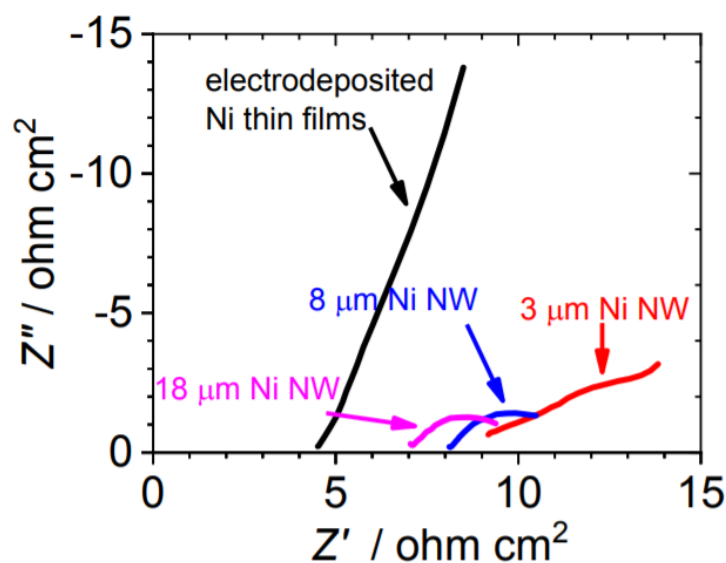
Figure 4.18 High-frequency part of the IES spectra recorded at 1.49 V vs. RHE.

4.5   Conclusion

Long Ni NWs were synthesized by electrodeposition through an AAO membrane. The Ni NWs have a diameter of *ca.* 300 nm. Detailed structural analysis showed that each Ni NW is composed of a central Ni metallic core and surrounded by a $Ni(OH)_2$ crust that thickens from 10 to 20 nm after extensive electrochemical testing. The 1D Ni nanowires are densely packed in a brush-like array structure, with a packing density between that expected for ideal square and hexagonal packing. The NW–NW distance was kept constant at *ca.* 80 nm, and thus the aspect ratio of the electrolyte-filled volume between pairs of NWs is decreased from 2.7% to 0.4% as the NW length is increased by 1 order of magnitude up to 20 μm. A proportional relationship is observed between the electrochemically active Ni surface area probed by CV and either NW length or NW surface area, confirming that the accessibility of the electrolyte along its axis is not restricted despite the huge restriction at the openings of the electrolyte-filled volume. Likewise, the proportionality between C_{eff} and calculated NW surface area suggests that the accessibility of the electrolyte along the NW axis is not restricted. All data point to the OER being kinetically controlled in the overpotential range investigated here, with very little (if any) mass-transport limitation of dissolved oxygen, ionic migration within the pores, or bubble occlusion effects. The governing factor affecting the electrocatalytic properties of closely packed 20 μm long Ni NW arrays for the OER is the enhanced Ni surface area for the ordered 1D nanostructures, which translates into a significant 200 mV decrease of the OER overpotential at 10 mA cm^{-2}. These vertically aligned 1D NWs allow us to increase the electrochemically active

surface area of a Ni plate by a factor of 130 without introducing any limitation by diffusion. This can be due to fact that the 1D NWs are almost perfectly aligned. It is expected that they could serve as an ideal platform to support better catalytic materials without showing any limitation due to mass transport.

5 HYDROGEN BUBBLE TEMPLATING OF FRACTAL NI CATALYSTS FOR WATER OXIDATION IN ALKALINE MEDIA

5.1 Abstract

Dynamic hydrogen bubble templating of Ni (Ni DHBT) electrodes was used to prepare highly porous films with enhanced properties toward the oxygen evolution reaction (OER). Upon varying the electrodeposition conditions, Ni films with a macroporous primary structure and highly porous cauliflowerlike secondary structure were formed. These films are able to develop an extended electrochemically active surface area, up to 270-fold increase compared to a Ni plate. They exhibit stable overpotential (η_{250} = 540 mV) at j = 250 mA cm^{-2} geometric in 1 M KOH electrolyte, which is 300 mV less positive than at the Ni plate. Fe incorporation onto these Ni DHBT structures can further lower OER overpotentials to η_{250} = 310 mV. Ni DHBT films are remarkably stable over prolonged polarization and are characterized by a low Tafel slope (29 mV/decade) that extends up to j = 100 mA cm^{-2} geometric, attributed to both superaerophobic characteristics with a contact angle of *ca.* 160° between the surface and an air bubble and superhydrophilic characteristics with less than 25° between the surface and a water droplet.

5.2 Introduction

Electrochemical water splitting is a promising approach to provide clean and storable chemical fuels (H_2 and O_2). When connected to renewable energy sources whose production is intermittent, water electrolyzers can play a fundamental role in the development of a sustainable energy network. Several approaches to water splitting catalytic processes, such as microbial, photo, and photoelectro, still present sluggish oxygen evolution reaction (OER) kinetics that limits the overall efficiency of the process. Recently, there has been a renewed interest in the study of materials exhibiting good activity and stability for the OER. Among OER materials, oxide compounds are the most active [168], notably binary noble metal oxides [169] (Ru, Ir) and those having complex structures (perovskite [170], spinel [171], layered [172]). Nevertheless, in strongly alkaline media (pH ≥ 13), Ni metallic alloys continue to attract a lot of attention with recent promising achievements in terms of sustained activity [173].

In combination with improving the intrinsic catalytic properties of OER catalysts, microstructuring and nanoengineering of the electrode surface are also mandatory. Indeed, microstructuring helps to increase the number and surface density of reactive

sites having good electronic connectivity to the underlying substrate and easy access to the electrolyte, while nanoengineering of the electrode surface facilitates the escape of gas bubbles. The latter aspect is particularly important for applications and device operation in practical electrolysis conditions ($j \geq 100$ mA cm^{-2}). Indeed, the release of O_2 bubbles at large current density is known to alter the reaction efficiency due to overpotentials associated with greater bubble resistance [174]. The mechanisms responsible for this increased inefficiency include O_2 bubble formation leading to a net decrease of the available underlying catalytic Ni sites; O_2 bubbles coalescing near the Ni surface which may also cause large ohmic losses due to the formation of nonconductive gas layers; and pH modification (increase) which may lead to possible instability of the catalyst's corrosion processes. In this context, it is of utmost importance to facilitate the release of gas bubbles from the surface of electrodes participating in gas evolving reactions like oxygen evolution.

The size, size distribution, adsorption, and residency time of gas bubbles on the electrodes can be varied through ultragravity [175]–[177] and ultrasonic treatment [178], leading to decreased overpotentials and increased current density. However, these methods are difficult to implement in industrial production and not cost-effective for commercial systems. More recently, it was reported that passive control of the bubble behavior can be accomplished through nanoengineering of the electrode surface to impart intrinsically active materials with carefully tailored porosity that facilitate the detachment of oxygen bubbles from the surface and, in turn, improved the extrinsic (overall) performances of electrodes. These electrodes are termed "superaerophobic" as gas bubbles trapped at their surfaces typically exhibit very large contact angles [179]. In the literature, several oxides and hydroxides containing various amounts of Ni, Co, Fe, and Zn superaerophobic electrodes with nanoengineered surface have shown improved OER characteristic [180]–[184]. This improvement of the extrinsic properties of electrodes for gas evolving reactions through nanoengineering of the electrode surface is not restricted to the OER and was also observed for other reactions, such as hydrogen evolution [108], [149], [185]. Indeed, our ability to prepare materials and electrodes with optimized porosity has reignited interest in research areas involving Li batteries [186], capacitors [187], sensors [188] and catalysis [189]. However, in most of these studies, the materials investigated and the methods used to impart the necessary nanoengineered characteristics to the electrode surface are not relevant to industrial applications and commercial devices.

In this study, electrodeposition was used to prepare porous Ni electrodes with high surface area values, ensuring that practical OER current densities could be reached at lower overpotential. To do so, we applied a dynamic hydrogen bubbling template (DHBT) method to prepare polycrystalline Ni electrodes with morphological features that facilitate the release of oxygen bubbles during the OER. During the cathodic Ni deposition, hydrogen bubbles are concomitantly evolved due to the large cathodic potential applied. This leads to a nanoengineered electrode surface with an open porosity that reaches the underlying substrate. These deposits easily prepared using a fabrication process that could be scaled up. They are adherent, superaerophobic, and mechanically stable under vigorous oxygen evolving conditions and present very interesting OER properties.

5.3 Experimental Section

5.3.1 Synthesis of Porous Ni Electrodeposits

Galvanostatic deposition (2 A cm^{-2}) from an aqueous solution of 0.1 M NiCl$_2$·6H$_2$O (ACROS Organics, ACS Reagent) and 2 M NH$_4$Cl (Fisher Chemical, Trace Metal grade) was used to obtain fractal Ni foams with a honeycomblike primary and cauliflowerlike secondary structure. These electrodes will be denoted as Ni DHBT (dynamic hydrogen bubble template) since both Ni deposition and H$_2$ evolution are occurring simultaneously. In all cases, commercial Ni plates (Alfa Aesar, Puratronic 99.9945% (metal basis)) were used as substrates. The films were deposited on one face of 1 cm × 1 cm Ni substrates. The electrodes were then sealed in bent glass tubes (90° angle) so that the electrode surface was maintained in a vertical position and the Ni substrate uncovered face was not exposed to the electrolyte. In all cases, the exposed surface area was 1 cm^2. A saturated calomel electrode (SCE) and Pt gauze (Alfa Aesar, 99.9%) were used as reference and counter electrodes, respectively. For sake of clarity, all electrode potential values were converted to the reversible hydrogen electrode (RHE) scale. The distance between the counter and the working electrode was fixed at *ca.* 5 mm. Ni electrodeposition was carried out using a Solartron 1480 A multipotentiostat for durations (T$_d$) up to 550 s. The faradaic efficiency for the Ni electroplating process was *ca.* 27 ± 8%, independently of the deposition duration. Following electroplating, the porous Ni electrodeposits were rinsed with water and dried under an Ar stream.

5.3.2 Physical Characterization of Porous Ni Electrodeposits

The surface morphologies of porous Ni films were characterized by scanning electron microscopy (SEM) (JEOL, JSM-6300F) and thicknesses were measured by SEM

cross-section analysis. Energy dispersive X-ray (EDX, VEGA3 TESCAN) measurements were performed to determine the Fe content. Contact angle measurements were performed as following. Images of water droplets and (captive) air bubbles in contact with the electrode surface were captured by a Panasonic CCD camera (model GP-MF552). The volumes of the water droplet and air bubble were 5 µL in both cases. Contact angles were calculated using ImageJ software with the Dropsnake plugin.

5.3.3 Electrochemical Characterization and OER Performances

Electrochemical characterization in Ar-saturated (Air Liquid, 99.999%) 1 M KOH (Fisher Chemical, ACS Reagent grade) was conducted in a conventional three-electrode system, using a Pt gauze and a saturated calomel electrode as auxiliary and reference electrodes, respectively. The working electrode and the counter electrode were not separated by a membrane. The solution (70 mL) was agitated by Ar bubbling. The distance between the working and the counter electrode was 5 mm. Following a period of 10 min under open circuit potential (OCP) conditions, cyclic voltammograms (CV) (50 mV s^{-1}) with different potential windows (0.5 to 1.4 V, 0.5 to 1.6 V, and 0.5 to 1.9 V) were performed until steady-state potentiodynamic features were obtained. The last CV was recorded at 5 mV s^{-1}. Galvanostatic oxidation was carried out at 10 mA cm^{-2} for 15 min and then at 250 mA cm^{-2} for 15 min, followed by a last CV (0.5 to 1.9 V, 5 mV s^{-1}). This sequence was systematically applied to every Ni electrode studied in this work in order to ensure full conversion of nickel to β-Ni(OH)$_2$. The ohmic drop was measured by electrochemical impedance spectroscopy (EIS) and an ohmic drop correction was manually applied to all potential values mentioned below.

In some cases, CVs and polarization curves were recorded in 1 M KOH electrolyte spiked with Fe. In those cases, the concentration of Fe was varied between 0 and 10 ppm through the addition of FeCl$_2$·6H$_2$O (Alfa Aesar, 98%).

EIS measurements in the OER potential range were obtained following 10 min polarization (from 1.44 to 1.49 V) between 0.01 Hz and 200 kHz using a FRA Analyzer (Solartron 1255B). Fitting to the de Levie equation was carried out by using Zview, with the de Levie element in series with the solution resistance and an inductor to model the typical wiring artifact seen at high frequencies. The values of R$_{ct}$ and C$_{dl}$ were derived from the fitted parameters, and so, the software does not provide a standard error for them, but a naive error propagation argument suggests that their standard errors are of the order of 5%.

72

Simulations of the transmission-line differential equations for porous electrodes [159], [190]–[193] were performed by solving the ac and dc equations together as a system using Maple's default boundary value ODE solver, with an absolute error tolerance of 10–7 and a maximum number of mesh points of 256. For this purpose, the two complex ac differential equations were converted to the four real differential equations below. The results were verified by comparing with those of Lasia [159], [190]–[193] (who used a different method). The differential equations were scaled to represent the quantities on a geometric area basis (rather than for a single pore), in which they take the following form:

Equation 5.1

$$\frac{dE(X)}{dX} = -R_\Omega J(X); \frac{dJ(X)}{dX} = -j(E(X))$$

$$\text{With } E(0) = E_0; J(1) = 0$$

Equation 5.2

$$\frac{d\tilde{E}(X)}{dX} = -R_\Omega \tilde{J}(X); \frac{d\tilde{J}(X)}{dX} = -\left(i\omega C_{dl} + \frac{dj(E(X))}{dE(X)}\right)\tilde{E}(X)$$

$$\text{With } \tilde{E}(0) = 1; \tilde{J}(1) = 0$$

Here X is the dimensionless distance into the pore, from 0 at the pore entrance to 1 at the pore base and E(X) and Ẽ(X) are the dc and ac (phasor) potentials down the pores. The quantities J(X) and J̃(X) are the dc and ac current densities (in solution) down the pores and R_Ω is the total solution resistance (Ω cm^2) within the pores, all with respect to geometric area and for the total number of pores in that area. The quantities C_{dl} (F cm^{-2}) and j (A cm^{-2}) are the local (specific) double-layer capacitance and current density on the pore walls, scaled by the roughness factor; the current density is assumed to have a Tafel potential dependence, as discussed below. The potential at the pore entrance, E_0, is taken to be the experimental iR-corrected potential. The output is the predicted impedance Z = Ẽ (0)/J̃ (0) = 1/J̃(0).

5.4   Results and Discussion

5.4.1   Morphology of Ni DHBT Films

The morphological features of as-deposited Ni DHBT films are shown in Figure 5.1. All electrodeposition parameters remained the same (−2 A cm^{-2} in 0.1 M NiCl$_2$·6H$_2$O + 2 MNH$_4$Cl) except for electrodeposition times (T_d). As seen in Figure 5.1A-D, increasing Td led to a gradual increase of the Ni film thicknesses, from *ca.* 35 μm for T_d = 50 s up to 220 μm for T_d = 450 s. The deposited mass of Ni increased linearly up to 100 mg

cm^{-2} for T_d = 450s (see Figure 5.2). The porosity of the films, calculated from the deposited mass and the measured thickness, varies between 30 and 50%. The mechanical stability of films deposited for longer duration (T_d = 550 s) is poor, with some parts detaching from the substrate upon rinsing, which causes the deposited mass to level off. The cross-section SEM micrographs of Figure 5.1A-D also show that there are numerous voids along the observed dendritic structure of the films. Most of these voids are extending from the film surface to the underlying Ni plate substrate.
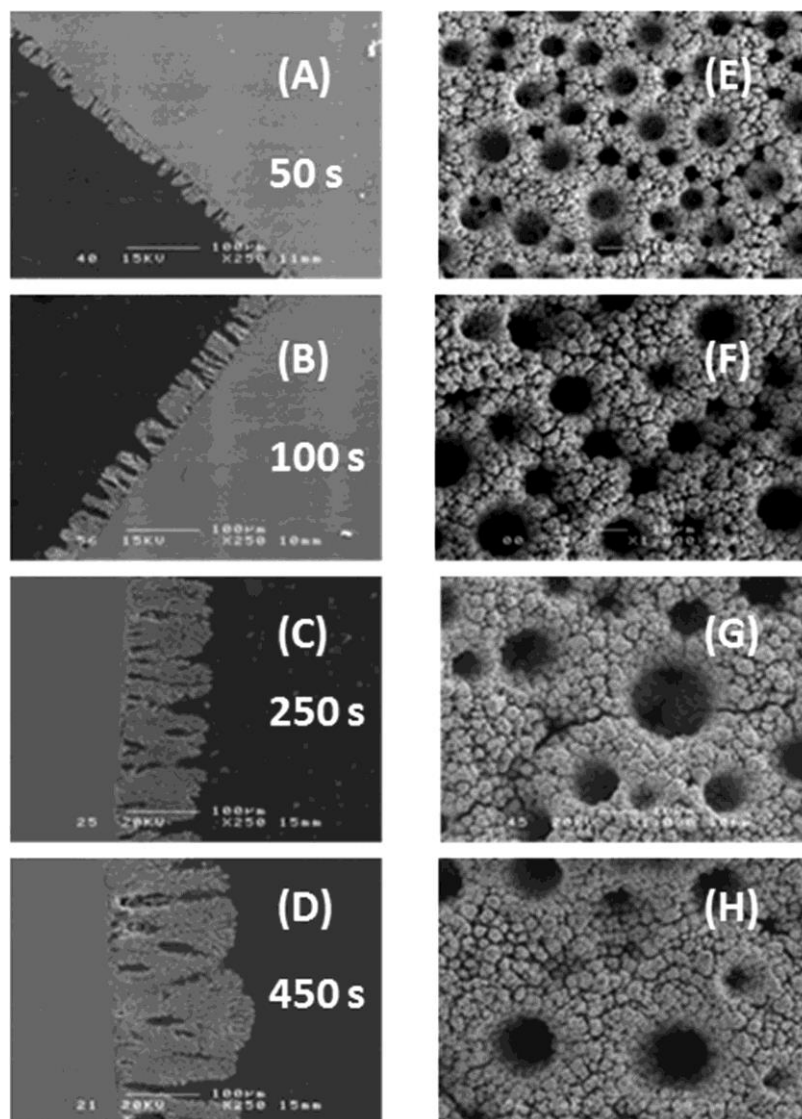
Figure 5.1 Effect of electrodeposition time (values inserted for each sample) on the morphological features of Ni DHBT. The deposition conditions are the following: −2 A cm^{-2} in 0.1 M NiCl$_2$·6H$_2$O + 2MNH$_4$Cl; cross-section (A–D) and corresponding top-view images (E–H).

From top-view SEM micrographs (Figure 5.1E–H), micrometer-sized pores are observed at the surface of the films, with pore diameter varying between 10 and 30 µm. Lower pore density and larger pore diameter are obtained for increased deposition

74

times. This is typical of metal electrodeposition under vigorous hydrogen evolution (DHBT films) [194]–[205]. In all cases, the pore walls exhibit a highly porous cauliflower-like secondary structure, with much smaller pore diameter (typically less than 500 nm). The structure seen in Figure 5.1 was observed over the entire 1 cm^2 geometric surface area of the deposits. It is expected that similar Ni structures could be formed on substrates with much larger geometric surface areas.
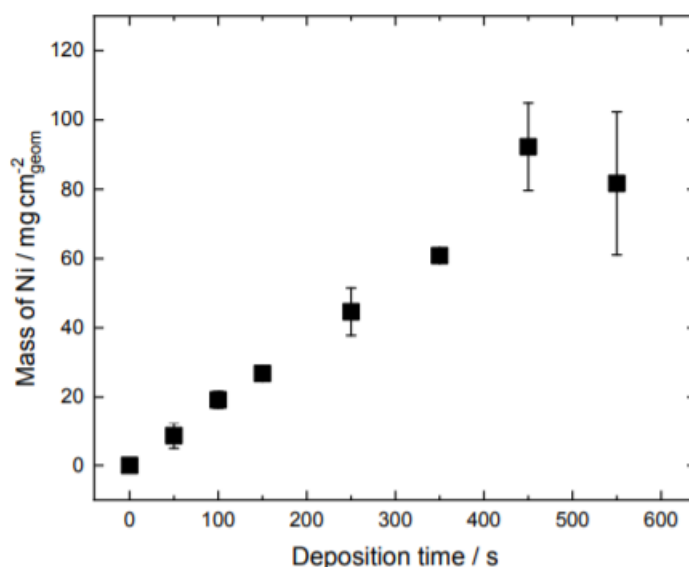
Figure 5.2 Effect of deposition times on the mass of Ni coatings. The substrate was a 1 cm^2 Ni plate in all cases.

Contact angle measurements on captive air bubbles at the surface of Ni DHBT films were performed, and representative results are displayed in Figure 5.3. The contact angle of an air bubble increases from *ca.* 139° for Ni plate to *ca.* 160° for Ni DHBT films, independently of the DHBT deposition times. Enhanced air bubble contact angles were recently reported at laser-ablated Ni roughened plates (164°) as compared to Ni plates (126°) [206]. Complementary water contact angle measurements were also performed to assess the hydrophilicity of Ni DHBT films, essential for ensuring wetting of the porous structure of Ni DHBT films and good contact of the latter with surface-active sites. To do so, sessile drop experiments were performed (5 µL of deionized H_2O) (see Figure 5.3). Ni DHBT films presented superhydrophilic properties, with contact angles well below 25°, testament to the strong affinity of Ni DHBT films toward water molecules. For the sake of comparison, Ahn *et al.* recently reported contact angle values of 30° and 42° for highly hydrophilic needle-like and cauliflower Ni electrodes, respectively [207]. In contrast, much larger

contact angles (69°) were recorded on Ni plate, consistent with independent water contact angle studies on Ni plates (70 ± 3°) [206], [207].
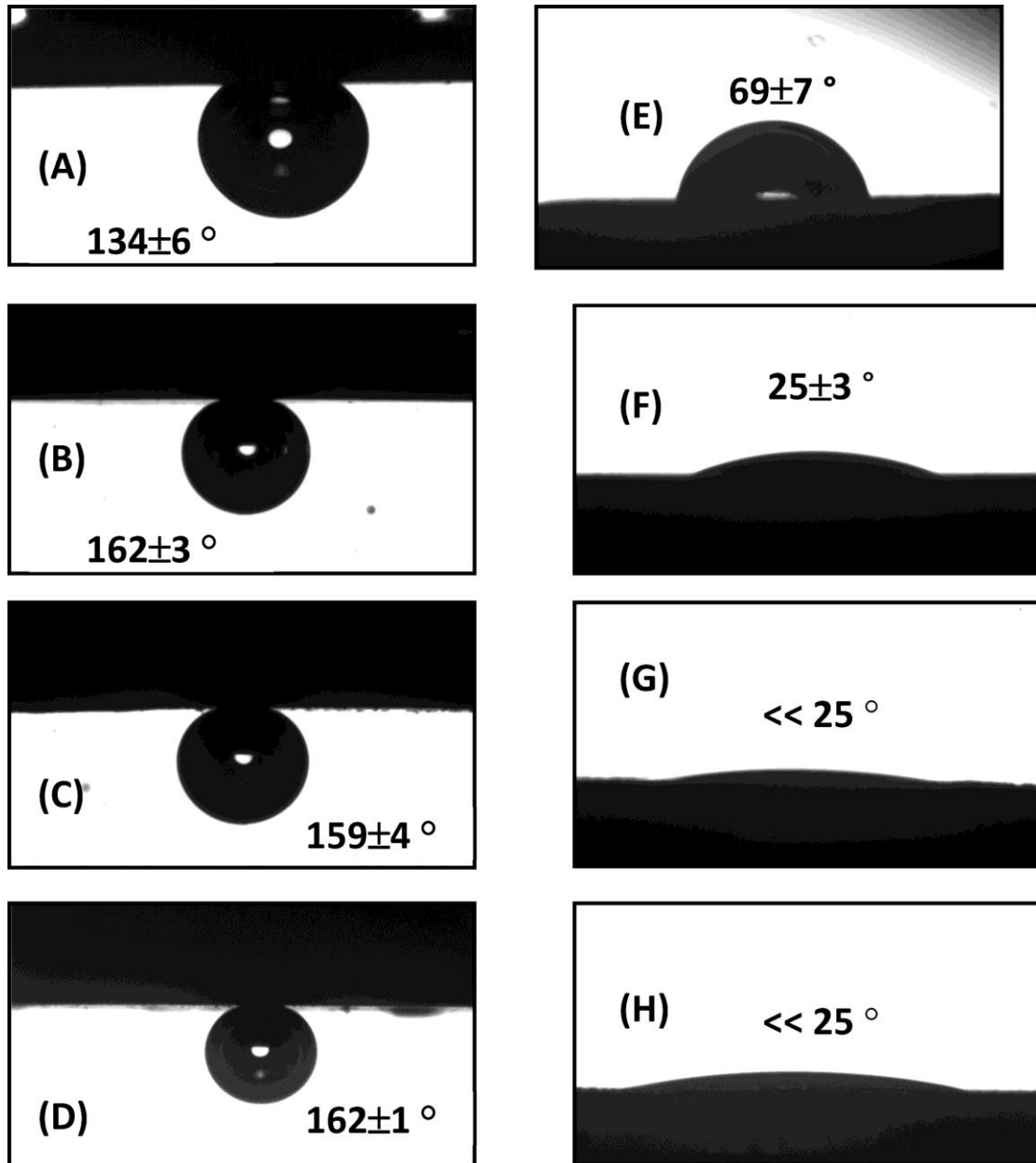
Figure 5.3 Contact angle images for a 5 μL air bubble (A–D) and a 5 μL water droplet (E–H) on Ni plate (A, E); Ni DHBT with $T_d = 50s$ (B, F); Ni DHBT with $T_d = 250s$ (C, G); and Ni DHBT with $T_d = 450s$ (D, H).

According to the Wenzel's model, the apparent contact angle on a rough surface, θ_r, is given by the following equation:

Equation 5.3

$$\cos\theta_r = r\cos\theta \text{ with } \cos\theta = \frac{\alpha_{13} - \alpha_{12}}{\alpha_{23}}$$

where α_{12}, α_{13}, and α_{23} denote the interfacial tensions of the solid–liquid, solid–gas, and liquid–gas interfaces, respectively, r is the ratio of the true area of the solid surface

to the apparent area, and θ is the Young's contact angle as defined for an ideal surface of the same material. Because r is by definition greater than or equal to 1, Equation 5.3 predicts that roughness enhances the wetting/nonwetting intrinsic properties of any material, the extent of which is defined by the value of r.

An alternative way to deal with porous solid surfaces is to use [208], [209] :

Equation 5.4

$$\cos \theta_f = \left(\frac{L}{l}\right)^{D-2} \cos \theta$$

where L and l are the upper and lower limit lengths of fractal behavior, respectively, and D is the fractal dimension of the solid surface, with $2 \leq D \leq 3$. A fractal analysis based on the SEM cross-section image of the thicker Ni DHBT film (T_d = 450 s) was conducted (see Figure 5.4). The value of $(L/l)^{D-2}$ given by such calculation is 6.5. However, using the water contact angle of Ni plate as a reference, Equation 5.4 predicts that $\cos \theta_f$ = 2.3, which is obviously not possible. This discrepancy may be caused by air trapped beneath the water droplet. In these conditions, wetting follows the Cassie–Baxter wetting regime and Equation 5.4 can be rewritten as Equation 5.5 [210].
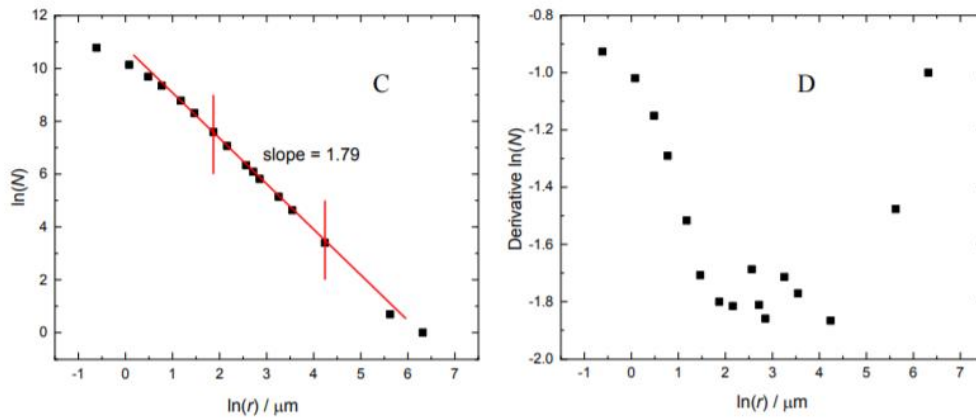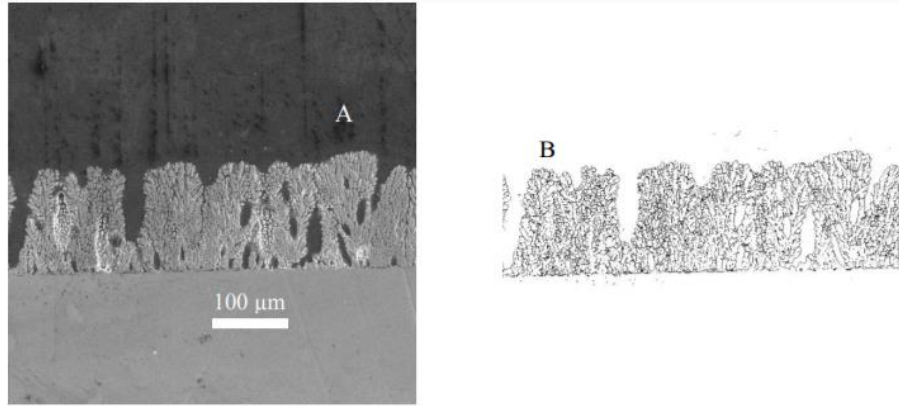
Figure 5.4 In (A), the original SEM cross-section image of a Ni DHBT film (T$_d$ = 450 s) at ×500 magnification. In (B), the contour image extracted from (A). In (C), ln – ln plot of box count N vs. box size r. In (D), Derivative plot of ln(N) vs. ln(r).

Equation 5.5

$$\cos\theta_f = \left(\frac{L}{l}\right)^{D-2} f_s\cos\theta + f_s - 1$$

with f_s being the fraction of the surface that is wetted by water. So, assuming that f_s = 0.6 (the water droplet is wetting 60% of the Ni DHBT film underneath), the contact angle measurements are in agreement with the fractal analysis. The use of Equation 5.5 implies that Ni DHBT films should be treated like porous materials and that partial spontaneous invasion of liquid inside the texture of these films is taking place through capillary action. Further decrease of θf could be achieved by increasing $(L/l)^{D-2}$ and/or f_s. This could be achieved through modification of the Ni DHBT deposition conditions. Also, it should be noted that the above discussion on the wetting property is based on the ex-situ contact angle observations. It reflects the hydrophilic properties of Ni DHBT film, but the air entrapment assumption used in Equation 5.5 would not necessarily be valid in the real gas evolution situations. So, future *in situ* observations on the contact

78

angle measurement should be made to evaluate the full benefits of Ni DHBT films in releasing the bubbles, but this is however outside of the scope of the present study.

5.4.2 Electrochemical Characterization

The electrochemical properties of porous Ni DHBT coatings were first determined through CV measurements. Following repetitive potential cycles until the formation of a hydrous Ni oxide deposit was achieved [211], steady-state CV profiles were obtained and are shown in Figure 5.5. All Ni DHBT CVs exhibit a large oxidation (at *ca.* 1.41 V) and reduction peak (at *ca.* 1.28 V), whose intensities grow with the film thicknesses. The assignment of these peaks will be discussed later. For each Ni DHBT electrode, the ratio between the anodic (Q_a) and the cathodic (Q_c) Coulombic charge of this redox transition remained similar, with a mean value of *ca.* 1.00 ± 0.13. Q_a values were found to increase continuously from 62 ± 4 mC cm^{-2} for Td = 50s to 539 ± 57 mC cm^{-2} for T_d = 450s (Figure 5.6). These values correspond to electrochemically active surface enhancement factors of *ca.* 30 and 270, respectively, considering the Qa value of a commercial Ni plate as a reference (2.1 ± 0.1 mC cm^{-2}). Once normalized to the deposited mass, m (Figure 5.6), the ratio Q_a/m is remarkably constant. This is a clear indication that the material deposited at the beginning of the deposition period is not occluded by that deposited at the end of the deposition process. This is consistent with the presence of numerous small (<500 nm) and large (10–30 µm) pores seen in Figure 5.1. For comparison, there is a factor of *ca.* 25 increase between the Q_a values of Ni foams and Ni DHBT films (Figure 4.7). The good mechanical stability, highly porous structure and tremendous capacity of Ni DHBT films to store charge makes it an attractive material and/or substrate for low-cost pseudo supercapacitor devices, as charge density values in excess of 500 mC cm^{-2} observed for Ni DHBT of 450 s are well above those reported recently for hierarchical porous Ni/NiO electrodes [212]. Higher electrochemically active surface areas were obtained for Ni DHBT of 550 s (660 mC cm^{-2}); however, these later films have mechanical stability issues (some part of the deposits might detach from the substrate), causing a large dispersion in the data (see the error bar in Figure 5.6). In the future, a subsequent heat-treatment might help improve the mechanical stability of the thickest films through sintering of Ni grains, therefore allowing the preparation of adherent films with larger electrochemically active surface areas. In this work, however, no such heat-treatment was applied and this aspect will be investigated in an upcoming study.
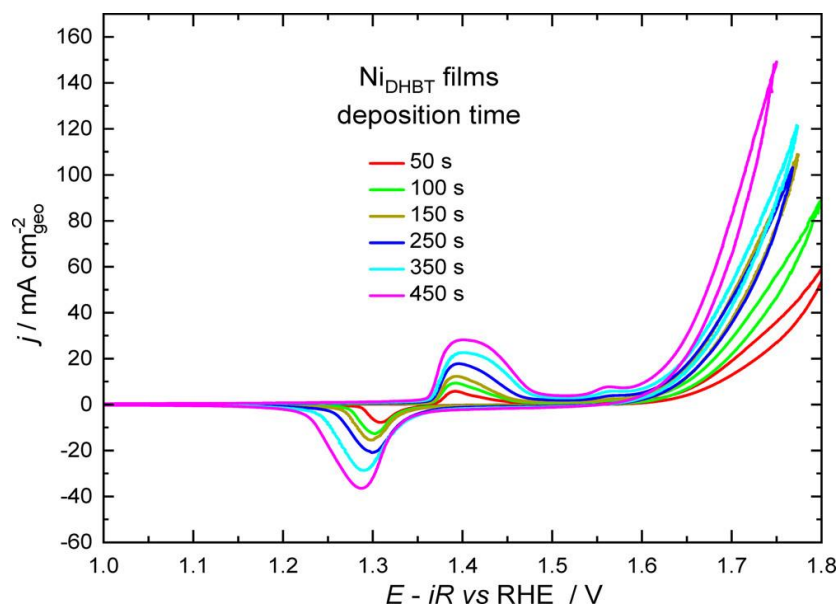
Figure 5.5 Cyclic voltammograms (5 mV s⁻¹) in 1 M KOH for Ni electrodes obtained through the dynamic hydrogen bubble template electrodeposition method. The electrodeposition time is shown for each electrode.
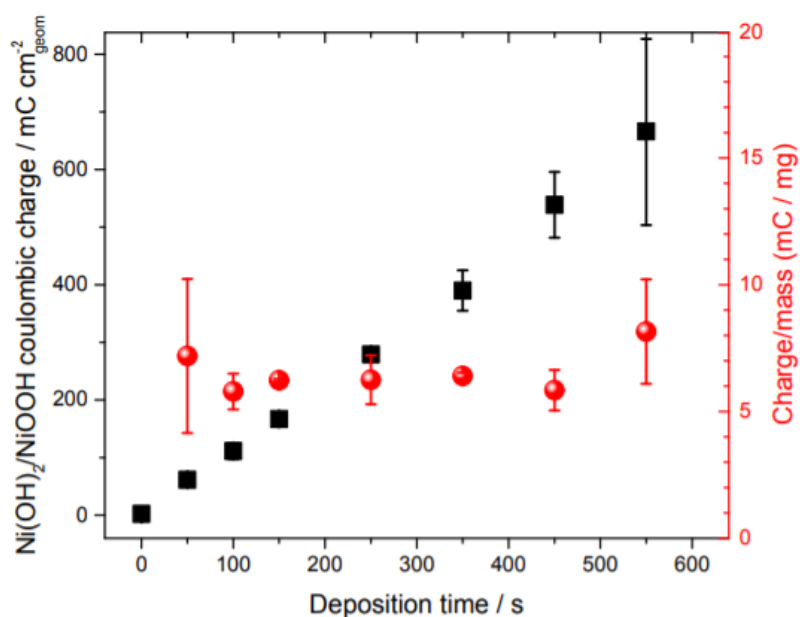
Figure 5.6 Effect of deposition times on the coulombic charge, Q_a, of the redox transition observed at ca 1.41 V, obtained from CV profiles recorded at 50 mV s⁻¹ in 1 M KOH. The y-axis on the right-hand side displays the ratio between Q_a and the mass of the deposits. The fact that the Q_a / mass ratio doesn't vary with the deposition times indicates that the porous structure allows full access of the electrolyte to all the deposited material.
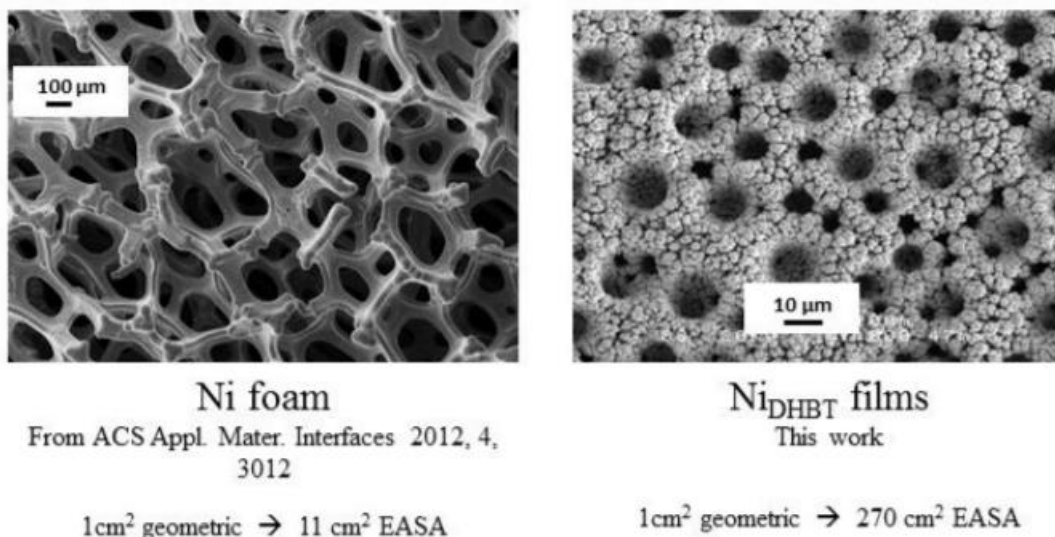
Figure 5.7 SEM micrographs of Ni foam (1mm thick) and NiDHBT film.

On the thinnest Ni DHBT films (T_d = 50 s), the main oxidation peak is centered at *ca.* 1.39 V. It corresponds to the well-known α-$Ni(OH)_2$/γ-NiOOH transition [141], [211]. There is also a shoulder at *ca.* 1.43 V, which is attributed to β-$Ni(OH)_2$/β-NiOOH transition. Both contributions are always observed as the Ni DHBT film thickens (Figure 5.8), but the relative intensity of the β-$Ni(OH)_2$/β-NiOOH transition increases steadily from the thinnest to the thicker films, as can be assessed from the relative intensity at 1.39 and 1.43 V. The position and the relative intensity of both transitions do not vary with the scan rate (not shown). However, for the moment, we do not have an explanation to understand why the ratio between these two components vary with the film thicknesses.
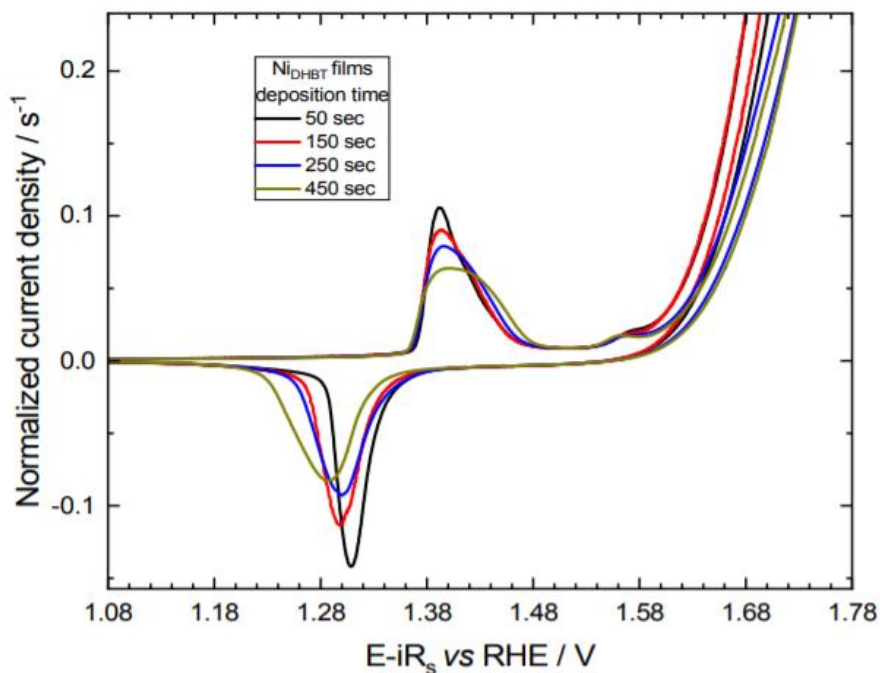
Figure 5.8 Normalized current density vs. electrode potential curve. These curves were obtained following normalization of the CVs shown in Figure 5.5 by the corresponding Q_a values. The unit of the y-axis is thus s^{-1} and the area under the Ni(OH)$_2$/NiOOH redox transition has unit of V s^{-1}. Upon division by the scan rate (5 mV s^{-1}), the area under each Ni(OH)$_2$/NiOOH redox transition is dimensionless and has a value of 1.

All Ni DHBT films exhibit an additional oxidation wave at *ca.*1.56 V, whose intensity increases with thickness. This oxidation wave is attributed to formation of Ni (IV) species, potentially at the edges of γ-Ni(OH)$_2$/γ-NiOOH domains [141], [213]. At more positive potentials (E ≥ 1.60 V), O$_2$ evolution occurred with high current densities, which systematically increased upon increasing Ni DHBT film thickness. For Ni DHBT films of 50 and 450 s, current density values of *ca.*25 mA cm^{-2} were obtained at 1.72 and 1.64 V, respectively. Conversely, at 1.64 V, the OER current density increased by a factor of 5, from 5 to 25 mA cm^{-2}, upon increasing Ni DHBT deposition times from 50 to 450 s.

Galvanostatic experiments (250 mA cm^{-2}) were performed on Ni DHBT electrodes in 1 M KOH. The corresponding results are presented in Figure 5.9A. Stable potentials were obtained for Ni DHBT electrodes right from the beginning of experiments. In contrast, a gradual increase of the potential was observed for bare Ni plates during the first 10 min of electrolysis. For longer electrolysis periods, the OER potential of Ni plates stabilized at 2.05 V. It should be noted that the electrochemical behaviors presented in Figure 5.9A were reproducibly obtained for a minimum of three different Ni electrodes (see Figure 5.10). In Figure 5.9B, the iR-corrected overpotentials

reached after 15 min of electrolysis at +250 mA cm^{-2}, η_{250}, are plotted with respect to the deposition time. There is *ca.* 300 mV difference between η_{250} of Ni plate and the best performing Ni DHBT films. As shown previously, Q_a is directly proportional to the deposition time (Figure 5.6) and can be used as an indirect measure of the electrochemically active surface area. Figure 4.11 shows that E_{250} values of Ni DHBT films scale linearly with Q_a plotted on a semilogarithmic scale, which is the behavior expected if all the material making up the Ni DHBT films is involved in the OER. This suggests that, even at high current density (250 mA cm^{-2}) and for the thicker films, the electrolyte has access to the whole porous structure and that the O$_2$ bubbles do not lead to a decrease of the available Ni catalytic sites.
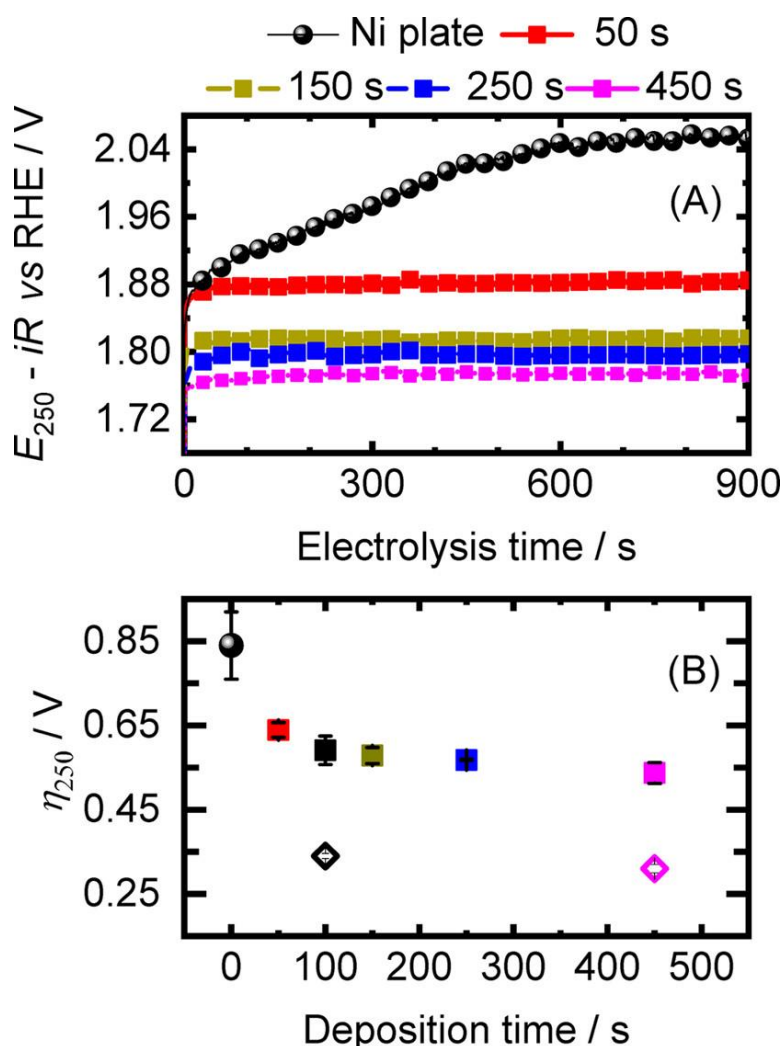
Figure 5.9 (A) Chronopotentiometric curves at +250 mA cm^{-2} in 1 M KOH for Ni DHBT electrodes prepared at different electrodeposition times. (B) Corresponding potential values recorded at t = 900 s. The error bars were obtained from three independent measurements performed on a set of three electrodes prepared in the same conditions (three replicates, see Figure 5.10). The open symbols (◊) are for Ni DHBT electrodes measured in 1 M KOH spiked with 10 ppm of Fe impurities.
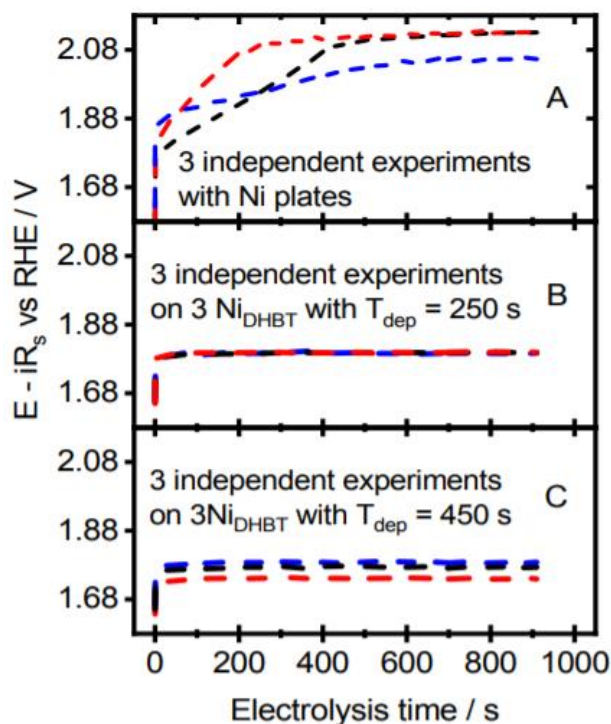
Figure 5.10 Chronopotentiometric curves at +250 mA cm^{-2} in 1 M KOH for different Ni plates and Ni DHBT electrodes; (A) Ni plates, (B) Ni DHBT with T_d = 250 s, and (C) Ni DHBT with T_d = 450 s. The error bars shown in Figure 5.9B were obtained from these measurements.
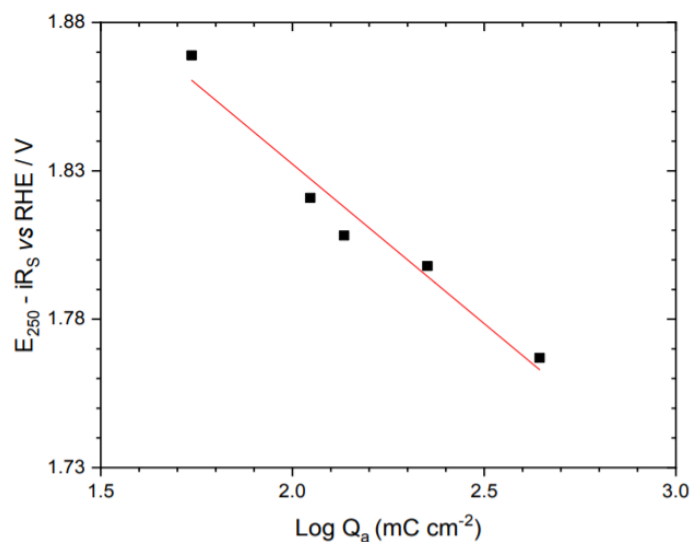
Figure 5.11 Variation of the IRs-corrected electrode potential reached after 15 minutes of electrolysis at +250 mA cm^{-2} with respect to Q_a, the coulombic charge of the Ni(OH)$_2$/NiOOH transition.

According to the seminal work of Boettcher [141] and Corrigan [77], the observation of a redox transition at 1.56 V before the onset for the OER in Figure 5.5 is a clear signature of Ni(OH)$_2$ aged or cycled in a rigorously Fe-free electrolyte. In contrast, the same studies indicate that cycling or aging of Ni(OH)$_2$ in Fe-contaminated KOH

84

solution, even at the ppm level, leads to a huge improvement of the activity for the OER. Accordingly, potential cycling of Ni DHBT electrodes 1 M KOH electrolyte spiked with 10 ppm of $FeCl_2$ was performed. As seen in Figure 5.12A, the onset potential for the OER is shifted negatively by at least 100 mV in the presence of Fe impurities, pointing toward a reduction of the energy barriers of some of the intermediates in the OER process. This occurs even if the charge under the redox peaks centered at *ca.* 1.39 V is hardly changed (although the shape of the oxidation and reduction peaks are slightly modified), suggesting that the surface density of active sites was not changed. The Fe content of these electrodes remains low (0.6%, as determined by EDX analysis). Galvanostatic curves ($j = 250$ mA cm^{-2}) recorded in 1 M KOH spiked with 10 ppm $FeCl_2$ are shown in Figure 5.12B. These potential *vs.* time curves are as stable as they are in the absence of Fe impurities. The two sets of SEM micrographs taken before and after electrolysis are virtually undistinguishable from one another (Figure 5.13), indicating that the electrode structure is morphologically stable even under vigorous O_2 evolution. This is consistent with the CVs of electrodes taken at the beginning and the end of the polarization period being almost superimposed on each other (Figure 5.14).
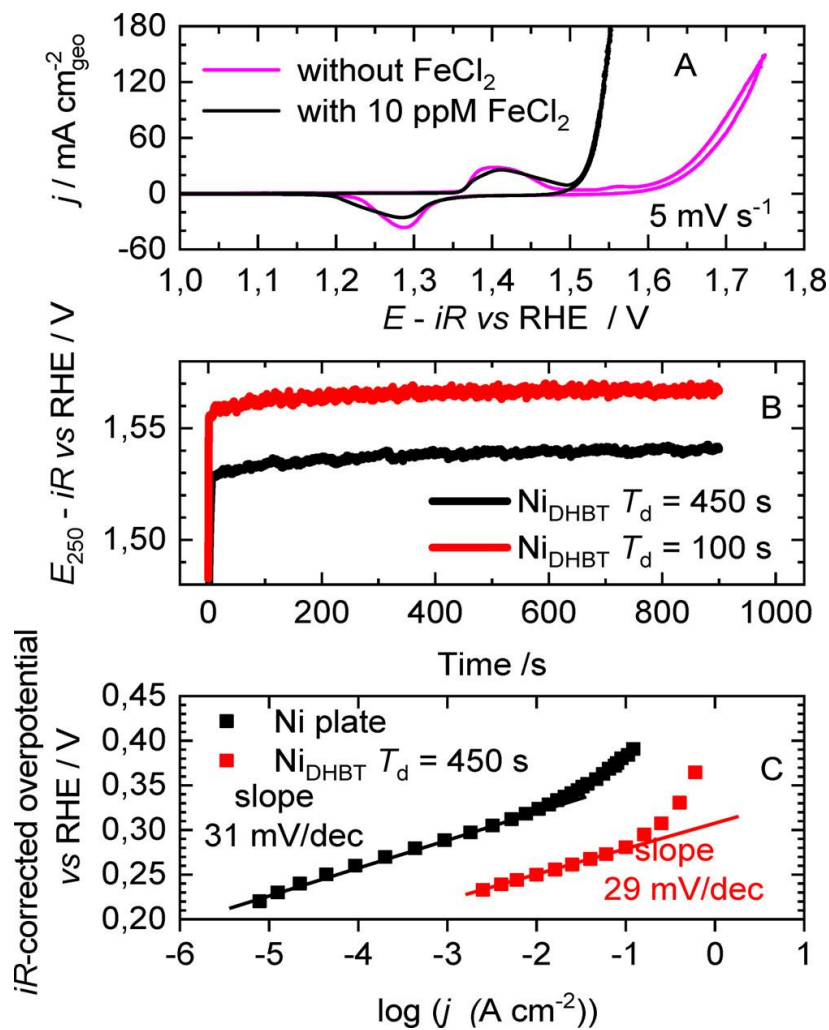
Figure 5.12 (A) Effect of the presence of FeCl$_2$ (10 ppm) on the CVs of Ni DHBT film. (B) Chronopotentiometric curves recorded at +250 mA cm^{-2} in 1 M KOH spiked with FeCl$_2$(10 ppm). (C) Variation of the iR-corrected overpotential vs. the logarithm of the steady-state current density, j. The electrolyte was 1 M KOH spiked with 10 ppm FeCl$_2$. The Tafel slopes are 31 and 29 mV dec^{-1} for Ni plate and Ni DHBT film, respectively.
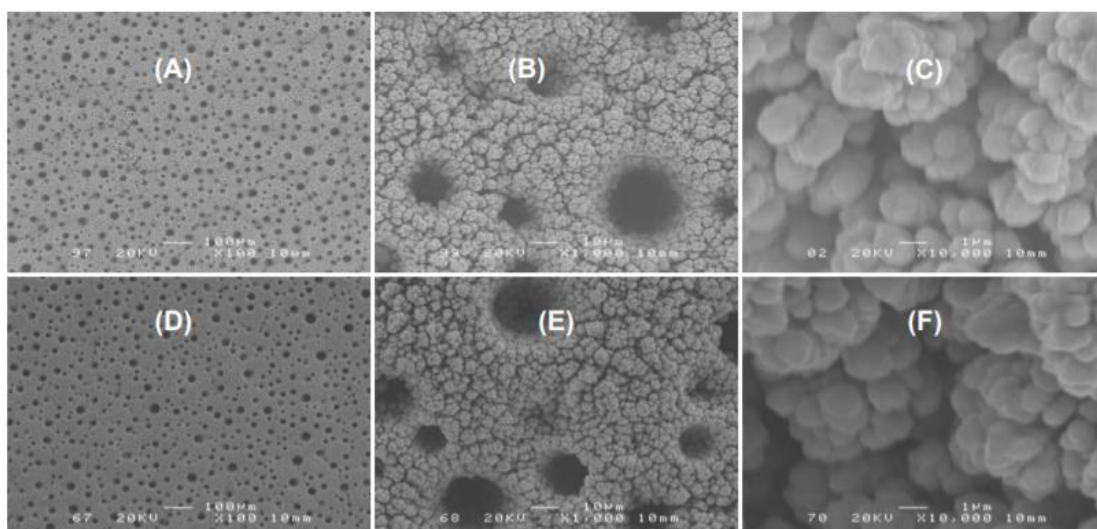
Figure 5.13 SEM images for Ni DHBT films with $T_d = 450$ s prior to (A, B and C) and after (D, E and F) polarization at 250 mA cm^{-2} for 15 min in 1M KOH. No morphological change due to strong O$_2$ gas evolution was observed.
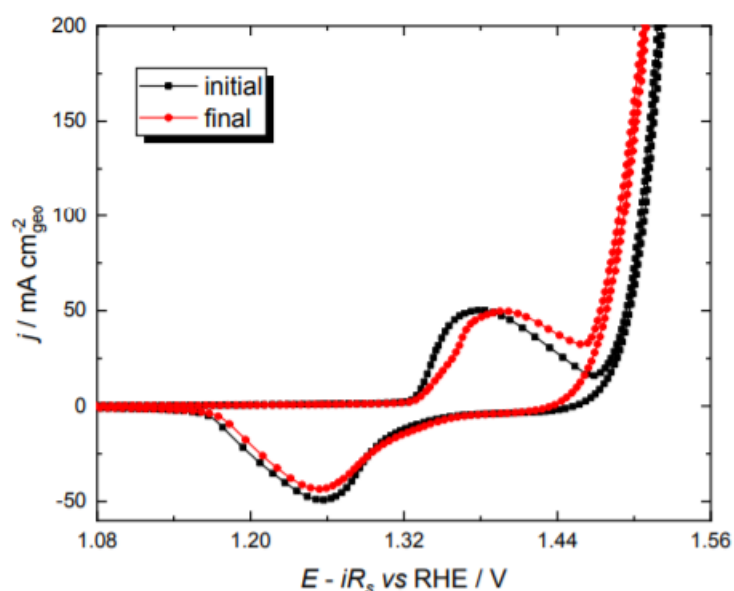
Figure 5.14 CVs of Ni DHBT films with $T_d = 450$ s recorded before and after the data of Figure 5.12C were taken. The electrolyte was 1M KOH spiked with 10 ppm FeCl$_2$ and the CV profiles were recorded at 5 mV s^{-1}. The charge under the redox peaks centered at ca 1.39 V is hardly changed, although the shape of the oxidation and reduction peaks are slightly modified.

Figure 5.12C shows the steady-state iR-corrected potential *vs.* log(j) curves (Tafel plot) on both Ni plate and the best performing Ni DHBT electrode ($T_d = 450$ s) with 10 ppm FeCl$_2$ in the electrolyte. The Tafel slopes are 31 and 29 mV dec^{-1} for Ni plate and Ni DHBT, respectively, which indicates that the mechanisms responsible for the OER are the same on both electrodes. Even if the Ni DHBT films have an EASA that is 270× larger than an Ni plate, Fe impurities are interacting with the Ni sites at this extended

surface in the same way they are with Ni sites distributed on a flat surface. Part of the reason for this behavior might be related to the open structure of Ni DHBT films that is not hampering the diffusion of Fe impurities through the film and their interaction with Ni sites. This assertion is supported by the results of Figure 5.6, showing that the anodic charge, Q_a, of the redox transition at *ca.* 1.41 V scales linearly with T_d (and thus the mass of the film). The data of Figure 5.12C also shows that, in the "Tafel region", there is a factor *ca.* 230× difference of the (apparent) current density between both substrates, very close from the 270× increase of the EASA determined previously. This means that almost all the extended surface area of Ni DHBT film have been modified by Fe impurities and is active for the OER.

In order to clearly correlate the enhanced OER property to the 3D structure of Ni DHBT films, a series of EIS measurements was performed. The impedance spectra of Figure 5.15 show the classic features associated with porous electrodes: a small potential-independent feature at high frequencies whose shape is dependent on pore geometry but is a 45° line for pores of uniform cross section and a low-frequency semicircle reflecting the reaction on the pore walls, with a potential-dependent diameter that is the charge-transfer resistance. The de Levie impedance, Equation 5.6 [131], in series with the solution resistance and an inductor (not shown) to describe high-frequency wiring artifacts gave excellent fits to the data (Figure 5.15).
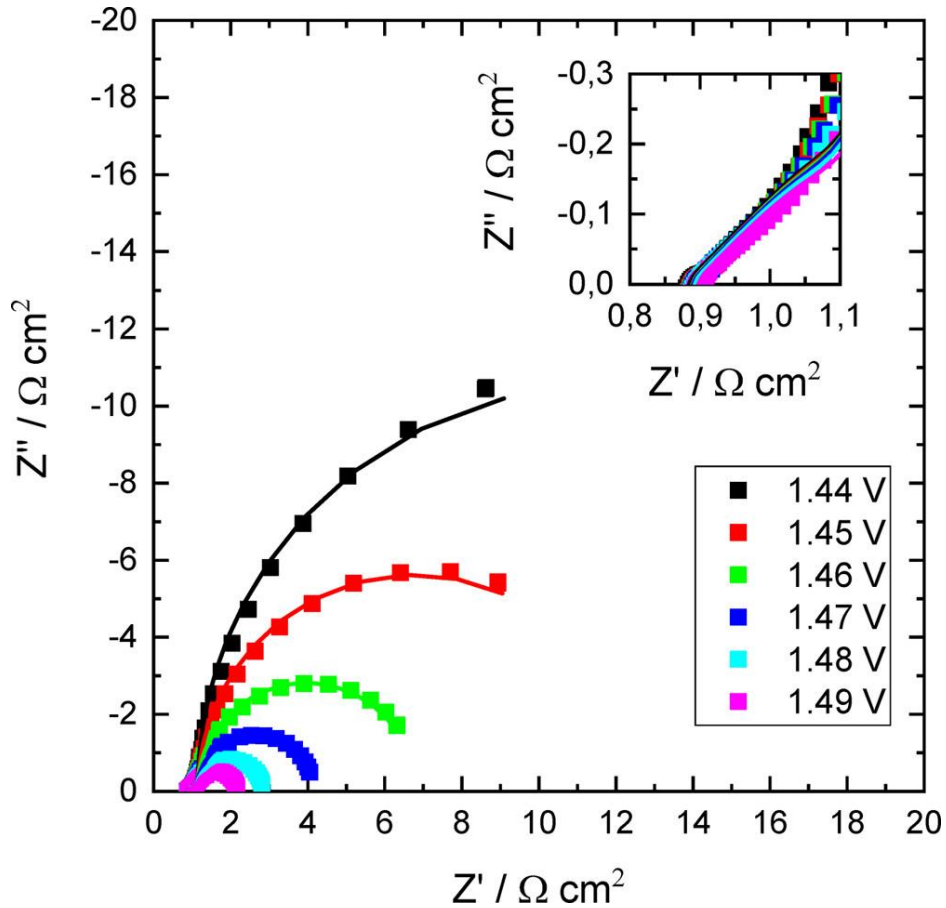
Figure 5.15 Measured (scattered points) and fitted (solid lines) EIS plots on a Ni DHBT film (T_d = 450 s) at different potentials. The electrolyte was 1 M KOH spiked with 10 ppm FeCl$_2$. The high-frequency features are shown in the inset.

Equation 5.6

$$Z = \frac{R_\Omega}{\Lambda^{1/2}} coth(\Lambda^{1/2}) \text{ with } \Lambda = i\omega c_{dl} + \frac{1}{r_{ct}}$$

The parameters c_{dl} and r_{ct} are the double-layer capacitance and charge-transfer resistance on the pore walls combined with some geometric factors. The equation is usually written for a single cylindrical pore, but scaling by the geometric area per pore gives the experimental impedance for all the pores on a geometric area basis. In this case, the total pore wall capacitance and total charge-transfer resistance, which is related to the local pore wall values through the roughness factor, may be extracted from the fitted parameters by

Equation 5.7

$$C_{dl} = c_{dl}/R_\Omega$$

Equation 5.8

$$R_{ct} = r_{ct}R_\Omega$$

Values for these parameters are shown in Table 5.1. The capacitance and charge-transfer resistance values obtained in this way were not significantly different from those found by fitting only the low-frequency semicircle to a parallel C_{dl}–R_{ct} circuit. This is expected since for small values of x, $\coth(x^{1/2})/x^{1/2} \approx 1/3 + x^{-1}$ and $Z_{pore} \approx R_\Omega/3 + (i\omega C_{dl} + 1/R_{ct})^{-1}$.

Table 5.1 Parameters from EIS Fits

iR-corrected potential *vs.* RHE (V)	R_s (Ω cm^2)	c_{dl} (s)	R_Ω (Ω cm^2)	r_{ct}	R_{ct} (Ω cm^2)	C_{dl} (F cm^{-2})
1.439	0.88	0.78	0.81	26.07	21.04	0.97
1.449	0.88	0.75	0.82	13.78	11.24	0.92
1.458	0.88	0.69	0.78	7.24	5.64	0.88
1.466	0.88	0.65	0.75	3.95	2.97	0.87
1.473	0.88	0.64	0.73	2.30	1.68	0.87
1.479	0.89	0.64	0.71	1.46	1.04	0.91

Although the theory is usually written in terms of cylindrical pores, it is easily extended to arrays of pores with uniform cross section down the pore [214], [215], and geometry enters only through the total wall area per geometric area. The same equation has also been derived from a macrohomogeneous model by Paasch *et al.* [216], where the pore geometry is arbitrary but with features small compared to the depth of the porous structure. Candy *et al.* [217] showed experimentally that the impedance is insensitive to the pore geometry and that a pore of stacked spheres gave similar results to cylindrical pores. So, the fact that the measured impedance here closely fits the de Levie equation despite the complex geometry is not surprising.

There are some geometric factors that do lead to departure from this equation. A distribution of pore sizes of the same geometry gives similar results at high frequencies, but a new frequency dispersion arises at low frequencies [218], [219]. On the other hand, nonuniform pores, with significantly different cross sectional areas going down the pore, affect the shape of the high-frequency part of the pore impedance [167]. Neither of these features are seen here. Secondary pores off the primary pore,

or fractal structures, show linear behavior at high frequencies, but with angles much less than 45° [130], [220]. Although the structures here are fractal, this is not reflected in the impedance, perhaps because secondary pores are inactive, which is in line with the value of fs = 0.6 determined previously from the analysis of the contact angle data, or the behavior is dominated by pores with larger cross sections.

Although the de Levie/Paasch derivations of Equation 5.1 assume uniform structures, they neglect the fact that the local interfacial current density going down the pore will not be uniform because the solution potential and hence the local overpotential is changing down the pore. Lasia [191] numerically solved the transmission line differential equations to allow for a change in local overpotential and showed that the discrepancy between the fitted and local charge transfer resistance can be as high as a factor of 2. Accordingly, we sought to correct for this factor. Lasia divided the pores into small sections and used an integration method, and Nguyen and Paasch [221] likewise divided the pore into small sections and used a transfer matrix method. However, here we used a standard differential equation solver, which automatically adjusts the mesh size down the pore to give the required accuracy (see the Experimental Section). Initially we used the fitted R_{ct} and C_{dl} values and assumed that the local current–potential relationship within the pores was the same as the Tafel slope measured at that dc potential. Taking the 1.47 V data as an example (Figure 5.16), the predicted impedance is too high (blue curve), with the (iR-corrected) low-frequency intercept 15% higher than the experimental values, suggesting that the real current–potential relationship within the pores has a 15% lower Tafel slope. Making this change, and leaving the other parameters (R_{Ω} and C_{dl}) constant, gives excellent agreement with the experimental data, both in the Nyquist plot (red curve) and Bode plot (not shown). The simulations show that the reason is that the change in overpotential going down the pore is 1.5 mV. While this seems small, the steep current–potential (Tafel) relationship means that this amounts to a significant change in current density, and consequently, the measured impedance is significantly affected. The effect is less noticeable on the actual Tafel plots, predicting only a 4 mV dec^{-1} change from a smooth surface to the porous material, which is within the variation from sample to sample.
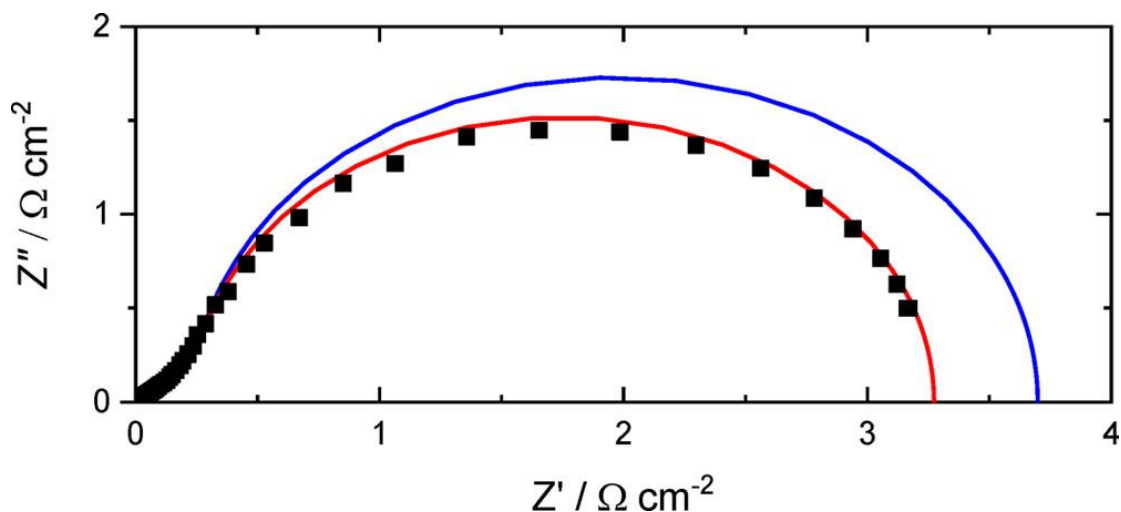
Figure 5.16 Measured EIS plot (scatter points) on a Fe-modified Ni DHBT film (T_d = 450 s) at potential 1.47 V vs. RHE. Solid lines are simulation results of solving Equation 5.1 and 5.2. The blue line assumes the measured Tafel slope at 1.47 V (31 mV dec^{-1}) is valid also within the pores; the red line assumes an adjusted relationship (27 mV dec^{-1}) applies within the pores.

In recent years, activities for the OER were judged by the potential required to oxidize water at a current density of 10 mA cm^{-2}, a metric relevant to solar fuel synthesis [222]. As shown in Figure 5.12C, the overpotential at 10 mA cm^{-2}, η_{10}, of the best Ni DHBT film is 250 mV, which is 70 mV lower than the best performing materials reported in that study that review some of the most promising electrode materials. For applications in electrolyzers, comparison at much larger current density must be made. In presence of 10 ppm FeCl$_2$, η_{250} values as small as 310 mV were reached for the Ni DHBT electrode with Td = 450 s. In comparison, Guo and Li recently reported an OER overpotential at 100 mA cm^{-2}, η_{100}, of 312 mV in 1 M KOH for iron-doped nickel hydroxide prepared at room temperature on Ni foam [223], which is already better than those reported in previous works [224], [225]. However, from the data of Figure 5.12C, this is still 32 mV larger than the overpotential recorded on Ni DHBT at the same current density. Elsewhere, FeCoNi deposited on Ni foam were shown to deliver 75 mA cm^{-2} at an overpotential of 320 mV in 1 M KOH [226], which is 44 mV larger than at Ni DHBT films (η_{75} = 276 mV from Figure 5.12C).

There are several reasons that can explain the performances of Ni DHBT films. There is no doubt that the increased electrochemically active surface area of Ni DHBT films, as compared to Ni plates, is in part responsible for the improved OER performance. As stated previously (Figure 5.11), the electrochemically active surface area of Ni DHBT films is fully accessible to the electrolyte and participates in the O$_2$ evolution reaction. However, this measure of the active area was performed in a potential region where no gas evolution is occurring. Owing to the porous structure of Ni DHBT films,

one could have expected that, at more positive potential in the OER region, O_2 bubbles could increase the electrolyte resistance and/or be responsible for occlusion of some of the pores. However, this is not what is observed, and the EIS data of Table 5.1 shows that the double layer capacitance is constant in the potential region where the 29 mV dec^{-1} Tafel slope is observed. This indicates that occlusion of Ni active sites by O_2 bubbles is not a limiting factor.

It is undeniable that the low Tafel slope (29 mV dec^{-1}) is a major factor contributing to the performance of the Ni DHBT films. On Ni DHBT films, the 29 mV dec^{-1} Tafel slope is observed over a range of current densities that far exceed that of Ni plate. Indeed, the "low Tafel slope region" extends up to 100 mA cm^{-1} on Ni DHBT films while it is limited to 5 mA cm^{-2} on Ni plate. This striking difference is partly responsible for the increased performance of the Ni DHBT films and must be related to their different morphologies.

As described in the introduction, recent reports have shown that the morphology of the electrodes has an impact on the adhesion force of gas bubbles to the surface and the detachment diameter of the same gas bubbles upon release. Indeed, both the adhesion force and the detachment diameter of gas bubbles are diminished through nanostructuring of the electrode surface [150], [227]. According to what is referred to in the literature as the Fritz correlation, there is a linear relationship between the gas bubble detachment diameter from a surface and its water contact angle [228]. As mentioned earlier, the water contact angle decreases from 60° to less than 25° as a result of the fractal geometry of the Ni DHBT electrode. Enhanced air bubble contact angle, which is a direct consequence of increased hydrophilicity, translates into smaller bubble adhesive forces on the electrode surface (and smaller residency time), along with smaller radius of the contact plane between air bubble and the electrode surface (and thus larger contact area between the electrolyte and the electrode active sites). The significant decrease of the adhesion force and detachment diameter of gas bubbles resulting from nanostructuring of the electrode will need to be confirmed by independent measurements but this could also help understand the morphological stability of Ni DHBT films under vigorous oxygen evolving conditions.

We have succeeded in developing a robust and mechanically stable electrode made of a cheap and sustainable material. These Ni DHBT films are wetted by the electrolyte ($f_s = 0.6$), translating in very large electrochemically active surface area. They also exhibit a superaerophobic character responsible for small air bubble contact angle and small air bubble adhesive force, both factors further contributing to maximize the

surface area contact between the active sites of the electrolyte and the electrolyte even in conditions where strong O_2 evolution is occurring. This translates into a small overpotential even in conditions where vigorous oxygen evolution is occurring. On this matter, it is worth remembering that Ni DHBT films are prepared by electrodeposition in conditions where hydrogen evolution occurs concomitantly with Ni metal deposition. As mentioned earlier, the faradaic efficiency for Ni deposition is close to 30%, which means that a large fraction of the current is used to generate hydrogen gas that escapes the electrode in the form of gas bubbles. The implication of this is that, right from their formation, Ni DHBT films are templated in such a way that gas bubbles can freely escape the growing film without causing any damage to its structure. The existence of several paths through which gas bubbles can escape without causing damage to the film might also have proven to be a critical factor in the stability of the Ni DHBT films. From a broader viewpoint, such gas bubble-architectured materials represent an attractive design of active and stable catalysts for other gas evolving electrochemical reactions.

5.5   Conclusions

It was shown that dynamic hydrogen bubble templating could be used to prepare Ni DHBT films with a fractal structure, which exhibit improved OER properties compared to Ni plate. The best performing Ni DHBT films are highly porous and have an electrochemically accessible surface area increased by a factor of 270 as compared to the underlying Ni plate. They are mechanically robust and do not degrade under vigorous oxygen evolution. In presence of 10 ppm $FeCl_2$, OER overpotential at 250 mA cm^{-2} is only 310 mV. This is due to both the porous nature of the deposit and the superaerophobic nature of the fractal Ni films, which leads to an increase of the contact angle of a trapped air bubble and a significant decrease of the adhesion force of O_2 gas bubbles. Industrial applications of these Ni DHBT templates could be envisioned depending on the availability of suitable pieces of equipment for dynamic hydrogen bubble templating on substrates with larger geometrical surface area. Investigations are planned for scaling the additive manufacturing of fractal Ni-based coatings for use in advanced electrolysis cell configurations, to further examine transport enhancement in relevant industrial systems and its tolerance to commercially relevant alkaline solutions.

6 THE ROLE OF IR DECORATION IN ACTIVATING MULTI-SCALE FRACTAL SURFACE IN POROUS NI DBHT FOR THE OER

6.1 Abstract

Interfacial engineering of electrocatalysts is a pivotal approach for promoting the energy conversion efficiency of water electrolysis systems. Anchoring clusters or even a single atom of a foreign element on the surface of a substrate, usually 3D structured, can intrinsically alter the substrate's local electronic structure leading to superior electrocatalytic activity. Herein, we report a simple method to decorate a 3D fractal Ni electrode with Ir atoms via a galvanic replacement reaction. The resulting electrode has a very low Ir loading of 1.6 μmol cm^{-2}. Iridium atoms are present as 4.3 nm diameter nanoclusters at the electrode surface. The activity for the OER of 3D fractal Ni electrode was improved by decoration with Ir, resulting in an overpotential of 195 mV at 10 mA cm^{-2} and a Tafel slope of 44 mV dec^{-1}. Apart from increasing the intrinsic electrocatalytic activity for the OER because of the presence of more active iridium atom, the galvanic exchange reaction results also in a factor of 8-10 increase of the electrochemically active surface area due to the creation/activation of a secondary pore structure that contribute to the better electrocatalytic performance of the resulting electrode. Finally, using *operando* acoustic emission, it is demonstrated that the presence of nanoclusters of iridium reduces the O_2 bubble size formed during the OER, causing a less drastic decrease of the electrochemically active surface area resulting from the blocking effect of O_2 bubbles. All these three effects concur to improve the OER performance of 3D fractal Ni electrode.

6.2 Introduction

A power-to-gas (P2G) system is composed of a series of technologies that convert instantaneous energies, such as renewable energy or the surplus energy in power grids, into stable gas fuel [229]. Such system offers a promising prospect to solving the energy crisis that human society is facing. Water electrolysis is a core component of the whole P2G conversion system. Water electrolysis involves two gas evolution reactions: the hydrogen evolution reaction (HER) and the oxygen evolution reaction (OER). Due to the sluggishness of the OER kinetics limiting the overall efficiency of water electrolysis, improvement of the existing OER electrocatalysts is required.

Currently, the state-of-the-art electrocatalysts for the OER in acidic solutions are IrO_2 and RuO_2 [230]–[233]. However, their loadings should be minimized in order to find

application in large-scale commercial devices because of their low abundance and high cost. The recent progress in developing Ni-based material as alternative electrocatalysts for the OER have shown that Ni-based materials, such as NiFe layered double hydroxides (LDHs), NiS_x, Ni_xP_y, and $NiSe_x$ have good performance in alkaline water electrolysis [234]. The Ni-based electrocatalysts used for the OER in alkaline electrolyte have the merits of low cost and long-term stability. However, their electrocatalytic activity towards the OER still needs to be improved to achieve performance comparable with that of noble metal-based electrocatalysts.

Recently, there has been a resurgence in the study of bimetal and multi-metal electrocatalysts for the OER. Enormous efforts have been devoted to incorporating minimal amounts of noble metal into transition metal (Ni, Fe, or Co) supports to improve the electrocatalytic activity. Through interfacial engineering, the surface chemical composition and electronic structure of materials can be tuned to specific forms that favor the OER [85]. By this means, the intrinsic activities of electrocatalysts can be greatly promoted. For instance, Feng *et al.* reported that IrCoNi porous hollow nanocrystals have an overpotential of 303 mV for the OER at 10 mA cm^{-2} [86]; Li *et al.* synthesized $Co_xNi_{1-x}O$ nanowire arrays with as low as 0.57 wt.% of Ir atoms incorporated in the structure, exhibiting an overpotential of 260 mV for the OER at 10 mA cm^{-2} [87]; and the Ir doped NiV layered double hydroxides reported by Li *et al.* exhibited excellent catalytic properties with an OER overpotential of 203 mV at 10 mA cm^{-2} [88].

More recently, single-atom catalysts (SACs) have drawn more and more attention [89], [235]. SACs are defined as atomically dispersed metal atoms (usually noble metal atoms) anchored on supports such as metals, metal oxides, or layered double hydroxides. SACs optimize the utilization of the active species and the formation of synergetic coupling between the anchored atoms and the underneath support, which would play an important role in improving the electrocatalyst activity. For example, with a 0.45 wt.% ruthenium loading on CoFe layered double hydroxides, the electrocatalyst can achieve an overpotential of 198 mV for the OER at 10 mA cm^{-2} and a small Tafel slope of 39 mV dec^{-1} [91]. An overpotential as low as 200 mV at 10 mA cm^{-2} for the OER can be achieved by atomically dispersed Ir (1.3 wt. %) on NiFe/Ni core−shell nanowires [92]. Zhang *et al.* demonstrated that Au decoration (0.4 wt.%) can cause charge redistribution of active sites in NiFe layered double hydroxides and results in a 6-fold OER activity enhancement [93].

Most of the heterogeneous electrocatalysts synthesized through interfacial engineering approaches have a 3D porous structure as support. Various artificially created forms such as foams, nanowires, and nanoparticles can increase the roughness and porosity of electrodes and thus increase the exposure of active sites of electrocatalysts. This strategy can maximize catalyst utilization of materials, leading to improvement in the apparent performance of the electrocatalyst. However, this strategy should meet its limit when the resultant increase in the structures' roughness impedes the mass transport of reactant and/or products [236]. This limitation would be even more complicated in water electrolysis since bubbles are generated on the electrode surface during both the OER and the HER. Dynamic bubble occupation on the electrode surface or even in the internal structure of a 3D porous electrode would significantly reduce the accessibility of active sites, increase overpotentials of reactions, and cause undesirable energy losses [237], [238]. In this context, hydrophilic electrodes seem an ideal solution to counteract the bubble occupation of catalytically active sites. Hydrophilic surface of catalyst could achieve fast release of gas bubbles and reduce the bubble departure size. Thus, a variety of attempts have been made to realize gas management by altering the wettability of electrodes and this approach has gained more and more research attention in electrocatalyst design.

Most studies about the wettability of porous electrodes for the OER focus on measuring the contact angle of the electrodes under static conditions and recording the bubble departure sizes. A low contact angle is associated with a high hydrophilicity, and that property reduces the bubble departure size and bubble coverage. This direct correlation between hydrophilicity and bubble coverage holds only for the topmost plane of an electrode in the ideal Wenzel wetting state. However, as gas evolution is a dynamic process, the alternate gas/liquid wetting of any phase takes place on the utmost external plane of the electrode and in the internal space of a 3D structured electrode. Metastable Cassie wetting state, hemi-wicking state, or mixed wetting state [109], [111], [113], [239], in which gas is trapped in the internal pores of an electrode, are often observed for gas evolution reactions. This is especially true for reactions occurring at high current densities and in electrocatalysts with tortuous pores or in the gas diffusion layers during PEM or AEM water electrolysis [114], [240]. In fact, the wetting condition in a 3D porous electrode is heterogeneous, and depends on the surface energy (intrinsic contact angle) of the material and the local topology of the electrode [241]. The shift of the wetting state (or dynamic wetting) should be taken into consideration when assessing bubble coverage. Hence, the study of dynamic wetting in porous electrocatalysts must rely on *in-operando* techniques. However, direct

visualization of bubble saturation within porous electrodes by computed tomography or by an optical camera are challenging to realize [102], [239], [242]. In comparison, acoustic emission (AE) detection is an easy, cost-effective, and non-deconstructive testing (NDT) technique [243].

In an aqueous environment, volume pulsation of a gas bubble caused by bubble formation, detachment from a rigid wall, coalescence, or splitting will produce a decaying sinusoidal pulse of sound. This sound wave can propagate through liquid or solid media and be readily detected by a hydrophone immersed in the liquid or an AE sensor attached on the boundary of the reservoir. Using the Minnaert equation [133], the bubble's diameter can be extracted from the frequency of the sound wave. Using AE, it is then possible to monitor bubble sizes during the OER, and to further assess the wetting conditions in heterogeneous OER electrocatalysts.

In this article, Ir decoration was applied on a porous Ni electrode with a 3D hierarchical structure. The Ir decoration enhances both the intrinsic activity of the Ni electrode for the OER and also improves the dynamic wetting conditions in the internal structure of the electrode. The reasons underlying both phenomena were revealed by diverse physical and electrochemical characterizations, as well as *in-operando* AE characterization.

6.3   Experimental section

6.3.1   Preparation of Ni DHBT electrode and its modification by Ir

A Ni rod (Sigma-Aldrich, 99.99%) was inserted into a custom-built electrochemical cell and was used as the substrate for the electrodeposition of a porous Ni film. Only the circular base (0.32 cm2) was exposed to the electrolyte. The porous Ni films were prepared through the dynamic hydrogen bubble templating (DHBT) method reported in [110]. Deposition was performed for 450 s at -2 A cm^{-2} in a 0.1 M NiCl$_2$·6H$_2$O + 2 M NH$_4$Cl electrolyte. Then, samples were thoroughly rinsed with deionized water (Millipore Milli-Q, resistivity 18.2 MΩ cm). They will be denoted as Ni DHBT films in the following sections. Some of the samples were subsequently immersed in 0.01 M HCl or 0.001 M K$_2$IrCl$_6$ + 0.01 M HCl solution for up to 20 hours. These later samples were denoted as Ir/Ni DHBT.

6.3.2   Dissolution of Ni in acid solution traced by inductively coupled plasma atomic emission spectroscopy

The amount of Ni and Ir in the electrolyte solution (100 mL) was determined by inductively coupled plasma (ICP) spectroscopy (lateral-view ARCOS, SPECTRO

Analytical Instruments, Kleve, Germany). For these measurements, Ni plates (Alfa Aesar, Puratronic 99.9945% metal basis) of 1 cm^2 were used as substrates. The procedure described above was followed for the preparation of Ni/DHBT and Ir/Ni DHBT films. The concentrations of Ni and Ir in the electrolyte following immersion for 0 to 21 hours were measured by external calibration with at least 5 standard solutions prepared in 0.01 M HCl, along with internal standardization using an argon emission line (at 404.442 nm). All calibration curves were linear, with an R2 value of >0.9999.

6.3.3 Physical Characterization of Ir/Ni DHBT

The surface morphology of Ni DHBT and Ir/Ni DHBT films were probed by scanning electron microscopy (SEMs) using a VEGA3 TESCAN SEM and a FEI Magellan ultrahigh-resolution SEM operated between 1 keV to 2 keV incident energy for imaging. Energy dispersive X-ray (EDX) mapping was performed to assess the film compositions. X-ray diffraction (XRD) patterns were obtained using a Bruker D8 Advance X-ray diffractometer with a weighted average Cu Kα1 and Cu Kα2 radiation at 1.5418 Å. The data were collected in the 2θ range from 30° to 95°, the step size was 0.02 degrees, and the counting time was 2 seconds per step.

6.3.4 Electrochemical characterizations

Electrochemical measurements were carried out in a custom-built electrochemical cell with a Pt mesh (Alfa Aesar, 99.9%) as the counter electrode and a saturated calomel electrode (SCE) as the reference electrode. The potentials were converted relative to the reversible hydrogen electrode (RHE) following the equation $E_{RHE} = E_{SCE} + 0.242$ V $+ 0.059V \times$ pH. Most electrochemical measurements were performed in 1M KOH electrolyte (pH = 13.5) prepared with deionized water (Millipore Milli-Q, resistivity 18.2 MΩ cm) and KOH (Sigma-Aldrich, 99.99% trace metals basis).

A Solartron 1480 potentiostat was used for the electrochemical measurements, and a Solartron 1255B frequency analyzer was used for the electrochemical impedance spectroscopy (EIS) measurements. For each measurement, the uncompensated resistance, Ru, was determined at open circuit potential (OCP) by taking the high frequency intercept of the Nyquist plot measured between 0.01Hz and 200kHz.

Prior to cyclic voltammetry (CV) measurements, all samples were immersed at OCP in 1M KOH electrolyte for 15 min. Then, CV scans at a scan rate of 50 mV s^{-1} were recorded between −0.1 to 1.5 V *vs.* RHE until stable CVs were obtained. Stable CVs were obtained after 50 cycles. All CVs shown in this study were recorded at 5 mV s^{-1} after the above-described procedure was applied.

Electrochemical Impedance Spectroscopy (EIS) measurements between 0.01 Hz and 200 kHz with 10 mV amplitude were conducted after a constant potential was applied to the electrode during 5 min. These conditions were sufficient for the electrode to reach a steady state current. The electrode potential was varied from 1.44 to 1.49 V in the regime of the OER.

Electrochemical impedance data were fitted using a transmission line model (TLM) and the de Levie Equation [244] (Equation 6.1). The complex nonlinear least squares (CNLS) fitting program of Matlab® was used.

Equation 6.1

$$Z = R_u + \frac{R_\Omega}{\Lambda^{1/2}} coth(\Lambda^{1/2}) \text{ with } \Lambda = i\omega c_{dl} + \frac{1}{r_{ct}}$$

where cdl and r_{ct} are the double-layer capacitance and charge-transfer resistance on the pore walls, respectively, R_Ω is the total solution resistance (Ω cm^2) within the pores, and R_u is the uncompensated resistance.

6.3.5 Acoustic Emission tests during OER

Acoustic emission measurements were conducted in a custom-built three-electrode electrochemical cell, using a piezoelectric sensor (R6A, Mistras) and a detecting system (1283 USB AE Node, Mistras). A cylindrical Ni rod was used as substrate. Ni DHBT and Ir/Ni DHBT coatings were deposited on one side of the Ni rod. On the other side, the AE sensor was connected. The AE sensor was not in contact with the electrolyte. The center of the AE sensor and the working electrode were aligned on a common axis. Silicon grease and Kapton tape are applied between the Ni rod and the AE sensor to minimize the air gap and electrically isolated them from one another. Positive current varying from 0.3 mA cm^{-2} to 6.6 mA cm^{-2} were applied on the working electrode to generate O_2 bubbles. During the OER, pulsed AE signals with an amplitude larger than 28 dB were recorded and counted as discrete AE events. Data processing of the AE events were conducted using the AEwin software (Mistras). For each AE event, the peak frequency was determined by Fourier transform in AEwin.

6.3.6 Surface Characterization by XPS

X-ray photoelectron spectroscopy (XPS) measurements were performed using a VG Escalab 220i-XL instrument equipped with an Al Kα source. Freshly prepared Ni and Ir/Ni DHBT films were introduced into the XPS vacuum chamber for drying overnight right after they were prepared. Also, some deposits were analyzed after their electrochemical characterization. The same procedure was followed. These samples

are denoted post-EC Ni DHBT and post-EC Ir/Ni DHBT. Data fitting was performed with the CasaXPS software using Shirley background subtractions. For surface charging correction, the C 1s peak at 284.8eV was used as a reference.

6.4 Results and discussions

6.4.1 Physical-chemical characterization

The mechanisms responsible for the spontaneous deposition of Ir on Ni substrate was previously studied [245], [246]. In an acidic electrolyte, dissolution of metallic Ni occurs according to Equation 6.2 and Equation 6.3. Metallic Ir deposition occurs according to Equation 6.3.

Equation 6.2

$$2H^+ + Ni \rightleftarrows H_2 + Ni^{2+}$$

Equation 6.3

$$[IrCl_6]^{2-} + 2Ni \rightleftarrows Ir + 2Ni^{2+} + 6Cl^-$$
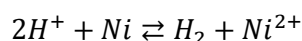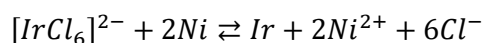
The concentration of Ni and Ir in solution was measured as a function of the immersion time (Figure 6.1) for Ni DHBT films immersed in 0.01 M HCl and 0.001 M K_2IrCl_6 + 0.01 M HCl. In both cases, the Ni concentration increases linearly with immersion time, indicating that Ni is dissolved. In HCl only, Equation 6.2 governs the reaction, and the dissolution rate of Ni is 3.80 ppm h^{-1} cm^{-2} (6.5×10^{-8} mol ml^{-1} h^{-1} cm^{-2}). In the presence of K_2IrCl_6, reaction in Equation 6.3 also occurs, and the dissolution rate of Ni increases to 4.49 ppm h^{-1} cm^{-2} (7.7×10^{-8} mol ml^{-1} h^{-1} cm^{-2}). This is a difference of 1.2×10^{-8} mol ml^{-1} h^{-1} cm^{-2} of Ni. At the same time, the Ir concentration in the electrolyte decreases slowly, at a rate of 1.6 ppm h^{-1} cm^{-2} or 0.8×10^{-8} mol ml^{-1} h^{-1} cm^{-2}. The presence of Ir^{+4} in solution should increase the Ni dissolution rate by 1.6×10^{-8} mol ml^{-1} h^{-1} cm^{-2} if both reactions in Equation 6.2 and Equation 6.3 are occurring simultaneously. Instead, the dissolution rate of Ni is only increases by 1.2×10^{-8} mol ml^{-1} h^{-1} cm^{-2}. This indicates that both reactions in in Equation 6.2 and Equation 6.3 are not occurring simultaneously, most probably because they are competing for the same Ni sites at the electrode surface.
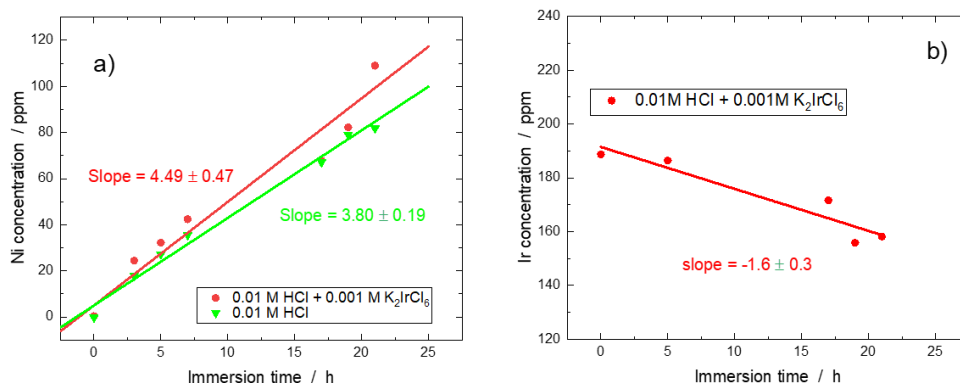
Figure 6.1 Variation of the concentrations of a) Ni and b) Ir in solution upon immersion of Ni DHBT films.

Three-dimensional porous Ni DHBT films were electrodeposited on flat Ni substrates. Figure 6.2 shows that Ni DHBT films have an interconnected cauliflower-like structure with pore diameters varying between 10 and 30 µm. This unique structure results from simultaneous Ni electrodeposition and hydrogen bubble formation and release occurring at large negative potential, typically between -4 V *vs.* RHE, applied to reach a deposition current of -2 A cm^{-2}.
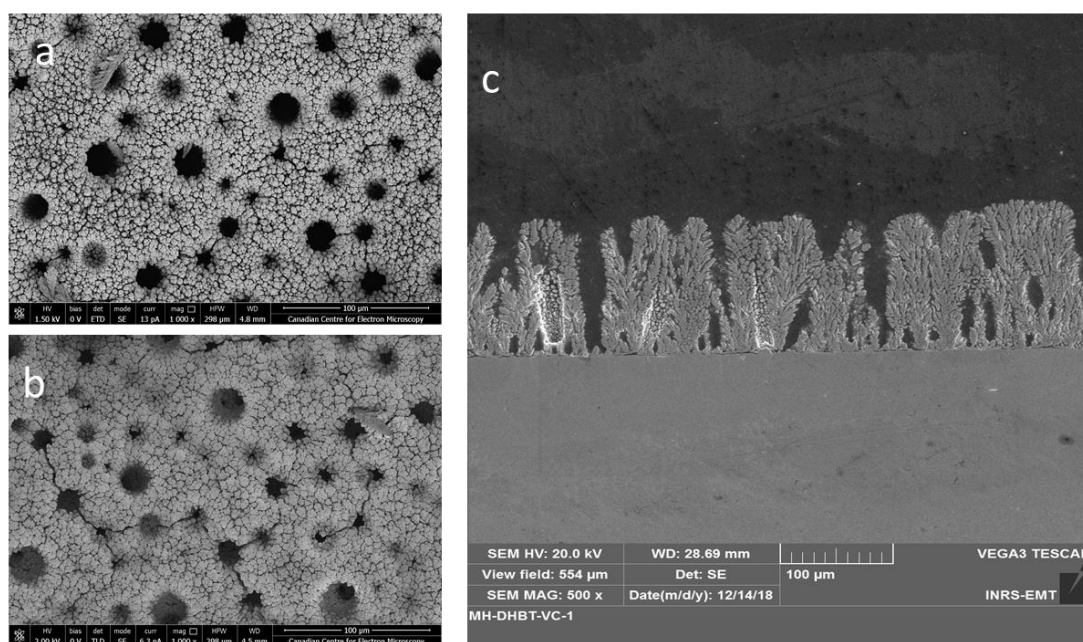
Figure 6.2 SEM image of a) Ni DHBT surface; b) Ir/Ni DHBT surface; c) of Ni DHBT cross-section.

High-resolution SEM was used to probe the internal structure of the films. It is seen that Ni DHBT films are made of granular Ni covered by flake-like nanosheets (Figure 6.3a). Ir decoration of Ni DHBT films (Ir/Ni DHBT) was performed by immersing freshly prepared Ni/DHBT electrodes in a 0.001 M K$_2$IrCl$_6$ + 0.01 M HCl precursor solution. The morphology of a Ir/Ni DHBT film after 17 h of immersion is shown in Figure 6.3b

and Figure 6.3b. No change in the morphology of the films was observed compared to pristine Ni DHBT films. For comparison, a freshly prepared Ni DHBT film was immersed for 17h in a 0.01 M HCl solution (without K_2IrCl_6), hereafter denoted as corroded Ni DHBT. Again, no change of morphology was seen (Figure 6.3c). The Ir / Ir + Ni atomic ratio after 17 h of immersion, as determined from EDX analysis, was 0.3 %.
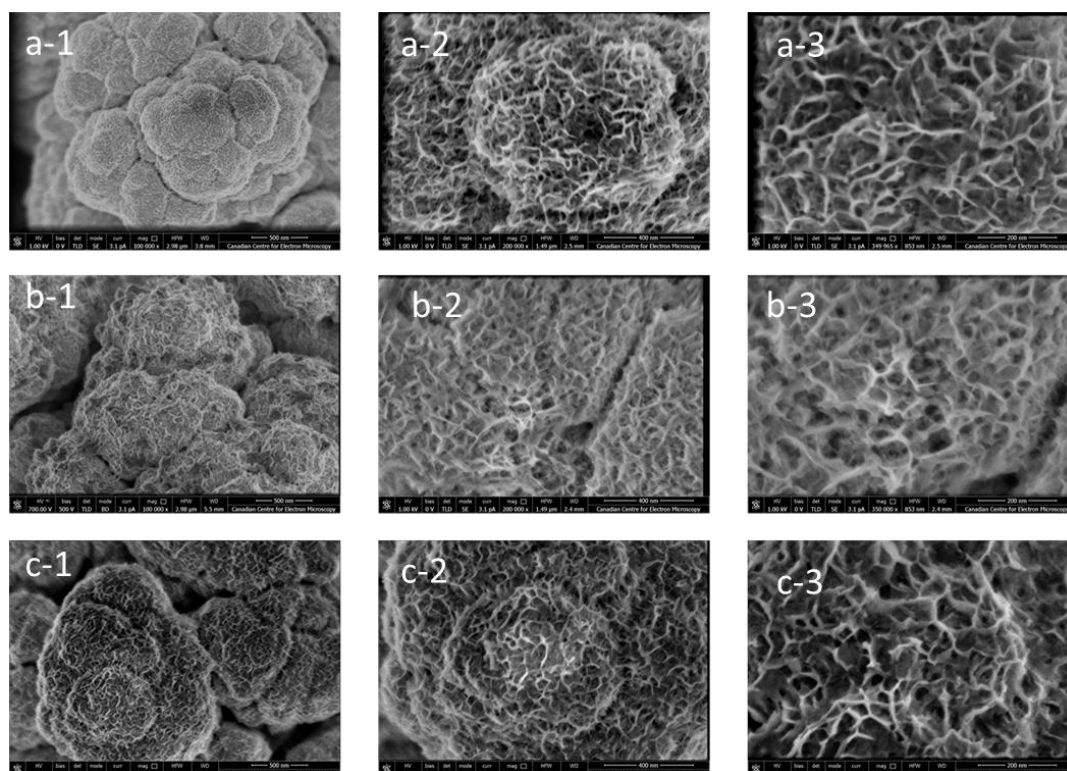
Figure 6.3 High resolution SEM images of a) Ni DHBT, b) Ir/Ni DHBT and c) corroded Ni DHBT at different magnifications.

XPS measurements were conducted right after Ni DHBT and Ir/Ni DHBT coatings were prepared. Figure 6.4a shows the Ni 2p core levels of both electrodes. For as-prepared Ni DHBT, peaks are observed at 852.8eV and 870.1eV that are assigned to metallic Ni 2p3/2 and Ni 2p1/2 core levels, respectively [247]. Ni 2p3/2 and Ni 2p1/2 core level peaks are seen also at 856.4 and 874.1 eV, which are assigned to Ni hydroxide or Ni oxyhydroxide. The 3p core level peaks of metallic Ni and Ni hydroxide or Ni oxyhydroxide are observed at 66.3 and 68.0 eV, respectively [248]. In the case of Ir/Ni DHBT, Ir 4f7/2 and Ir 4f5/2 core level peaks are observed at 60.4 and 63.5 eV, respectively. They are assigned to metallic iridium [249], which is consistent with Equation 6.3 describing the mechanisms underlying the galvanic reaction. Following immersion in the Ir containing solution, there is almost no metallic Ni left at the surface. From the XPS data, the Ir / Ir + Ni surface atomic ratio is 5.3 %, much larger than the

one determined from EDX measurements which are more bulk sensitive. This reflects the fact that Ir atoms are located at the electrode surface.
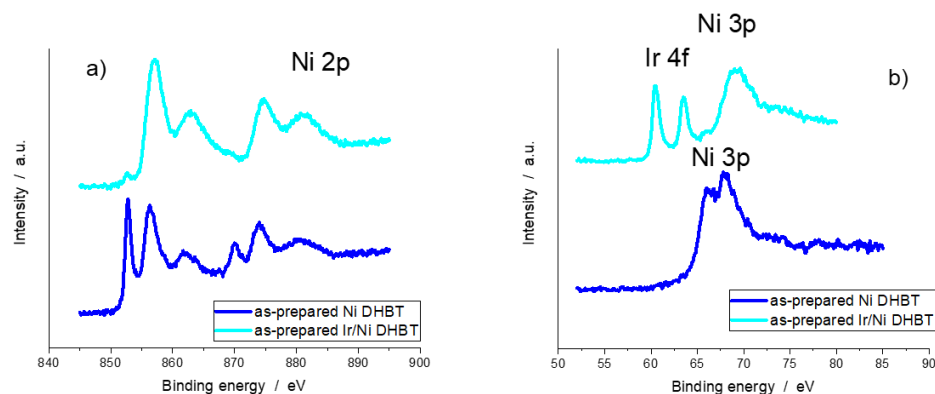
Figure 6.4 XPS for freshly prepared Ni DHBT film and Ir/Ni DHBT film: a) Ni 2p core level and b) Ir 4f and Ni 3p core levels.

The X-ray diffraction of Ni and Ir/Ni DHBT film were identical (Figure 6.5). This suggests that the bulk of both Ni DHBT and Ir/Ni DHBT films is composed only of polycrystalline Ni, and that metallic Ir decoration is occurring only at the surface. Most probably, the amount of Ir atoms at the electrode surface is too small to be detected by XRD performed in the Bragg-Brentano geometry.
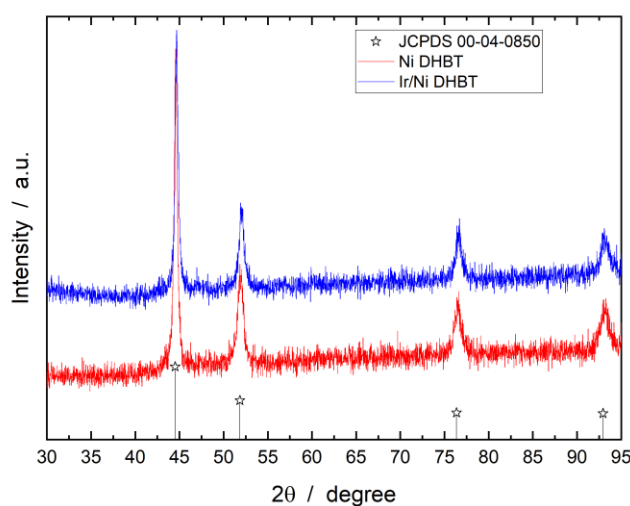
Figure 6.5 XRD patterns of Ni DHBT and Ir/Ni DHBT films. The stars indicate the reference pattern of Ni taken from the JCPDS card 00-04-0850.

6.4.2 Electrochemical characterization

Steady-state CVs of Ni, Ir/Ni DHBT and corroded Ni DHBT films recorded in 1M KOH at 5 mV s^{-1} are shown in Figure 6.6a-b. On Ni DHBT, no peaks were observed between

-0.1V and 0.3 V. Redox peaks in that potential region are associated with the reversible Ni/α-Ni(OH)$_2$ transition. These peaks are no longer observed once α-Ni(OH)$_2$ is converted to β-Ni(OH)$_2$. This last transition occurs at potential more positive than *ca.* 0.5 V [153], [250]. Steady-state CVs shown in Figure 6.6 were recorded after a series of CVs performed between −0.10 to 1.5 V *vs.* RHE, in a potential region where α-Ni(OH)$_2$ was irreversibly converted to β-Ni(OH)$_2$. Therefore, the redox peaks associated with the reversible Ni/α-Ni(OH)$_2$ transition were not expected.
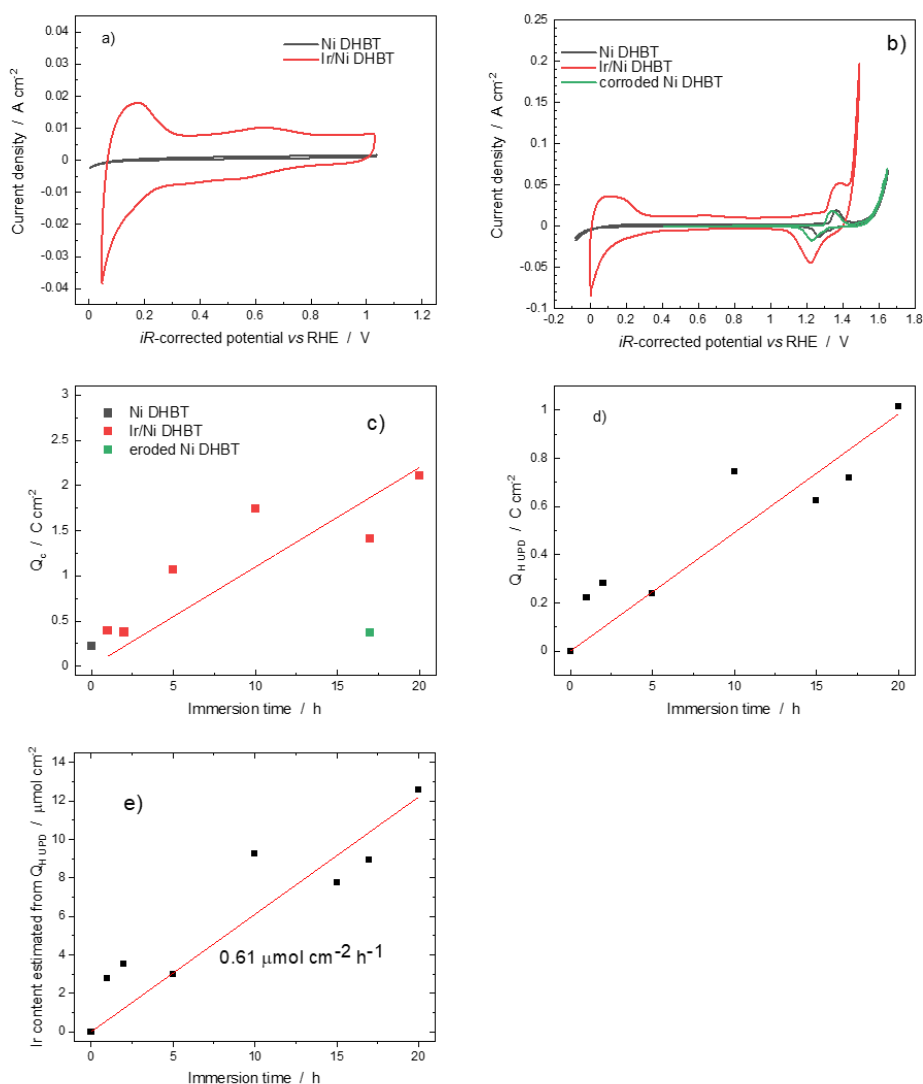
Figure 6.6 In a) and b), CVs of Ni, Ir/Ni and corroded Ni DHBT films in 1 M KOH at 5 mV s^{-1}. In c), variation of the charge, Q$_c$, under the reduction peak of Ni(OH)$_2$ with the immersion time. In d), variation of the charge, Q$_{H\ UPD}$ with the immersion time. In e), variation of the Ir content with the immersion time.

In contrast, CVs of Ir/Ni DHBT exhibited (Figure 6.6a) a pair of oxidation and reduction peaks in that region (at *ca.* 0.15 V). They were associated with the underpotential deposition/stripping of hydrogen, H$_{upd}$, on metallic Ir [251], [252]. On the Ir/Ni DHBT

film, there were two broad redox peaks (oxidation peak at *ca.* 0.64V and reduction peak at *ca.* 0.53V), which are attributed to the reversible Ir (III)/Ir(IV) redox transition. From 1.1 to 1.4 V (Figure 6.6b), the oxidation and reduction peaks associated with the $Ni(OH)_2/\beta$-NiOOH redox couple were observed at 1.38 V and 1.26 V, respectively [110]. The background current density between 0.4 and 1.1 V was larger on Ir/Ni DHBT compared to Ni DHBT. This is consistent with the conversion of Ir to iridium oxyhydroxide in this potential region [253]. All this evidence points to the fact that both Ni and Ir are present on the electrode surface and can participate in various redox reactions.

In the CVs of Figure 6.6b, there was a steep increase of current at potentials more positive than 1.6 V for Ni DHBT and corroded Ni DHBT, and at potentials greater than 1.43 V for Ir/Ni DHBT. This current increase was associated with oxygen evolution. Clearly, Ir/Ni DHBT was the most active electrode for the OER. It is worth nothing that erosion of Ni DHBT through soaking in HCl had only a marginal effect on the OER characteristic compared to pristine Ni DHBT. Clearly, the presence of Ir^{+4} ions in solution is the key to increasing the OER performance of the DHBT electrode.

Steady-state CVs of Ir/Ni DHBT electrode after different immersion times were recorded (Figure 6.7). The relative amount of Ni atoms participating in an electrochemical reaction was evaluated by integration of the charge, Q_c, under the cathodic peak at *ca.* 1.25 V. Q_c increases steadily with the immersion time, from 0.222 C cm^{-2} to 2.112 C cm^{-2} after 20 h of immersion in a solution containing Ir^{+4} (Figure 6.6c). This is a factor of ten difference. In contrast, Q_c of corroded Ni DHBT is only 0.368 C cm^{-2} after 17 h of immersion, only a factor of 1.7 larger than pristine Ni DHBT. Therefore, even if the dissolution rate of Ni is only marginally increased from 3.80 to 4.49 ppm h^{-1} cm^{-2}, the presence of Ir^{+4} in solution greatly increased the number of Ni atoms able to participate in the $Ni(OH)_2/\beta$-NiOOH redox reaction . One possible explanation for the significant increase of Q_c is that the Ir modification procedure had permanently altered the porous structure of the film and/or its wettability, the electrolyte having more readily access to a larger fraction of the Ni porous structure after immersion in the Ir+4 containing solution.
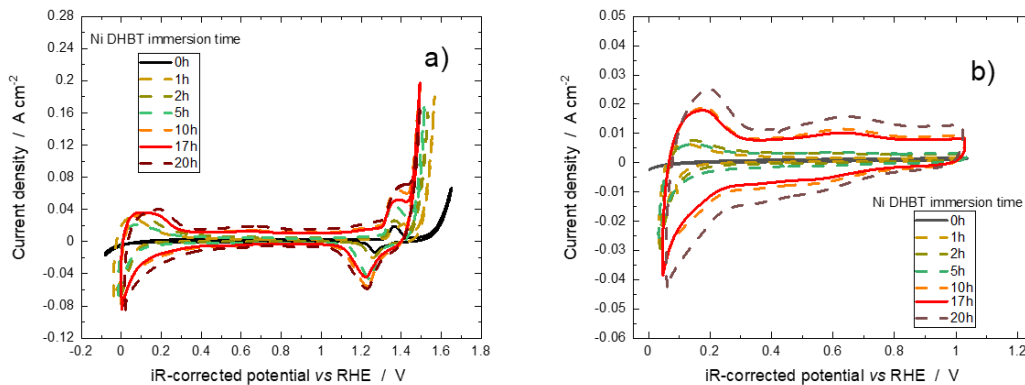
Figure 6.7 Cyclic voltammograms (5 mV s⁻¹) in 1 M KOH of Ir/Ni DHBT electrodes after different immersion time. In a) the potential window extends from -0.1 to 1.7 V. In b), a restricted potential window is shown.

Following immersion, Ir atoms at the electrode surface are mostly in a metallic state Similar to Pt, hydrogen atom can be underpotentially deposited and stripped from Ir metal [251], [252]. The relative amount of Ir atoms able to participate in an electrochemical reaction was evaluated from the integration of the stripping peak of hydrogen underpotentially deposited on Ir, Q_{HUPD}. The CVs used to evaluate Q_{HUPD} were obtained on as-immersed electrodes, before they were polarized in the potential region where the OER occurs. These results are shown in Figure 6.8a, and the method used to calculate Q_{HUPD} is illustrated in Figure 6.8b. The variation of Q_{HUPD}, and the corresponding Ir surface concentration, are shown in Figure 6.6d and Figure 6.6e, respectively. There is a linear relationship between the concentration of Ir atoms at the electrode surface and the immersion time.
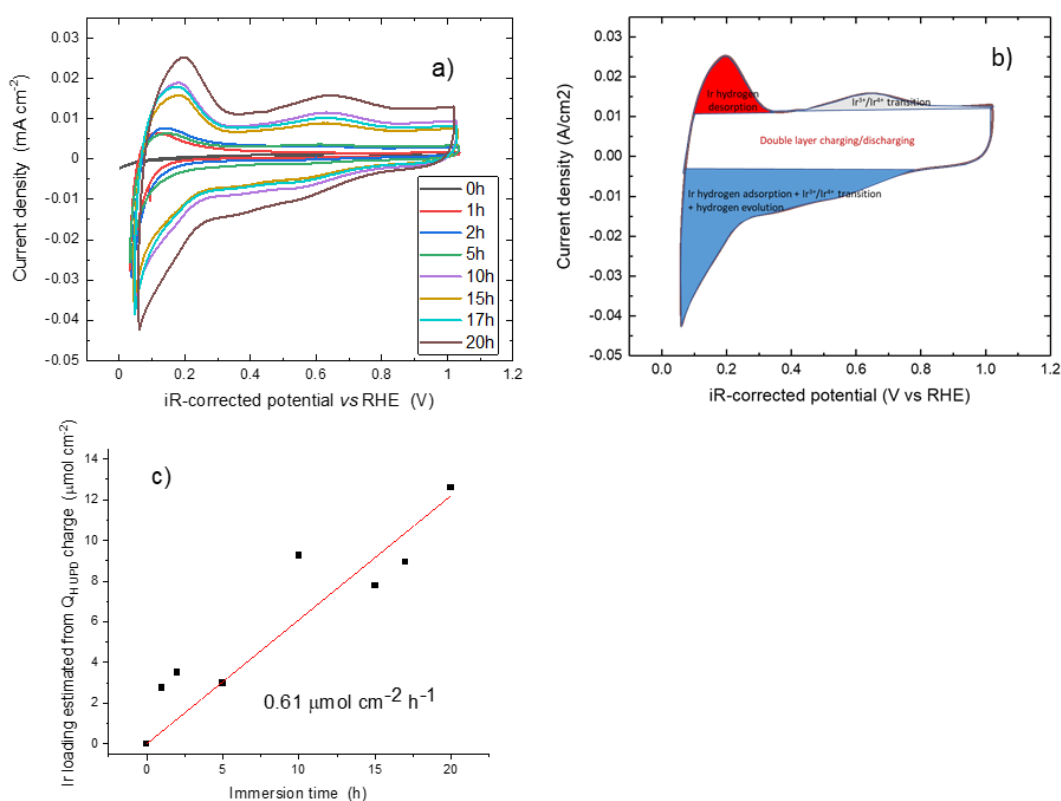
Figure 6.8 a) CVs of Ir/Ni DHBT before extensive electrochemical characterization in the OER region. b) Assignment of different sections in CV diagram. The white, gray, red and blue areas represent the double layer charging/discharging, the Ir(+III) to Ir(+IV) transition, hydrogen desorption and a mixture of hydrogen adsorption, the Ir(+IV) to Ir(+III) transition and hydrogen evolution, respectively. c) Variation of the estimated Ir loading determine from $Q_{H\ UPD}$ with respect to the immersion time.

The Ir surface content estimated from Q_{HUPD} is 6.1×10^{-7} mol h^{-1} cm^{-2}. In comparison, it was determined from ICP measurements that Ir atoms were removed from the immersion solution at a rate of 8.0×10^{-7} mol h^{-1} cm^{-2}. The former value was a measure of the electrochemically accessible Ir atoms, while the latter was the total amount of Ir atoms deposited at the electrode surface. This suggests that Ir atoms are arranged into small clusters at the electrode surface instead of being deposited as single atoms.

For the Ir/Ni DHBT sample immersed 20 h, Q_{HUPD} is 1.01 C. The Ir specific charge density for the adsorption of hydrogen is 210 µC cm$^{-2}_{Ir}$ [251], [252]. Hence, the surface area of Ir exposed to the electrolyte is 0.48 m2. For this sample, the total amount of Ir atoms deposited on the electrode surface was 1.6×10^{-6} mol, as determined by ICP measurements, which amounts to 3.1 mg of Ir. The ratio of surface area to mass is thus 154.8 m^2 g^{-1}. If one assumes a cuboctahedron cluster shape, then an estimation of the size of Ir clusters can be obtained. The ratio between the surface area and the mass of clusters varied with its diameter. According to Drault *et al.*, a cuboctahedron

cluster with 2869 Ir atoms and a diameter of 4.3 nm has a ratio of surface area to mass of 154.8 m^2 g^{-1} [254]. Accordingly, we can infer that Ir atoms exist at the surface of the Ir/Ni DHBT electrode as 4.3 nm clusters and there is a total of 4.7×10^{15} clusters for an electrode geometrical surface area of 1 cm^2.

6.4.3   OER performance

The activity for the OER of Ni and Ir/Ni DHBT films was investigated through chronopotentiometry measurements at 10 mA cm^{-2} (Figure 6.9a). The potential stabilizes rapidly to its steady-state value. In the case of Ni and Ir/Ni DHBT after 20h of immersion, the iR-corrected overpotentials were 323 mV and 195mV, respectively. The effect of the immersion time, and thus of the amount of Ir atoms, on the overpotential at 10 mA cm^{-2}, η_{10}, is depicted in Figure 6.9b. The overpotential decreased exponentially with increasing immersion time, with an exponential decay constant of 1.9 h. In comparison, η_{10} of corroded Ni DHBT (17 h) was 327 mV, almost identical to the value of pristine Ni DHBT. The increased activity of Ir/Ni DHBT compared to both Ni DHBT and corroded Ni DHBT could be due to the observed increase of electrochemically active surface area, as assessed by Q_c, and the presence of Ir atoms at the electrode surface. The relative importance of these two factors will be established later.
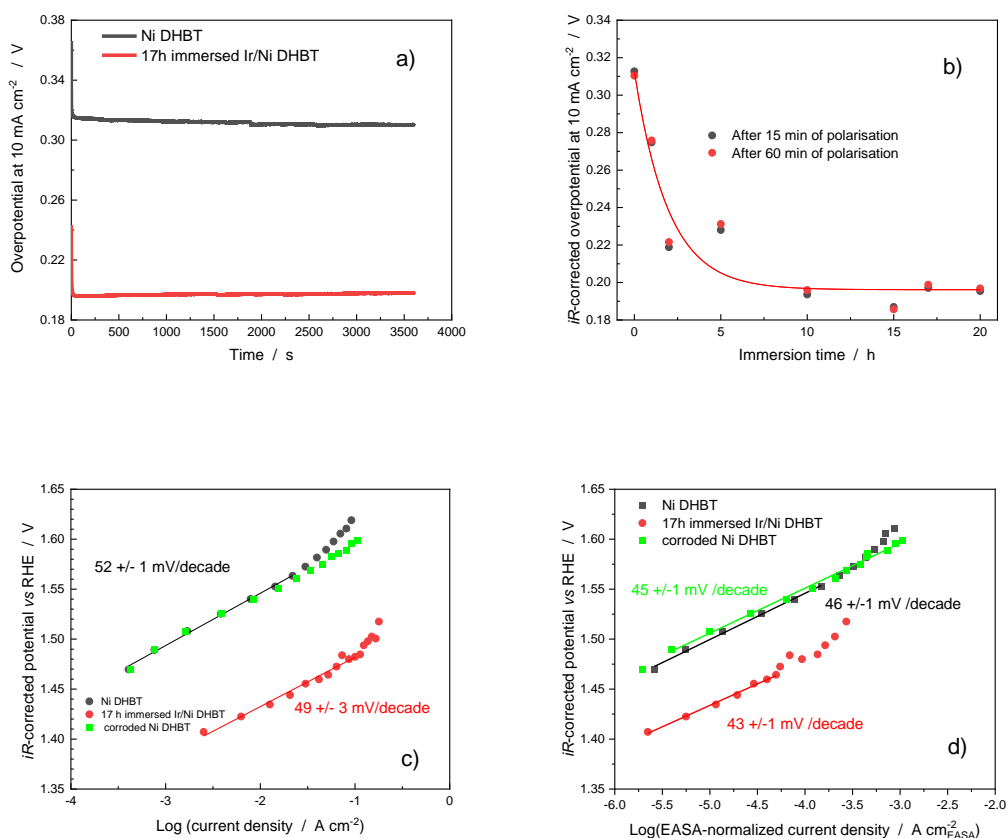
Figure 6.9 In a) Chronopotentiometric curves at 10 mA cm^{-2}; b) iR-corrected overpotentials for the OER recorded at 10 mA cm^{-2} of Ir/Ni DHBT electrodes immersed for different periods of time in 0.01 M HCl and 0.001 M K$_2$IrCl$_6$; c) Tafel plots of selected electrodes expressed as A per geometric cm^2; d) Tafel plots of selected electrodes normalized to the EASA surface area. All OER measurements were performed in 1M KOH electrolyte.

Figure 6.9c shows the iR-corrected potential *vs.* log(j) curves (Tafel plots) of Ni DHBT, corroded Ni DHBT and 17h-immersed Ir/Ni DHBT films. Tafel plots of replicates of the best performing electrodes are shown in Figure 6.10. The Tafel plot of corroded Ni DHBT is almost superimposable on Ni DHBT. Tafel plots of Ni DHBT and Ir/Ni DHBT showed a linear behavior in the current range between 1 and 100 mA cm^{-2}. Ni DHBT exhibited a Tafel slope of 52 mV dec^{-1} and an exchange current density of 7.9×10^{-6} mA cm^{-2}. Ir/Ni DHBT had a similar Tafel slope (49mV dec^{-1}) but a much larger exchange current density of 7.9×10^{-4} mA cm^{-2}. This is a factor of 100 times larger than on Ni DHBT. The similarity between the Tafel slopes suggests that the rate-determining step for the OER on Ni DHBT and Ir/Ni DHBT is the same, and the OER is proceeding with the same mechanism on both electrodes [255].
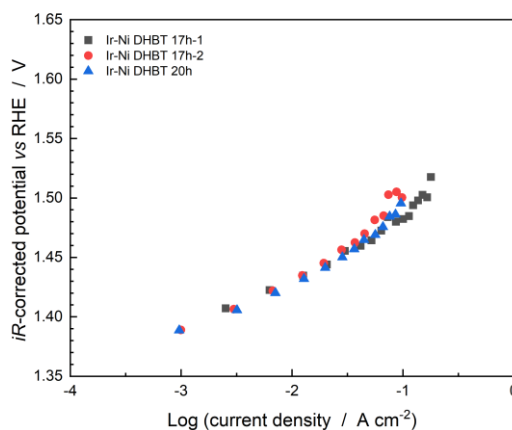
Figure 6.10 Tafel plots of replicates of the best performing electrodes taken in 1M NaOH.

Tafel plots of Ni DHBT coatings evaluated in 1.0 M KOH spiked with Fe had a 30mV dec^{-1} slope and the exchange current density was 2.0×10^{-9} mA cm^{-2} [110]. In terms of overpotential, this translates into η_{10} = 250 mV. For comparison, η_{10} of Ir/Ni DHBT measured in 1.0 M KOH (Figure 6.9c) is 195 mV, which is 55 mV less.

6.4.4   XPS characterization

The surface electronic structure of Ni and Ir/Ni DHBT electrodes following the OER was investigated by X-ray photoelectron spectroscopy measurements. Figure 6.11a and Figure 6.11b shows the Ir 4f core level peaks of Ir/Ni DHBT electrode before (as-deposited) and after electrochemical characterization in the OER region. After electrochemistry, the metallic Ir peaks at 60.4 and 63.5 eV are barely discernible, and two additional peaks were observed at 62.9 and 65.6 eV that corresponds to the Ir 4f7/2 and Ir 4f5/2 core levels, respectively. These peaks are assigned to iridium oxide [256]. This is consistent with data from the literature, showing that a monolayer of iridium oxide was starting to form at potential more positive than *ca.* 0.6V *vs.* RHE [257], and that a thick oxide layer was growing at potentials larger than 1.3V *vs.* RHE [258].

The Ni 2p3/2 core level peaks of Ni and Ir/Ni DHBT electrodes after electrochemistry are shown in Figure 6.11c and Figure 6.11d, respectively. As expected from the fact that large positive potentials have been applied to these electrodes, both samples show typical line shapes of oxidized Ni, with only very small features at 852.8eV and 870.1eV assigned to metallic Ni 2p3/2 and Ni 2p1/2 core levels, respectively.
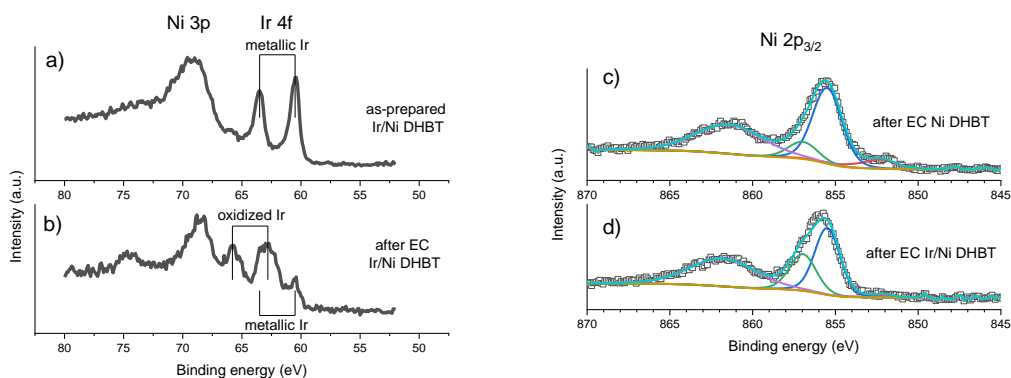
Figure 6.11 In (a and b), XPS data of Ir 4f and Ni 3p core levels. In (c and d), XPS data of Ni 2p3/2 core level peaks

Fitting of the Ni 2p3/2 peaks was achieved using two components at 855.4 eV and 856.9 eV, which according Ratcliff *et al.* are assigned to Ni^{2+} and Ni^{3+}, respectively [247]. There was no evidence of a peak at 854.0 eV that could be assigned to NiO [259]. Following the OER, the Ni^{3+}/Ni^{2+} ratio is 0.23:1 and 0.58:1 for Ni and Ir/Ni DHBT films, respectively. The Ni^{3+} state is usually ascribed to the creation of vacancies in $Ni(OH)_2$ or to the presence of NiOOH [247], [258]–[261]. It was shown elsewhere that the wettability of Ni electrode is increased by the presence of a higher amount of defects (vacancies) [262], and that NiOOH is more hydrophilic than $Ni(OH)_2$ [263]. Based on this evidence, one could argue that the increased hydrophilic character of Ir/Ni DHBT compared to Ni DHBT have an influence on the electrocatalytic properties of this electrode, especially on the way oxygen bubbles formed and detached from the electrode. This is going to be investigated through acoustic emission data recorded during the OER.

6.4.5 *Operando* AE detection of bubbles during the OER

In a porous media, the following equation is valid

Equation 6.4

$$P_g - P_w = P_c = -\frac{2\gamma \cos \theta}{r_c}$$

where P_g is the gas pressure (in Pa), P_w is the water pressure (in Pa), P_c is the capillary pressure (in Pa), γ is the surface tension of the electrolyte (in N m^{-1}), θ is the contact angle that the electrolyte would make with a flat surface of identical nature and structure (in radians or degrees), and r_c is the radius of the pore throat (in m). Increasing the hydrophilicity of the material through an increase in the ratio of Ni^{3+} /

Ni^{2+} would decrease the contact angle, which means that both P_g and P_c would be decreased. For a bubble to escape from the porous structure of an electrode, P_g should be larger than P_c. Accordingly, if the value of P_g of Ir/Ni DHBT is smaller than P_g of Ni DHBT, this translates into a smaller expected bubble size for the former electrode compared to the latter.

The verification of that hypothesis demands an investigation of the trapped gas in the porous DHBT electrodes. However, applying visualization technologies, like high-speed camera or computed tomography, to directly observed trapped gas bubbles in porous films is challenging [113], [114], [238], [242], [264]–[266]. In contrast, acoustic emission (AE) detection is a robust and straightforward method to assess *operando* of gas bubbles on a gas evolving electrode. With an AE sensor in close proximity to the working electrode, the acoustic signal generated by vibrating gas bubbles can be recorded. Then, the AE signal can be used to count the number of gas bubbles. Based on the work of Vazquez *et al.* [134], the bubble size can be determined using the Minnaert equation (Equation 6.5), which relates the AE frequency to the diameter of a bubble.

Equation 6.5

$$f_0 = \frac{1}{\pi D} \sqrt{\frac{3\gamma P^0}{\rho}}$$

where f_0 is the frequency of a bubble (in Hz), D is the bubble diameter (in m), and γ is the polytropic coefficient (without unit), P_0 is the ambient pressure (in Pa) and ρ is the density of water (in kg m^{-3}).

Figure 6.12a shows the schematic of the acoustic detection system in combination with a three-electrode electrochemical cell setup. With this setup, the AE events during the OER were detected. With Ni and Ir/Ni DHBT electrodes, the AE events happened only upon the application of an anodic current (Figure 6.13). The AE signal was measured at 6.6 mA cm^{-2} for 300s. The peak frequencies of all AE events were translated into bubble size using the Minnaert equation (Equation 6.5). The distribution of bubble sizes is shown in Figure 6.12c, and the moving average of bubble size with respect to electrolysis time are shown in Figure 6.12d. For Ni DHBT, there are two main populations of bubbles, centered at 137 and 157 μm diameter. For Ir/Ni DHBT, bubbles with 137 and 157 μm diameters are present, but there were a larger number of bubbles with diameter between 80 and 130 μm. All this makes it so that the mean bubble diameter on Ni DHBT is 140 μm compared to 125 μm for Ir/Ni DHBT (Figure 6.12d).

As shown in Figure 6.14 and Figure 6.15, the mean bubble diameter of both Ni and Ir/Ni DHBT is independent of the current density between 1 and 6.6 mA cm^{-2}. Measurements at larger current density could not be performed since the AE detector was saturated. On Ir/Ni DHBT, there is a sizeable reduction of the bubble size compared to Ni DHBT, which is ascribed to the increase hydrophilicity of the former electrode compared to the latter.
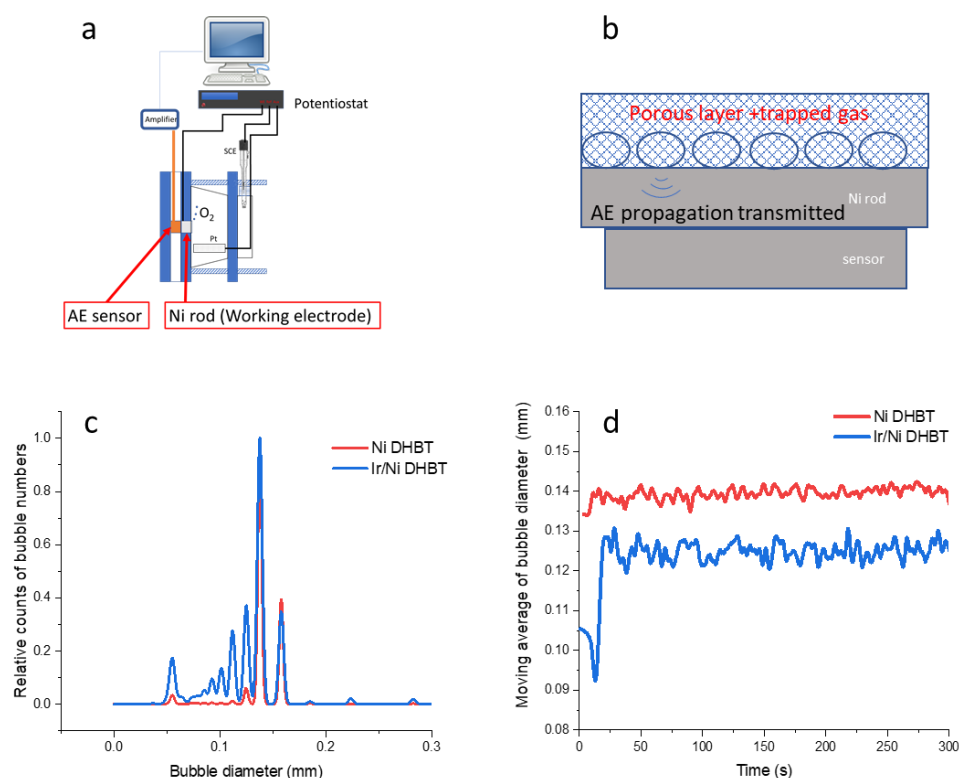
Figure 6.12 a) Schematic representation of the experimental setup used for the AE measurements; b) Schematic representation of the AE wave propagation of trapped bubbles; c) Bubble size distributions determined by the AE method. Measurements were performed at a current density of 6.6 mA cm^{-2} during 300s. For clarity, the distributions have been normalized to the maximum values of each plot; d) Moving averages of bubble diameter versus electrolysis time.
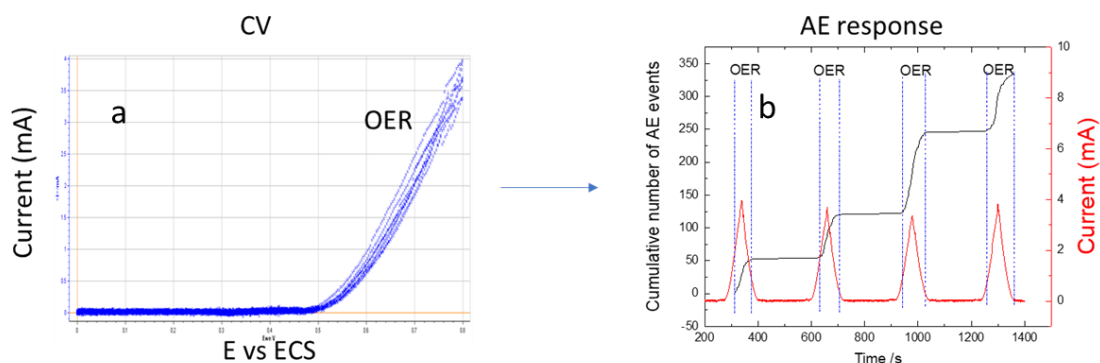
Figure 6.13 In (a), CVs of a Ni plate taken in 1M KOH at 5 mV s⁻¹. In (b), variation of current and cumulative number of AE events as a function of time.
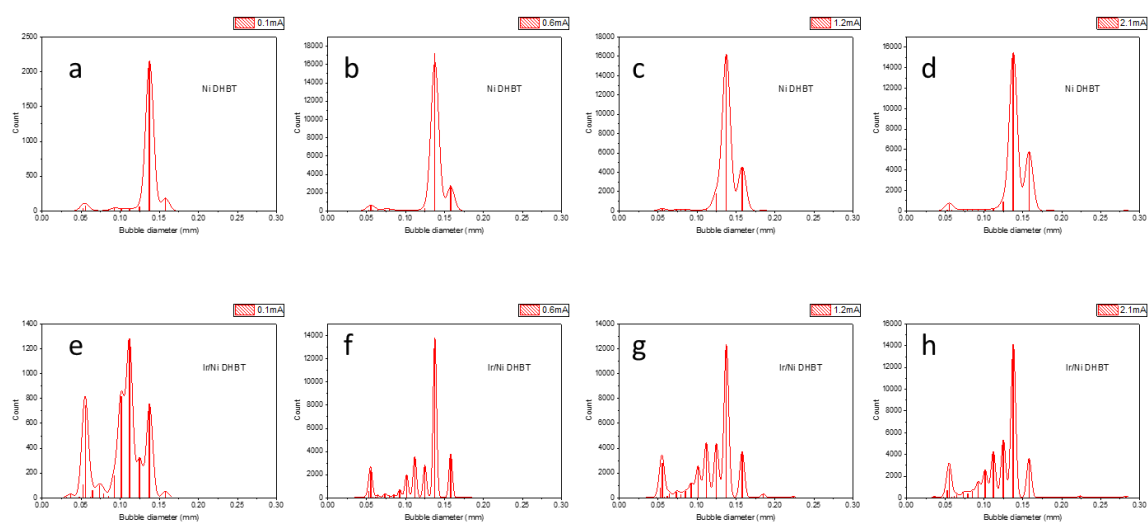
Figure 6.14 Bubble size distributions determined by the AE method for a) to d) Ni DHBT, and e to h) Ir/Ni DHBT at current density of 0.3 mA cm⁻² (first column), 1.9 mA cm⁻² (second column), 3.8 mA cm⁻² (third column), and 6.6 mA cm⁻² (fourth column).
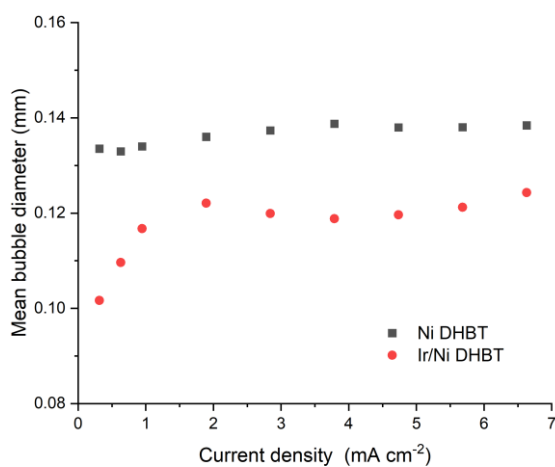
Figure 6.15 Average bubble diameter measured by AE at different current densities for Ni DHBT and Ir/Ni DHBT electrode.

6.4.6 EIS characterization

EIS measurements were conducted at different potentials for Ni DHBT and 17h immersed Ir/Ni DHBT films (Figure 6.16). The EIS spectra of both electrodes display a straight line in the high frequency region and one depressed semicircle in the low frequency region. The shape of the high frequency line does not change with the electrode potential. This is an indication that the features in the high-frequency response were not related to the OER kinetics. It is known that features in the high frequency region of EIS spectra are related to the electrode porosity [130], [267]. The inclination of this line with respect to the horizontal-axis was 45° and 22.5° for Ni and 17 h immersed Ir/Ni DHBT electrode, respectively, indicating that the porous structures of these electrodes differ greatly. Corroded Ni DHBT electrodes share the same 45° line as observed for Ni DHBT (Figure 6.17), indicating that exposure to HCl only was not enough to modify the porous structure of the electrode.
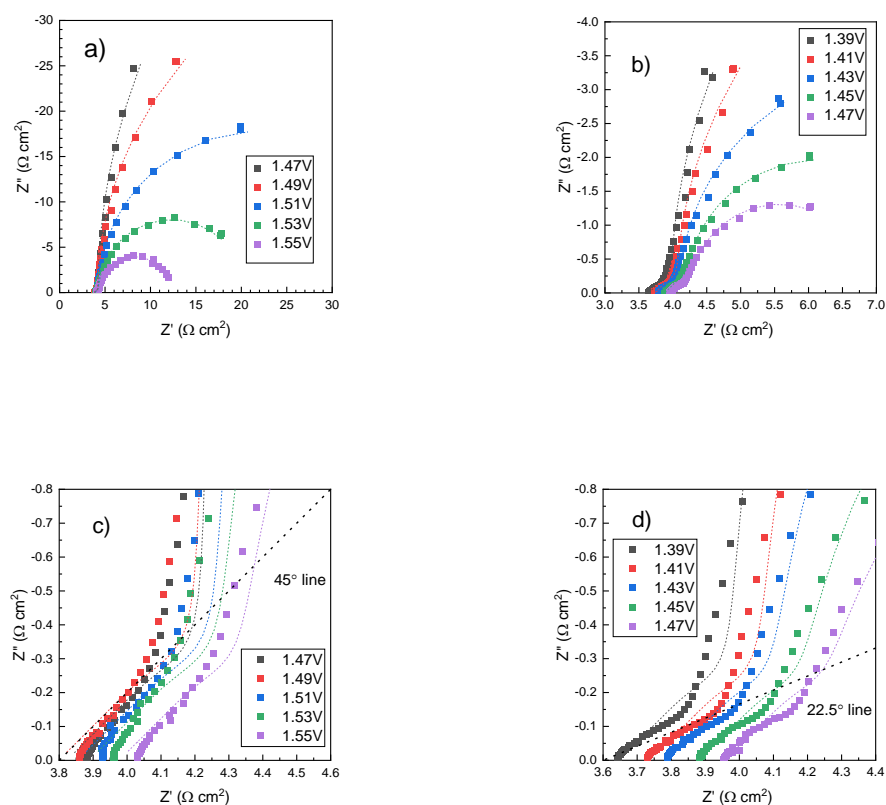
Figure 6.16 Measured (scattered points) and fitted (dotted lines) EIS plots on a) Ni DHBT and b) 17 h immersed Ir/Ni DHBT. The high-frequency features of Ni DHBT and 17 h immersed Ir/Ni DHBT are shown in c) and d), respectively.
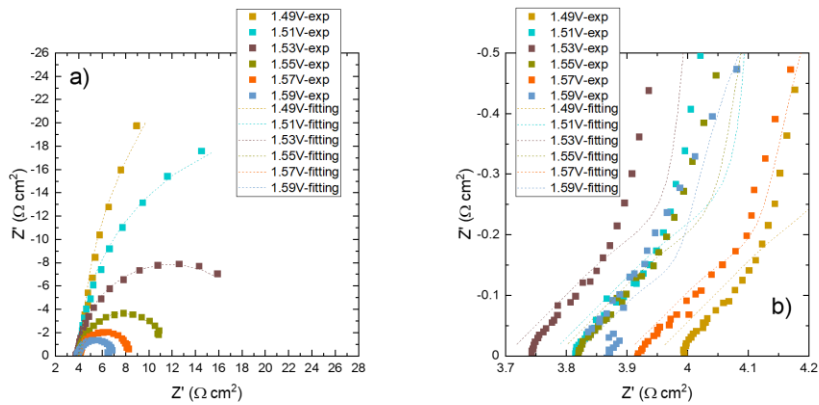
Figure 6.17 EIS plots of eroded Ni DHBT electrodes. The experimental data are given as scattered data points, while the fitted data are represented by the dotted lines. The same data are shown at different scales in a) and b).

The EIS data were fitted using a transmission line model and the de Levie Equation 6.1. The fitted curves are shown in Figure 6.16 along with the experimental data. The fit to both electrodes is excellent in the low frequency region. The de Levie equation also yielded a good fit for the 45° line observed for Ni DHBT and corroded Ni DHBT. In contrast, it failed to account for the 22.5° line observed in the high frequency region of Ir/Ni DHBT. This was expected from the transmission line model on which the de Levie equation is based and a more detailed model to account for the porosity of Ir/Ni DHBT electrode needs to be developed.

The de Levie equation used to fit the EIS data is based on a transmission line model that assumes that pores are parallel with a cross-sectional shape independent of depth. As mentioned earlier, the EIS data of Ni DHBT and corroded Ni DHBT follow the de Levie equation, which suggests that simple parallel pores are present. This is shown schematically in Figure 6.18a, where only the primary pore structure exists. However, the actual pore geometry could be branch-like as illustrated in Figure 6.18b, with a secondary pore structure that exists but remains inert on Ni DHBT and corroded Ni DHBT coatings. In that case, the simple pore model would still be adequate to explain the EIS results.
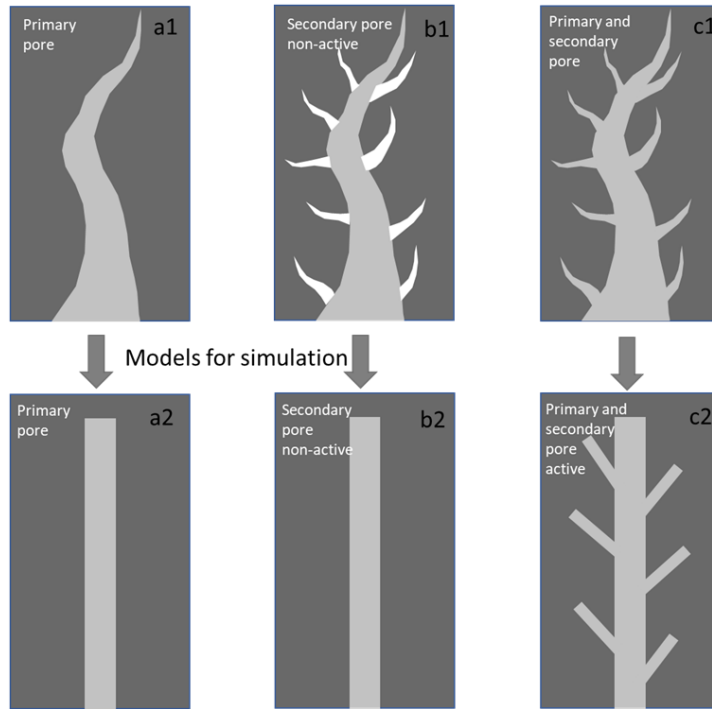
Figure 6.18 In a1)–c1) Schematic representations of the pores with different accessibility conditions: a) only primary pores are present; b) there primary and secondary pores are present but the secondary pores are non-active; c) primary and secondary pores are present and both are active. The gray area represents the electrochemically active region, while the white area represents non-active regions. In a2)-c2) Idealized models for EIS simulation used to represent the schematic drawings of a1)-c1), respectively.

Alternatively, the actual pore geometry could be branch-like as illustrated in Figure 6.18c, with a secondary pore structure that exists but is active and contributes to the EIS response. Accounting for the primary and secondary pore structure depicted in Figure 6.18c was achieved using the following equations [130]

Equation 6.6

$$Z = R_s + \cfrac{1}{\cfrac{1}{Z_{flat}} + \cfrac{n_{pore,1}}{Z_{pore,1}}}$$

Equation 6.7

$$z_{pore,1} = \sqrt{R_{\Omega,pore1} z_1^*} \coth \sqrt{\frac{R_{\Omega,pore1}}{z_1^*}} X_1$$

Equation 6.8

$$z_1^* = \left[\frac{1}{\left(\frac{1}{z_{pore,2}/(n_{pore,2}\xi)} + (1-\xi)(\frac{1}{R_{ct}^*} + i\omega C_{dl}^*) \right)} \right] \frac{1}{2\pi r_1}$$

Equation 6.9

$$z_{pore,2} = \sqrt{R_{\Omega,pore2}\, z_2^*}\, coth \sqrt{\frac{R_{\Omega,pore2}}{z_2^*}}\, X_2$$

Equation 6.10

$$z_2^* = \left(\frac{1}{\frac{1}{R_{ct}^*} + i\omega C_{dl}^*} \right) \frac{1}{2\pi r_2}$$

where the z_{flat} is the impedance of the flat part outside the orifice of pores, z_1^* and z_2^* are the electrode interfacial impedance per unit length in the primary pore and secondary pore, respectively; $z_{pore,1}$ and $z_{pore,2}$ are the impedance of primary and secondary pores, respectively; $R_{\Omega,pore1}$ and $R_{\Omega,pore2}$ are the solution resistance per unit length in the primary pore and secondary pore, respectively; r_1 and r_2 represent the primary pore and secondary pore, respectively; X_1 and X_2 represent the length of the primary pore and secondary pore, respectively; ξ is the area fraction of secondary pore on the primary pore wall; $n_{pore,1}$ is the number of primary pores; $n_{pore,2}$ is the number of secondary pore per unit area of primary pore wall; R_{ct}^* is the specific charge transfer resistance in Ω cm^2; and C_{dl}^* represents the intrinsic double layer capacitance per unit area.

Figure 6.19 shows a simulation of the EIS data of Ni DHBT where only the primary pores were considered (ξ = 0). All the parameters were optimized using CNLS fittings, and the fitting parameters are presented in Table 6.1. The diameter and length of the primary pores were fixed at 22 µm and 95 µm to be consistent with the SEM micrographs. As shown in Figure 6.19, the agreement between the fitted and the experimental data of Ni DHBT is excellent, and the 45° line at high frequency is well accounted for. This is not surprising considering that the expression for the pore impedance (Equation 6.6-Equation 6.10) is identical to the de Levie equation when ξ = 0, and that the de Levie equation was giving a good fit of the high frequency region for Ni DHBT.

Table 6.1 The parameters used for the EIS simulation of Ni DHBT and Ir/Ni DHBT

	Ni DHBT		Ir/Ni DHBT	
	Formula	value	Formula	value
R_s		4.02Ω		4.02Ω
Z_{flat}	$1/[(\frac{1}{R_{ct}^*} + i\omega C_{dl}^*)$ x2.5S_1]		$1/[(\frac{1}{R_{ct}^*} + i\omega C_{dl}^*)$ x2.5S_1]	
r_1		11μm		11μm
r_2		-	$0.3r_1$	
X_1		95μm		95μm
X_2		-	$0.3X_1$	
$n_{pore,1}$		4.2×10^6 cm^{-2}		4.2×10^6 cm^{-2}
$n_{pore,2}$		-	$1/s_2$	
$R_{\Omega,pore1}$	ρ/s1		ρ/s_1	
$R_{\Omega,pore2}$		-	ρ/s_2	
R_{ct}^*		586Ω cm^2		586Ω cm^2
C_{dl}^*		390μF cm^{-2}		390μF cm^{-2}
ξ		0		0.3
ρ		586 Ω cm		586 Ω cm

Figure 6.19 a) Nyquist plot of EIS measurements for Ni DHBT at 1.51V and 17h immersed Ir/Ni DHBT at 1.49V (scattered data points). The solid lines show the simulated data for Ni DHBT (blue curve) and 17h immersed Ir/Ni DHBT (green curve). b) A zoom of the high frequency region (gray region in figure a). The data used for the fitted curves are shown in Table S1.

The EIS data of Ir/Ni DHBT were fitted using the same parameters for primary pores and $\xi = 0.3$ to account for the presence of secondary pores. As seen in Figure 6.20, this value gives the best fit to the high frequency EIS data of Ir/Ni DHBT. It was shown elsewhere that the Ni DHBT substrate has a fractal surface [110]. Therefore, it was hypothesized that the secondary pores occupied 30% of the primary pore wall area, that the diameter of the secondary pores was 30% of the primary pore diameter, and that the length of the secondary pores was 30% of the primary pore length. The parameters used of the fit are given in Table 6.1. Again, the agreement between the fitted and the experimental data of Ir/Ni DHBT is excellent (Figure 6.19). According to the branched pore model of Itagaki [130], fractal structures with both primary and secondary pores having a cylindrical shape yields a straight line in the high frequency region, with an inclination of 22.5°. For Ir/Ni DHBT, the EIS data in the high frequency region suggests that both the primary and the secondary pore structure is accessible.
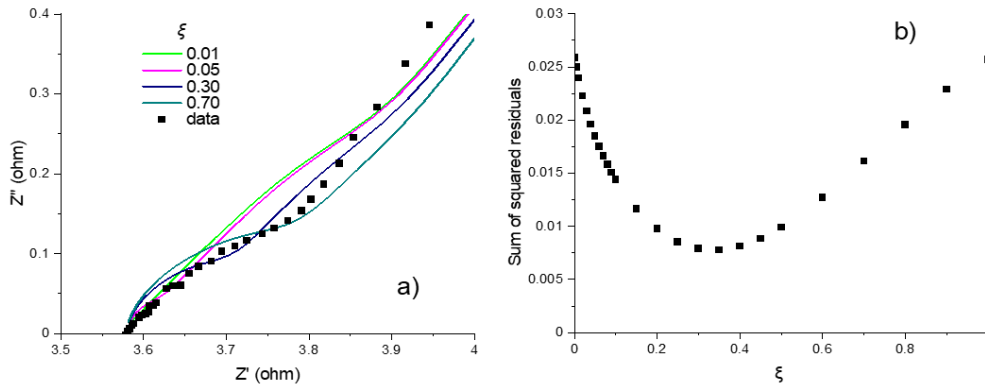
Figure 6.20 In a), simulations of EIS data for Ir/Ni DHBT in the high-frequency region using different values of ξ. In b), sum of squared residuals as a function of ξ. It was shown elsewhere that the Ni DHBT substrate has a fractal surface. So, in each case, the EIS simulation was obtained by assuming that the secondary pores occupied of ξ *100 % of the primary pore wall area, that the diameter of the secondary pores was ξ *100 % of the primary pore diameter, and that the length of the secondary pores was ξ *100 % of the primary pore length.

The double-layer capacitance, C_{dl}, and the total charge-transfer resistance, R_{ct}, of the electrodes can be extracted from the parameters characterizing the depressed semi-circle observed in the low frequency region, using the following equations

Equation 6.11

$$C_{dl} = \frac{c_{dl}}{R_\Omega}$$

Equation 6.12

$$R_{ct} = r_{ct}R_\Omega$$

Figure 6.21a and Figure 6.21b shows plots of log(1/R_{ct}) *vs.* potential of Ni and 17h immersed Ir/Ni DHBT electrodes. As expected, the slope of the current density (Tafel plot) and log(1/R_{ct}) *vs.* potential curves are the same.
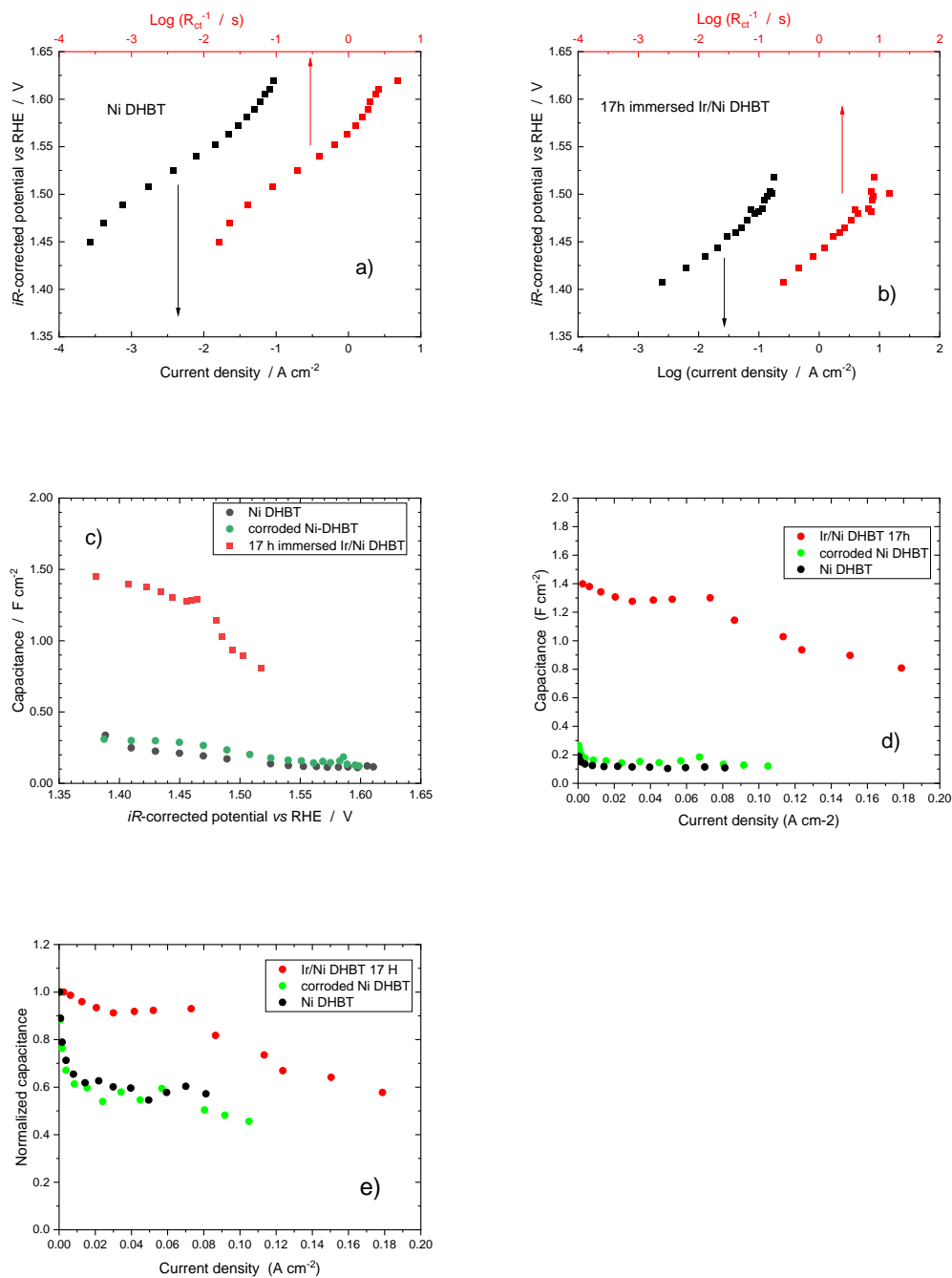
Figure 6.21 In a) and b), iR-corrcetd potential versus Log(R^{-1}_{ct}) determined from EIS (red data points). In a) Ni DHBT and b) 17 h immersed Ir/Ni DHBT coatings. For comparison, the corresponding Tafel plots are also given as black data points. In c), variation of the capacitance with respect to potential. In d), variation of capacitance with respect to current density. In e), variation of normalized capacitance with respect to current density.

Figure 6.21c shows the variation of C_{dl} as a function of potential of Ni DHBT, 17 h immersed Ir/Ni DHBT, and corroded Ni DHBT films. Again, comparing Ni DHBT and corroded Ni DHBT, there was almost no variation of the double layer capacitance

following immersion in HCl only. In contrast, at the lowest electrode potential, there was almost a factor of 6 increase of C_{dl} following immersion in 0.01 M HCl and 0.001 M K_2IrCl_6. These results are consistent with those found earlier through integration of the charge under the cathodic peak associated with the reduction of $Ni(OH)_2$ (Q_c values).

EIS data were acquired from *ca.* 1.37 to 1.52 V. In this potential range, oxygen bubbles form and continuously detach from the electrode surface. It is therefore expected that the resistance of the solution will increase and thus the ohmic drop. This was observed in Figure 6.16c and Figure 6.16d, as a gradual increase of the intercepts between the EIS data and the X-axis was observed as the electrode potential was increased to more positive values. However, this effect was already taken into consideration since the iR-corrected electrode potentials were used to draw the Tafel plots. The presence of O2 bubbles was also expected to decrease the EASA by reducing the contact area between the electrode surface and the electrolyte. This effect was captured in Figure 6.21c, where the capacitance values of all electrodes decreased as the electrode potential is increased in the potential region where the OER is occurring. The current density increases as the OER overpotential is increased, which translates into an increase for O_2 gas emitted by the electrode, thus decreasing the accessibility of the electrolyte to the electrode's active sites. To account for the difference in the electrocatalytic activity of the electrodes, Figure 6.21d and Figure 6.21e show plots of the capacitance and the normalized capacitance with respect to the current density. While the capacitance of Ir/Ni DHBT decreases steadily with the current density, the capacitance of Ni DHBT and corroded Ni DHBT decrease by 40% of their original values as the current density reaches 0.02 A cm^{-2}, and they continue to decline steadily as the current is further increased. In comparison, current density as large as 0.14 A cm^{-2} should be reached for the Ir/Ni DHBT electrode to lose 40% of its original capacitance value. It should be emphasized that this difference in behavior results from the presence of Ir^{+4} cation in the immersion solution as it is not observed on corroded Ni DHBT. This reflects the fact that the Ir/Ni DHBT electrode is more capable of releasing the oxygen gas produced during the electrolysis of water, which is consistent with the fact that the size of the oxygen bubbles is reduced by almost 15% compared to the Ni DHBT electrode.

In Figure 6.9c, at any given potential, there is a factor of 175 difference between the current density of Ni DHBT and Ir/Ni DHBT. This difference in activity is due to the presence of iridium, as immersing the Ni DHBT electrode in an acidic solution containing no Ir^{+4} cations result in only a marginal increase in the activity of the

electrode. We have shown that iridium acts at different scales to enhance the electrocatalytic activity of the electrode for the OER. Firstly, iridium increases the active electrochemical surface of the electrode by promoting the creation of a network of secondary pores, or by activating a network of secondary pores already present in the Ni DHBT electrode but inactive before the electrode was immersed in the solution containing Ir^{+4} cations. The other effect of iridium is to increase the hydrophilicity of the electrode, resulting in a decrease in the size of the oxygen bubbles and, as discussed above, a less drastic decrease of the active electrochemical surface area as the current for the OER increases. Therefore, to account for these two effects of iridium, the Tafel plots of Ni DHBT and Ir/Ni DHBT shown in Figure 6.9c, which are expressed with respect to the geometric surface area, were normalized by the capacitance values measured at each electrode potential, assuming a value of 470 μF cm^{-2} for the specific double layer capacitance [37]. Normalization by the capacitance measured in the potential range where the OER is taking place accounts for (i) the increase of the EASA that occurs due to immersion of the electrode in a solution containing Ir^{+4} cations that was discussed in Figure 6.6c, and (ii) the decrease of the EASA due to the presence of oxygen bubbles on the electrode surface that was discussed in Figure 6.21c and Figure 6.21d. The EASA-normalized Tafel plots of Ni DHBT and Ir/Ni DHBT electrodes are shown in Figure 6.9d. Once these two effects on the Tafel slopes are taken into account, the differences observed between the Ni DHBT and the Ir/Ni DHBT electrode should be attributed to the catalytic activity of iridium. As seen in Figure 6.9d, there is still a factor of 33 difference between the intrinsic activity of Ni/DHBT and Ir/Ni DHBT. This is not really surprising, as the intrinsic activity of iridium oxides/hydroxides is higher than nickel oxides/hydroxides. Therefore, it is expected that the presence of a large number (a total of 4.7×10^{15} iridium clusters per cm^2) of small iridium particles (*ca.* 4.3 nm diameter) on the surface of Ni DHBT will contribute to increase the intrinsic electrocatalytic activity of the electrode for the OER.

6.5   Conclusion

3D porous Ni DHBT films possess a fractal structure, providing a large electrochemical active surface area and super-aerophobic surface properties to the electrode, which are beneficial for the OER [110]. In this work, it was shown that galvanic replacement of Ni by Ir atoms leads to a drastic increase of the electrocatalytic properties of 3D porous Ni DHBT substrate for the OER. This can be explained not only by the high intrinsic electrocatalytic activity of iridium for the OER but also by the galvanic reaction leading to the creation/activation of a secondary pore structure that increases the electrochemically active surface area of the electrode by a factor of *ca.* 8-10.

Moreover, the Ir/Ni DHBT electrode has superior hydrophilic properties that contribute also to the improvement of the electrocatalytic properties by reducing the O_2 bubble size causing a less drastic decreases of the electrochemically active surface area of the electrode as a result of the blocking effect of O_2 bubbles. The best electrode achieved an overpotential for the OER of only 195 mV at 10 mA cm^{-2}, the OER displayed a small overpotential of 195 mV. This is remarkable considering the low Ir amount involved. This study provides a way to optimize the OER performance for nanostructured Ni-based electrodes.

7 CONCLUSIONS AND FUTURE WORKS

7.1 Conclusion

In the first project, we investigated the application of Ni nanowire arrays for the oxygen evolution reaction (OER). In this study, electrochemical templating through porous membranes were used to form arrays of micrometer long Ni nanowires (up to 20 μm) and pore size less than 200 nm, giving an aspect ratio of 0.4%. Detailed structural and electrochemical characterization, including Electrochemical Impedance Spectroscopy (EIS), was conducted to assess the electrocatalytic properties of these Ni NW arrays for OER in 1M KOH. Three different methods, namely, SEM geometry measurements, the α-Ni(OH)$_2$ charge method, and the EIS capacitance method, were used to assess how the current varies with the NW length and the Electrochemically active surface area (EASA). The three different ways are all in agreement, and the current increases with NW length and EASA precisely and only because of the surface area effect. The most surprising result is that the OER process occurs with the same intrinsic catalytic activity at the top and the bottom of these deep pores, and gas is evolved without any significant effects of electrolyte resistance, mass transport, or bubble occlusion of the pores. The governing factor affecting the electrocatalytic properties of Ni NW arrays is the enhancement of Ni surface area by the ordered 1D nanostructures, which translates into a significant 200 mV decrease of the OER overpotential at 10 mA cm^{-2}. These vertically aligned 1D NWs increase the electrochemically active surface area of a Ni plate by a factor of 130 without introducing any limitation by diffusion. This can be because the 1D NWs are almost perfectly aligned. It is expected that they could serve as an ideal platform to support better catalytic materials.

The second project used the dynamic hydrogen bubble templating (DHBT) method to prepare highly porous Ni foams with enhanced properties toward the OER. Upon varying the electrodeposition conditions, Ni films with a macro-porous primary structure and highly porous cauliflowerlike secondary structure were formed. These films can develop an extended electrochemically active surface area, up to a 270-fold increase than a Ni plate. These Ni DHBT films are wetted by the electrolyte (60%), translating into an extensive electrochemically active surface area. They also exhibit a superaerophobic character responsible for slight air bubble contact angle and small air bubble adhesive force. Both factors further contribute to maximizing the contact between the active sites of the electrode and the electrolyte even in conditions where substantial O$_2$ evolution is occurring. EIS measurements and simulations regarding the porous nature of electrodes were applied on Ni DHBT under OER potentials to

correlate the enhanced OER property to the 3D structure of Ni DHBT films. This was a successful attempt in developing a robust and mechanically stable electrode made of cheap and sustainable material.

In the third project, the effort has been made to increasing the intrinsic activity of the 3D Ni DHBT electrode by further decorating it with a small amount of Ir. The spontaneous deposition of Iridium was achieved on Ni DHBT by galvanic replacement reaction. The resulting electrode has very low Ir loadings (0.26 atom %). Nevertheless, a trace amount of Ir at the surface of the Ni DHBT electrode yields to significant improvement of the OER kinetics, resulting in an overpotential of 195 mV at 10 mA cm^{-2}. This figure makes the Ir-decorated Ni DHBT electrode one of the best performing Ni-based OER catalysts reported so far. From the EIS simulation regarding the changes of high-frequency feature between Ni DHBT and Ir-decorated Ni DHBT, it was revealed that during OER, the Ni DHBT showed limit secondary pore accessibility for electrolyte while the latter was improved in the Ir-decorated Ni DHBT. This observation motivated us to probe the bubbles generated on the 3D electrode through the *in-operando* acoustic emission method. It was found that there were tiny bubbles trapped in the 3D electrode affecting its internal wetting conditions and that the Ir-decorated Ni DHBT exerts better performance to resist bubble occupation in the porous structure. This ability of Ir-decorated Ni DHBT is attributed to its high intrinsic hydrophilicity of the internal walls. From the XPS measurement, the higher ratio of Ni^{3+} species in Ir-decorated Ni DHBT may be responsible for its higher intrinsic hydrophilicity.

From those three projects, it can be concluded that constructing ordered thin Ni 3D supports would help, to some extent, expose more active sites, facilitate bubble transport and thus promote OER performance. In comparison, the stochastic and highly porous Ni 3D support can vastly increase the exposure of active sites while reducing surface bubble coverage during OER. Further study to optimize stochastic Ni foam supports should focus on improving its internal wetting conditions, which could be achieved through defect management that alters the intrinsic hydrophilicity.

7.2   Future works

It was implied in chapter 6 that the Ir doping on fractal Ni foam (Ni DHBT) could alter the intrinsic hydrophilicity of Ni surface, and this mild change of hydrophilicity results in more pore filling with electrolyte during OER. In this scenario, fractal Ni foam act as an amplifier for the hydrophilicity effect, because on a flat surface the hydrophilicity effect on the bubble coverage won't be so severe to observe. With this idea, the fractal Ni foam could serve as a platform to study the wetting effects upon doping with different

noble metal elements (such as Pt, Ru, Pd, Au). Specifically, the trend in the change of hydrophilicity could be predicted by comparing the H_2O adsorption energies through numerical simulations (DFT). Then, the predicted trend of wetting could be tested by investigating the decorations of Ni DHBT by other noble metal elements. Their internal wetting conditions are to be probed through the EIS and acoustic emission approach. It would be meaningful to verify if the wetting effect that Ir doping played on a Ni DHBT can be reproduced by other elements.

In another aspect, the present studies on the OER performance are all realized in a home-built electrochemical cell. For the application of Ni DHBT or Ir/Ni DHBT in alkaline water electrolysis, it would be promising to re-examine their OER performances in a bipolar water electrolysis cell. The working conditions such as current density, temperature and electrolyte flow rate are to be optimized.

8 LIST OF PUBLICATIONS

2018   M. Hao, S. Garbarino, S. Prabhudev, T. Borsboom-Hanson, G. A. Botton, D. A. Harrington, and D. Guay (2018). Vertically aligned Ni nanowires as a platform for kinetically limited water-splitting electrocatalysis. The Journal of Physical Chemistry C, 123(2), 1082-1093.

2019   M. Hao, V. Charbonneau, N. N. Fomena, J. Gaudet, D. R. Bruce, S. Garbarino, D. A. Harrington, and D. Guay. (2019). Hydrogen Bubble Templating of Fractal Ni Catalysts for Water Oxidation in Alkaline Media. ACS Applied Energy Materials, 2(8), 5734-5743.

2021   D. Guay, J. Gaudet, M. Hao, V. Charbonneau, S. Garbarino, S. J. Thorpe, P. H. A. Sobrinho. Porous ni electrodes and a method of fabrication thereof. U.S. Patent Application No 16/870,886, 11 nov. 2021.

2022   M. Hao, B. D. Assresahegn, J. Gaudet, L. Roué, N. Zaker, G. A. Botton, L. Miner, A. A. Hejami, D. Beauchemin, S. Thorpe, D. A. Harrington, D. Guay. The role of Ir decoration in activating multi-scale fractal surface in porous Ni DBHT for the OER. In submission.

9 REFERENCE

[1] Z. W. She, J. Kibsgaard, C. F. Dickens, I. Chorkendorff, J. K. Nørskov, and T. F. Jaramillo, "Combining theory and experiment in electrocatalysis: Insights into materials design," *Science (80-.).*, vol. 355, no. 6321, p. eaad4998, Jan. 2017.

[2] A. Kozbial *et al.,* "Study on the surface energy of graphene by contact angle measurements," *Langmuir*, vol. 30, no. 28, pp. 8598–8606, Jul. 2014.

[3] G. B. Darband, M. Aliofkhazraei, and S. Shanmugam, "Recent advances in methods and technologies for enhancing bubble detachment during electrochemical water splitting," *Renewable and Sustainable Energy Reviews*, vol. 114. Elsevier Ltd, p. 109300, 01-Oct-2019.

[4] IRENA, "Innovation landscape brief: Renewable Power-to-Hydrogen, International Renewable Energy," 2019.

[5] T. N. Vezirolu and F. Barbir, "Hydrogen: the wonder fuel," *Int. J. Hydrogen Energy*, vol. 17, no. 6, pp. 391–404, 1992.

[6] K. Mazloomi and C. Gomes, "Hydrogen as an energy carrier: Prospects and challenges," *Renew. Sustain. Energy Rev.*, vol. 16, no. 5, pp. 3024–3033, Jun. 2012.

[7] A. van Wijk and J. Chatzimarkakis, "Green Hydrogen for a European Green Deal," *Hydrog. Eur.*, p. 39, 2020.

[8] S. van Renssen, "The hydrogen solution?," *Nature Climate Change*, vol. 10, no. 9. Nature Publishing Group, pp. 799–801, 27-Aug-2020.

[9] A. Majumdar, J. M. Deutch, R. S. Prasher, and T. P. Griffin, "A framework for a hydrogen economy," *Joule*, vol. 5, no. 8, pp. 1905–1908, Aug. 2021.

[10] IRENA, "Renewable Power : Sharply Falling Generation Costs," *Int. Renew. Energy Agency*, 2016.

[11] IRENA, *Green Hydrogen Cost Reduction: Scaling up Electrolysers to Meet the 1.5 C Climate Goal.* 2020.

[12] S. Anantharaj, S. R. Ede, K. Sakthikumar, K. Karthick, S. Mishra, and S. Kundu, "Recent Trends and Perspectives in Electrochemical Water Splitting with an Emphasis on Sulfide, Selenide, and Phosphide Catalysts of Fe, Co, and Ni: A Review," *ACS Catalysis*, vol. 6, no. 12. American Chemical Society, pp. 8069–8097, 02-Dec-2016.

[13] L. Han, S. Dong, and E. Wang, "Transition-Metal (Co, Ni, and Fe)-Based Electrocatalysts for the Water Oxidation Reaction," *Adv. Mater.*, vol. 28, no. 42, pp. 9266–9291, 2016.

[14] L. Peng and Z. Wei, "Catalyst Engineering for Electrochemical Energy Conversion from Water to Water: Water Electrolysis and the Hydrogen Fuel Cell," *Engineering*, vol. 6, no. 6. Elsevier, pp. 653–679, 01-Jun-2020.

[15] Y. Li *et al.*, "Recent Advances on Water-Splitting Electrocatalysis Mediated by Noble-Metal-Based Nanostructured Materials," *Advanced Energy Materials*, vol. 10, no. 11. John Wiley & Sons, Ltd, p. 1903120, 01-Mar-2020.

[16] H. Chen, X. Liang, Y. Liu, X. Ai, T. Asefa, and X. Zou, "Active Site Engineering in Porous Electrocatalysts," *Advanced Materials*, vol. 32, no. 44. John Wiley & Sons, Ltd, p. 2002435, 01-Nov-2020.

[17] J. Zhang, Q. Zhang, and X. Feng, "Support and Interface Effects in Water-Splitting Electrocatalysts," *Adv. Mater.*, vol. 31, no. 31, p. 1808167, Aug. 2019.

[18] M. Kuang, P. Han, L. Huang, N. Cao, L. Qian, and G. Zheng, "Electronic Tuning of Co, Ni-Based Nanostructured (Hydr)oxides for Aqueous Electrocatalysis," *Adv. Funct. Mater.*, vol. 28, no. 52, p. 1804886, Dec. 2018.

[19] R. De Levie, "The electrolysis of water," *J. Electroanal. Chem.*, vol. 476, no. 1, pp. 92–93, Oct. 1999.

[20] D. Penchini, G. Cinti, G. Discepoli, and U. Desideri, "Theoretical study and performance evaluation of hydrogen production by 200 W solid oxide electrolyzer stack," *Int. J. Hydrogen Energy*, vol. 39, no. 17, pp. 9457–9466, Jun. 2014.

[21] M. Schalenbach, A. R. Zeradjanin, O. Kasian, S. Cherevko, and K. J. J. Mayrhofer, "A perspective on low-temperature water electrolysis - Challenges in alkaline and acidic technology," *International Journal of Electrochemical Science*, vol. 13, no. 2. pp. 1173–1226, 2018.

[22] V. R. Stamenkovic, D. Strmcnik, P. P. Lopes, and N. M. Markovic, "Energy and fuels from electrochemical interfaces," *Nat. Mater.*, vol. 16, no. 1, pp. 57–69, Dec. 2016.

[23] N. Danilovic, R. Subbaraman, D. Strmcnik, V. R. Stamenkovic, and N. M. Markovic, "Electrocatalysis of the HER in acid and alkaline media," *J. Serbian Chem. Soc.*, vol. 78, no. 12, pp. 2007–2015, 2013.

[24] D. Strmcnik *et al.*, "Improving the hydrogen oxidation reaction rate by promotion of hydroxyl adsorption," *Nat. Chem.*, vol. 5, no. 4, pp. 300–306, 2013.

[25] L. Han, S. Dong, and E. Wang, "Transition-Metal (Co, Ni, and Fe)-Based Electrocatalysts for the Water Oxidation Reaction," *Advanced Materials*, vol. 28, no. 42. John Wiley & Sons, Ltd, pp. 9266–9291, 01-Nov-2016.

[26] F. Yu, L. Yu, I. K. Mishra, Y. Yu, Z. F. Ren, and H. Q. Zhou, "Recent developments in earth-abundant and non-noble electrocatalysts for water electrolysis," *Materials Today Physics*, vol. 7. pp. 121–138, 2018.

[27] A. Parra-Puerto, K. L. Ng, K. Fahy, A. E. Goode, M. P. Ryan, and A. Kucernak, "Supported Transition Metal Phosphides: Activity Survey for HER, ORR, OER, and Corrosion Resistance in Acid and Alkaline Electrolytes," *ACS Catal.*, vol. 9, no. 12, pp. 11515–11529, 2019.

[28] Z. Zhao *et al.*, "Surface-Engineered PtNi-O Nanostructure with Record-High Performance for Electrocatalytic Hydrogen Evolution Reaction," *J. Am. Chem. Soc.*, vol. 140, no. 29, pp. 9046–9050, Jul. 2018.

[29] M. M. Rashid, M. K. Al Mesfer, H. Naseem, and M. Danish, "Hydrogen Production by Water Electrolysis: A Review of Alkaline Water Electrolysis, PEM Water Electrolysis and High Temperature Water Electrolysis," *Int. J. Eng. Adv. Technol.*, no. 3, pp. 2249–8958, 2015.

[30] A. Hauch *et al.*, "Recent advances in solid oxide cell technology for electrolysis," *Science (80-.).*, vol. 370, no. 6513, Oct. 2020.

[31] B. Pitschak and J. Mergel, "Electrolytic processes," *Hydrog. Fuel Cell Technol. Mark. Perspect.*, pp. 187–207, Jan. 2015.

[32] S. A. Grigoriev, V. N. Fateev, D. G. Bessarabov, and P. Millet, "Current status, research trends, and challenges in water electrolysis science and technology," *Int. J. Hydrogen Energy*, vol. 45, no. 49, pp. 26036–26058, Oct. 2020.

[33] S. Shiva Kumar and V. Himabindu, "Hydrogen production by PEM water electrolysis – A review," *Mater. Sci. Energy Technol.*, vol. 2, no. 3, pp. 442–454, Dec. 2019.

[34] W. Kreuter and H. Hofmann, "Electrolysis: the important energy transformer in a world of sustainable energy," *Int. J. Hydrogen Energy*, vol. 23, no. 8, pp. 661–666, Aug. 1998.

[35] D. M. F. Santos, C. A. C. Sequeira, and J. L. Figueiredo, "Hydrogen production

by alkaline water electrolysis," *Quim. Nova*, vol. 36, no. 8, pp. 1176–1193, 2013.

[36]   W. Ju *et al.*, "Lab-Scale Alkaline Water Electrolyzer for Bridging Material Fundamentals with Realistic Operation," *ACS Sustain. Chem. Eng.*, vol. 6, no. 4, pp. 4829–4837, Apr. 2018.

[37]   R. Phillips and C. W. Dunnill, "Zero gap alkaline electrolysis cell design for renewable energy storage as hydrogen gas," *RSC Adv.*, vol. 6, no. 102, pp. 100643–100651, Oct. 2016.

[38]   M. David, C. Ocampo-Martínez, and R. Sánchez-Peña, "Advances in alkaline water electrolyzers: A review," *J. Energy Storage*, vol. 23, pp. 392–403, Jun. 2019.

[39]   S. Marini, P. Salvi, P. Nelli, R. Pesenti, M. Villa, and Y. Kiros, "Oxygen evolution in alkali with gas diffusion electrodes," *Int. J. Hydrogen Energy*, vol. 38, no. 26, pp. 11496–11506, Aug. 2013.

[40]   M. Koj, J. Qian, and T. Turek, "Novel alkaline water electrolysis with nickel-iron gas diffusion electrode for oxygen evolution," *Int. J. Hydrogen Energy*, vol. 44, no. 57, pp. 29862–29875, Nov. 2019.

[41]   H. Dau, C. Limberg, T. Reier, M. Risch, S. Roggan, and P. Strasser, "The Mechanism of Water Oxidation: From Electrolysis via Homogeneous to Biological Catalysis," *ChemCatChem*, vol. 2, no. 7. pp. 724–761, 2010.

[42]   J. Rossmeisl, A. Logadottir, and J. K. Nørskov, "Electrolysis of water on (oxidized) metal surfaces," *Chem. Phys.*, vol. 319, no. 1–3, pp. 178–184, 2005.

[43]   J. K. Nørskov, T. Bligaard, B. Hvolbæk, F. Abild-Pedersen, I. Chorkendorff, and C. H. Christensen, "The nature of the active site in heterogeneous metal catalysis," *Chem. Soc. Rev.*, vol. 37, no. 10, pp. 2163–2171, Sep. 2008.

[44]   F. Lu, M. Zhou, Y. Zhou, and X. Zeng, "First-Row Transition Metal Based Catalysts for the Oxygen Evolution Reaction under Alkaline Conditions: Basic Principles and Recent Advances," *Small*, vol. 13, no. 45, p. 1701931, Dec. 2017.

[45]   M. Yu, E. Budiyanto, and H. Tüysüz, "Principles of Water Electrolysis and Recent Progress in Cobalt-, Nickel-, and Iron-Based Oxides for the Oxygen Evolution Reaction," *Angew. Chemie - Int. Ed.*, 2021.

[46]   M. Cooke, "The Art of Writing Reasonable Organic Reaction Mechanisms," *Phytochemistry*, vol. 60, no. 1, p. 99, May 2002.

[47] I. C. Man *et al.*, "Universality in Oxygen Evolution Electrocatalysis on Oxide Surfaces," *ChemCatChem*, vol. 3, no. 7, pp. 1159–1165, 2011.

[48] J. Rossmeisl, A. Logadottir, and J. K. Nørskov, "Electrolysis of water on (oxidized) metal surfaces," *Chem. Phys.*, vol. 319, no. 1–3, pp. 178–184, Dec. 2005.

[49] J. Rossmeisl, Z. W. Qu, H. Zhu, G. J. Kroes, and J. K. Nørskov, "Electrolysis of water on oxide surfaces," *J. Electroanal. Chem.*, vol. 607, no. 1–2, pp. 83–89, Sep. 2007.

[50] T. Reier, H. N. Nong, D. Teschner, R. Schlögl, and P. Strasser, "Electrocatalytic Oxygen Evolution Reaction in Acidic Environments – Reaction Mechanisms and Catalysts," *Adv. Energy Mater.*, vol. 7, no. 1, p. 1601275, Jan. 2017.

[51] H. B. Tao *et al.*, "Revealing Energetics of Surface Oxygen Redox from Kinetic Fingerprint in Oxygen Electrocatalysis," *J. Am. Chem. Soc.*, vol. 141, no. 35, pp. 13803–13811, Sep. 2019.

[52] E. Fabbri, A. Habereder, K. Waltar, R. Kötz, and T. J. Schmidt, "Developments and perspectives of oxide-based catalysts for the oxygen evolution reaction," *Catal. Sci. Technol.*, vol. 4, no. 11, pp. 3800–3821, 2014.

[53] K. S. Exner, "Is Thermodynamics a Good Descriptor for the Activity? Re-Investigation of Sabatier's Principle by the Free Energy Diagram in Electrocatalysis," *ACS Catal.*, pp. 5320–5329, 2019.

[54] J. Cheng, P. Hu, P. Ellis, S. French, G. Kelly, and C. M. Lok, "Brønsted-Evans-Polanyi relation of multistep reactions and volcano curve in heterogeneous catalysis," *J. Phys. Chem. C*, vol. 112, no. 5, pp. 1308–1311, Feb. 2008.

[55] H. Ooka, J. Huang, and K. S. Exner, "The Sabatier Principle in Electrocatalysis: Basics, Limitations, and Extensions," *Front. Energy Res.*, vol. 9, p. 155, May 2021.

[56] R. A. V. Santen, M. Neurock, and S. G. Shetty, "Reactivity theory of transition-metal surfaces: A brønsted-evans- polanyi linear activation energy-free-energy analysis," *Chem. Rev.*, vol. 110, no. 4, pp. 2005–2048, Apr. 2010.

[57] M. T. M. Koper, "Analysis of electrocatalytic reaction schemes: Distinction between rate-determining and potential-determining steps," *J. Solid State Electrochem.*, vol. 17, no. 2, pp. 339–344, Oct. 2013.

[58] M. T. M. Koper, "Thermodynamic theory of multi-electron transfer reactions:

Implications for electrocatalysis," *J. Electroanal. Chem.*, vol. 660, no. 2, pp. 254–260, Sep. 2011.

[59] G. Q. Han *et al.*, "Three dimensional nickel oxides/nickel structure by in situ electro-oxidation of nickel foam as robust electrocatalyst for oxygen evolution reaction," *Appl. Surf. Sci.*, vol. 359, pp. 172–176, Dec. 2015.

[60] X. Li, X. Hao, A. Abudula, and G. Guan, "Nanostructured catalysts for electrochemical water splitting: Current state and prospects," *J. Mater. Chem. A*, vol. 4, no. 31, pp. 11973–12000, Aug. 2016.

[61] V. Vij *et al.*, "Nickel-based electrocatalysts for energy-related applications: Oxygen reduction, oxygen evolution, and hydrogen evolution reactions," *ACS Catal.*, vol. 7, no. 10, pp. 7196–7225, 2017.

[62] F. Lyu, Q. Wang, S. M. Choi, and Y. Yin, "Noble-Metal-Free Electrocatalysts for Oxygen Evolution," *Small*, vol. 15, no. 1, p. 1804201, Jan. 2019.

[63] Y. Chen, K. Rui, J. Zhu, S. X. Dou, and W. Sun, "Recent Progress on Nickel-Based Oxide/(Oxy)Hydroxide Electrocatalysts for the Oxygen Evolution Reaction," *Chem. - A Eur. J.*, vol. 25, no. 3, pp. 703–713, Jan. 2019.

[64] Z. P. Wu, X. F. Lu, S. Q. Zang, and X. W. Lou, "Non-Noble-Metal-Based Electrocatalysts toward the Oxygen Evolution Reaction," *Adv. Funct. Mater.*, vol. 30, no. 15, p. 1910274, Apr. 2020.

[65] O. Diaz-Morales, I. Ledezma-Yanez, M. T. M. Koper, and F. Calle-Vallejo, "Guidelines for the Rational Design of Ni-Based Double Hydroxide Electrocatalysts for the Oxygen Evolution Reaction," *ACS Catal.*, vol. 5, no. 9, pp. 5380–5387, Aug. 2015.

[66] M. Alsabet, M. Grden, and G. Jerkiewicz, "Electrochemical Growth of Surface Oxides on Nickel. Part 1: Formation of α-Ni(OH) 2 in Relation to the Polarization Potential, Polarization Time, and Temperature," *Electrocatalysis*, vol. 2, no. 4, pp. 317–330, Dec. 2011.

[67] R. J. Smith, R. E. Hummel, and J. R. Ambrose, "The passivation of nickel in aqueous solutions-II. An in situ investigation of the passivation of nickel using optical and electrochemical techniques," *Corros. Sci.*, vol. 27, no. 8, pp. 815–826, Jan. 1987.

[68] M. E. G. Lyons and M. P. Brandon, "The oxygen evolution reaction on passive oxide covered transition metal electrodes in alkaline solution part ii - cobalt," *Int.*

J. Electrochem. Sci., vol. 3, no. 12, pp. 1425–1462, 2008.

[69] K. Juodkazis, J. Juodkazytė, R. Vilkauskaitė, and V. Jasulaitienė, "Nickel surface anodic oxidation and electrocatalysis of oxygen evolution," *J. Solid State Electrochem.*, vol. 12, no. 11, pp. 1469–1479, 2008.

[70] D. S. Hall, D. J. Lockwood, C. Bock, and B. R. MacDougall, "Nickel hydroxides and related materials: A review of their structures, synthesis and properties," *Proceedings of the Royal Society A: Mathematical, Physical and Engineering Sciences*, vol. 471, no. 2174. Royal Society of London, 08-Feb-2015.

[71] R. Subbaraman *et al.*, "Trends in activity for the water electrolyser reactions on 3d M(Ni,Co,Fe,Mn) hydr(oxy)oxide catalysts," *Nat. Mater.*, vol. 11, no. 6, pp. 550–557, May 2012.

[72] J. C. Conesa, "Electronic Structure of the (Undoped and Fe-Doped) NiOOH O2 Evolution Electrocatalyst," *J. Phys. Chem. C*, vol. 120, no. 34, pp. 18999–19010, Sep. 2016.

[73] Q. He *et al.*, "Nickel Vacancies Boost Reconstruction in Nickel Hydroxide Electrocatalyst," *ACS Energy Lett.*, vol. 3, no. 6, pp. 1373–1380, 2018.

[74] B. H. R. Suryanto, Y. Wang, R. K. Hocking, W. Adamson, and C. Zhao, "Overall electrochemical splitting of water at the heterogeneous interface of nickel and iron oxide," *Nat. Commun.*, vol. 10, no. 1, pp. 1–10, Dec. 2019.

[75] M. B. Stevens, C. D. M. Trang, L. J. Enman, J. Deng, and S. W. Boettcher, "Reactive Fe-Sites in Ni/Fe (Oxy)hydroxide Are Responsible for Exceptional Oxygen Electrocatalysis Activity," *J. Am. Chem. Soc.*, vol. 139, no. 33, pp. 11361–11364, Aug. 2017.

[76] Y. Jin, S. Huang, X. Yue, H. Du, and P. K. Shen, "Mo- and Fe-Modified Ni(OH)2/NiOOH Nanosheets as Highly Active and Stable Electrocatalysts for Oxygen Evolution Reaction," *ACS Catal.*, vol. 8, no. 3, pp. 2359–2363, Mar. 2018.

[77] D. A. Corrigan, "The Catalysis of the Oxygen Evolution Reaction by Iron Impurities in Thin Film Nickel Oxide Electrodes," *J. Electrochem. Soc.*, vol. 134, no. 2, pp. 377–384, 1987.

[78] D. Friebel *et al.*, "Identification of highly active Fe sites in (Ni,Fe)OOH for electrocatalytic water splitting," *J. Am. Chem. Soc.*, vol. 137, no. 3, pp. 1305–1313, Jan. 2015.

[79] L. Trotochaud, S. L. Young, J. K. Ranney, and S. W. Boettcher, "Nickel-Iron oxyhydroxide oxygen-evolution electrocatalysts: The role of intentional and incidental iron incorporation," *J. Am. Chem. Soc.*, vol. 136, no. 18, pp. 6744–6753, May 2014.

[80] J. Wang *et al.*, "Non-precious-metal catalysts for alkaline water electrolysis: Operando characterizations, theoretical calculations, and recent advances," *Chem. Soc. Rev.*, vol. 49, no. 24, pp. 9154–9196, Dec. 2020.

[81] S. Wang, A. Lu, and C. J. Zhong, "Hydrogen production from water electrolysis: role of catalysts," *Nano Converg.*, vol. 8, no. 1, pp. 1–23, Feb. 2021.

[82] C. Han *et al.*, "Catalytic Activity Boosting of Nickel Sulfide toward Oxygen Evolution Reaction via Confined Overdoping Engineering," *ACS Appl. Energy Mater.*, vol. 2, no. 8, pp. 5363–5372, Aug. 2019.

[83] J. Wang *et al.*, "Recent progresses of micro-nanostructured transition metal compound-based electrocatalysts for energy conversion technologies," *Sci. China Mater.*, vol. 64, no. 1, pp. 1–26, Sep. 2021.

[84] S. Jin, "Are Metal Chalcogenides, Nitrides, and Phosphides Oxygen Evolution Catalysts or Bifunctional Catalysts?," *ACS Energy Lett.*, vol. 2, no. 8, pp. 1937–1938, Aug. 2017.

[85] Q. Shao, P. Wang, and X. Huang, "Opportunities and Challenges of Interface Engineering in Bimetallic Nanostructure for Enhanced Electrocatalysis," *Adv. Funct. Mater.*, vol. 29, no. 3, p. 1806419, Jan. 2019.

[86] J. Feng *et al.*, "Iridium-Based Multimetallic Porous Hollow Nanocrystals for Efficient Overall-Water-Splitting Catalysis," *Adv. Mater.*, vol. 29, no. 47, p. 1703798, Dec. 2017.

[87] X. Li, W. Xue, R. Mo, S. Yang, H. Li, and J. Zhong, "In situ growth of minimal Ir-incorporated CoxNi1-xO nanowire arrays on Ni foam with improved electrocatalytic activity for overall water splitting," *Chinese J. Catal.*, vol. 40, no. 10, pp. 1576–1584, Oct. 2019.

[88] S. Li *et al.*, "Ir-O-V Catalytic Group in Ir-Doped NiV(OH)2 for Overall Water Splitting," *ACS Energy Lett.*, vol. 4, no. 8, pp. 1823–1829, Aug. 2019.

[89] A. Wang, J. Li, and T. Zhang, "Heterogeneous single-atom catalysis," *Nature Reviews Chemistry*, vol. 2, no. 6. Nature Publishing Group, pp. 65–81, 01-Jun-2018.

[90]   X. Cui, W. Li, P. Ryabchuk, K. Junge, and M. Beller, "Bridging homogeneous and heterogeneous catalysis by heterogeneous single-metal-site catalysts," *Nat. Catal.*, vol. 1, no. 6, pp. 385–397, Jun. 2018.

[91]   P. Li *et al.*, "Boosting oxygen evolution of single-atomic ruthenium through electronic coupling with cobalt-iron layered double hydroxides," *Nat. Commun.*, vol. 10, no. 1, pp. 1–11, Dec. 2019.

[92]   X. Luo *et al.*, "Single-Atom Ir-Anchored 3D Amorphous NiFe Nanowire@Nanosheets for Boosted Oxygen Evolution Reaction," *ACS Appl. Mater. Interfaces*, vol. 12, no. 3, pp. 3539–3546, Jan. 2020.

[93]   J. Zhang *et al.*, "Single-Atom Au/NiFe Layered Double Hydroxide Electrocatalyst: Probing the Origin of Activity for Oxygen Evolution Reaction," *J. Am. Chem. Soc.*, vol. 140, no. 11, pp. 3876–3879, Mar. 2018.

[94]   J. D. Benck, T. R. Hellstern, J. Kibsgaard, P. Chakthranont, and T. F. Jaramillo, "Catalyzing the hydrogen evolution reaction (HER) with molybdenum sulfide nanomaterials," *ACS Catal.*, vol. 4, no. 11, pp. 3957–3971, Oct. 2014.

[95]   A. Peugeot, C. E. Creissen, D. Karapinar, H. N. Tran, M. Schreiber, and M. Fontecave, "Benchmarking of oxygen evolution catalysts on porous nickel supports," *Joule*, vol. 5, no. 5, pp. 1281–1300, May 2021.

[96]   P. Wang, T. Jia, and B. Wang, "A critical review: 1D/2D nanostructured self-supported electrodes for electrochemical water splitting," *J. Power Sources*, vol. 474, p. 228621, Oct. 2020.

[97]   Y. J. Kim *et al.*, "Highly efficient oxygen evolution reaction via facile bubble transport realized by three-dimensionally stack-printed catalysts," *Nat. Commun.*, vol. 11, no. 1, pp. 1–11, Oct. 2020.

[98]   J. Zhang *et al.*, "Cation vacancy stabilization of single-atomic-site Pt 1 /Ni(OH) x catalyst for diboration of alkynes and alkenes," *Nat. Commun.*, vol. 9, no. 1, pp. 1–8, Mar. 2018.

[99]   Y. Zhao *et al.*, "Ni3+ doped monolayer layered double hydroxide nanosheets as efficient electrodes for supercapacitors," *Nanoscale*, vol. 7, no. 16, pp. 7168–7173, Apr. 2015.

[100]   Z. Fu, J. Hu, W. Hu, S. Yang, and Y. Luo, "Quantitative analysis of Ni 2+ /Ni 3+ in Li[Ni x Mn y Co z]O 2 cathode materials: Non-linear least-squares fitting of XPS spectra," *Appl. Surf. Sci.*, vol. 441, pp. 1048–1056, May 2018.

[101] T. Kadyk, D. Bruce, and M. Eikerling, "How to Enhance Gas Removal from Porous Electrodes?," *Sci. Rep.*, vol. 6, no. 1, pp. 1–14, Dec. 2016.

[102] P. Van Der Linde *et al.*, "Gas bubble evolution on microstructured silicon substrates," *Energy Environ. Sci.*, vol. 11, no. 12, pp. 3452–3462, Dec. 2018.

[103] H. T. Phan, N. Caney, P. Marty, S. Colasson, and J. Gavillet, "Surface wettability control by nanocoating: The effects on pool boiling heat transfer and nucleation mechanism," *Int. J. Heat Mass Transf.*, vol. 52, no. 23–24, pp. 5459–5471, Nov. 2009.

[104] J. Hao, W. Yang, Z. Huang, and C. Zhang, "Superhydrophilic and Superaerophobic Copper Phosphide Microsheets for Efficient Electrocatalytic Hydrogen and Oxygen Evolution," *Adv. Mater. Interfaces*, vol. 3, no. 16, p. 1600236, Aug. 2016.

[105] X. Shan *et al.*, "An Engineered Superhydrophilic/Superaerophobic Electrocatalyst Composed of the Supported CoMoSx Chalcogel for Overall Water Splitting," *Angew. Chemie - Int. Ed.*, vol. 59, no. 4, pp. 1659–1665, Jan. 2020.

[106] F. Li, D. Zhang, R. C. Xu, W. F. Fu, and X. J. Lv, "Superhydrophilic Heteroporous MoS2/Ni3S2 for Highly Efficient Electrocatalytic Overall Water Splitting," *ACS Appl. Energy Mater.*, vol. 1, no. 8, pp. 3929–3936, Aug. 2018.

[107] H. Zhao and Z. Y. Yuan, "Surface/interface engineering of high-efficiency noble metal-free electrocatalysts for energy-related electrochemical reactions," *J. Energy Chem.*, vol. 54, pp. 89–104, Mar. 2021.

[108] Z. Lu *et al.*, "Ultrahigh hydrogen evolution performance of under-water 'superaerophobic' MoS2 nanostructured electrodes," *Adv. Mater.*, vol. 26, no. 17, pp. 2683–2687, May 2014.

[109] D. I. Yu *et al.*, "Wetting state on hydrophilic and hydrophobic micro-textured surfaces: Thermodynamic analysis and X-ray visualization," *Appl. Phys. Lett.*, vol. 106, no. 17, p. 171602, Apr. 2015.

[110] M. Hao *et al.*, "Hydrogen Bubble Templating of Fractal Ni Catalysts for Water Oxidation in Alkaline Media," *ACS Appl. Energy Mater.*, vol. 2, no. 8, pp. 5734–5743, Aug. 2019.

[111] A. Synytska, L. Ionov, K. Grundke, and M. Stamm, "Wetting on fractal superhydrophobic surfaces from 'core-shell' particles: A comparison of theory

and experiment," *Langmuir*, vol. 25, no. 5, pp. 3132–3136, Mar. 2009.

[112] F. Yang, M. J. Kim, M. Brown, and B. J. Wiley, "Alkaline Water Electrolysis at 25 A cm−2 with a Microfibrous Flow-through Electrode," *Adv. Energy Mater.*, vol. 10, no. 25, p. 2001174, Jul. 2020.

[113] R. Iwata *et al.*, "Bubble growth and departure modes on wettable/non-wettable porous foams in alkaline water splitting," *Joule*, vol. 5, no. 4, pp. 887–900, Apr. 2021.

[114] T. Kou *et al.*, "Periodic Porous 3D Electrodes Mitigate Gas Bubble Traffic during Alkaline Water Electrolysis at High Current Densities," *Adv. Energy Mater.*, vol. 10, no. 46, p. 2002955, Dec. 2020.

[115] G. F. Li, M. Divinagracia, M. F. Labata, J. D. Ocon, and P. Y. Abel Chuang, "Electrolyte-Dependent Oxygen Evolution Reactions in Alkaline Media: Electrical Double Layer and Interfacial Interactions," *ACS Appl. Mater. Interfaces*, vol. 11, no. 37, pp. 33748–33758, Sep. 2019.

[116] K. Bromberger, J. Ghinaiya, T. Lickert, A. Fallisch, and T. Smolinka, "Hydraulic ex situ through-plane characterization of porous transport layers in PEM water electrolysis cells," *Int. J. Hydrogen Energy*, vol. 43, no. 5, pp. 2556–2569, Feb. 2018.

[117] S. Ravi, R. Dharmarajan, and S. Moghaddam, "Measurement of Capillary Radius and Contact Angle within Porous Media," *Langmuir*, vol. 31, no. 47, pp. 12954–12959, Nov. 2015.

[118] J. Zhang *et al.*, "Electrochemical Preparation and Post-treatment of Composite Porous Foam NiZn Alloy Electrodes with High Activity for Hydrogen Evolution," *Sci. Reports 2018 81*, vol. 8, no. 1, pp. 1–8, Oct. 2018.

[119] J. H. Donaldson, J. D. Istok, M. D. Humphrey, K. T. O'Reilly, C. A. Hawelka, and D. H. Mohr, "Development and Testing of a Kinetic Model for Oxygen Transport in Porous Media in the Presence of Trapped Gas," *Groundwater*, vol. 35, no. 2, pp. 270–279, Mar. 1997.

[120] C. Li *et al.*, "Electrochemical Deposition: An Advanced Approach for Templated Synthesis of Nanoporous Metal Architectures," *Acc. Chem. Res.*, vol. 51, no. 8, pp. 1764–1773, Aug. 2018.

[121] S. W. Chee, S. F. Tan, Z. Baraissov, M. Bosman, and U. Mirsaidov, "Direct observation of the nanoscale Kirkendall effect during galvanic replacement

reactions," *Nat. Commun. 2017 81*, vol. 8, no. 1, pp. 1–8, Oct. 2017.

[122] A. Papaderakis, I. Mintsouli, J. Georgieva, and S. Sotiropoulos, "Electrocatalysts Prepared by Galvanic Replacement," *Catal. 2017, Vol. 7, Page 80*, vol. 7, no. 3, p. 80, Mar. 2017.

[123] A. Papaderakis *et al.*, "Oxygen Evolution at IrO2 Shell-Ir-Ni Core Electrodes Prepared by Galvanic Replacement," *J. Phys. Chem. C*, vol. 120, no. 36, pp. 19995–20005, 2016.

[124] J. F. Moulder, W. F. Stickle, P. E. Sobol, and K. D. Bomben, "Handbook of X-ray Photoelectron Spectroscopy Edited by," *Google Sch.*, pp. 1–261, 1993.

[125] G. Li and P. Y. A. Chuang, "Identifying the forefront of electrocatalytic oxygen evolution reaction: Electronic double layer," *Appl. Catal. B Environ.*, vol. 239, pp. 425–432, Dec. 2018.

[126] A. Lasia, *Electrochemical impedance spectroscopy and its applications*, vol. 9781461489. Springer New York, 2014.

[127] J. B. Jorcin, M. E. Orazem, N. Pébère, and B. Tribollet, "CPE analysis by local electrochemical impedance spectroscopy," *Electrochim. Acta*, vol. 51, no. 8–9, pp. 1473–1479, Jan. 2006.

[128] G. J. Brug, A. L. G. van den Eeden, M. Sluyters-Rehbach, and J. H. Sluyters, "The analysis of electrode impedances complicated by the presence of a constant phase element," *J. Electroanal. Chem.*, vol. 176, no. 1–2, pp. 275–295, Sep. 1984.

[129] R. Kant and M. B. Singh, "Theory of the Electrochemical Impedance of Mesostructured Electrodes Embedded with Heterogeneous Micropores," *J. Phys. Chem. C*, vol. 121, no. 13, pp. 7164–7174, Apr. 2017.

[130] M. Itagaki, Y. Hatada, I. Shitanda, and K. Watanabe, "Complex impedance spectra of porous electrode with fractal structure," *Electrochim. Acta*, vol. 55, no. 21, pp. 6255–6262, Aug. 2010.

[131] R. de Levie, "Electrochemical Responses of Porous and Rough Electrodes," *Adv. Electrochem. Electrochem. Eng.*, vol. 6, no. 1, pp. 329-397., 1967.

[132] C. B. Scruby, "An introduction to acoustic emission," *J. Phys. E.*, vol. 20, no. 8, p. 946, Aug. 1987.

[133] M. Minnaert, " XVI. On musical air-bubbles and the sounds of running water ,"

London, Edinburgh, Dublin Philos. Mag. J. Sci., vol. 16, no. 104, pp. 235–248, Aug. 1933.

[134] A. Vazquez, R. Manasseh, and R. Chicharro, "Can acoustic emissions be used to size bubbles seeping from a sediment bed?," *Chem. Eng. Sci.*, vol. 131, pp. 187–196, Jul. 2015.

[135] M. A. Hickner, "Strategies for developing new anion exchange membranes and electrode ionomers," *Electrochem. Soc. Interface*, vol. 26, no. 1, pp. 69–73, Apr. 2017.

[136] K. F. L. Hagesteijn, S. Jiang, and B. P. Ladewig, "A review of the synthesis and characterization of anion exchange membranes," *J. Mater. Sci.*, vol. 53, no. 16, pp. 11131–11150, Aug. 2018.

[137] Y. Zheng *et al.*, "Water Uptake Study of Anion Exchange Membranes," *Macromolecules*, vol. 51, no. 9, pp. 3264–3278, May 2018.

[138] E. M. Schibli, A. G. Wright, S. Holdcroft, and B. J. Frisken, "Morphology of Anion-Conducting Ionenes Investigated by X-ray Scattering and Simulation," *J. Phys. Chem. B*, vol. 122, no. 5, pp. 1730–1737, Feb. 2018.

[139] X. Luo, A. Wright, T. Weissbach, and S. Holdcroft, "Water permeation through anion exchange membranes," *J. Power Sources*, vol. 375, pp. 442–451, Jan. 2018.

[140] D. A. Corrigan, "The Catalysis of the Oxygen Evolution Reaction by Iron Impurities in Thin Film Nickel Oxide Electrodes," *J. Electrochem. Soc.*, vol. 134, no. 2, pp. 377–384, Feb. 1987.

[141] L. Trotochaud, S. L. Young, J. K. Ranney, and S. W. Boettcher, "Nickel-Iron oxyhydroxide oxygen-evolution electrocatalysts: The role of intentional and incidental iron incorporation," *J. Am. Chem. Soc.*, vol. 136, no. 18, pp. 6744–6753, May 2014.

[142] F. Lu, M. Zhou, Y. Zhou, and X. Zeng, "First-Row Transition Metal Based Catalysts for the Oxygen Evolution Reaction under Alkaline Conditions: Basic Principles and Recent Advances," *Small*, vol. 13, no. 45, p. 1701931, Dec. 2017.

[143] N. T. Suen, S. F. Hung, Q. Quan, N. Zhang, Y. J. Xu, and H. M. Chen, "Electrocatalysis for the oxygen evolution reaction: Recent development and future perspectives," *Chem. Soc. Rev.*, vol. 46, no. 2, pp. 337–365, Jan. 2017.

[144] J. S. Kim, B. Kim, H. Kim, and K. Kang, "Recent Progress on Multimetal Oxide

Catalysts for the Oxygen Evolution Reaction," *Adv. Energy Mater.*, vol. 8, no. 11, p. 1702774, Apr. 2018.

[145] G. Feng, Y. Kuang, Y. Li, and X. Sun, "Three-dimensional porous superaerophobic nickel nanoflower electrodes for high-performance hydrazine oxidation," *Nano Res.*, vol. 8, no. 10, pp. 3365–3371, Oct. 2015.

[146] Q. Zhang, P. Li, D. Zhou, Z. Chang, Y. Kuang, and X. Sun, "Superaerophobic Ultrathin Ni–Mo Alloy Nanosheet Array from In Situ Topotactic Reduction for Hydrogen Evolution Reaction," *Small*, vol. 13, no. 41, p. 1701648, Nov. 2017.

[147] J. He, B. Hu, and Y. Zhao, "Superaerophobic Electrode with Metal@Metal-Oxide Powder Catalyst for Oxygen Evolution Reaction," *Adv. Funct. Mater.*, vol. 26, no. 33, pp. 5998–6004, Sep. 2016.

[148] Y. Li, H. Zhang, M. Jiang, Y. Kuang, X. Sun, and X. Duan, "Ternary NiCoP nanosheet arrays: An excellent bifunctional catalyst for alkaline overall water splitting," *Nano Res.*, vol. 9, no. 8, pp. 2251–2259, Aug. 2016.

[149] M. S. Faber, R. Dziedzic, M. A. Lukowski, N. S. Kaiser, Q. Ding, and S. Jin, "High-performance electrocatalysis using metallic cobalt pyrite (CoS 2) micro- and nanostructures," *J. Am. Chem. Soc.*, vol. 136, no. 28, pp. 10053–10061, Jul. 2014.

[150] Y. Li *et al.*, "Under-Water Superaerophobic Pine-Shaped Pt Nanoarray Electrode for Ultrahigh-Performance Hydrogen Evolution," *Adv. Funct. Mater.*, vol. 25, no. 11, pp. 1737–1744, Mar. 2015.

[151] P. A. Van Aken and B. Liebscher, "Quantification of ferrous/ferric ratios in minerals: New evaluation schemes of Fe L23 electron energy-loss near-edge spectra," *Phys. Chem. Miner.*, vol. 29, no. 3, pp. 188–200, Apr. 2002.

[152] M. H. Martin, J. Galipaud, A. Tranchot, L. Roué, and D. Guay, "Measurements of hydrogen solubility in CuxPd100-x thin films," *Electrochim. Acta*, vol. 90, pp. 615–622, 2013.

[153] M. Alsabet, M. Grden, and G. Jerkiewicz, "Electrochemical Growth of Surface Oxides on Nickel. Part 1: Formation of α-Ni(OH) 2 in Relation to the Polarization Potential, Polarization Time, and Temperature," *Electrocatalysis*, vol. 2, no. 4, pp. 317–330, 2011.

[154] R. F. Scarr, "The Mechanism of Oxygen Evolution on Nickel, Platinum, and Other Metals and Alloys," *J. Electrochem. Soc.*, vol. 116, no. 11, p. 1526, Nov.

1969.

[155] M. R. Gennero de Chialvo and A. C. Chialvo, "Oxygen evolution reaction on thick hydrous nickel oxide electrodes," *Electrochim. Acta*, vol. 33, no. 6, pp. 825–830, Jun. 1988.

[156] M. E. G. Lyons and M. P. Brandon, "A comparative study of the oxygen evolution reaction on oxidised nickel, cobalt and iron electrodes in base," *J. Electroanal. Chem.*, vol. 641, no. 1–2, pp. 119–130, Mar. 2010.

[157] T. Zhou *et al.*, "Transition metal ions regulated oxygen evolution reaction performance of Ni-based hydroxides hierarchical nanoarrays," *Sci. Rep.*, vol. 7, no. 1, p. 46154, Dec. 2017.

[158] A. Lasia, "Impedance of Porous Electrodes," in *Electrochemical Impedance Spectroscopy and its Applications*, New York, NY: Springer New York, 2014, pp. 203–250.

[159] C. Hitz and A. Lasia, "Experimental study and modeling of impedance of the her on porous Ni electrodes," *J. Electroanal. Chem.*, vol. 500, no. 1–2, pp. 213–222, Mar. 2001.

[160] F. Seland, R. Tunold, and D. A. Harrington, "Impedance study of methanol oxidation on platinum electrodes," *Electrochim. Acta*, vol. 51, no. 18, pp. 3827–3840, May 2006.

[161] T. S. Ramulu *et al.*, "Nanowires array modified electrode for enhanced electrochemical detection of nucleic acid," *Biosens. Bioelectron.*, vol. 40, no. 1, pp. 258–264, Feb. 2013.

[162] X. Zhang, D. Li, L. Bourgeois, H. Wang, and P. A. Webley, "Direct electrodeposition of porous gold nanowire arrays for biosensing applications," *ChemPhysChem*, vol. 10, no. 2, pp. 436–441, Feb. 2009.

[163] D. A. Harrington and P. Van Den Driessche, "Mechanism and equivalent circuits in electrochemical impedance spectroscopy," *Electrochim. Acta*, vol. 56, no. 23, pp. 8005–8013, Sep. 2011.

[164] H. K. Mutha *et al.*, "Porosimetry and packing morphology of vertically aligned carbon nanotube arrays via impedance spectroscopy," *Nanotechnology*, vol. 28, no. 5, p. 05LT01, Feb. 2017.

[165] R. Jurczakowski, C. Hitz, and A. Lasia, "Impedance of porous Au based electrodes," *J. Electroanal. Chem.*, vol. 572, no. 2, pp. 355–366, Nov. 2004.

[166] R. Jurczakowski, C. Hitz, and A. Lasia, "Impedance of porous gold electrodes in the presence of electroactive species," *J. Electroanal. Chem.*, vol. 582, no. 1–2, pp. 85–96, Aug. 2005.

[167] H. Keiser, K. D. Beccu, and M. A. Gutjahr, "Abschätzung der porenstruktur poröser elektroden aus impedanzmessungen," *Electrochim. Acta*, vol. 21, no. 8, pp. 539–543, Aug. 1976.

[168] N. T. Suen, S. F. Hung, Q. Quan, N. Zhang, Y. J. Xu, and H. M. Chen, "Electrocatalysis for the oxygen evolution reaction: Recent development and future perspectives," *Chemical Society Reviews*, vol. 46, no. 2. Royal Society of Chemistry, pp. 337–365, 21-Jan-2017.

[169] Y. Cheng and S. P. Jiang, "Advances in electrocatalysts for oxygen evolution reaction of water electrolysis-from metal oxides to carbon nanotubes," *Prog. Nat. Sci. Mater. Int.*, vol. 25, no. 6, pp. 545–553, 2015.

[170] J. Suntivich, K. J. May, H. A. Gasteiger, J. B. Goodenough, and Y. Shao-Horn, "A perovskite oxide optimized for oxygen evolution catalysis from molecular orbital principles," *Science (80-.).*, vol. 334, no. 6061, pp. 1383–1385, Dec. 2011.

[171] M. Li *et al.*, "Facile synthesis of electrospun MFe2O4 (M = Co, Ni, Cu, Mn) spinel nanofibers with excellent electrocatalytic properties for oxygen evolution and hydrogen peroxide reduction," *Nanoscale*, vol. 7, no. 19, pp. 8920–8930, 2015.

[172] Q. Kang *et al.*, "Effect of interlayer spacing on the activity of layered manganese oxide bilayer catalysts for the oxygen evolution reaction," *J. Am. Chem. Soc.*, vol. 139, no. 5, pp. 1863–1870, 2017.

[173] O. Diaz-Morales, D. Ferrus-Suspedra, and M. T. M. Koper, "The importance of nickel oxyhydroxide deprotonation on its activity towards electrochemical water oxidation," *Chem. Sci.*, vol. 7, no. 4, pp. 2639–2645, Mar. 2016.

[174] K. Zeng and D. Zhang, "Recent progress in alkaline water electrolysis for hydrogen production and applications," *Prog. Energy Combust. Sci.*, vol. 36, no. 3, pp. 307–326, 2010.

[175] H. Cheng, K. Scott, and C. Ramshaw, "Intensification of Water Electrolysis in a Centrifugal Field," *J. Electrochem. Soc.*, vol. 149, no. 11, p. D172, Oct. 2002.

[176] M. Wang, Z. Wang, and Z. Guo, "Understanding of the intensified effect of super gravity on hydrogen evolution reaction," *Int. J. Hydrogen Energy*, vol. 34, no. 13,

pp. 5311–5317, Jul. 2009.

[177] M. Wang, Z. Wang, and Z. Guo, "Water electrolysis enhanced by super gravity field for hydrogen production," *Int. J. Hydrogen Energy*, vol. 35, no. 8, pp. 3198–3205, Apr. 2010.

[178] S. De Li, C. C. Wang, and C. Y. Chen, "Water electrolysis in the presence of an ultrasonic field," *Electrochim. Acta*, vol. 54, no. 15, pp. 3877–3883, Jun. 2009.

[179] Z. Lu, Y. Li, X. Lei, J. Liu, and X. Sun, "Nanoarray based 'superaerophobic' surfaces for gas evolution reaction electrodes," *Mater. Horizons*, vol. 2, no. 3, pp. 294–298, 2015.

[180] Y. Li, P. Hasin, and Y. Wu, "NixCo3-XO4 nanowire arrays for electrocatalytic oxygen evolution," *Adv. Mater.*, vol. 22, no. 17, pp. 1926–1929, May 2010.

[181] B. Lu, D. Cao, P. Wang, G. Wang, and Y. Gao, "Oxygen evolution reaction on Ni-substituted Co3O4 nanowire array electrodes," *Int. J. Hydrogen Energy*, vol. 36, no. 1, pp. 72–78, Jan. 2011.

[182] Z. Lu *et al.*, "Three-dimensional NiFe layered double hydroxide film for high-efficiency oxygen evolution reaction," *Chem. Commun.*, vol. 50, no. 49, pp. 6479–6482, May 2014.

[183] X. Liu *et al.*, "Hierarchical Zn x Co3-xO4 nanoarrays with high activity for electrocatalytic oxygen evolution," *Chem. Mater.*, vol. 26, no. 5, pp. 1889–1895, Mar. 2014.

[184] Q. Yang, T. Li, Z. Lu, X. Sun, and J. Liu, "Hierarchical construction of an ultrathin layered double hydroxide nanoarray for highly-efficient oxygen evolution reaction," *Nanoscale*, vol. 6, no. 20, pp. 11789–11794, Sep. 2014.

[185] D. Kong, H. Wang, Z. Lu, and Y. Cui, "CoSe2 nanoparticles grown on carbon fiber paper: An efficient and stable electrocatalyst for hydrogen evolution reaction," *J. Am. Chem. Soc.*, vol. 136, no. 13, pp. 4897–4900, Apr. 2014.

[186] D. H. Nam, R. H. Kim, D. W. Han, and H. S. Kwon, "Electrochemical performances of Sn anode electrodeposited on porous Cu foam for Li-ion batteries," *Electrochim. Acta*, vol. 66, pp. 126–132, Apr. 2012.

[187] M. G. Jeong, K. Zhuo, S. Cherevko, W. J. Kim, and C. H. Chung, "Facile preparation of three-dimensional porous hydrous ruthenium oxide electrode for supercapacitors," *J. Power Sources*, vol. 244, pp. 806–811, Dec. 2013.

[188] X. Niu, H. Zhao, C. Chen, and M. Lan, "Enhancing the Electrocatalytic Activity of Pt-Pd Catalysts by Introducing Porous Architectures," *ChemCatChem*, vol. 5, no. 6, pp. 1416–1425, Jun. 2013.

[189] Y. Wang, H. Arandiyan, J. Scott, A. Bagheri, H. Dai, and R. Amal, "Recent advances in ordered meso/macroporous metal oxides for heterogeneous catalysis: A review," *J. Mater. Chem. A*, vol. 5, no. 19, pp. 8825–8846, May 2017.

[190] P. Los, A. Lasia, H. Ménard, and L. Brossard, "Impedance studies of porous lanthanum-phosphate-bonded nickel electrodes in concentrated sodium hydroxide solution," *J. Electroanal. Chem.*, vol. 360, no. 1–2, pp. 101–118, Nov. 1993.

[191] A. Lasia, "Impedance of porous electrodes," *J. Electroanal. Chem.*, vol. 397, no. 1–2, pp. 27–33, Nov. 1995.

[192] R. K. Shervedani and A. Lasia, "Kinetics of Hydrogen Evolution Reaction on Nickel-Zinc-Phosphorous Electrodes," *J. Electrochem. Soc.*, vol. 144, no. 8, pp. 2652–2657, Aug. 1997.

[193] A. Lasia, "Nature of the two semi-circles observed on the complex plane plots on porous electrodes in the presence of a concentration gradient," *J. Electroanal. Chem.*, vol. 500, no. 1–2, pp. 30–35, Mar. 2001.

[194] H. C. Shin, J. Dong, and M. Liu, "Nanoporous Structures Prepared by an Electrochemical Deposition Process," *Adv. Mater.*, vol. 15, no. 19, pp. 1610–1614, Oct. 2003.

[195] H. C. Shin and M. Liu, "Copper foam structures with highly porous nanostructured walls," *Chem. Mater.*, vol. 16, no. 25, pp. 5460–5464, 2004.

[196] C. González-Buch, I. Herraiz-Cardona, E. Ortega, J. García-Antón, and V. Pérez-Herranz, "Study of the catalytic activity of 3D macroporous Ni and NiMo cathodes for hydrogen production by alkaline water electrolysis," *J. Appl. Electrochem.*, vol. 46, no. 7, pp. 791–803, Jul. 2016.

[197] M. Fan, S. Garbarino, G. A. Botton, A. C. Tavares, and D. Guay, "Selective electroreduction of CO2 to formate on 3D [100] Pb dendrites with nanometer-sized needle-like tips," *J. Mater. Chem. A*, vol. 5, no. 39, pp. 20747–20756, Oct. 2017.

[198] H. C. Shin and M. Liu, "Three-dimensional porous copper-tin alloy electrodes for rechargeable lithium batteries," *Adv. Funct. Mater.*, vol. 15, no. 4, pp. 582–

586, Apr. 2005.

[199] S. Cherevko and C. H. Chung, "Impact of key deposition parameters on the morphology of silver foams prepared by dynamic hydrogen template deposition," *Electrochim. Acta*, vol. 55, no. 22, pp. 6383–6390, Sep. 2010.

[200] Y. Li, Y. Y. Song, C. Yang, and X. H. Xia, "Hydrogen bubble dynamic template synthesis of porous gold for nonenzymatic electrochemical detection of glucose," *Electrochem. commun.*, vol. 9, no. 5, pp. 981–988, May 2007.

[201] S. Cherevko, X. Xing, and C. H. Chung, "Hydrogen template assisted electrodeposition of sub-micrometer wires composing honeycomb-like porous Pb films," *Appl. Surf. Sci.*, vol. 257, no. 18, pp. 8054–8061, Jul. 2011.

[202] J. Yin, J. Jia, and L. Zhu, "Macroporous Pt modified glassy carbon electrode: Preparation and electrocatalytic activity for methanol oxidation," *Int. J. Hydrogen Energy*, vol. 33, no. 24, pp. 7444–7447, Dec. 2008.

[203] K. Zhuo, M. G. Jeong, and C. H. Chung, "Highly porous dendritic Ni-Sn anodes for lithium-ion batteries," *J. Power Sources*, vol. 244, pp. 601–605, 2013.

[204] B. J. Plowman, L. A. Jones, and S. K. Bhargava, "Building with bubbles: the formation of high surface area honeycomb-like films via hydrogen bubble templated electrodeposition," *Chem. Commun.*, vol. 51, no. 21, pp. 4331–4346, Feb. 2015.

[205] Ying Li, Wen-Zhi Jia, and Yan-Yan Song, and X.-H. Xia*, "Superhydrophobicity of 3D Porous Copper Films Prepared Using the Hydrogen Bubble Dynamic Template," *Chem. Mater.*, vol. 19, no. 23, pp. 5758–5764, Nov. 2007.

[206] G. Ou *et al.,* "Large-scale hierarchical oxide nanostructures for high-performance electrocatalytic water splitting," *Nano Energy*, vol. 35, pp. 207–214, May 2017.

[207] S. H. Ahn *et al.,* "Effect of morphology of electrodeposited Ni catalysts on the behavior of bubbles generated during the oxygen evolution reaction in alkaline water electrolysis," *Chem. Commun.*, vol. 49, no. 81, pp. 9323–9325, 2013.

[208] R. D. Hazlett, "Fractal applications: Wettability and contact angle," *J. Colloid Interface Sci.*, vol. 137, no. 2, pp. 527–533, Jul. 1990.

[209] S. Shibuichi, T. Onda, N. Satoh, and K. Tsujii, "Super water-repellent surfaces resulting from fractal structure," *J. Phys. Chem.*, vol. 100, no. 50, pp. 19512–

19517, Dec. 1996.

[210] A. Synytska, L. Ionov, K. Grundke, and M. Stamm, "Wetting on fractal superhydrophobic surfaces from 'core-shell' particles: A comparison of theory and experiment," *Langmuir*, vol. 25, no. 5, pp. 3132–3136, Mar. 2009.

[211] R. L. Doyle, I. J. Godwin, M. P. Brandon, and M. E. G. Lyons, "Redox and electrochemical water splitting catalytic properties of hydrated metal oxide modified electrodes," *Phys. Chem. Chem. Phys.*, vol. 15, no. 33, pp. 13737–13783, Jul. 2013.

[212] Chao Zhang, Lihua Qian, Ke Zhang, Songliu Yuan, Junwu Xiao, and Shuai Wang, "Hierarchical porous Ni/NiO core–shells with superior conductivity for electrochemical pseudo-capacitors and glucose sensors," *J. Mater. Chem. A*, vol. 3, no. 19, pp. 10519–10525, May 2015.

[213] D. K. Bediako, B. Lassalle-Kaiser, Y. Surendranath, J. Yano, V. K. Yachandra, and D. G. Nocera, "Structure-activity correlations in a nickel-borate oxygen evolution catalyst," *J. Am. Chem. Soc.*, vol. 134, no. 15, pp. 6801–6809, Apr. 2012.

[214] H. K. Mutha *et al.*, "Porosimetry and packing morphology of vertically aligned carbon nanotube arrays via impedance spectroscopy," *Nanotechnology*, vol. 28, no. 5, 2017.

[215] M. Hao *et al.*, "Vertically Aligned Ni Nanowires as a Platform for Kinetically Limited Water-Splitting Electrocatalysis," *J. Phys. Chem. C*, vol. 123, no. 2, pp. 1082–1093, Jan. 2019.

[216] G. Paasch, K. Micka, and P. Gersdorf, "Theory of the electrochemical impedance of macrohomogeneous porous electrodes," *Electrochim. Acta*, vol. 38, no. 18, pp. 2653–2662, Dec. 1993.

[217] J. P. Candy, P. Fouilloux, M. Keddam, and H. Takenouti, "The characterization of porous electrodes by impedance measurements," *Electrochim. Acta*, vol. 26, no. 8, pp. 1029–1034, Aug. 1981.

[218] H. K. Song, Y. H. Jung, K. H. Lee, and L. H. Dao, "Electrochemical impedance spectroscopy of porous electrodes: The effect of pore size distribution," *Electrochim. Acta*, vol. 44, no. 20, pp. 3513–3519, Jun. 1999.

[219] M. Musiani, M. Orazem, B. Tribollet, and V. Vivier, "Impedance of blocking electrodes having parallel cylindrical pores with distributed radii," *Electrochim.*

Acta, vol. 56, no. 23, pp. 8014–8022, Sep. 2011.

[220] Y. Gourbeyre, B. Tribollet, C. Dagbert, and L. Hyspecka, "A Physical Model for Anticorrosion Behavior of Duplex Coatings," *J. Electrochem. Soc.*, vol. 153, no. 5, p. B162, Mar. 2006.

[221] P. H. Nguyen and G. Paasch, "Transfer matrix method for the electrochemical impedance of inhomogeneous porous electrodes and membranes," *J. Electroanal. Chem.*, vol. 460, no. 1–2, pp. 63–79, Jan. 1999.

[222] C. C. L. McCrory, S. Jung, J. C. Peters, and T. F. Jaramillo, "Benchmarking heterogeneous electrocatalysts for the oxygen evolution reaction," *J. Am. Chem. Soc.*, vol. 135, no. 45, pp. 16977–16987, 2013.

[223] C. X. Guo and C. M. Li, "Room temperature-formed iron-doped nickel hydroxide on nickel foam as a 3D electrode for low polarized and high-current-density oxygen evolution," *Chem. Commun.*, vol. 54, no. 26, pp. 3262–3265, Mar. 2018.

[224] X. Lu and C. Zhao, "Electrodeposition of hierarchically structured three-dimensional nickel-iron electrodes for efficient oxygen evolution at high current densities," *Nat. Commun.*, vol. 6, p. 6616, 2015.

[225] G. Dong *et al.*, "In situ formation of highly active Ni-Fe based oxygen-evolving electrocatalysts via simple reactive dip-coating," *J. Mater. Chem. A*, vol. 5, no. 22, pp. 11009–11015, Jun. 2017.

[226] Y. Li *et al.*, "Electrodeposited ternary iron-cobalt-nickel catalyst on nickel foam for efficient water electrolysis at high current density," *Colloids Surfaces A Physicochem. Eng. Asp.*, vol. 506, pp. 694–702, Oct. 2016.

[227] Zhiyi Lu, Yingjie Li, Xiaodong Lei, Junfeng Liu, and Xiaoming Sun, "Nanoarray based 'superaerophobic' surfaces for gas evolution reaction electrodes," *Mater. Horizons*, vol. 2, no. 3, pp. 294–298, Apr. 2015.

[228] W. Fritz, "Berechnung des maximalvolumes von dampfblasen," *Phys. Zeitschr*, vol. 36, pp. 379–384, 1935.

[229] A. Lewandowska-Bernat and U. Desideri, "Opportunities of power-to-gas technology in different energy systems architectures," *Appl. Energy*, vol. 228, pp. 57–67, Oct. 2018.

[230] Y. Ping, G. Galli, and W. A. Goddard, "Electronic structure of IrO2: The role of the metal d orbitals," *J. Phys. Chem. C*, vol. 119, no. 21, pp. 11570–11577, May 2015.

[231] N. T. Suen, S. F. Hung, Q. Quan, N. Zhang, Y. J. Xu, and H. M. Chen, "Electrocatalysis for the oxygen evolution reaction: Recent development and future perspectives," *Chem. Soc. Rev.*, vol. 46, no. 2, pp. 337–365, 2017.

[232] Y. Li *et al.*, "Recent Advances on Water-Splitting Electrocatalysis Mediated by Noble-Metal-Based Nanostructured Materials," *Advanced Energy Materials*, vol. 10, no. 11. 2020.

[233] L. She, G. Zhao, T. Ma, J. Chen, W. Sun, and H. Pan, "On the Durability of Iridium-Based Electrocatalysts toward the Oxygen Evolution Reaction under Acid Environment," *Adv. Funct. Mater.*, vol. 32, no. 5, p. 2108465, Jan. 2022.

[234] V. Vij *et al.*, "Nickel-based electrocatalysts for energy-related applications: Oxygen reduction, oxygen evolution, and hydrogen evolution reactions," *ACS Catal.*, vol. 7, no. 10, pp. 7196–7225, Oct. 2017.

[235] X. Cui, W. Li, P. Ryabchuk, K. Junge, and M. Beller, "Bridging homogeneous and heterogeneous catalysis by heterogeneous single-metal-site catalysts," *Nat. Catal.*, vol. 1, no. 6, pp. 385–397, 2018.

[236] Z. W. She, J. Kibsgaard, C. F. Dickens, I. Chorkendorff, J. K. Nørskov, and T. F. Jaramillo, "Combining theory and experiment in electrocatalysis: Insights into materials design," *Science (80-.).*, vol. 355, no. 6321, p. eaad4998, Jan. 2017.

[237] A. Angulo, P. van der Linde, H. Gardeniers, M. Modestino, and D. Fernández Rivas, "Influence of Bubbles on the Energy Conversion Efficiency of Electrochemical Reactors," *Joule*, vol. 4, no. 3. Cell Press, pp. 555–579, 18-Mar-2020.

[238] F. Yang, M. J. Kim, M. Brown, and B. J. Wiley, "Alkaline Water Electrolysis at 25 A cm−2 with a Microfibrous Flow-through Electrode," *Adv. Energy Mater.*, vol. 10, no. 25, p. 2001174, Jul. 2020.

[239] A. Rawal *et al.*, "Metastable wetting model of electrospun mats with wrinkled fibers," *Appl. Surf. Sci.*, vol. 551, p. 149147, Jun. 2021.

[240] M. Maier *et al.*, "Diagnosing Stagnant Gas Bubbles in a Polymer Electrolyte Membrane Water Electrolyser Using Acoustic Emission," *Front. Energy Res.*, vol. 8, p. 268, Oct. 2020.

[241] M. Ramiasa, J. Ralston, R. Fetzer, and R. Sedev, "The influence of topography on dynamic wetting," *Adv. Colloid Interface Sci.*, vol. 206, pp. 275–293, Apr. 2014.

[242] J. K. Lee *et al.*, "Critical Current Density as a Performance Indicator for Gas-Evolving Electrochemical Devices," *Cell Reports Phys. Sci.*, vol. 1, no. 8, p. 100147, Aug. 2020.

[243] A. Vazquez, R. M. Sanchez, E. Salinas-Rodríguez, A. Soria, and R. Manasseh, "A look at three measurement techniques for bubble size determination," *Exp. Therm. Fluid Sci.*, vol. 30, no. 1, pp. 49–57, Oct. 2005.

[244] R. de Levie, "On the impedance of electrodes with rough interfaces," *J. Electroanal. Chem. Interfacial Electrochem.*, vol. 261, no. 1, pp. 1–9, Mar. 1989.

[245] M. Duca, E. Guerrini, A. Colombo, and S. Trasatti, "Activation of Nickel for Hydrogen Evolution by Spontaneous Deposition of Iridium," *Electrocatalysis*, vol. 4, no. 4, pp. 338–345, Aug. 2013.

[246] S. R. Mellsop, A. Gardiner, and A. T. Marshall, "Spontaneous Deposition of Iridium onto Nickel Substrates for the Oxygen Evolution Reaction," *Electrocatalysis*, vol. 7, no. 3, pp. 226–234, May 2016.

[247] E. L. Ratcliff *et al.*, "Evidence for near-Surface NiOOH Species in Solution-Processed NiO x Selective Interlayer Materials: Impact on Energetics and the Performance of Polymer Bulk Heterojunction Photovoltaics," *Chem. Mater.*, vol. 23, no. 22, pp. 4988–5000, Nov. 2011.

[248] S. Bhattar *et al.*, "110th Anniversary: Dry Reforming of Methane over Ni-and Sr-Substituted Lanthanum Zirconate Pyrochlore Catalysts: Effect of Ni Loading," *Ind. Eng. Chem. Res.*, vol. 58, no. 42, pp. 19386–19396, Oct. 2019.

[249] Y. Zhang *et al.*, "Atomic Iridium Incorporated in Cobalt Hydroxide for Efficient Oxygen Evolution Catalysis in Neutral Electrolyte," *Adv. Mater.*, vol. 30, no. 18, p. 1707522, May 2018.

[250] M. Hao *et al.*, "Vertically Aligned Ni Nanowires as a Platform for Kinetically Limited Water-Splitting Electrocatalysis," *J. Phys. Chem. C*, vol. 123, no. 2, pp. 1082–1093, Jan. 2019.

[251] R. Gómez and M. J. Weaver, "Electrochemical Infrared Studies of Monocrystalline Iridium Surfaces. Part 2: Carbon Monoxide and Nitric Oxide Adsorption on Ir(110)," *Langmuir*, vol. 14, no. 9, pp. 2525–2534, Apr. 1998.

[252] R. Woods, "Hydrogen adsorption on platinum, iridium and rhodium electrodes at reduced temperatures and the determination of real surface area," *J. Electroanal. Chem. Interfacial Electrochem.*, vol. 49, no. 2, pp. 217–226, Jan.

1974.

[253] T. Reier *et al.*, "Molecular insight in structure and activity of highly efficient, low-Ir Ir-Ni oxide catalysts for electrochemical water splitting (OER)," *J. Am. Chem. Soc.*, vol. 137, no. 40, pp. 13031–13040, Oct. 2015.

[254] F. Drault, C. Comminges, F. Can, L. Pirault-Roy, F. Epron, and A. Le Valant, "Palladium, Iridium, and Rhodium Supported Catalysts: Predictive H2 Chemisorption by Statistical Cuboctahedron Clusters Model," *Mater. 2018, Vol. 11, Page 819*, vol. 11, no. 5, p. 819, May 2018.

[255] Y. H. Fang and Z. P. Liu, "Tafel Kinetics of Electrocatalytic Reactions: From Experiment to First-Principles," *ACS Catal.*, vol. 4, no. 12, pp. 4364–4376, Dec. 2014.

[256] J. F. Moulder, W. F. Stickle, P. E. Sobol, and K. D. Bomben, *Handbook of X-ray photoelectron spectroscopy: a reference book of standard spectra for identification and interpretation of XPS data*. Eden Prairie Minn.: Physical Electronics Inc., 1992.

[257] A. Papaderakis *et al.*, "Oxygen Evolution at IrO2 Shell–Ir−Ni Core Electrodes Prepared by Galvanic Replacement," *J. Phys. Chem. C*, vol. 120, no. 36, pp. 19995–20005, Sep. 2016.

[258] J. Mozota and B. E. Conway, "Surface and bulk processes at oxidized iridium electrodes—I. Monolayer stage and transition to reversible multilayer oxide film behaviour," *Electrochim. Acta*, vol. 28, no. 1, pp. 1–8, Jan. 1983.

[259] M. Alsabet, M. Grden, and G. Jerkiewicz, "Electrochemical Growth of Surface Oxides on Nickel. Part 2: Formation of β-Ni(OH)2 and NiO in Relation to the Polarization Potential, Polarization Time, and Temperature," *Electrocatalysis*, vol. 5, no. 2, pp. 136–147, Apr. 2014.

[260] J. R. Manders *et al.*, "Solution-Processed Nickel Oxide Hole Transport Layers in High Efficiency Polymer Photovoltaic Cells," *Adv. Funct. Mater.*, vol. 23, no. 23, pp. 2993–3001, Jun. 2013.

[261] S. Uhlenbrock, C. Scharfschwerdt, M. Neumann, G. Illing, and H. J. Freund, "The influence of defects on the Ni 2p and O 1s XPS of NiO," *J. Phys. Condens. Matter*, vol. 4, no. 40, p. 7973, Oct. 1992.

[262] Q. Zhou *et al.,* "Active-Site-Enriched Iron-Doped Nickel/Cobalt Hydroxide Nanosheets for Enhanced Oxygen Evolution Reaction," *ACS Catal.*, vol. 8, no.

6, pp. 5382–5390, Jun. 2018.

[263] M. J. Eslamibidgoli, A. Groß, and M. Eikerling, "Surface configuration and wettability of nickel(oxy)hydroxides: A first-principles investigation," *Phys. Chem. Chem. Phys.*, vol. 19, no. 34, pp. 22659–22669, Aug. 2017.

[264] Y. J. Kim *et al.*, "Highly efficient oxygen evolution reaction via facile bubble transport realized by three-dimensionally stack-printed catalysts," *Nat. Commun.*, vol. 11, no. 1, pp. 1–11, 2020.

[265] Y. Li *et al.*, "High-speed characterization of two-phase flow and bubble dynamics in titanium felt porous media for hydrogen production," *Electrochim. Acta*, vol. 370, p. 137751, Feb. 2021.

[266] K. Li *et al.*, "Visualizing highly selective electrochemical CO2 reduction on a molecularly dispersed catalyst," *Mater. Today Phys.*, vol. 19, p. 100427, Jul. 2021.

[267] A. Lasia, *Electrochemical impedance spectroscopy and its applications*, vol. 9781461489. 2014.